UAB
Universitat Autònoma de Barcelona

Use of Inkjet Printing to Obtain YBa2Cu3O7-x Thick Films by TLAG-CSD Process

Adrià Pacheco Aceña

Universitat Autònoma de Barcelona

PhD Thesis

Use of Inkjet Printing to Obtain $YBa_2Cu_3O_{7-x}$ Thick Films by TLAG-CSD Process

Adrià Pacheco Aceña

2023

Supervised by:

Dra. Susagna Ricart Miró

Prof. Teresa Puig Molina

Tutored by:

Dr. Ramón Yáñez López

ICMAB

PhD program in Materials Science

Chemistry Department - Science Faculty

CSIC

Susagna Ricart Miró, Científica Titular a l'Institut de Ciència de Materials de Barcelona, Teresa Puig Molina, Professora de Investigació a l'Institut de Ciència de Materials de Barcelona, i Ramón Yáñez López, Professor a la Universitat Autònoma de Barcelona.

CERTIFIQUEN

que Adrià Pacheco Aceña, Graduat en Química, ha dut a terme sota la seva direcció el treball que porta per títol "Superconducting YBCO thick films by Inkjet Printing Technology through TLAG-CSD Process'' i queda recollit en aquesta memòria per optar al Grau de Doctor.

I per a que així consti, signen el present certificat.

Dr. Susagna Ricart Miró Prof. Teresa Puig Molina Dr. Ramón Yáñez López

Adrià Pacheco Aceña

Bellaterra, 2023

A la meva família

A la Victòria i els meus amics

Contents

Acknowledgments

I would start to profusely thank the institution and its people (ICMAB-CSIC) that have allowed me to perform the Philosophical Degree Program (PhD) in Materials Science with them and have made this thesis possible.

First, thanks to my thesis directors and supervisors Dr. Susagna Ricart, Prof. Teresa Puig and Dr. Ramón Yañez for the opportunity to work and study with them; their unconditional support, good guidance and confidence let me finish and present the results of this thesis. Also, I want to thank Prof. Teresa Puig and Prof. Xavier Obradors for letting me be part of the Superconducting Materials and Large Scale Nanostructures (SUMAN) group, which has been the best years of my professional career.

Thanks to the collaboration of scientific experts in characterization fields. I want to deeply thank A. Crespi, J.B. Esquius, F.J. Campos, N. Romà, L. Morrone, M. Gerbolés, V. Lloveras, J. Oró, K. Gupta, J. Farjas, P. Roura, B. Bozzo, A.E. Carrillo and F. Vallés for all the characterization measurements done throughout this thesis. I would like to thank all my fellow PhD students and co-workers; C. Pop, J. Banchewski, A. Romanov, M. Sieger, F. Pino, M. De Palau, J. Bailo, R. Vlad, K. Gupta, A. Kethamkuzhi, P. Barusco, G. Telles, P. Machado, M. Mirjolet, A. Fernandez, M. Tristany, F. Vallés, J. Jareño, L. Soler, B. Villarejo and specially D. García and L. Saltarelli, for all the good moments we had during these years.

I acknowledge financial support from Spanish Ministry of Science, Innovation and Universities through the “Severo Ochoa” Program for Centres of Excellence in FUNFUTURE (CEX2019-000917-S), SUMATE project (RTI2018-095853-B-C21, co-financed by the European Regional Development Fund, MCIU/AEI/FEDER, UE) and IMPACT project (ERC-2019-PoC-874964). Also ULTRASUPERTAPE project (ERC-2014-ADG-669504) and from the Catalan Government with 2017-SGR-1519.

Finally, to all my friends, to my fiancé V. Perea, and of course to my all family, specially to my parents J. Pacheco and F. Aceña and my sisters A. and N. Pacheco. Their love and unconditional support means the world to me.

Moltes gràcies a tothom!

Index of Abbreviations

Ac – Acetate (CH_3COO^-)

AC – Alternating Current

APC – Artificial Pinning Centres

BCS - Bardeen–Cooper–Schrieffer theory

BYF – Barium-Yttrium Fluoride complex

CCs – Coated Conductors

CSD - Chemical Solution Deposition

DoD – Drop-on-Demand

EA - Ethanolamine

EGA - Evolved Gas Analysis

FF – Fluorine-Free

FTIR – Fourier-Transformed Infrared

Hc - Critical Magnetic Field

HF – Hydrofluoric Acid

HTS – High Temperature Superconductors

IBAD - Ion Beam Assisted Deposition

ICMAB – Institut de Ciència de Materials de Barcelona (ICMAB-CSIC)

IJP - Inkjet Printing

Jc - Critical Current Density

LAO - (00l)-oriented single-crystal substrate of $LaAlO_3$

LF – Low Fluorine

LSMO - Lanthanum strontium manganite ($La_{1-x}Sr_xMnO_3$) buffer layer

LTS – Low-Temperature Superconductors

MOCVD - Metalorganic Chemical Vapour Deposition

MOD - Metalorganic Decomposition

MS – Mass Spectrometry

OM – Optical Microscopy

PLD – Pulsed Laser Deposition

PPMS - Physical Properties Measurement System

Prop - Propionate

Prop – Propionate ligand (CH_3CH_2COO)

PTFE – Polyethylene Terephthalate

RABiTS - Rolling Assisted Biaxial Textured Substrates

RE – Rare Earth

SQUID - Superconducting Quantum Interference Device (SQUID) magnetometer

STO - (00l)-oriented single-crystal substrate of $SrTiO_3$

SuNAM - SuNAM Co,. Ltd. South Korea Manufacturers and suppliers

Tc - Critical Temperature

TEM – Transmission Electron Microscopy

TFA – Trifluoroacetate

TGA – Thermogravimetric Analysis

TLAG – Transient Liquid Assisted Growth

TMA - Thermomechanical Analysis

UV - Ultraviolet

XRD – X-ray Diffraction

YBCO - $YBa_2Cu_3O_{7-\delta}$

MOTIVATION

The discovery of superconductivity, and specifically the High Temperature Superconducting (HTS) materials, present an opportunity to transition from the non-sustainable fossil fuel consumption to the usage of more sustainable green energies (among others), motivated by their special electrical properties. The unique properties of a superconductor, mostly regarding their capacity to achieve large current transport without losses, makes them suitable for the application of novel strategies for high power managing and transportation. Among HTS materials, the c-oriented epitaxial $YBa_2Cu_3O_{7-\delta}$ (YBCO) currently presents the most efficient electrical performance, and it's the most studied of them.

The initial push of the superconducting industry was made with several film deposition techniques to achieve epitaxial growth, necessary to transport large electric currents through the YBCO material. Fabrication techniques were initially based on the use of high vacuum techniques, such as PLD or MOCVD, which highly increases its manufacture costs. However, Chemical Solution Deposition (CSD) methods later appeared as an alternative methodology. The availability of low-cost chemical solutions of metalorganic compounds and the high control during the synthesis, makes it a very successful synthetic route for the production of high-quality and scalable materials at industrial level.

Moreover, Printed Electronics have emerged on the last decades with strong potential, like Inkjet Printing (IJP) deposition. It enables to used Chemical Solution Deposition (CSD) by the deposition of chemical solutions in the form of small drops, at a range of picolitres (pL), on a predefined pattern. Therefore, this opened high prospection into CCs tapes with the use of reel-to-reel compatible deposition methodologies, attractive at industrial scale. The idea of achieving high film thickness in one single deposition of REBCO precursors was the aim of this Thesis.

A novel drop-on-demand IJP deposition methodology for the preparation of thick YBCO films based on Fluorine-free (FF) precursor solutions is presented. The advantage relies on the high throughput advantages of the FF precursors if used in combination with TLAG growth (Transient Liquid Assisted Growth of CSD layers) with ultrafast growth rates (>1000 nm/s). The use of different additives, deposition and evaporation strategies, together with the rheological properties of the solution, its thermogravimetric analysis, such as the decomposition pathways of the precursors and the identification of stress-relief mechanisms, have been analysed using advanced in-situ characterization techniques in order to obtain homogenous depositions and defect-free pyrolized films with high thicknesses (~1000 nm. YBCO films). The work of this Thesis is distributed and described in the following chapters:

- Chapter 2: Description of Materials and Methods used throughout the thesis.
- Chapter 3: Inkjet Printing deposition on the homemade apparatus. Description of the procedure, analysis and discussion of the results. Use of in-situ characterization techniques with the intention to achieve crack-free thick samples at fast rates of deposition.
- Chapter 4: Inkjet Printing deposition using a discrete grid methodology. Description of the procedure and the characterization tools used for the correct optimization of the process to ensure good film homogeneity and crack-free thick layers. Description of high-throughput experimentation (HTE) and chemical combinatorial studies.
- Chapter 5: Inkjet Printing deposition using a continuous grid methodology to obtain defect-free thick samples, with or without substrate heating, over single crystals and CCs substrates. Discussion of the results by using in-situ characterization techniques. Evaluation of the compatibility of the TLAG growth method for thick inkjet printed films.

The combination of Inkjet Printing technologies and TLAG-CSD allows the fabrication of YBCO films with high throughput in a reproducible way, thus reducing the cost of a scalable industrial process of superconducting coated conductors of interest for the market.

1.

INTRODUCTION

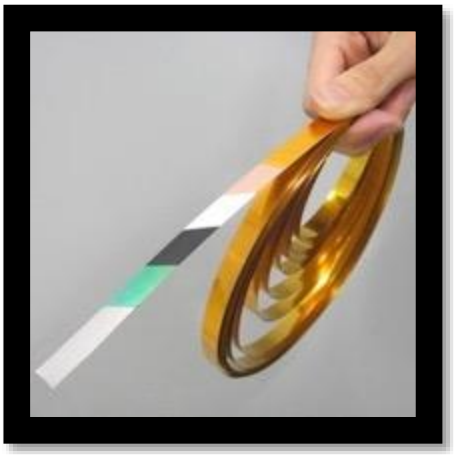

The discovery of high temperature superconducting materials supposes an opportunity to transition from the non-sustainable fossil fuel consumption to the usage of more sustainable green energies. The unique properties of the superconductor materials, regarding their capacity to achieve large current transport without energy losses, make them suitable for high power generation, transmission and distribution applications.

Here, we describe the theoretical concepts related to the superconducting phenomenon, the chemical solution deposition methodology, as well as the combination of Inkjet Printing technologies with TLAG-CSD methods for the reproducible synthesis of thick YBCO films. Inkjet printing deposition methods are complex systems, relying in the proper jetting of precursor solution drops and its rheology to achieve thick homogenous films. In this chapter we will describe the concepts of inkjet printing, as well as fluid dynamics and the influence of the rheological parameters of the solution, affecting jetting, wetting and proper liquid distribution to reach thick homogenously distributed YBCO layers.

1.1 The Superconductivity phenomenon

Nowadays, superconducting materials are used in many applications, starting from the generation of electrical power, transmission (power cables), distribution (transformers) and end-use machinery (motors, medical devices), with perspectives on the generation of renewable source energies, reducing CO_2 emissions and further reduce other impacts on the environment like with fusion reactors [**1-6**], making them attractive to the general market. However, the superconductivity phenomenon is still a relatively young theory, and is a subject of debate in relation to its properties at microscopic scale due to its implications in quantum mechanics, based on the BCS theory and the formation of Cooper pairs, outside of the classical physics.

The superconducting phenomenon was first discovered by K. Onnes in 1911 by cooling mercury in liquid helium (4.2K). The metal properties below a certain temperature gave rise to a perfect diamagnetic behaviour, known as Meissner effect, which consisted of the expulsion of magnetic flux from the interior of the material, but also to a zero electrical resistance, which could, in principle, lead to astonishing amounts of electrical current transportation [**7**].

The superconducting phenomenon is limited by three magnitudes, different for every superconducting material. When surpassing any of these magnitudes, superconductivity is lost in the material. These are: the critical temperature (Tc), which is the transition temperature of the material from the superconducting state to its normal state, which depend on the material; the critical magnetic field (Hc), if the applied magnetic field rises above the critical field value, the material breaks the superconducting state; and the critical current density (Jc), which is the representation of the maximum current density achieved by the superconducting material at a given temperature and magnetic field. From the application point of view, it is desirable that the superconducting material displays the highest possible values of these parameters [**7-9**].

1.1.1 Types of superconductors

Superconducting materials can be divided in type I and type II superconductors. Usually, type I superconductors have a very low Tc but also a very low Hc, and consequently Jc, so their applications are limited to electronic devices. These are low temperature superconductors (LTS), such as metal elements. Instead, type II superconductors have two critical fields (Hc_1 and Hc_2) [7]. Between these two different critical magnetic fields, type II superconductors enter a new state, called mixed state. Tc can be low or high, as well as Hc_1, Hc_2 or Jc. Type II superconductors are metal alloys (like NbTi and Nb_3Sn families) and high temperature superconductors (HTS), among others.

For type II superconductors, below the first critical field Hc_1, the material is in the Meissner state, expelling magnetic flux from the interior and showing a perfect diamagnetic behaviour, with a similar performance as type I ones [**8**]. However, differently to type I, once H_{c1} is surpassed, instead of losing the superconducting state, the material enters a mixed state, where the magnetic field is able to penetrate into the material through quantized cylindrical magnetic fluxes, called vortices, as represented in Figure 1.1:

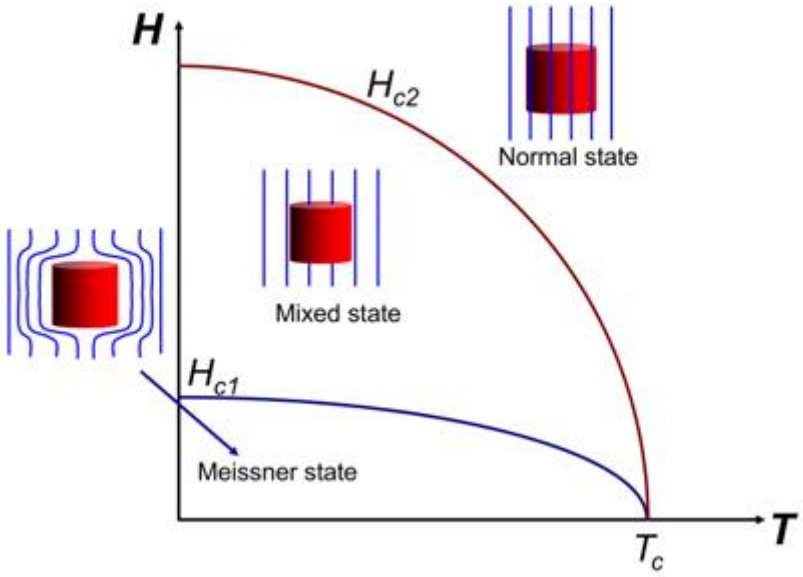

Figure 1.1. *H-T diagram for type II superconductors, showing the Meissner and mixed states.*

The vortices are in fact several interfaces between the normal and the superconducting state of the material; inside those vortices, the material remains in its normal state. Considering the vortices as cylindrical, its core radius takes the value of coherence length (ξ), which is surrounded by coupled electrons, called Cooper pairs, responsible for the superconductivity phenomenon [**9**]. The coherence length is then the distance between the electrons forming the Cooper pair. Additionally, the decay distance from a superconducting interface to a normal one of the magnetic field is called penetration depth (λ). In the case of the vortex, the penetration length denotes the distance where the superconducting currents circulate. Since those currents generate a flux quantum in each vortex, the magnetic flux that each vortex generates is quantized [**10**].

The motion of the vortices is influenced by both the current and magnetic field that each vortex experience. It is important to remark that vortex motion generates dissipation (due to the non-electron pairing of the vortex core electrons), which limit the ability to transport current at zero resistance. If those vortices remain static however, high current percolation can be achieved without destroying the superconducting state [**11-13**]. As long as the magnetic field applied increases, from Hc_1 to Hc_2, the number of vortices in the superconducting material increases. Above Hc_2, the vortex core overlap producing a homogenous magnetic flux that penetrates the whole material with no Cooper pair formation. At this point, the superconducting state breaks, transitioning to its fully normal state.

The motion of the vortices is determined by the Lorentz force (equation 1.1), which is induced by the current that circulates through the material once it is in the mixed state. This force depends on the amount of current and the magnetic field applied. Since the forces induce movement on the vortices, and the vortices core are in the normal state of the material, dissipation of energy occurs based on the electric field, being unable to properly transport current at zero resistance, thus locally breaking the superconducting state [**14**].

The Lorentz force and the electric field are represented in the following equations:

$$F_L = J \times B \quad (1.1)$$

$$E = B \times v \quad (1.2)$$

Being F_L the Lorentz force, J the current density, E the electric field, v the local vortex velocity and B the magnetic field induction.

In order to avoid such energy dissipation, vortices must remain static (v = 0). One very effective way to keep vortices is to pin them in material imperfections where the superconductivity is already lost. This series of defects should have similar dimensions as the vortex core. Therefore, there is always a strong effort to control and tune the microstructure of superconductors. For HTS, where the coherence length is of just a few nanometers, such defects are oxygen vacancies, non-superconducting secondary phases, nanoparticles (NPs) up to strain fields, dislocations or twin boundaries. Such effective crystalline defects are called vortex pinning centres, by which added synthetically, are usually called artificial pinning centres (APC) [**15-17**].

The artificial pinning centres induce an opposite force to the Lorentz force onto the vortices that is called pinning force (F_p) [**18**]. Only if the Lorentz force is superior to the pinning force, vortices are able to move, thus dissipation occurs. This implies that there exists a maximum current density that would keep vortices immobilized, generating no dissipation, called the critical current density, Jc. If the current density exceeds Jc, vortices move and T dissipation occurs.

$$Fp = Jc \times B \quad (1.3)$$

In a H-T diagram, we are able to differentiate between these two possible outcomes by an irreversibility line. Separating the regions where, despite being in the superconducting state, the material shows electrical resistance, thus Jc is zero, from a region where the artificial pinning centres are effectively pinning the vortices, allowing the supercurrent to percolate (Jc is different from zero). The superconducting state finally vanishes above Hc_2 (T) [**6**].

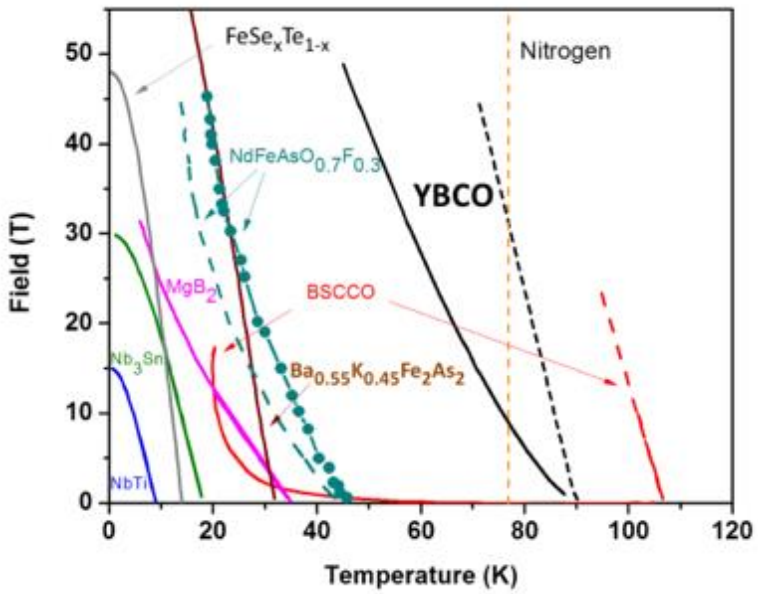

Figure 1.2. *H-T diagram for different commercial superconductors. The dashed line represents the theoretical superconducting limits, while the solid line are the real barriers or irreversibility lines [].*

Since in terms of application, superconductors are usually required to show no dissipation, it is desirable that the superconductor material has the highest irreversibility line as possible (see figure 1.2). Among the superconducting materials, the cuprate family of superconductors, and specially YBCO, display high irreversibility lines together with a high Tc [**19**]. At 77K, the temperature of liquid nitrogen, and even though YBCO does not have the highest critical temperature, it exhibits the highest irreversibility line, thus becoming one of the most well studied materials by being one of the most suitable materials for applications.

1.1.2 Cuprate Superconducting Materials

As describe in the last section, cuprates are very promising candidates for many applications. However, the superconducting performance of the cuprate family is strongly affected by various factors such as their anisotropy, complex flux-pinning centres, and grain-boundary weak-link effects, which were major constraints in realizing practical application for many years [**20-21**]. Nonetheless, with the current state-of-the-art, these related issues were solved, as will be described in the next section.

Among the different cuprates, yttrium-barium-copper oxide ($YBa_2Cu_3O_{7-\delta}$ or YBCO) is the material with the best performance. First discovered in 1987, with a Tc of 92K, its large critical current and high irreversibility field makes it ideal for applications [**22-23**]. YBCO, like the rest of the superconducting cuprates family, has a short coherence length (ξ= 1.41±0.04nm [**24**]) which limits effective flux pinning centres to nanometric non-superconducting defects. For this reason, artificial vortex pinning centres are added into the material to reach high critical currents. One of the most effective APC has been the development of what is called superconducting nanocomposites [**25]**.

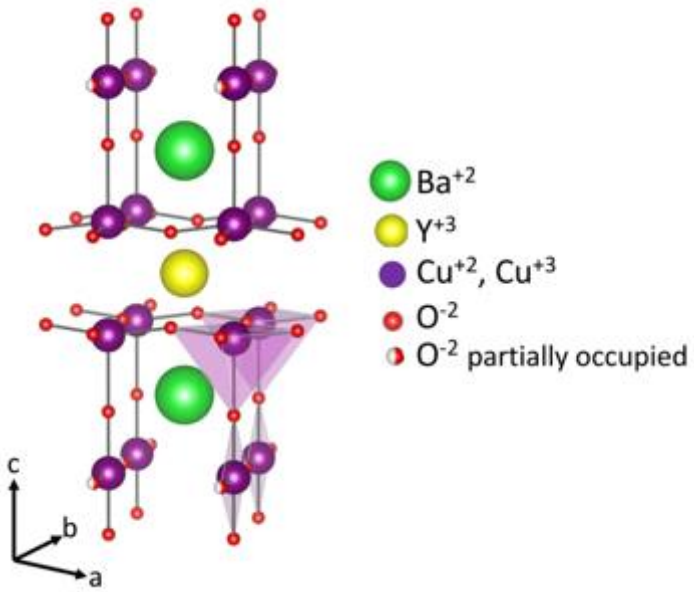

Figure 1.3. *YBCO perovskite crystalline structure showing the CuO planes and the CuO chains.*

$YBa_2Cu_3O_{7-\delta}$ has an orthorhombic structure (Fig. 1.2) which can be described by the stacking along the c-axis of three pseudo-cubic ABA perovskite units, $BaCuO_3$ (A) -$YCuO_3$ (B)- $BaCuO_3$ (A), with some degree of oxygen deficiency, given by δ. The oxygen doping state determines the Tc of YBCO, with a maximum for $\delta = 0.07$ with Tc ~ 92 K [**26**]. The presence of superconductivity can be ascribed to a mixed-valence character of copper due to oxygen deficiency [**27-28**].

The CuO_2 planes located around the central $YCuO_3$ unit are the ones carrying the superconductivity. These planes are separated by charge reservoir layers containing CuO chains that determine the final Cooper pair density in the Cu_2O planes. Due to the anisotropic character of YBCO, current percolation is not the same in all crystallographic directions. Therefore, during crystallization of YBCO films, all grains must be biaxially oriented in the right direction (c-axis perpendicular to the substrate plane) in order to reach the maximum superconducting performance.

Consequently, the transport current of these materials is strongly limited by the grain boundaries of the crystal; they become barriers to achieve current percolation if high angles are reached [**29**]. Therefore, to find method to grow YBCO biaxially aligned films was crucial to reach competitive performances for applications.

1.1.3 Coated Conductors

Cuprate superconducting compounds such as YBCO are ceramic oxide materials. This implies that they are brittle materials, difficult to process, which require a substrate with enough flexibility to enable the fabrication of long tapes. So, new substrate technologies had to be developed. Coated conductors are based on a multilayer architecture deposited on metallic substrates. To reach the full potential of HTS superconductors as an engaging material in industry, for example for power applications, some technological barriers must be accounted [**30-37**].

The manufacture of HTS materials must have a reduced and competitive cost to be attractive for the market, while still showing high superconducting performances [**30**]. In this regard, the selection of the substrate is dictated by both the film/substrate and thermal expansion coefficient mismatches but also chemical compatibility [**31**]. For this reason, the introduction in the manufacturing process of a template, which induces the desired biaxial texture on YBCO, is absolutely crucial not only to increase competitiveness but to make it suitable for the actual applications.

In the case of YBCO, the development of coated conductors (CC's) (initially referred to second generation conductors (2G) to distinguish them from the unsuccessful first generation (for YBCO) powder-in-tube), was an appealing solution [**36-37**]. Coated conductors are based on a multilayer architecture, with the superconducting layer deposited on top of a successive number of oxide buffer layers deposited on flexible metallic substrates. Finally, the superconducting layer is protected with a silver and copper layers.

There are two principal approaches to achieve long length biaxally textured coated conductors. One is based on the substrate technology called Rolling Assisted Biaxial Textured Substrates (RABiTS) [**38**], and the other is based on the Ion Beam Assisted Deposition (IBAD) technology [**39-41**]. In the RABiTS procedure, the metallic substrate itself, being usually Ni-based, is textured by thermomechanical treatments, which provides an adequate textured template for the subsequent deposition of buffer and YBCO coatings.

In the IBAD approach, a double ion beam irradiates non-textured substrates (usually hastelloy). One serves to deposit an oxide layer (usually MgO or YSZ) and the other, an Ar beam directed in a particular angle, eliminates the grains of this oxide layer growing with a non-epitaxial relationship. In both substrates' technologies, the selection of the successive buffer layers is dictated by the thermal expansion coefficient, the mismatch and the chemical compatibility [**38-41**].

However, in contrast to the use of (00l)-oriented single-crystal substrates ($SrTiO_3$ (STO) or $LaAlO_3$ (LAO)), the metallic substrates, the first layer used in the fabrication of CCs, has an inherent granularity on the microscopic scale which usually is translated into the final structure and more importantly in the YBCO layer [**30**]. Since there is a strong dependence of Jc with grain misorientation of the layer beyond 4-5º [**36**], there was a requirement for a continuous improvement of the texture quality. Nowadays, most fabrication industries are using the IBAD technology which has demonstrated a biaxial texture of 2-3º, enabling superconducting CC's performances alike those achieved with YBCO films grown on single crystals.

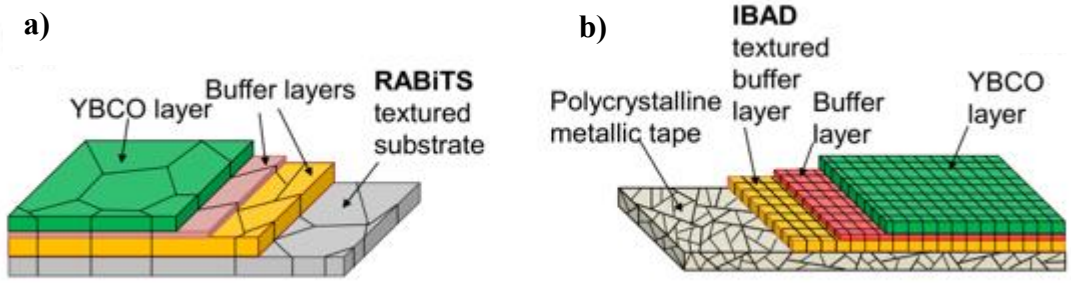

Figure 1.4. *Coated Conductors (CC's). a) RABITS architecture and b) IBAD architecture approach.*

Another of the limitations that needs to be solved, for the generation of YBCO superconductors, is related to vortex pinning. There is the requirement to create efficient artificial pinning centres to impede vortex motion as much as possible. In this respect, the development of nanocomposites (superconducting layers with dispersed non-superconducting nanophases) has emerged as one of the best solutions [**42**]. Cost-effective scalable deposition processes are necessary to make CCs attractive at industrial scale. To that end, the implementation of chemical solution deposition (CSD) methods in combination with printing technologies is a huge opportunity. Printing technologies adapted to reel-to-reel fabrication like slot die, dip coating or inkjet printing have been investigated [**43**]. However, the latter has been the less investigated of them. It is the purpose of this thesis to deepen into this technique and evaluate the possibilities that it has to offer.

1.2 Chemical Solution Deposition Methods

Chemical solutions deposition (CSD) methods are widely known for the preparation of functional materials, especially for ceramic oxides, achieving high performances on bulk, coatings or nanoparticles among other materials [**44-47**]. The technique relies on the optimization of chemical solutions containing the cation precursors necessary to form the subsequent functional materials, with a high degree of control over the composition, such as its stoichiometry, opening the possibility for the preparation of a wide range of materials with different compositions. Furthermore, the ability to scale-up its manufacturing process makes it an attractive methodology for industry in various applications.

The flexibility of the CSD methods allow for the design of many chemical solutions that involve different chemical precursors, solvents, and additives, which usually determines its final thickness and quality of the samples, based on total molar concentration and rheological properties. This mainly involves an optimized ink being able to obtain homogenous depositions and homogenous distribution of the microstructure for a proper efficiency on further applications [**44-45**]. The CSD methodology is based upon three main steps, which consist of the design and preparation of the precursor solution (1), its deposition (2) and a thermal treatment after the deposit (3).

It is important that the designed precursor solution matches well with the characteristics and parameters of the deposition technique used to obtain homogenous films. For a proper wetting of the substrate, being the adjustment of the rheological properties of the solution to avoid thickness variations (striations) or crack formation, the solution parameters must be properly controlled [**48**]. Usual CSD techniques are spin-coating, slot die coating and dip coating, among others; or inkjet printing, which in this case will be the main deposition technique used for the preparation of samples throughout this thesis. Finally, once the precursor solution is deposited onto a substrate, a thermal treatment is performed to obtain the desired material.

There are different synthetic routes for the processing of CSD films. Depending on the designed precursor solution, different thermal conditions may be employed to control film densification and crystallization for the proper preparation of the desired oxide phase. Among them, there are the sol-gel processes that uses alkoxides; the Metal Organic Decomposition (MOD) routes that use carboxylate salts; the diol and suspension process; the nitrate, citrate or the Pechini routes; and other hybrid processes [**47**].

For the fabrication of YBCO films, the conventional synthetic treatment is carried out by the Metalorganic Decomposition (MOD) route, one of the most used synthetic routes to obtain functional oxide films [**49**]. MOD routes consist of the use of metalorganic precursors with the desired stoichiometry in appropriate solvents, usually of organic nature such as alcohols and carboxylic acids [**50**], which allows for the characterization of the solution as a simple mixture of the starting compounds.

Following the MOD route for the preparation of YBCO films, a first thermal treatment at low temperatures (500ºC) in oxidizing atmospheres is performed after deposition, which results on the decomposition of the organic matter present in the solution, called a pyrolysis process. This process leads to a mixture of amorphous and nanocrystalline intermediates. Afterwards, a posterior thermal treatment at higher temperatures (>800℃), crystallize the material into the desired ceramic oxide phase.

The MOD process is a very straightforward synthetic route, but it possesses some limitations. For example, film porosity and the complexity of controlling the structural evolution throughout the whole process are important issues associated with this methodology. During the thermal treatment, all the organic matter present in the solution is decomposed, which may lead to an excessive weight loss, causing film cracking [**47**]. The requirements to avoid the formation of defects in the film must be fulfilled by first optimizing the chemical solution.

1.2.1 The Precursor Solution

For the chemical solution deposition (CSD) methods, the solution plays a major role in the process. For instance, the physicochemical properties of the solution will affect the liquid-substrate interaction, which will affect the liquid distribution over the substrate and its homogeneity during deposition [**51**]. For this reason, the usability of the precursor solution for proper homogenous depositions will be by controlling its physicochemical properties such as solution viscosity, density, contact angle, surface tension and the evaporation rate of the carrier solvents, among others. The evaluation of these parameters, whose objective is the proper development of crack-free and homogenous coatings, is crucial. To obtain homogeneous and reproducible films, all the parameters affecting deposition must be properly fine-tuned, therefore, all the components present in the solution must properly optimized. To do so, the solution contains several components necessary to carry out the MOD synthetic route:

- Solvent: The choice of the carrier solvent will strongly determine the deposition process. The solubility, boiling point, vapour pressure and polarity of the ink are the main parameters determined by the solvents used. While the polarity and solubility are important to obtain homogenous solutions, the boiling point and vapour pressure are especially important since, and based on the molecular characteristics, the carrier solvent will severely affect the rheology of the prepared ink and the liquid redistribution over the substrate.

- Solute: The solutes or precursor salts are those chemical components that will be found in the final crystalline phase of the desired material, matching with its proper stoichiometric ratio. Obviously, the selection of the precursor salts must account for a proper dissolution in appropriate solvents. Precipitation of the precursor salts, specially before deposition, produce deviations of the calculated stoichiometry. The selection of the solute, according to the chemical nature of the solvents and themselves, must be made to ensure that the solution does not require any corrections.

- Additives: Additives are chemical compounds (monomers, polymers, stabilizers, surfactants…) used to alter the properties of the solution; either by changing its rheological properties, to achieve a better distribution of the liquid and wetting control; a better dissolution of the precursor salts to improve solution stability, or to avoid the formation of defects on the samples. The additives decompose during the thermal treatment and are not present in the final ceramic oxide phase of the material, but its properties are helpful to avoid undesired side-effects that can occur during the process.

While single solvent inks are usually preferred since the evaporation rate plays a big role in the film homogeneity, the use of additives and co-solvents could enhance the solubility of the precursors ensuring a complete dissolution of the precursors and further solution stability. In the present case, binding different carboxylate ligands to the metals, due to the use of carboxylic acids as co-solvents, produces ligand substitutions of the initial precursors salts and homogenous and stable precursor solutions [**52**].

The use of short carbon chain precursor salts and solvents are very important for the correct processing of the films, using the above-mentioned thermal treatment, as they do not leave any by-product after decomposition [**50**]. As an alternative to minimize the limitations of the MOD strategy, short carbon chains compounds ensure their complete elimination after its thermal decomposition.

In addition, it lowers the organic content of the precursors, further reducing film shrinkage after deposition, decreasing the problems associated to film cracking. In contrast, the use of large carbon-chain carboxylate ligand or acetylacetonate-type compounds may produce film cracking due to an excessive weight loss. Regarding the usage of short carbon chain ligands, carboxylates such as acetates or propionates are the most used precursors in the CSD-MOD techniques due to its fast decomposition with no further impurities or left-overs [**50-53**].

1.2.2 CSD Methods for YBCO Synthesis

CSD methods are widely known for YBCO synthesis, and used in our laboratories [5**4-57**]. Such initial CSD approaches included the use of solutions based on trifluoroacetate (TFA) metalorganic salts, usually referred to as the TFA-CSD route [**58-61**]. The pyrolysis of these precursors forms BaF_2 or mixed Yttrium-Barium Fluoride compounds (BYF) in order to avoid the $BaCO_3$ intermediate precursor, which is difficult to eliminate during the subsequent YBCO thermal crystallization process. But the decomposition of such precursors during the crystallization process it is also the limiting reaction of the process.

Barium Fluoride slowly reacts with water vapour to form the desired $YBa_2Cu_3O_{7-x}$ and hydrofluoric acid (HF) gas, which is highly corrosive. The crystallization is driven by a solid-gas reaction that suffers from low growth rates (1 nm/s) [**54**]. The chemical equations involved in the process are described as follows

$$Y(CF_3COO)_{3(s)} + Ba(CF_3COO)_{2(s)} + Cu(CF_3COO)_{2(s)} \rightarrow Y_2O_{3(s)} + BaF_{2-x}O_{x(s)} + CuO_{(s)} \quad (1.4)$$

$$Y_2O_{3(s)} + BaF_{2-x}O_{x\,(s)} + CuO_{(s)} + H_2O_{(g)} \rightarrow Ba_{1-z}Y_zF_{2-x}O_{x\,(s)} + CuO_{(s)} + H_2O_{(g)} \rightarrow$$

$$YBa_2Cu_3O_{7-x(s)} + HF_{(g)} \uparrow \quad (1.5)$$

To reduce the amount of formed HF, more recent research is directed towards reducing the Fluorine content, called Low-Fluorine routes [**62-63**], where some of the trifluoroacetate salts are replaced with Fluorine-free precursor salts. Still, the chemical reactions and growth mechanism is the same, and as such, are affected by the same limitations since the crystallization is driven by a solid-gas reaction that suffers from low growth rates, while HF is still formed during the thermal treatment. As a possible alternative, new routes have been explored by using full Fluorine-Free precursor solutions. Although less explored, non-halogen carboxylate-based solutions have been reported [**64-67**].

These routes (FF), have been found to be troublesome due to the formation of highly stable $BaCO_3$ after the organic removal during pyrolysis, and subsequently, difficult to decompose during the YBCO crystallization process. For this synthetic method, the Fluorine-Free (FF) route, several Yttrium, Barium and Copper non-halogen carboxylate salts are employed as metal precursors to prepare YBCO film samples, following the CSD-MOD methodology. For example, during pyrolysis, the general chemical equations associated to the process is described as follows (being R any organic ligand, such acetate):

$$Y(RCOO)_{3(s)} + Ba(RCOO)_{2(s)} + Cu(RCOO)_{2(s)} \rightarrow Y_2O_{3(s)} + BaCO_{3(s)} + CuO_{(s)} + H_2O + CO_2 \quad (1.6)$$

During pyrolysis, all the Fluorine-free organic matter present in the solution decompose to form an amorphous nanocrystalline mixture composed of mostly orthorhombic $BaCO_3$ and nanoparticles of Y_2O_3 and CuO. The decomposition of $BaCO_3$ during YBCO crystallization, which is obtained after pyrolysis, is the limiting step of the reaction, affecting its growth rates. To minimize the limitations of the FF route, several research groups have developed novel methodologies by using liquid-based mediated strategies [**68-69**], taking advantage of the high Yttrium diffusion in the liquid, much larger than in solids, to reach faster crystallization growth rates for the preparation of YBCO films.

1.2.2.1 Transient Liquid Assisted Growth (TLAG-CSD) Method

A recent work by the ICMAB group [**70-71**] describes the growth of YBCO films from propionate-based precursors through a so-called Transient Liquid Assisted Growth (TLAG-CSD) process. Transient Liquid Assisted Growth (TLAG) is an ultrafast non-equilibrium growth process mainly governed by kinetic parameters, consisting on the crystallization of YBCO mediated by the dissolution of Yttrium oxide nanoparticles in the Ba-Cu-O liquid and controlled by the Y supersaturation of the liquid. Once Y diffusion reaches the growth interface [**70**], epitaxial growth if favoured (given the right substrate mismatch) and an ultrafast liquid mediated YBCO crystallization occurs.

Reported studies of liquid-based mediated growth of REBCO have been presented [**72-74**], taking advantage of the high atomic diffusion of Y in the liquid, much larger than in solids, to reach very fast crystallization growth rates. Respect to other processes however, non-equilibrium TLAG presents novel characteristics such as the transient liquid nature, its high tenability, large temperature and PO_2 windows to work with and the relevance of kinetic parameters (heating ramp, pressure ramp, gas velocity) in the determination of epitaxy and supersaturation conditions. Remarkably, with TLAG we can obtain even two orders of magnitude larger growth rates than with conventional methods, thus 100-1000 nm/s have been demonstrated [**71**].

The high growth rate is due to a much faster diffusion of a formed eutectic liquid compared to a solid-state crystallization [**70**]. The transient liquid of TLAG is a Ba-Cu-O melt, whose composition is determined by the solution stoichiometry. This method requires a high control of the supersaturating conditions, which are better achieved when using a certain solution stoichiometric ratio, being $YBa_2Cu_{4.66}$ or (3-7) composition (see Figure 1.5), which coincides with the eutectic composition between Barium and Copper oxides, facilitating the formation of the melt.

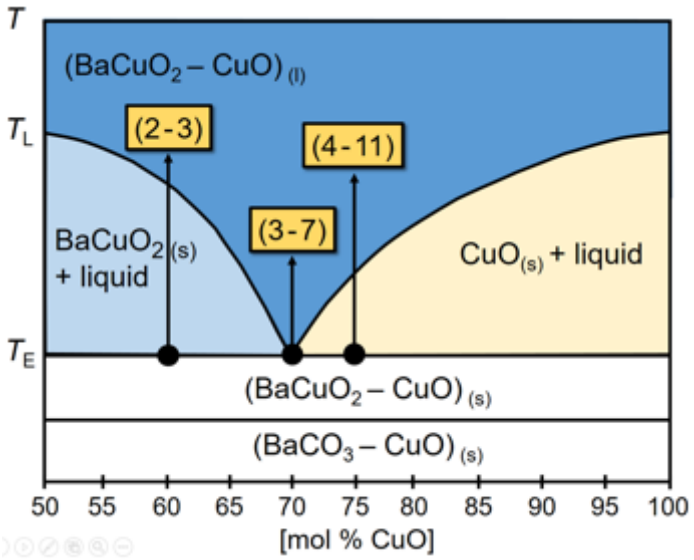

Figure 1.5. *Phase diagram of the Ba-Cu-O liquid formation. 3Ba:7Cu stoichiometry has a eutectic point at lower temperatures.*

To control the process, it is crucial to identify the main kinetic parameters that bring the system out of equilibrium. The transient liquid of TLAG is a Ba-Cu-O melt that varies in oxidation state depending on the T – P_{O2} region, which was later confirmed through in-situ XRD studies [**71**]. Thus, the liquid phase is able to change in a continuous way from [$BaCuO_2$ + CuO] (l) to $BaCu_2O_2$ (l), with the Cu oxidation state changing from Cu(II) to Cu(I).

TLAG is a non-equilibrium process, kinetically favouring the formation of the transient liquid able to grow YBCO films based on the Yttrium solubility and diffusion in the Ba-Cu-O melts. It requires to control the formation of the transient liquid in a region where YBCO is thermodynamically stable, while the supersaturating conditions of the liquid induce proper c-axis nucleation. The kinetic factors govern the nucleation and growth processes. There are many factors influencing the ultrafast growth of epitaxial TLAG films:

- As higher the nucleation densities are, higher the growth rates will be. In this sense, high supersaturation conditions must be reached to obtain a good performance of the process. However, being TLAG a non-equilibrium process, Y dissolution is strongly influenced by the kinetic parameters. In liquid assisted processes to grow YBCO, supersaturation is determined by the amount of Y dissolved in the liquid. The parameter is given by:

$$\Delta\mu = kTln\frac{C_\delta}{C_e} = kTln(\sigma + 1) \quad (1.7)$$

  where $\Delta\mu$ is the chemical potential change, C_δ is the actual concentration of Y in the liquid, C_e is the equilibrium concentration of Y in the liquid and σ is the relative supersaturation.

- The amount of liquid generated at the growth conditions. Since the highest growth rate values are obtained in the full liquid region, the presence of solid phases could disturb the growth process.

- The growth rate should also be influenced by the liquid properties, like viscosity. The continuous change of the liquid composition through the T-P_{O2} region (by the Cu oxidation state) will produce changes in the liquid properties, which imply different situations for proper nucleation, as they are different liquids. Neither of the liquid compositions can be excluded, as each liquid phase induce high growth rates and does not have a higher yield of the reaction than the other liquid compositions. The difference between the liquids relies on the oxidation state of Cu (which can be 2+ or 1+).

These conditions will affect film composition, porosity and crystallinity during the TLAG process, so the exact values delimiting these kinetic regions might shift when these parameters are changed. It is known that these Ba-Cu-O liquids are very reactive and corrosive especially towards high temperatures, but the substrate texture quality should not be affected by the TLAG growth conditions (especially on metallic substrate architectures).

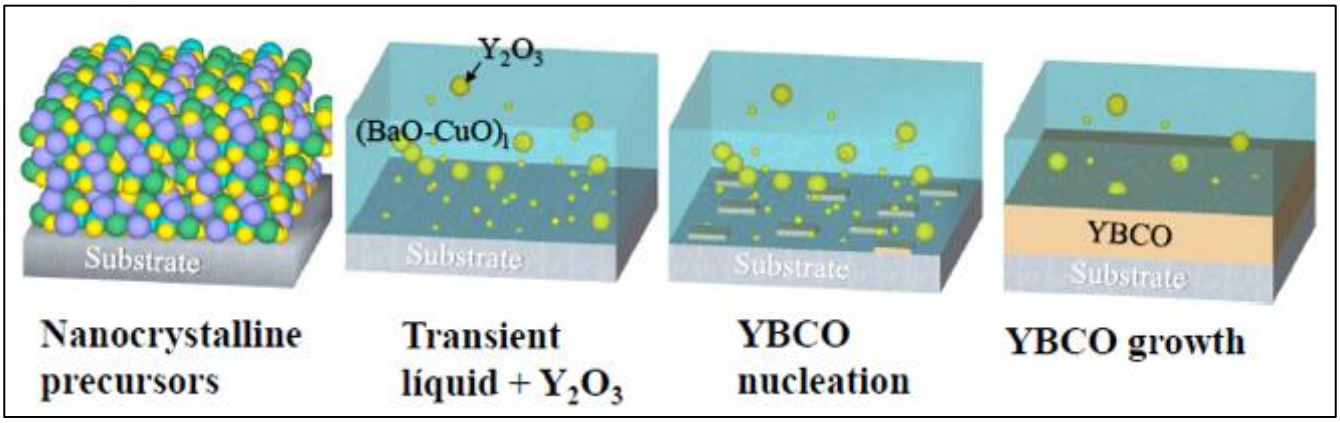

Figure 1.6. *Illustrative representation of YBCO growth from the TLAG-CSD method. A liquid-solid nucleation process where Y is dissolved from the Y_2O_3 nanoparticles reacts with the Ba-Cu-O liquid to form YBCO.*

In the TLAG-CSD method, the transient liquid can be reached through two main routes: the temperature route (T-route) and the oxygen partial pressure route (P_{O2}-route) [**70**]. So TLAG transient liquids can be obtained upon melting of two barium-cuprate phases, distinguished by the copper oxidation state, depending on the TLAG route used. Each route has its own characteristics to reach the desired melting liquid and its subsequent YBCO crystallization. Depending on the temperature and oxygen partial pressures, the TLAG-CSD method allow for the reaction of the $BaCO_3$ with CuO to form $BaCuO_2$ or $BaCu_2O_2$ or a combination of both. The equations of the process, can be described as:

1) High PO_2 values: $$BaCO_{3(s)} + CuO_{(s)} \rightarrow BaCuO_{2(s)} + CO_{2(g)} \uparrow \quad (1.8)$$
2) Low PO_2 values: $$BaCO_{3(s)} + CuO_{(s)} \rightarrow BaCu_2O_{2(s)} + CO_{2(g)} \uparrow \quad (1.9)$$

Each TLAG route can be described as:

- T-route: The system is heated up at constant P_{O2} in the region of YBCO stability. As the $BaCO_3$ reacts with CuO, an intermediate $BaCuO_2$-CuO transient liquid is formed and YBCO crystallizes from the Y_2O_3 dissolution in the liquid and Y diffusion to the substrate interface. In T-route, the reaction of $BaCO_3$ with copper oxide can be accelerated by the formation of the Ba-Cu-O liquid at the same time. For that matter, in T-route the heating ramps of the process is what defines the kinetic parameters of the process. When the ramps are very high (>4.5ºC/s), the reaction forms the melt immediately:

$$BaCO_{3(s)} + CuO_{(s)} \rightarrow (BaCuO_{2(s)}) + CuO_{(s)} + CO_{2(g)} \uparrow \rightarrow [BaCuO_2 + CuO]_{(l)} \xrightarrow{Y_2O_3} YBa_2Cu_3O_{7-x(s)} + CuO_{(s)} \quad (1.10)$$

- P_{O2}-route: The system is heated up at a low P_{O2} region, where YBCO is not thermodynamically stable. Here, a $BaCO_3$ elimination reaction occur leading to the formation of an intermediate $BaCu_2O_2$ solid phase. Upon a fast P_{O2} increase, which is in fact a pressure jump into the region where YBCO is stable, the $BaCu_2O_2$ solid phase leads to the formation of the transient liquid, through which Y_2O_3 is dissolved, and YBCO is able to crystallize. P_{O2}-route offers the possibility to decouple the $BaCO_3$ reaction with the copper oxide from the crystallization of YBCO, which enables a separated optimization of each step.

As in P-route the reactions occur separately, the chemical equations related to each part of the process, occurring in fractions of seconds once the pressure jump has been made, and can be described as (see also Figure 1.7):

Low PO2

$$CuO_{(s)} \leftrightarrow Cu_2O_{(s)} \quad (1.11)$$

$$BaCO_{3(s)} + Cu_2O_{(s)} \leftrightarrow BaCu_2O_{2(s)} + Cu_2O_{(s)} + CO_{2(g)} \quad (1.12)$$

High PO2

$$BaCu_2O_{2(s)} + O_{2(g)} + Cu_2O_{(s)} \rightarrow BaCuO_{2(s)} + CuO_{(s)} \quad (1.13)$$

$$BaCuO_{2(s)} + CuO_{(s)} \rightarrow [BaCu^{I+\,or\,II+}O]_{(l)} + Y_2O_{3(s)} \rightarrow YBa_2Cu_3O_{7-\delta} + CuO_{(s)} \quad (1.14)$$

Throughout this thesis, the growth of epitaxial YBCO films with homogenous elemental distribution was attempted through the TLAG-CSD method using the P-route. However, both routes have been succeeding in achieving good c-axis nucleation epitaxy and good performances. With proper control of these kinetic parameters, films with high critical current densities (J_C = 2.5 MA/cm^2 at 77K, s.f. (H=0)) and with growth rates between 100-2000 nm s^{-1} are reached, which are up to 3 orders of magnitude higher than other reported methods [**75**].

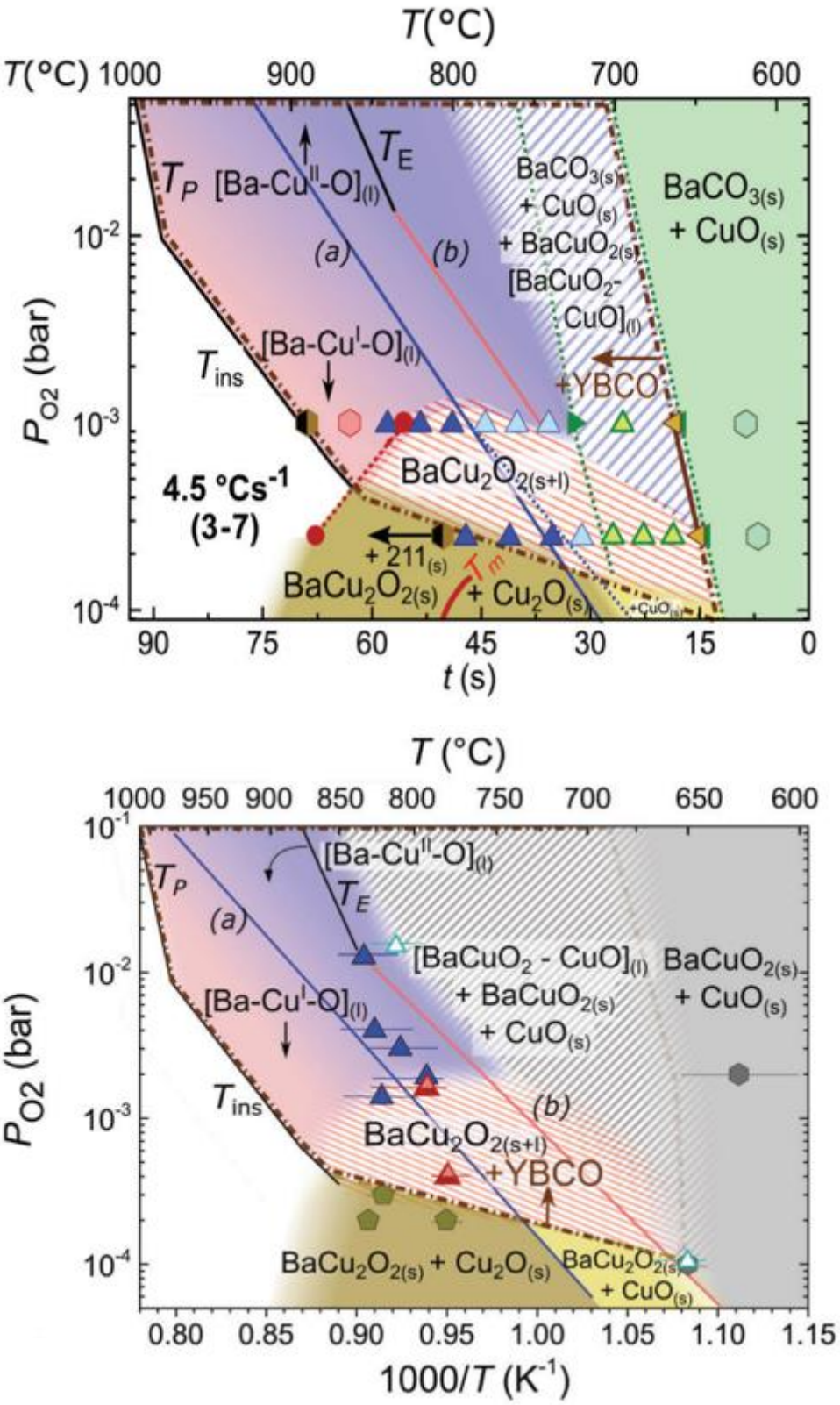

Figure 1.7. *P_{O2}-T Phase Diagrams of (a) T-route (4.5 ºC/s) and (b) P-route, showing the decomposition of $BaCO_3$, transformation to BaCuO species and the crystallization zone of YBCO. The T-route and P-route growth approximations are also shown. Extracted from S. Rasi et al [**50**].*

1.3 Inkjet Printing deposition

Currently the production costs of the superconductor materials are usually high due to the manufacture techniques used for, such as high vacuum methods, which are costly processes. Chemical Solution Deposition (CSD) methods appear as a preferred cheaper methodology for the synthesis of functional oxides due to the use of low-cost chemical solutions and its high control during the synthesis, which makes it an attractive synthetic route for the production of high-quality materials. The deposition of chemical solutions are recurrent methods both in lab scale and industrial processes thanks to its improvability and reproducibility. Moreover, and especially in the case of using Fluorine-Free solutions, it embraces a greener approach due to the use of non-halogen content solutions, which make them more attractive for the general market.

On the other hand, printed electronics have emerged on the last few decades with a very strong potential for many applications such as polymer chemistry, optoelectronics, home-made printers or photosensitive materials [**76**]. Thus, Inkjet Printing can be used as a combination of Chemical Solution Deposition (CSD) and printed electronics methodologies, with high prospection into functional materials, through the use of reel-to-reel compatible manufacture processes, making it attractive at industrial scale to achieve higher thicknesses in one single depositions, which further reduce the costs of production for superconducting materials and coated conductor (CCs) tapes.

Inkjet Printing (IJP) relies on the deposition of chemical solutions in the form of small drops, at a range of picolitres (pL), enabling predefined patternings. Drop formation and ejection is then the most important part of the inkjet printing operational system, which occurs at the printhead. The high repeatability of drop ejection mechanisms allows to control the deposited volume of the patterning in a very precise manner, which in turn permits an accurate control of the drop volume to fine-tune film thickness [**77**].

Film thickness is an essential factor for determining the relation between the cost and the performance of a superconductor material. The current that is transported through the superconductor is directly related to the cost and the cross section of the material. As lower the €/kA·m of a superconductor is, the higher its competitiveness will be. One of the advantages of the production of YBCO films through IJP is that the thickness in one single deposition is significantly higher compared to other CSD techniques. Fast growth rates, low capital investment and simple processing which are key features of the TLAG-CSD method to reduce the cost per meter, in combination with IJP, which increases the thickness in one single deposition, may produce films with high critical currents ($I_C = J_C \cdot$ thickness) to push forward YBCO commercialization.

Other the advantages of this technology are the versatility of IJP to switch the deposited material or change the pattern designs, making it an interesting and useful technique [**78**]. A huge diversity of materials might be printed in diverse forms, such as lines, arrays, drawn forms or coatings, among other structures, which allows to cover a wide range of configurations. Inkjet printing technology enables to work in a broad range of substrates, reflecting the usefulness of this technology for a broad scope of production processes.

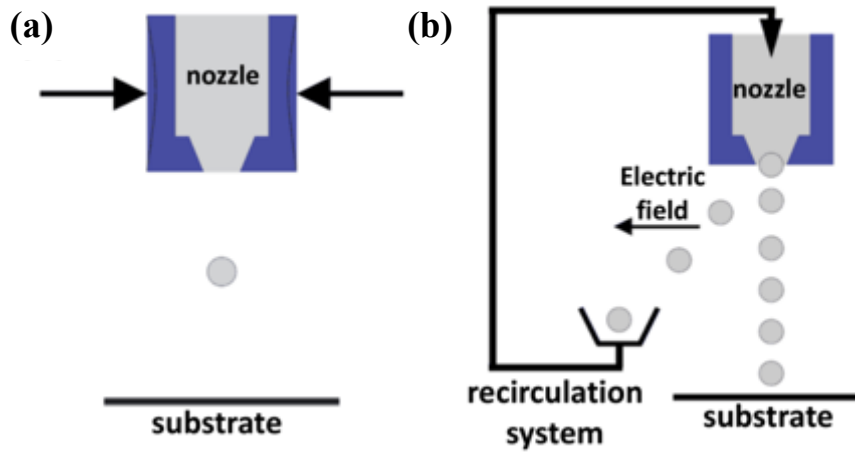

Figure 1.8. *Illustrative comparison between (a) Drop on Demand and (b) Continuous inkjet printing systems, extracted from M. Vilardell PhD thesis [**78**].*

The Inkjet printing systems are separated into two main categories (as seen in Figure 1.8), either Continuous Inkjet printing (CIJ) or Drop on Demand (DoD) inkjet printing [**79-80**]. Furthermore, DoD systems are also classified into three modalities, depending on the characteristics of the nozzle: thermal [**81**], piezoelectric [**82-83**], and electromagnetic processes. Throughout this thesis, the inkjet printing systems used will be piezoelectric DoD systems.

1.3.1 Continuous Inkjet Printing systems

In continuous inkjet printing technologies, the reservoir (where the ink is placed) is connected directly to the nozzle through a high-pressure pump, that directs the material to produce a continuous jetting of droplets at regular intervals. The jetted drops are in presence of an electrostatic field and acquire an electrostatic charge [**84-85**]. The now charged drops are directed by another electrostatic field, to either the substrate or the recirculation system for re-usage. Continuous inkjet printers are currently used in the industrial market.

The advantages of this technology are the fast velocity of the droplets, with very high drop ejection frequency (up to 100 KHz) and thus, prevention of nozzle clogging. The main disadvantage is the ink recycling system. Most of the drops are being recycled which require large volumes of ink. In addition, this process may cause contamination, and more importantly, produce changes on the ink concentration and rheological properties due to being exposed to the environment. Additionally, an electrical conducting fluid is required, which restricts ink formulation [**86**].

1.3.2. Drop-on-demand (DoD) inkjet printing systems

In Drop-on-demand (DoD) inkjet systems (as the apparels in this thesis), drops are only generated when required or imposed. DoD systems are more flexible with the ink composition, as they do not require conducting fluids. The system allows for a better control over the drop positions.

The Drop-on-demand (DoD) inkjet printing systems are the preferred technique for complex patterns and delicate materials [**87-88**]. They be categorized in three different modalities depending on the nozzle or printhead characteristics:

1) Thermal printheads [**89**]: They possess a thermal resistor causing a rapid vaporization of the ink, which forms a bubble once heated. This bubble starts to increase its volume which increases the pressure inside the nozzles' column, where the ink is located. Once the bubble collapses, the ink moves towards the collapsing bubble, resulting in a separation of the ink as a drop. Then the pressure decreases, and the nozzle becomes refilled again. Its the most common technique for desktop inkjet printers (Hewlett-Packard), but the ink composition is very restricted, as the fluid cannot be ignited but must possess a volatile component to form the vapour bubble, otherwise droplet ejection will not occur. Additionally, as the resistor can be heated up to 300ºC it further limits the ink composition that can be used.
2) Piezoelectric printheads [**90-91**]: In this case a piezoelectric actuator is the responsible to generate the drops. An electric field is applied across the piezoelectric material, causing a deformation that produces oscillations, squeezing the ink column and reducing its volume, to cause the ejection in the form of drops thought the orifice. Typically, piezoelectric printheads operate under negative pressures that stabilize the meniscus at the tip (orifice) of the nozzle. The drop volume will largely depend on the diameter of the nozzles' orifice, the applied waveform and its rheological properties. DoD techniques are used in domestic inkjet printers (Hewlett Packard) and industrial inkjet printheads (Microdrop Technologies).
3) Electromagnetic printheads: In this case, the nozzle is configured with a plunger assembly, which is made up of two components, one used to seal against the nozzle and a magnetic core at the other end. The ink is introduced in a pressurized manner, and a solenoid is used to open the valve, displacing the plunger each time a drop is required.

1.3.3 ICMAB studies on Inkjet Printing systems

At ICMAB, two PhD thesis were published regarding the optimization of the operational system as a flexible manufacturing method, made by Dr. Marta Vilardell [**78**], and the development of a process for the synthesis of thick YBCO films through CSD-MOD processes made by Dr. Bohores Villarejo [**92**], respectively. Both thesis proved the concept of inkjet printing devices as reliable systems for the preparation of superconducting materials through CSD methods, with very remarkable results [**93**]. For instance, the addition of polymeric additives in the solution to avoid solvent evaporation, by creating a polymer film induced by photo-polymerization, had shown very positive results for the preparation of thick YBCO films [**94**]. Such polymeric additive has been used recently in our group in the TFA-CSD and LF-CSD routes. By using a UV-curable varnish that acted as an ink viscosity enhancer, the film homogeneity was highly increased, showing very good performance on this synthetic Inkjet printing synthetic method.

For this reason, the optimization of the solution is crucial for the drop formation and its stability over time, its velocity and drop impact, drop merging and the overall liquid redistribution over the substrate, which may severely affect the homogeneity of the as-deposited films if not properly optimized. The changes in the plate velocity also severely affects the fluid behaviour during deposition. This implies that there is not one single answer to obtain reproducible and homogenous inkjet deposited samples, and that each inkjet printing modality requires different approaches and setup adjustments.

In our case, this thesis will be devoted to the usage of DoD Inkjet Printing devices for the preparation of thick YBCO films by means of the TLAG-CSD process using propionate-based precursor solutions. The proper analysis, design and compatibility studies of the ink, its accommodation to the DoD piezoelectric inkjet printing systems, available at ICMAB, and the correct deposition and processing of thick YBCO films will be described thoroughly in the next chapters.

1.4 Fluid dynamics and rheology of the precursor solution

In order to fulfil the requirements for homogenous depositions, the ink properties must be subjected to a strict control, whereby the most important factors taken into account will be ink stability, interaction with the nozzle, interaction with the substrate and the decomposition reactions of the solution precursors that take place during pyrolysis, especially regarding the film stress that is generated during such process. All these factors restrict the ink design by the availability of solvent, metal precursors and additives that can be used to achieve defect-free reproducible samples through the TLAG-CSD process. For inkjet printing depositions, the rheological characteristic of the solution plays a major role, since the viscous and surface tension forces at the printhead will determine the drop parameters and its proper stable jetting and drop formation [**95**].

The parameters involved in the correct deposition will be its drop volume and diameter, drop speed and the dimeter of the drop once it impacts with the substrate, which will have a direct output on the deposited film morphology [**96**]. As mentioned, inks should be formulated to meet the requirements described by the following:

- Its suitability for use in the inkjet printing setup, such as its solvent composition.
- Rheological requirements for reproducible drop ejection.
- Ink stability, where its concentration and rheological properties remain constant over time.
- Ink homogeneity and robustness, avoiding solute and additive precipitation over time.
- Adequate evaporation rate of the solvents to prevent nozzle clogging.
- Solvent evaporation after deposition, based in its vapour pressure and boiling point, to obtain a proper fixing of the ink to the substrate.
- Proper film quality after the pyrolysis, by controlling the decomposition steps of the organic matter, to achieve a homogenous distribution of the oxides and carbonates for proper TLAG growth.

For the proper drop ejection and deposition of chemical solutions by inkjet printing, the main parameters that affects the fluid motion are viscosity, surface tension and density. A short review of these parameters, focusing on their effect on the printing performance is detailed below.

1.4.1 Viscosity

The internal resistance that a fluid presents during its motion or spreading under an applied force represents the viscosity of a fluid, in this case of our chemical solution or ink. Since it is of major importance for the drop formation, the viscosity is one of the parameters that are primarily studied during the solution optimization. In particular, viscosity affects drop ejection and stability, being able to reduce oscillations after its formation.

While very low viscous fluids could cause air uptake into the nozzle due to the negative pressure applied at the printhead, high viscous fluids cause viscous dissipation during the mechanical deformation of the piezoelectric actuator, and the inertia will not be enough for the fluid to breakdown as a small drop. In both cases, drop generation will be inhibited or will be unstable, so a balance between them must be properly controlled [**97**].

The measurement principle is based on detecting the shear deformation applied on the sample with a rotational plate, since relating it to the Newton's second law of motion, the resulting shear of a fluid is directly proportional to the force applied and inversely proportional to the viscosity. An external force (F) applied to the fluid in a certain area, causes a deformation (D=x/h) based on the motion of the fluid in both the distance (x) and height (h) differences produced. Taking into account that the force is applied tangentially to a given area, there will be an interface between the plate and the ink, producing a fluid motion.

The speed of such flow is controlled by the internal resistance of the liquid, being the viscosity. The following equation describes such liquid interaction:

$$F = C \cdot A \cdot v/y \tag{1.10}$$

where the external force (F) is proportional to the shear rate ($v/y=\varphi$), derivative of the fluid speed in the direction perpendicular to the motion plate, the area (A), and the coefficient (C), which is the fluid viscosity (η), related to the rheological nature of the fluid. Such applied force can be translated into the shear stress:

$$\tau = F/A \tag{1.11}$$

Describing the flow behaviour of an ideal liquid, we have Newton's law of viscosity:

$$\tau = \eta \cdot dv/dy = \eta \cdot \varphi \tag{1.12}$$

The constant η is the coefficient of viscosity and it relates the resistance of a liquid or fluid against its deformation. It has units of [Ns/m^2] in SI units, or Pa·s. It can also be expressed in CGS as [$dyns/cm^2$] and this unit is called a poise (cP).

1.4.2 Surface tension

Surface tension is the dominant force for the drop shape and meniscus control, as it regulates the solution wetting on the printhead and later during the liquid-substrate interaction, which will determine the form of the drop. Usually, a liquid in absence of external forces tends to minimize its interfacial area. In order to extend that area, an external work (W) has to be performed against the cohesive forces of the fluid. This implies that at the surface of the liquid a higher free energy than the bulk is present.

Such extra energy, acting in parallel to the surface, is what appears to be the surface tension (γ). It has units of [N/m^2] in SI units, which is directly related to the number of bonds per unit area (A) and also its bond strength [**98**]:

$$dW = \gamma \cdot dA \tag{1.13}$$

$$\gamma = dW/dA = dW/l \cdot dX = F/l \tag{1.14}$$

The meniscus shape of a drop at equilibrium conditions can be numerically determined by solving the Young-Laplace equation, as stated in the following equation of capillarity:

$$\Delta p = \rho g h = \frac{2\gamma}{R} \tag{1.15}$$

Where Δp corresponds to Laplace pressure, the capillary driving force, directly related to density (ρ), gravitational acceleration (g) and change in height (h). Moreover, surface tension (γ) in function of the radii of curvature (R), will determine the drop shape caused by gravity and surface tension forces until the differential pressures are minimized (Δp→0).

For this reason, surface tension must be kept in a certain values range. Low surface tension liquids can lead to air uptake. Uncontrolled drop generation and formation of satellites is a main indicative of a low surface tension liquid. Conversely, large surface tension liquids will inhibit the drop formation due to a high wetting of the liquid at the column and at the printhead [**99**].

1.4.3 Density

Density impacts on the energy that is required to generate the drops, as it will require a higher kinetic energy to generate a drop of a denser liquid. In general terms, as the density increases, a higher oscillation of the liquid column to obtain a stable drop will be required.

Density (ρ) expressed in the SI units of kg/m^3 can be defined as a relationship between the mass (M) of a given liquid and its occupied volume (V) as:

$$\rho = m/V \tag{1.16}$$

1.4.4 Fluid dynamics of a drop

Considering a fluid, in this case our precursor solution, to have a uniform density, viscosity and surface tension, its motion can be explained by the Navier-Stokes equations [**100**]. The Navier-Stokes equations describe the evolution of the interface and flow along surfaces over time. The first Navier-Stokes equation accounts for the motion of the fluid (u) through space and time (t), along with any internal and external forces acting on it:

$$\partial u/\partial t = -(\nabla \cdot u)\, u - 1/\rho \nabla p + \eta \nabla^2 u + F \tag{1.17}$$

Each of the terms of the equation is related to one of the rheological properties of the given fluid or its velocity, being described as follows:

- $(\nabla \cdot u)\, u$ is the convection term, originating from the conservation of momentum.
- $1/\rho \nabla p$ is the pressure term, generated by the pressure differences within the fluid, ρ being the density of the fluid and p the pressure of the system.
- $\eta \nabla^2 u$ is the viscosity term, related to the motion of the fluid together with internal forces against deformation.
- F is the external force term where gravity or other interactions with the fluid are included.

To reduce the complexity of the equation, as a general assumption the fluid becomes incompressible. This constraint implies that flux flow is equal and stationary, which leads to the second Navier-Stokes equation, $\nabla \cdot u = 0$; being u the velocity field of the fluid.

1.4.4.1 Jetting Parameters

If the rheological fluid properties that impacts on fluid dynamics, such as density, surface tension and viscosity are again, uniformly distributed and included into independent dimensionless parameters, four forces acting on the fluid can be properly defined as [**101**]:

- Gravity force: $\rho l^3 g$
- Inertia: $\rho l^2 v^2$
- Surface tension: γl
- Viscous force: $\eta l v$

Where ρ is the density, γ is the surface tension and η is the viscosity of the fluid, l is a characteristic length (usually the nozzle diameter), v is the velocity of a body of liquid and g is the acceleration due to gravity.

Rearranging such non-dimensionalized values of the Navier-Stokes equations gave rise to a series of independent parameters that express the behaviour of a liquid [**100-101**]. The most important ones being the Reynolds number (Re), Weber number (We) and Bond number (Bo):

- $Re = \rho l v / \eta$, shows the ratio of inertial to viscous forces.
- $We = \rho l v^2 / \gamma$, is the balance between inertial and capillary forces.
- $Bo = \rho g l^2 / \gamma$, measures the importance of gravitational forces against capillary forces.

Finally, there is the Ohnesorge number (Oh) which relates the viscous to capillary and inertial forces present in the precursor solution, and in this case, at the tip of the nozzle. This parameter stablishes the drop generation mechanism to characterize a proper drop formation by:

$$\mathrm{Oh} = \frac{\eta}{\sqrt{\rho l \gamma}} \tag{1.18}$$

In the inkjet printing community however, the inverse of the Oh number, or Z number, is more commonly used. It is a dimensionless parameter, independent of drop velocity, which define a proper relationship between the different forces acting during drop formation, such as the inertial and surface forces with viscosity, establishing a correct drop formation by:

$$Z = \mathrm{Oh}^{-1} = \frac{\sqrt{\rho l \gamma}}{\eta} \tag{1.19}$$

As mentioned, Z number establishes an appropriate jetting of a fluid by inkjet printing apparels. Initially, the range was postulated to be 1>Z>10 [**102**] and a later work redefined it to Z values of 4>Z>14 [**96**] for a proper reproducibility, stability, and well-defined shape of drops for proper deposition of solution by inkjet printing.

In fact, we can use such well-defined parameters to stablish a delimitation on where the ink will be too viscous for its deposition (small Z numbers) or satellite formation during drop formation will occur due to low surface tension and viscosity (large Z numbers). In neither of the cases a proper inkjet deposition will be obtained, since the first will be unable to form drops and the latter unable to obtain homogenous distributed printed samples, since the formation of satellites (secondary drops with lower volume ejected together with the main droplet) will have a negative effect on the liquid distribution once it is deposited on top of a substrate.

1.4.4.2 Wetting of precursor solutions

Once a drop is generated, it will fall until it impacts on top of a substrate; when the drop is ejected, it accelerates as a consequence of gravity, until it reaches a stable velocity by which will impact on a given area. Both drop speed and the surface of the substrate will have an effect in liquid distribution through liquid-liquid interactions and liquid-solid interactions [**103-113**].

The impact of a drop on a substrate is a complex system controlled by several coexisting forces, mainly tension, gravitation and inertia [**108**]. For that effect, the Bond number (Bo) is usually considered, however since the drops are usually found to have small volumes (pL), surface energy and density of the drops ejected by the inkjet printer take precedence on the impact, and gravitational forces are mostly neglected. Thus, the dominant forces for inkjet printing drops will be capillarity and inertia.

When a drop of liquid falls onto a solid surface, the liquid will spread, remaining as a discrete drop on the solid once an equilibrium state is reached. The deposition then will be governed by an impact driven spreading by the resulting intermolecular liquid-solid interactions. The wetting degree will be a result of the adhesive forces that will cause the fluid to spread against its proper cohesive forces, forcing the liquid to recoil to minimize its surface [**107**].

Contact angle measurement is the preferred method to determine such relation between the adhesion and cohesion forces affecting a fluid deposited onto a surface. The contact angle is defined by the tangent of the drop with the solid, under the interfacial tensions present until a mechanical equilibrium is reached [**114-119**]. When the contact angle takes values lower than 90°, we can say that adhesive forces surpass cohesive forces. In the case of $\theta_C = 0°$, theoretically, an optimal wetting of the liquid onto the solid is reached.

Following Young's equation:

$$\gamma_{SG} - \gamma_{SL} - \gamma_{LG} \cdot \cos\theta_C = 0 \quad (1.16)$$

Where solid-gas, γ_{SG}, solid-liquid, γ_{SL}, and liquid-gas, γ_{LG} tensions, and θ_C is the contact angle.

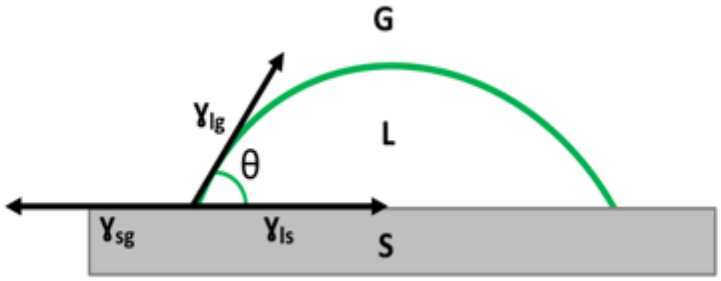

Figure 1.8. *Contact angle measurement (θ_C). It represents the angle between the liquid with the solid, controlled by the three phases of surface tension components [**78**].*

1.4.4.3 Coffee-ring effect on inkjet printing deposition

Once an ejected drop impacts the solid surface, the fluid moves outwards to compensate solvent evaporation [**120**]. Such drying of the liquid will result in the formation of dense and thicker rings, compared to the bulk, around the drop perimeter due to the expulsion of solid material and solvent drying.

In inkjet printing deposition this phenomenon can be found on all deposited drops, lines and full films. In the case of drops and lines, such effect can be avoided by either the continuous ejection of drops, forcing its overlapping, or the usage of high-boiling point solvents to avoid drying of the lines, among other factors. On the full deposited films, the effect is much more critical since liquid redistribution will occur due to a lower evaporation rate of the full wet film. Due to this issue, related to the deposition of films by inkjet printing systems, there has to be a strict control on the rheological properties of the inks.

For example, a profilometer analysis (Figure 1.9) reveals the 3-dimensional shape of a jetted drop once it has been dried on top of a substrate. Taking into account the rheological properties of the solution, such its surface tension, and as the solvent evaporates, the materials is expulsed towards the edges creating such characteristic form related to the coffee-ring effect.

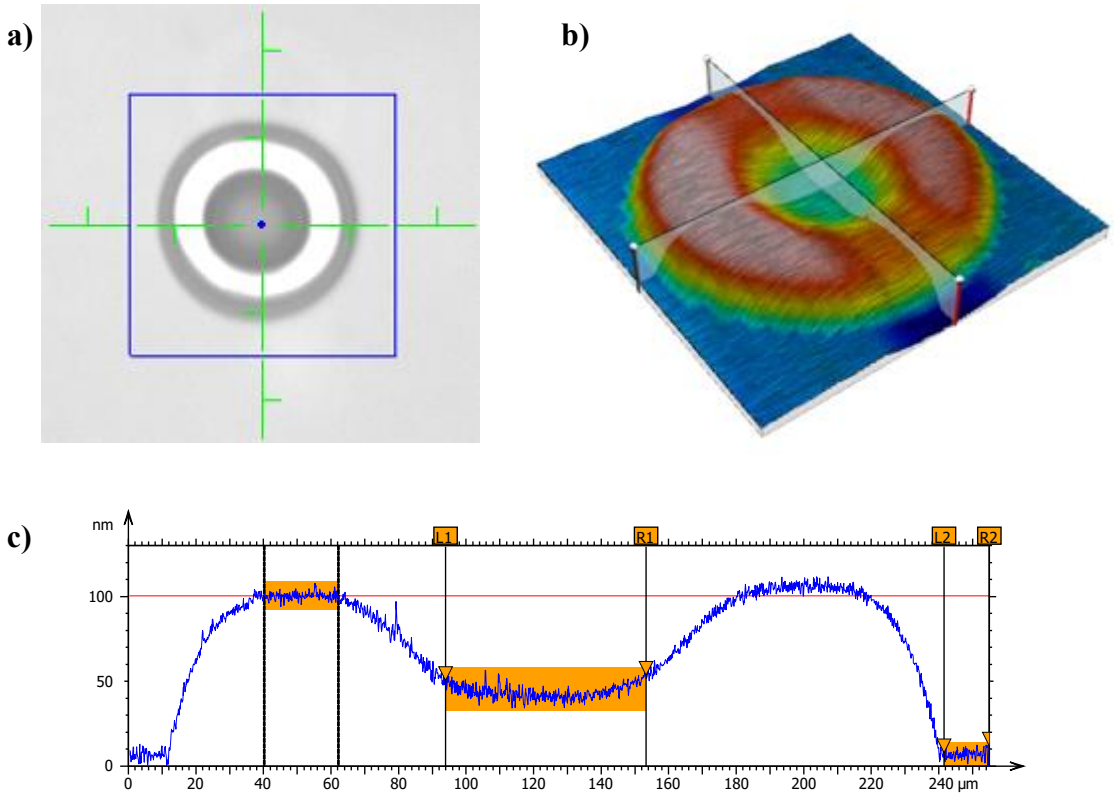

Figure 1.9. *3D profilometer analysis of a jetted drop. (a) OM image of the deposited drop. (b) 3D representation of the shape. (c) Measured thickness of the deposited drop in one direction, bulk=50nm, ring=100nm.*

Thickness variations between the material, expelled due to the coffee-ring effect, almost double in height the bulk of the dried drop (100nm vs 50nm). As a consequence, this effect can be extrapolated to dried lines and later on, dried films, as the jetted drops start to overlap and merge within themselves, expelling the material towards the edges as the solvent starts to evaporate. Taking into account such observations, the coffee-ring effect has to be minimized, as will be discussed in the next chapters.

2.

MATERIALS AND METHODS

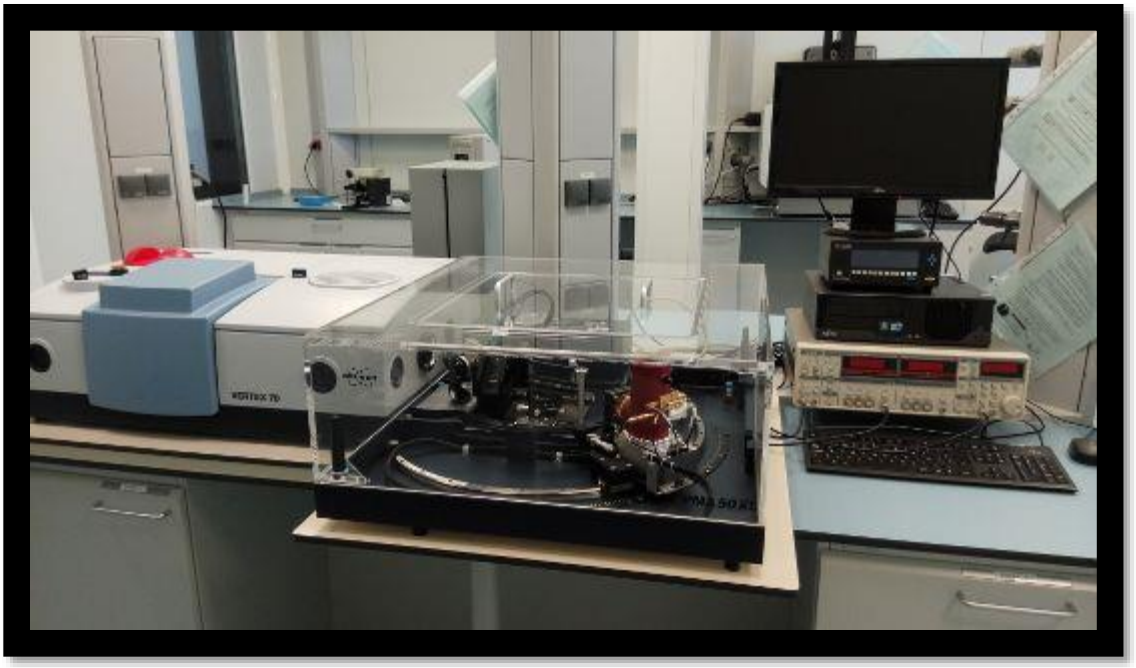

In this chapter, the description of the several experimental methodologies that have been used throughout the thesis are introduced. For chemical solution deposition methods, several requirements must be fulfilled in order to achieve good quality textured YBCO films, starting from the design, characterization and optimization of the solutions. Afterwards, several ex-situ and in-situ characterization techniques were carried out to evaluate the resulting composition of the samples and its properties.

2.1. Solution Preparation

As already mentioned in the previous chapter 1, the precursor solution composition (ink) required for CSD methods consist of the combination of the appropriate solutes for the desired functional material in its correct stoichiometry plus one or several solvents to ensure proper precursor salts stability. It also may include the use of some additive compounds.

Here, the selected ink stoichiometry (1:2:4'66 – Y:Ba:Cu) correlates with the Ba-Cu-O eutectic liquid composition ($3BaCuO_2$-4CuO or 3Ba-7Cu), which enables to better control the supersaturation value and crystallize easily the epitaxial YBCO films. The procedure consists of a combination of an adequate solvent mixture (from 50/50 to 30/70) of carboxylic acid with an alcohol. It could also include different $\%_{v/v}$ of a corresponding additive.

Subsequently, Barium and Copper precursor salts were slowly added under continuous stirring and kept for approximately 30 min. Finally, Yttrium salts were added to the mixture and left stirring at 30ºC until a homogeneous and transparent solution was obtained, i.e., typically 30-60 min. The precursor solutions were filtered through a PTFE membrane filter (pore size ~0.2 μm) and kept under argon atmosphere in a glass vial.

With this solution preparation protocol, we could ensure solution reproducibility, homogeneity and robustness to being used during several days. The correct characterization of the solution parameter was then carried out.

2.2 Solution Characterization

Different ink parameters were studied to ensure its practicability to be used on the inkjet printer, to obtain good homogeneity during the deposition and produce a smooth densification of the films, principally to avoid the appearance of defects.

The avoidance of defects on films, whose source was determined to be originated in both liquid movement during deposition and/or cracking during metalorganic decomposition, especially during the pyrolysis synthetic step of the process, are critical to ensure its process viability. It is directly dependent on the rheological properties of the solution and its water content.

2.2.1 Ink Rheology

The use of IJP to deposit thick samples requires control of process parameters to ensure a uniform deposition. Since it is being largely influenced by ink stability then, first of all, ink formulation as well as its physicochemical properties specifically its rheology, must be studied.

2.2.1.1 Density

Density measurements were made by weighting 1 mL of solution by a micropipette on a vial, several times, to ensure its proper reproducibility (its ranges usually comply between 0.95 to 1.1 g/cm^3).

2.2.1.2 Viscosity

Viscosity measurements were carried out with a HAAKE RheoStress RS600 from Thermo Electron Corporation with the Controlled Rate method coupled to the software Rheowin 4 Job Manager. For the measurements, a constant rotational speed and height between the solution holder and the rotational plate is set for all the tests. The viscosity values for the solution characterization were made at 21°C in a clean room class 10000 environment.

2.2.1.3 Surface Tension and Contact Angle

Surface tension and contact angles were evaluated with a Drop Shape Analyzer DSA 100 from KRÜSS. DSA (Drop Shape Analysis) methods determine the interfacial tensions of a fluid by fitting a curve of the drop shape using the software. This device has the option to measure both rheological properties by two different operation modes, being the sessile drop analysis for contact angle and pendant drop method for the surface tension [**121-122**]:

- Surface tension is measured by the pendant drop method. The surface tension of a fluid is determined by the shape of a pendant drop, which varies accordingly with the balance of surface tensions and external forces, such as gravity. To obtain the measure, a video with a high-resolution camera is recorded, while several drops are continuously falling from a needle of a known diameter. Once recorded, we select an image from the video, when the meniscus is minimum to fit it to the equation by using the software, obtaining its correspondent surface tension values.
- Contact angle measurements were made by sessile drop analysis. One drop of known µL volume is ejected from a needle onto a given substrate. At the very point of deposition, an image is obtained by the software, which also calculates the tangent obtained between the drop and the substrate, obtaining its contact angle, whose values comprise between >10º to 30º.

2.2.2 Water Content

The water content of the solutions is also critical for the deposition and final properties of the samples as inks with a higher value than 2% of water could compromise the process. Therefore, it was evaluated using the Karl-Fischer titration method [**123**] using a CA-310, coupled to an oven. The volumetric titration is based on a solution containing a base with a known concentration of Iodine. For each consumed mol of I_2, a mol of H_2O is detected, which makes it a very reliable coulometric technique.

2.3. Chemical Solution Deposition (CSD) Methods

2.3.1 Spin-coating

The procedure of spin-coating deposition was the same for all the chemical solutions prepared on this thesis. It is carried out in a clean room with maximum humidity of 30% and temperature of 21ºC:

A single crystal substrate is placed in the centre of the spin-coater's rotating chuck and a Nitrogen (N_2) flux connected to the internal part of the spin-coater (where the substrate is placed) is turned on, to ensure the humidity conditions during deposition to be lower than 10%, to avoid water absorbance on the surface of the printed samples. Just before deposition, the N_2 flux is reduced to minimum, to avoid having a direct and strong flux on the sample but maintaining humidity conditions stable. With the use of a volumetric glass Hamilton microsyringe, 15 µL of precursor solution are deposited at the centre of a single crystal substrate, either single-crystal (001) $SrTiO_3$ (STO) or single-crystal (001) $LaAlO_3$ (LAO). The spin-coater is then accelerated in 1s at a rate of 6000 rpm and held for 2 minutes, to allow complete coverage of the substrate with a homogeneous deposit of solution. The spin-coater stops automatically after 2 minutes, and the sample is placed on a preheated hot plate at 70ºC for 5 minutes to evaporate the solvent excess.

2.3.2 Drop-on-demand (DoD) inkjet printing of REBCO inks

For the correct deposition using Inkjet Printing apparels, studies on both the precursor solution or ink, together with its rheological properties and stability must be performed. But more importantly, with the printing conditions such as drop volume, drop speed, and drop diameter impact must be thoroughly analysed to obtain reproducible and homogenous depositions. For example, the selection of solvents, metal precursors and additives are of big importance for inkjet printing depositions due to homogenous liquid-substrate interactions need to be ensured, such as low contact angles and low liquid dispersion.

2.3.2.1 Drop Formation

In this thesis, a piezoelectric material is used as a printhead nozzle for the formation of drops in the range of picolitres. This drop formation arises from the oscillation of the actuator on the liquid column present inside the glass tube nozzle, resulting in the ejection of a drop after certain voltage is applied. For piezoelectric head nozzles, the drop is generated by using a certain applied voltage in the form of a wave [**124-125**]. A multinozzle head was used to load the solution on a piezoelectric nozzle, and the ejection parameters (voltage and pulse length) were adjusted to achieve a stable drop formation at a given pressure, being connected to a rotary pumpm, to form a stable meniscus (Figure 2.1).

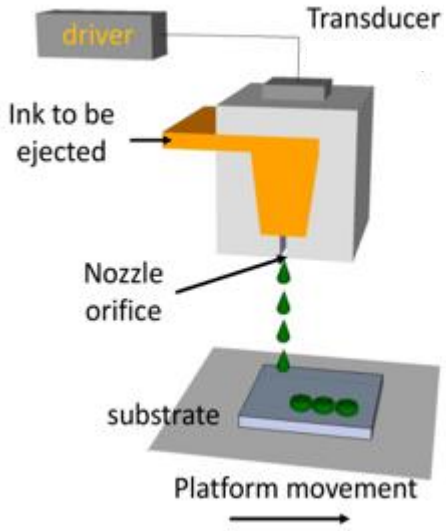

Figure 2.1. *Schematic representation of an inkjet printing deposition.*

The piezoelectric material present in the nozzle contracts and expands under a certain applied voltage, to alter the meniscus of the fluid at the tip at the nozzle, which have an applied pressure, breaking it to form drops with a small defined volume. The waveform voltage can be divided by segments, which can be modified to tune the pulse length or wavelength (μs). Another two important parameters that can be modified are the wave pulse width (V), and the wave frequency (Hz). Through the waveform, by modifying the wave pulse width and the wavelength, the drop volume and speed can be tuned [**92**].

Another consideration is the negative pressure applied to the nozzle. By creating a proper vacuum on the tip of the nozzle, the drop volume, and more importantly the drop ejectability and stability can be modified. Depending on the inkjet printing system used, the characteristics of the waveform are different, as well as the frequency used for each deposition modality, which implies some variations on the drop parameters. Moreover, by tuning the rheological properties of the precursor solution such as the viscosity and surface tension, the drop volume can also be fine-tuned. Depending on the nozzle apparel characteristics, these parameters for drop formation need to be re-adjusted in order to form the drop desired for each deposition.

In both inkjet printers used throughout the thesis, the printhead used consists on piezoelectric actuators using a lead zirconate titanate (PZT) material. Thanks to the piezoelectricity properties of such materials, once an electrical field is applied, the material suffers a mechanical deformation. In this particular case, the piezoelectric nozzles cause a squeeze in the liquid column present; it expands and contracts when a voltage differential is applied. The pulse length is also involved in the oscillation of the piezoelectric actuator. Once the waveform is applied, the material present in the glass column, in the form of a liquid solution, it also oscillates [**83**].

If the resulting oscillation has enough energy to overcome the viscous and surface tension forces of the liquid, it breaks, surpassing the viscous dissipation resulting in the generation of a single drop, for each pulse applied to the material, specifically drop volumes in the range of picolitres (pL). The waveform parameters will influence the drop formation: while the voltage applied can tune the drop volume of the drop, the pulse length modifies both drop volume but more specifically, its speed. As an example, low voltages and short pulses will generate smaller and faster drops [**90**]. However though, if the waveform is not able to surpass the viscous and tension forces, the drop will not be generated. On the contrary, very high voltages can produce the formation of undesired secondary drops.

The range of volume obtained is also thanks to the diameter of the nozzle. In fact, the different nozzles used may have different characteristics, in which the waveform applied must also be tuned in order to obtain similar drop parameters, especially if more than one nozzle are being used at the same time. Moreover, the drop impact diameter is also affected by the drop speed and the distance between the substrate and tip of the nozzle, which in turn modifies the shape and diameter once the drop impacts into the substrate, giving rise to different drop shapes, which may result in different liquid-substrate interactions, liquid movement and/or material accumulation at the edges of such substrate.

2.3.2.2 Drop pitch and Line pitch

Our inkjet printing systems can work as a drop on demand, meaning that a drop is generated with each voltage waveform applied, but by stablishing a certain frequency value, the drops can be continuously expelled. Whereas the nozzle position became fixed, the platform moves in two perpendicular directions, X and Y, in the range of the micrometers (μm). In principle, the frequency in which the drops are generated is used to determine the drop distance in one particular direction, in this case, the horizontal direction (X). Thus, the drop spacing in the X direction is determined by the frequency. The spacing between drops in the X direction is what is known as drop pitch.

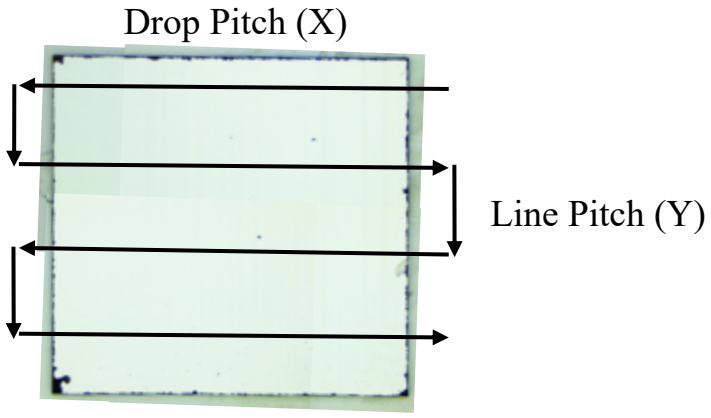

Figure 2.2. *Schematic representation of the horizontal direction or drop pitch (X) and the vertical direction or line pitch (Y).*

The motor also performs a lateral step with a micrometer resolution, which corresponds to the vertical direction (Y). This lateral step corresponds to the drop distance in Y direction, which is known as line pitch. Both parameters are important during deposition since it will determine the drop overlapping, responsible for film homogeneity after deposition.

2.3.2.3 Drop monitoring

Once the parameters involving the formation of drops are set, the drops can be monitored by means of a stroboscopic camera. By using a visual software, different in each inkjet printing system used, the parameters of the drop can be obtained; the drop volume, drop diameter and drop velocity can be studied, which will impact on how the deposition, and more specifically the homogeneity, by using its corresponding visual software.

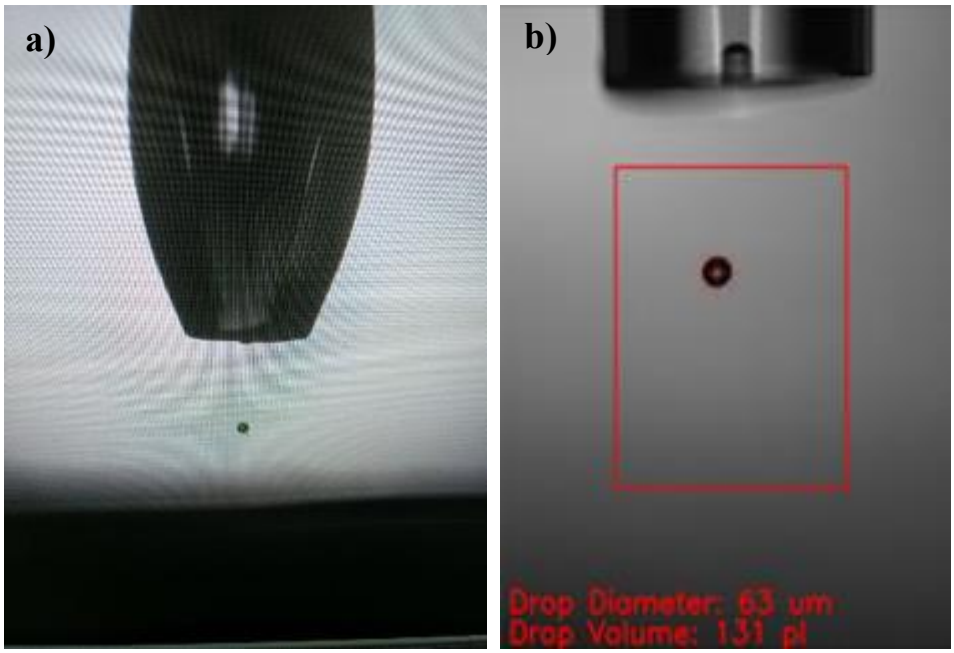

Figure 2.3. *Example of drop monitoring by using a stroboscopic camera. In this case, 1-butanol solvent is used. a) Homemade inikjet printer and b) MicroDrop inkjet printing, which system accounts for an automatic measurement of the drop parameters.*

2.3.2.4 Meniscus control

For the meniscus control, a pressure system is used, which creates a vacuum that results in the stabilization of the meniscus of the fluid [**126**]. Using such pressure systems, it ensures a continuous ejection of drops without nozzle clogging. Before and after deposition, the glass nozzle tip is wipe out with a fine cloth soaked in methanol to remove possible contaminants and dried material, which could alter the films homogeneity by adding undesirable impurities during the deposition.

2.3.2.5 Jetting Parameters of the inkjet printing systems

Here we present the optimized parameters employed in this work to achieve stable drop formation in each of the inkjet printing systems utilized, depending on the plate velocity and the modality used, described in Chapter 2.3 and summarized in Table 2.1 and 2.2. Typically, an increase in additives or total molar concentration requires higher voltages in order to achieve a stable drop formation. Then, as mentioned, the drop formation is achieved when the energy is high enough to overcome the surface tension and viscous forces of the inks prepared.

As observed, the specific parameters for the proper ejection of drops are different in each inkjet printing system used, which in turn affects the volume of the drops in the range of picolitres. Thus it is mandatory to optimize the drop and line pitches in each system, to obtain the best overlapping and achieve homogenous depositions, for each particular case. As above mentioned, there is not a particular solution to obtain a homogenous inkjet printed sample, it will depend largely on the setup of each of the Inkjet printer systems used and the nozzle characteristics of each apparel.

Table 2.1. *Jetting parameters employed for the drop formation in the homemade inkjet printing (chapter 3).*

Jetting parameters	**Value**
Voltage up (V)	30 - 40
Voltage down (V)	15 - 25
Pulse length (μs)	20
Substrate temperature (ºC)	21
Frequency (Hz)	Variable, depends on the drop pitch
Drop volume (pl)	80-120
Substrate / nozzle distance (mm)	~1
Drop velocity (m/s)	1.5 - 2
Pressure (bar)	0.65 – 0.9

Table 2.2. *Jetting parameters employed for the drop formation and Fast Mode (FM) or Slow Mode (SM) deposition of REBCO inks in the MicroDrop Inkjet Printing system (chapter 4 & 5).*

Jetting parameters	**Value**
Voltage up (V)	130 - 160
Voltage down (V)	0
Pulse length (μs)	20 - 30
Substrate temperature (ºC)	25 to 50ºC
Frequency (Hz)	1 (SM), variable (FM)
Drop volume (pl)	180-200
Drop size (μm)	70 ± 2
Substrate / nozzle distance (mm)	~1
Drop velocity (m/s)	2
Pressure (mbar)	18

2.4 Substrate Treatment

Except CCs, prior to deposition, the substrates were thermally treated at 900ºC for 5h under an Oxygen atmosphere to develop a flat-terraced surface, and thoroughly cleaned with acetone and methanol to remove any residues or impurities on the surface.

2.5 Pyrolysis

For thick samples, and especially those made by inkjet printing, pyrolysis implies the generation of mechanical stress due to the densification of the film, caused by the decomposition of the organic precursors, which causes a significant shrinking and mass loss, up to 50%, depending on the case. In this thesis, several heating ramps have been evaluated for Fluorine-free solutions to ensure a proper decomposition of the precursors and to avoid defects such as cracking in the samples.

2.5.1 Sample drying

After the deposition by spin-coating or inkjet printing, samples were usually dried for 5 minutes in a hot plate at 60ºC and placed on a tubular furnace afterwards. In some works, a photocurable polyacrylic ester-based commercial varnish is used as an additive, so after the deposition, the films followed a curing treatment with a with a LED lamp (λ = 395 nm), with an input power of 0.7 W. The curing time was set to 10 min.

2.5.2 Tubular furnaces

In the tubular furnace, after the drying, a pyrolysis procedure is performed. Different heating rates can be set, though for FF solutions the heating rate is usually of 5 ºC/min up to 240ºC and 3 ºC/min up to 500ºC in a humid oxygen flow of 0.12 L/min. Water vapour during pyrolysis enhance gas transport derived from the decomposition of organic matter, prevents Cu salts sublimation and helps on the chemical transformations.

2.5.3 Pyrolizer

What we call pyrolizer is in fact a small rectangular oven with a silver resistance used for heating the samples in a similar manner than tubular ovens.

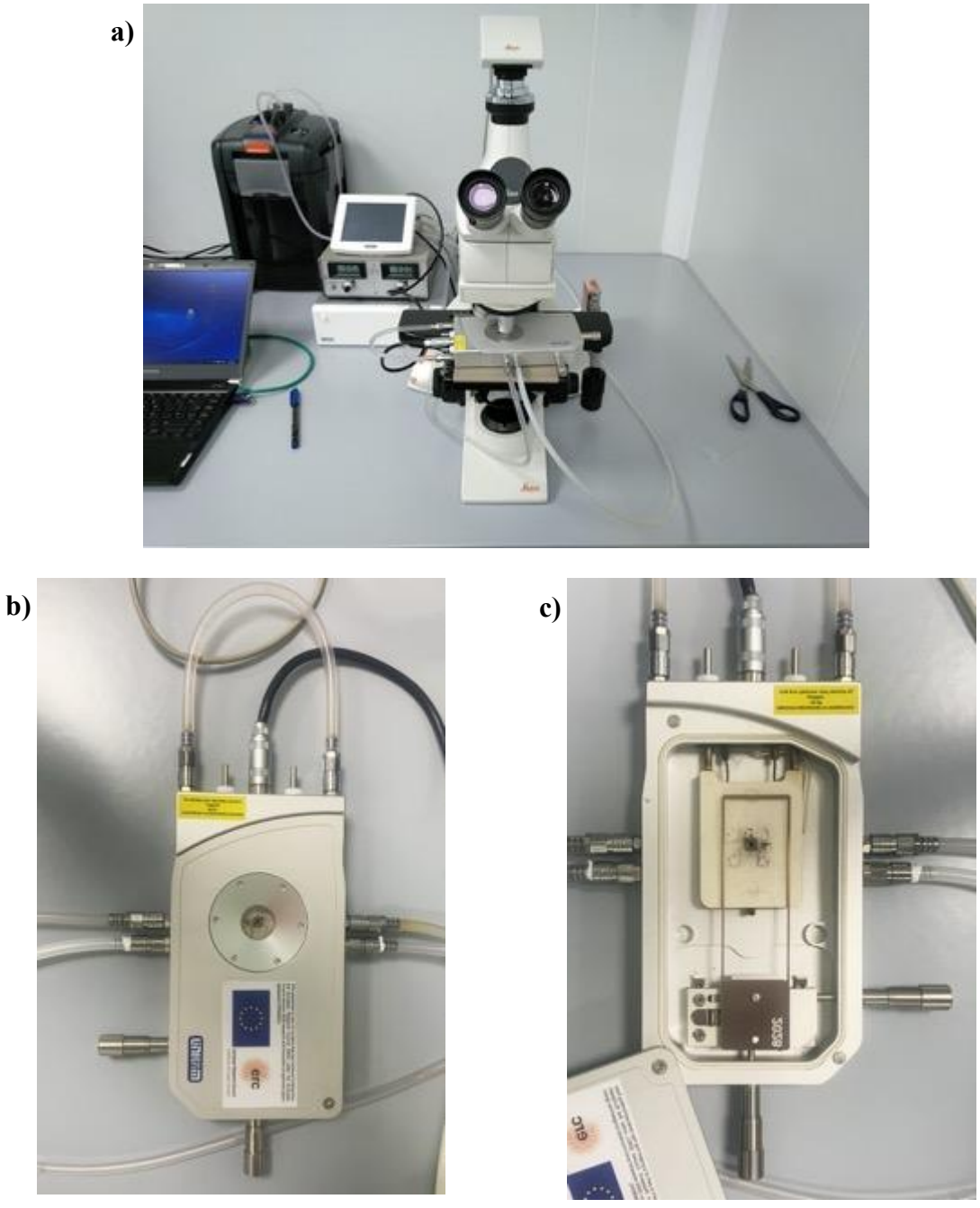

Figure 2.4. a) *Pyrolizer oven coupled to an Optical Microscope for in-situ optical imaging of the pyrolysis process. b) Pyrolizer oven. c) Open oven heating stage or compartment.*

This small furnace accounts with a small glass heat-resistance window in which, via optical microscopy, an in-situ visualization of the pyrolysis stage can be monitored. By coupling the optical microscope to the pyrolizer, it allows us to observe the whole pyrolysis stage and video-record the several densification steps of the film, together with the possible appearances of defects. The heating stage of the furnace has two main divergences from the tubular furnace:

- The pyrolyzer uses a heating mechanism in which a silver resistance, that can heat up at 50°C/min. This contrasts with the usual tubular ovens used for the pyrolysis, where the sample is placed at a specific isothermal position of the oven, because the heating mechanism relies on electrical resistances.

- Also, in contrast to the tubular furnace, the oxygen gas flow is different in the case of the pyrolyzer, because it collides with the silver resistance, distributing the gas around the sample, generating on this way the desired atmosphere but with more gas turbulence.

Even though this differences, the samples obtained with the pyrolyzer have similar microstructure composition than those obtained by standard tubular ovens, demonstrating to be a very useful in-situ analysis tool for the pyrolysis study.

2.6. Mass and Heat Evolution

In-situ characterization techniques for the mass evolution of the films prepared, especially in the pyrolysis process, were of very interest due to the capability to record and analyse the different steps of metalorganic decomposition. This technique allows us to differentiate between the decomposition of each metal carboxylate salt present in the solutions, its correspondent decomposition reaction pathways, solvent evaporation in the deposited films and moreover, its associated thermodynamic information. In this regard, Thermogravimetric Analysis (TGA) and Evolved Gas Analysis (EGA) coupled to Fourier-transform infrared spectroscopy (FTIR) spectrometer were performed at the University of Girona (UdG).

2.6.1 Thermogravimetric (TG) Analysis

In-situ characterization of the mass evolution in deposited films, using thermogravimetric analysis, give us information regarding the pathways of the reaction that the metal carboxylates undergo under temperature and an oxidant atmosphere, such as Oxygen gas. After the TG analysis, the samples also have been studied by XRD and FTIR techniques for a complete analysis of the microstructure.

Samples are analysed by depositing chemical solutions by either drop casting or spin coating in LAO single substrates. Samples are weighted in precision microbalances, before and after the pyrolysis process, to evaluate the complete transformation from carboxylates to its correspondent oxides and Barium carbonate.

Since no more transformations are expected after the 500ºC firing process, if not higher temperatures are set afterwards, we could analyse the mass evolution of the deposited films and extract the information, regarding its metalorganic decomposition at the several temperature stages of the process, in accordance to its weight loss.

Two aluminium crucibles are placed in the TG system, being a Mettler Toledo model TGA/DSC1 thermobalance. One of the crucibles being a blank substrate and the other the selected sample to study, for its proper mass evolution comparison. The TG conditions were like those used in the tubular ovens used, being a temperature program from 50 to 500 ºC at 5 K/min with an 80 mL/min humid O_2 gas. In addition, another temperature ranges from 500ºC to 850ºC at 25 K/min, can be set to study the carbonate decomposition using a 200 mL/min wet N_2. After the process, a purge gas of 30 ml/min N_2 to eliminate the last possible remnant decomposition by-products of the process is passed through the samples. Different oxygen partial pressures were obtained by mixing high purity N_2, O_2 or synthetic air (Air Liquide, ≥99.999%). Water-saturated gases at the reactive inlet were obtained by bubbling the carrier gas in water at 25°C and atmospheric pressure.

2.6.2 Evolved Gas Analysis (EGA)

The Evolved Gas Analysis is also a very useful in-situ technique for the proper evaluation of the releasing gases obtained as a by-product of the metalorganic decomposition. For this manner, an FTIR apparatus was used for the composition study.

EGA/FTIR was obtained by connecting the TGA gas outlet to an ALPHA Bruker FTIR gas analyzer via a 40 cm long steel tube heated to 200ºC to prevent gas condensation. The range of wavenumbers is from 500 to 4000 cm^{-1} with a step of 2 cm^{-1}.

2.7 Transient Liquid-assisted Growth (TLAG)

After the pyrolysis, all the organic material has been removed from the sample and only nanocrystalline phases in the form of Barium Carbonate with Yttrium and Copper oxides remains. As a final step of the whole CSD process, the samples were annealed at high temperatures under various conditions in order to grow the REBCO phases through the TLAG process.

As described in the introduction (Chapter 1.2), Transient Liquid-Assisted Growth (TLAG) is characterized for achieving high oriented epitaxial YBCO films by using either a rapid heating, known as T-route, where a Rapid Thermal Annealing oven is used, or a pressure jump known as P-route, where a home-made furnace is used, all under certain oxygen partial pressures [**71**]. In this thesis though, most of the effort was concentrated on the achievement of thick films defect-free pyrolized samples prior to growth, and most of the annealing crystallizations of YBCO were done using the P-route approach as the main last synthetic step of the TLAG-CSD route.

Figure 2.5. *P-route oven setup for the preparation of YBCO samples through the TLAG-CSD method.*

The homemade P-route annealing oven consists of the use of a high temperature tubular oven from MicroTest. Initially, the oven was static, and the samples were placed in a fixed isotherm zone of the oven to ensure a proper heating at the desired temperature. With time, a remotely controlled motor rail was included in the setup, achieving higher heating ramps and avoiding time-consuming processes. With this approach, the samples obtained were of much more quality, as it will be discussed in the next chapters, essentially because coarsening of the precursor phases could be avoided.

The total pressure control was achieved through electrovalves, while an oxygen sensor was used to pre-set the PO_2 at the desired value. Pressure values were tracked via LabVIEW interface using a remote connection to a pressure-meter. The use of remote control of electrovalves ensure the changes on oxygen partial pressures.

2.8. Sample characterization

The characterization of the samples was performed using several different techniques. The characterization is of most importance since it gives us insights on how the good performance samples must behave either visually or microstructurally. Surface morphology of the as deposited and pyrolized samples were evaluated by means of optical microscopy (OM) using a Leica DM1750M. However, other advanced techniques which involves surface and thickness analysis, microstructure analysis or mechanical properties were also carried out.

2.8.1 Surface and thickness analysis

For the development of thick films by inkjet printing technologies, thickness is one of the most important parameters to control. During the pyrolysis step of the TLAG-CSD process, densification on films occur, which due to film shrinkage, stress release phenomenon can occur, such as the formation of defects on the sample. We have measured the surface morphology and thickness of our samples by two different characterization techniques, one being a more destructive measurement, involving profilometry measurements, and the other being a non-destructive technique, which relies in interferometer measurements.

Non-destructive techniques are preferred because it allow us to later grow the measured samples. However, interferometer results were more qualitative values, thus it was mandatory to determine the exact thickness of the sample by profilometer measurements.

2.8.1.1 Interferometry measurements

For interferometry measurements, an interferometer apparatus from Filmetrics was used for the thickness measurements. Usually, these techniques have thickness limited boundaries, arising from 100nm to several μm thick samples, which were in the range of our prepared samples.

The interferometry measurements are based on the constructive interference that superimpose electromagnetic waves of the same frequency create, based on the refractive index of the material (n). Thickness determinations were done using a Filmetrics software.

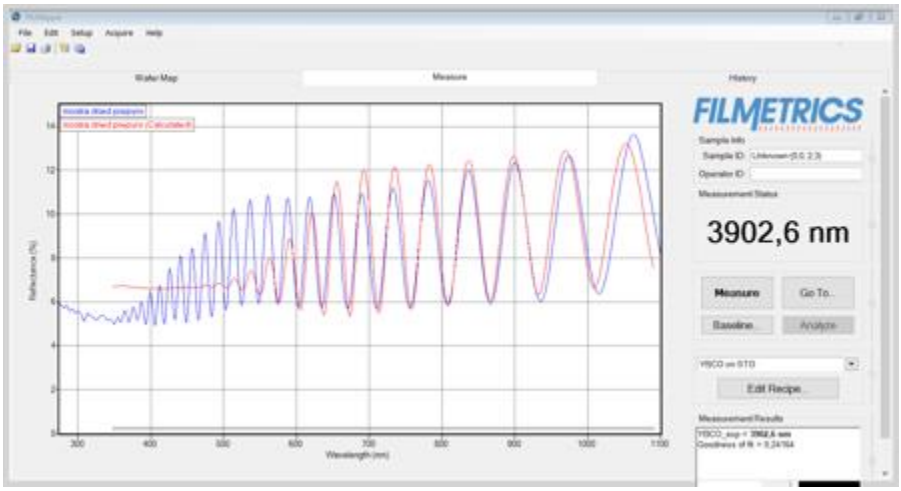

Figure 2.6. *Example of an interferometer thickness measurement.*

2.8.1.2 Profilometry measurements

In a more quantitative manner, profilometry measurements, using a P16+ profilometer from KLA Tencor, were performed to evaluate the surface morphology and thickness of pyrolized samples. The measurements were carried out by fixing the sample first in a microscope glass plaque. A cantilever measures the differences in thickness by selecting the appropriate distance within the substrate, being possible to measure by either a two-dimensional single screening or 3D measurements.

While the surface morphology could be done in a non-destructive manner, in order to identify the thickness striations at the surface's sample, for the measurements of film's thickness of pyrolized samples, a destructive etching procedure was performed using UV-curable polymeric resin.

After pyrolysis, the desirable part of the film for its thickness study was covered using a UV-curable polymeric resin. The samples were then heated at 70ºC at a heating plate for 5 minutes. Afterwards, the sample is soaked in an aqueous solution of 1:100 volumetric ratios of ortophosphoric acid. Once the etching of the undesirable part of the sample is done, the sample is washed with deionized water, acetone, and methanol subsequently and dried using technical nitrogen gas.

2.8.2 Infra-red spectrometry

Infrared spectroscopy is a very useful technique for the determination of organic chemical species present in both the solution and the as- deposited films by CSD methods. For the qualitative identification of the organic moieties of our carboxylate precursor solutions, a MID-IR electromagnetic radiation (4000-400cm^{-1}) spectrometers were used. Infra-red light can excite the different bond vibrations of the organic compounds present, by which their characteristic fingerprints could be identified and catalogued.

2.8.2.1 Fourier-Transformed Infrared Measurements

We used a Fourier-transform infrared spectroscopy (FTIR) spectrometer model Vertex 70 from Bruker, transmitting the IR light beam through the sample. These measurements can be performed if the film is deposited on STO or LAO single crystal because they are transparent in most of the electromagnetic spectrum of MID-IR. The two most important chemical species to be studied for the deposited and pyrolized were the alkane absorbance of the stretching mode (sp^3 C-H str.) of carboxylate ligands, a band between 2800-3050 cm^{-1}, and the characteristic stretching of the carbonate moieties present in the film after pyrolysis, which usually appear around 1400-1500cm^{-1} as a broad peak.

2.8.3 X-ray Analysis

X-ray diffraction is a very practical tool for the characterization of the samples, such as texture and composition, both after pyrolysis and high-temperature annealing, for the evaluation of the resulting microstructure and compounds after the several steps of the TLAG-CSD process.

The structural characterization was conducted by high-resolution X-ray diffraction (XRD) with a Bruker D8 Discover system (Cu K_α, X-ray energy = 8.049 keV) equipped with a Lynxeye XE energy-dispersive 1D detector. Also, the microstructure characterization of pyrolized films and the quantification of the amount of epitaxial material on the samples after growth were performed using a Bruker-AXS D8 Advance diffractometer (Cu K_α) equipped with a General Area Detector Diffraction System (GADDS). Following Bragg's law, the scattering radiation in a regular atom configuration, such as in a crystal structure we have:

$$2dsin\theta = n\lambda \tag{2.1}$$

Where λ is the wavelength of the incident X-ray, n is the reflection order, θ is the angle between the incident X-ray beam and the sample plane, and d is the inter-planar spacing between (hkl) planes.

A two-dimensional X-ray detector (2D X-ray) uses the radiation to generate diffraction patterns. The sample is rotated at given θ/2θ angles to obtain information about the texture and its microstructure composition. Additionally, the rotation in χ angles provides the texture out-of-plane. With the X-ray analysis we are also able to obtain the crystal orientation (i.e., epitaxial compositions). As the sample is analysed, the signal of the reflections will be detected as spots if the sample is epitaxial, while the polycrystalline phases, mostly undesired secondary phases in the case of c-oriented YBCO samples, will be obtained as a rings because of the produced random scattering.

2.8.4 Electron Microscopy

The spatial distribution, size, thickness and crystalline state of the precursor phases in pyrolyzed films were probed via high resolution transmission electron microscopy (HR-TEM) and high-angle annular dark field scanning transmission electron microscopy (STEM-HAADF). In addition, the thickness and crystalline state of the YBCO samples after TLAG were also probed with transmission electron microscopy (TEM). For this purpose, a FEI Tecnai F20 (S)TEM was operated at 200 kV. Energy-dispersive X-ray (EDX) spectroscopy measurements were carried out to verify the deposited composition.

2.8.5 Thermomechanical Analysis (TMA)

To test the mechanical properties of the films in order to understand the formation of defects such as crack formation in the sample, a novel mechanical testing technique was developed by Prof. Pere Roura, located in the Universitat de Girona (UdG). This technique is based on the displacement response of the film upon an applied loading force. For this purpose, a thermomechanical analysis (TMA) apparatus was used, with the TMA quartz cannula of a known diameter acting as the force tip. For the sample measurement, a TMA SETSYS evolution from SETARAM was used.

The film was deposited in 5x10 or 10x10 mm^2 LAO substrate and placed on a quartz support below the apparatus cannula. Altogether is placed inside a furnace which permits an accurate temperature control, where they are heated up at a constant heating rate of 10°C/minute up to 180ºC. Once the temperature is constant, the load is made to measure the film displacement. Using some mathematical approximations on the Stoke's law, film viscosity is extracted from the displacement curves while the samples were in the gel-liquid regime at a given temperature, 150ºC or 180ºC. The results are discussed in the Appendix C.

2.9. Superconducting Properties Analysis

To measure the superconducting properties of the as-grown YBCO thick film samples made by inkjet printing through the TLAG-CSD process, two different techniques were performed, being the Superconducting Quantum Interference Device (SQUID) magnetometer but also transport measurements.

2.9.1 Superconducting Quantum Interference Device (SQUID) magnetometer

The parameters to be measured by SQUID are the critical current density (J_C) dependence with temperature and magnetic field, and the critical temperature (T_C) value and transition width sharpness (ΔT_C). This is a non-destructive, very sensitive technique to detect extremely small magnetic fields, consisting of a magnetometer containing Josephson junctions in superconducting loops for the amplification of the pick-up signal [**127**].

SQUID DC-magnetometer Quantum Design equipped with a 7T and a helium cryostat was used to measure the sample superconducting performance using the Beam critical state model of a thin disk. For the measurement, the sample is placed inside the superconducting coil, where uniform magnetic fields are applied in parallel to the c-axis of our YBCO samples. As a result, a current proportional to the magnetic flux variation is induced in them. The SQUID sensor acts as a highly sensitive current-voltage converter detecting voltage variations proportional to sample's magnetization.

2.9.2 Transport measurements

The critical current density can be also determined from electrical transport measurements using I−V curves, more specifically with the critical current - electric field (J−E) curves. In this case, in contrast to SQUID magnetometry, this is a destructive technique.

Silver metal contacts are required, which are evaporated on top of the films and annealed, to ensure enough low resistance values. The J(E) curves of the YBCO tracks was measured in a four-point configuration.

In this four-point configuration, a DC-current is introduced until a desired value between two contacts is obtained. The magnetic field is applied to the current flow, parallel to the c-axis. The transport measurements were carried out in the Physical Properties Measurement System (PPMS) from Quantum Design equipped with a 9T magnet at ICMAB. Using these measurements, the J_C dependence with the magnetic field was characterized at different temperatures.

2.10. In-situ XRD synchrotron measurements

Synchrotron experiments were employed for the in-situ analysis of the growth of thick YBCO samples. In-situ XRD growth experiments were performed at the DiffAbs beamline, SOLEIL synchrotron facilities (France), using an X-ray beam energy of 18 keV and a XPAD (X-ray hybrid pixel area detector) area detector with acquisition times per image of 100 ms (see Appendix B).

The obtained images can be converted into Intensity *vs.* 2θ diffractograms considering the experiment geometry (sample and detector angular positioning) and using home-written Python code. Samples were heat treated in an Anton Paar DHS 1100 domed heating stage at rates of 25 ºC/min, 1 bar of total pressure and 1 mbar of oxygen partial pressure. An X-ray transparent Kapton dome, equipped with a double connection to the vacuum pumps and gas inlet/outlet systems, was utilized to seal the heating stage.

The total pressure control was achieved through electrovalves, while an oxygen sensor was used to adjust the O_2 concentrations at the desired values. Pressure values were tracked via LabVIEW interface using a remote connection to a pressure-meter. The heating set for the TLAG growth prepared at Soleil resembles to the homemade P-route annealing oven on its static configuration. The use of remote control of electrovalves ensure the changes on oxygen partial pressures. A T-route configuration could also be set by fixing the oxygen partial pressure, recorded with an oxygen sensor and an Anton Paar DHS 1100 heating stages at very high heating ramps.

3.

Fast Mode Inkjet Printing depositions of Fluorine-free precursor solutions using a UV-Curable Varnish additive

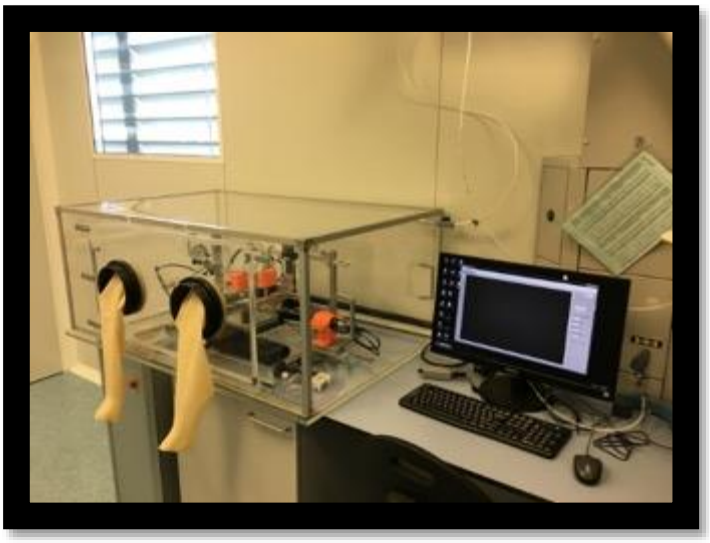

The development of thick YBCO films by the TLAG-CSD methodology involves several steps that must be guaranteed: the solution synthesis, deposition, pyrolysis and growth. In each step a set of parameters need to be properly controlled. In this thesis we have chosen ink jet printing deposition for the deposition of the layers, so the first step is to develop a precursor solution (ink), stable and homogenous, suitable for ink jet printing that should facilitate a reproducible defect-free pyrolysis with a microstructure composed of homogenously distributed nanocrystalline oxide precursors phases. Finally, the pyrolyzed layers should enable to reach high quality textured crystalline YBCO films. This chapter presents an ink design study, a printability analysis and a pyrolysis process based on previous knowledge of inks suitable for TFA film growth. The ink-jet printing apparatus (homemade) used is the same as that used in the group's previous studies.

3.1 Introduction to Fast Mode Inkjet Printing depositions of propionate-based precursor solutions using UV-Curable Varnish additives

Since our aim is to obtain a suitable chemical precursor solution for the deposition of the thickest YBCO films as possible, and in one single deposition, the solution needs to be properly optimized. As mentioned, for inkjet printing, the precursor solution has to match both a proper Z number, implying good rheological properties for drop formation, leading to the ejection of continuous and stable drops; and proper wetting of the substrate to obtain homogenous depositions. To guarantee the fulfilment of the requirements, some of the variables for the solution optimization were accounted:

- The metal precursor salts present in the solution.
- The solvents used and its volumetric ratio.
- Explore the concentration of the solution.
- Explore the rheology of the solution to obtain thicker films in one single deposition.
- The evaluation of additive compounds that could be beneficial for the stability of the solution, increase sample homogeneity, increase thickness, or help on the film densification during pyrolysis.

Considering such requirements, some basic characteristics for the reproducible design of these solutions were stipulated. Basically, and as we mentioned above (section 1.2), we needed to ensure: a proper precursor salts solubility based on the total metal concentration available without precipitation, good wettability of the substrates, low water absorption since the solution water content must be kept below a 2%wt. for its proper use [**128**], a certain viscosity requirement to reach the desired Z values for inkjet printing deposition, and finally the use of organic solvents with adequate boiling points to obtain good drop overlapping and homogeneous depositions. In this regard, we took special attention to the solvents used, the total metal concentration and the percentage of additives needed to ensure thick films in the range of 1μm after final growth, while keeping good homogeneity during deposition.

High boiling point solvents such as propionic acid (b.p. 141.2°C) and 1-butanol (b.p. 117.2°C) have demonstrated better film homogeneity during depositions by inkjet printing in the case of Low-Fluorine solutions previously used in our group [**92**]. The rheological parameters of the solutions with high boiling points differ from the low-boiling point solvents used on other type of CSD systems. High boiling point solvents allow a more stable jetting, being better for the avoidance of nozzle clogging and a more reproducible deposition.

To study the difference between the CSD deposition methods used in our group, the solutions were prepared in two different alcohols, either methanol, used on other CSD techniques like spin-coating or slot-die coating from our group, or 1-butanol, more specific for inkjet printing systems. It was of interest to check for the thickness of the films after pyrolysis by changing the metal concentration of the solution, because it allows us to obtain thicker films in one single deposition, thus avoiding time-consuming processes such as multideposition, i.e., the repetitive deposition of layers on top of the already pyrolized ones.

3.2. Experimental Section

3.2.1 Precursor Solution Synthetic Procedure

Several Yttrium, Barium and Copper acetates precursor solution were prepared. Yttrium (III) acetate hydrate $(CH_3COO)_3Y \cdot xH_2O$ (99.9 %, Sigma-Aldrich), Barium acetate $(CH_3COO)_2Ba$ (99.5 %, Sigma-Aldrich) and Copper (II) acetate $(CH_3COO)_2Cu$ (99.99 %, Sigma-Aldrich) were dried overnight at 50 ºC, in a vacuum oven to remove traces of water due to its hygroscopic nature. After that, the acetate precursors were sequentially dissolved at 35 ºC (Y→Ba→Cu), for the appropriate total metal concentration, in a 5 mL 80/20 solution of 1-butanol (Alfa Aesar, 99.4%) with propionic acid (99%, Sigma-Aldrich). The mixture resulted in a deep blue solution without any precipitates.

The total cation concentration was adjusted by controlling the amount of volume in a volumetric flask and then filtered. The volumetric ratio used 20/80 propionic acid/butanol ensured a proper dissolution of the salts, because previous attempts have shown that lower amounts of propionic acid led to precipitation in total metal concentrations of around 1-1,5M (∑metals) [**92**]. All solutions possessed a stoichiometry of 1:2:4,66 (Y:Ba:Cu, named from now on 3:7 stoichiometry), selected for the TLAG process [**70**].

In addition, another solution was prepared in order to compare the results obtained from inkjet printing deposition. This solution, called Low-Fluorine 4G solution results from the exchange of Yttrium acetate by Yttrium trifluoroacetate in 1-butanol and propionic acid as solvents, with a 1:2:3 stoichiometry (namely 2:3). This solution was already optimized by our group to obtain thick YBCO films by inkjet printing with good results in both deposition homogeneity and pyrolyzed film thickness in the range of 1.8-2µm in one single depositions with good superconducting film performances after growth following a TFA-CSD route [**128**].

3.2.2 Solution Characterization

There are some ink parameters that allow us to interpret if a particular solution produce reproducible depositions by Inkjet printing. One of them is the Z number, which has a defined range where the generation of stable drops can be accomplished without satellites, that is between 4 and 14 [**96**]. For that matter, a rheological study on the precursor solutions prepared is compulsory.

As it will be observed, the Z numbers of the methanol solutions do not fulfil the requirements for its proper drop ejection in inkjet printing, either due to the low viscous behaviour, higher contact angles and moreover the low boiling point of methanol (b.p. 64.7 ºC), which eventually leads to the generation of satellites and nozzle clogging. The rheological properties of the solutions prepared together with its computed Z number are described in the following Table 3.1.

Table 3.1. *Rheological properties of the precursor solutions prepared, with propionic acid as co-solvent.*

Co-Solvent	Methanol	Methanol	Butanol	Butanol	Butanol	Butanol (TFA)
Concentration (∑metals)	1	1.5	0.75	1	1.5	1
Viscosity (cP)	2	5	5	7	12	9
Contact angle (º)	20	28	>10	>10	17	10
Density (g/cm^3)	1	1.1	1	1	1.1	1.1
Surface tension (mN/m)	26	28	24	24	24	25
Z	27.2	9.3	9.8	7.4	4.4	5.8
Nomenclature	FF-M1	FF-M2	FF-B1	FF-B2	FF-B3	LF-4G

For this reason, we moved to 1-butanol as a solvent, due to its more optimal rheological properties for inkjet printing deposition. The wettability of the metalorganic solution over the substrates was increased with 1-butanol, so more homogenous films could be obtained in the inkjet printing deposition, specifically thanks to its lower contact angle. More viscous solutions allow for a better fixing of the liquid into the substrate, avoiding liquid redistribution during and after deposition, achieving better performances and more homogenous films.

As mentioned [**94**], previous results using TFA precursors for IJP deposition showed a superior wettability when using 1-butanol, avoiding nozzle clogging and obtaining good homogeneity on the samples after deposition, so it was concluded that a solution using 1-butanol was the best option for TFA precursors. In this study, we tried the different FF solutions and compared the results also with those previously obtained by spin coating [**70, 128**].

One of the other characterization techniques used to determine the nature of the metal precursors was FTIR, which allow us to identify the organic ligands present in the solution. The FTIR spectra of the solution prepared shares similar characteristics with the propionic acid rather than acetate moieties, suggesting at least a partial ligand exchange between the metal salts and the propionic acid present in excess in the solution.

The spectra exhibit the characteristic absorption peaks at 1466 and 1431cm^{-1}, all characteristic fingerprints of the ligands [**129**]. Notice the presence of the intense Cu propionates band at 1585 cm^{-1}, corresponding to the C=O stretching mode, next to their equivalent bands for the Ba-Prop and Y-Prop salt at 1546 cm^{-1} (the absorptions of both salts overlap). Also, a peak at 1299 cm^{-1} correspond to carboxylate fingerprints.

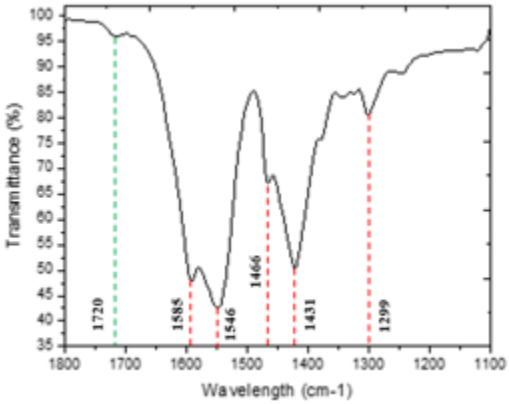

Figure 3.1. *FTIR spectra of a 1M precursor solution in 1-butanol with (3:7) stoichiometry (Solution FF-B2).*

To evaluate the coordination type of the metal ions to the carboxylate moieties, discerning from bidentate bridging ($\Delta\nu < 134.6 cm^{-1}$), bidentate chelating ($\Delta\nu > 134.6 cm^{-1}$) or monodentate ($\Delta\nu > 180$ cm^{-1}) coordination types [**130-138**], we calculate $\Delta\nu = \nu_{as} - \nu_s$, being the difference between the C=O symmetric and asymmetric stretching frequencies. $\Delta\nu$ indicates the carboxylate coordination to the ions. In this case, for the FF-B2 solution, a value of $\Delta\nu$ = 120 cm^{-1} is obtained, suggesting a bidentate bridging coordination [**128**]. Bidentate structures are advantageous since coordination of water molecules is hindered, making more robust solutions.

Additionally, the coordination mode of the ligand can be deduced from carboxylate peaks position. From previous works of our group [**132**], a certain quantity (around 20%) of unreacted barium acetate is present, giving rise to a mixture of barium-propionate-acetate crystalline structures, where a peak at 1546 cm^{-1} in the FTIR appears. Apart from that, we assume that the prepared Fluorine-Free solutions contain no more acetates. In addition, a peak at 1720 cm^{-1} corresponds to free propionic acid.

Therefore, from the FT-IR spectra it can be concluded that the synthesis of the solution was also successful, leading to stable and homogenous inks, without any precipitation for weeks in total metal concentrations. The results seem to indicate that the decomposition of the deposited and dried films, during the pyrolysis, will mostly correspond to the decomposition of Y, Ba and Cu propionates, obtained from their respective acetates by reacting them with propionic acid in excess. Additionally, the rheological analysis of the solutions enabled us to gather information regarding the properties and similarities between the above FF-solution and the solutions using TFA compounds.

3.2.3 Solution Evaluation

It is known that the film thickness (h) can be related to the deposited solution physical parameters through the Navier-Stokes equation in spin-coating deposition [**128**]:

$$h = \frac{c}{2w\rho_s}\left(\frac{3\eta\rho_l}{t}\right)^{1/2} \quad (3.1)$$

Where η is the viscosity, c the mass concentration (weight of solid film/weight of solution) and ρ_s and ρ_l are the solid and liquid densities respectively, while ω and t refers to the angular velocity and spinning time in spin-coating, respectively.

Following the equation, to obtain thick films, as higher the concentration of the solution is, thicker films are obtained in each deposition, so we expect to use an optimized solution with the highest concentration (mol/L) as possible. Before inkjet printing analysis, some of the precursors and solvents present on the chemical solutions were evaluated in order to achieve a better performance on the deposition, with the aim to achieve high thickness samples without defects. In this case, for our prepared solutions, we selected the 1M in 1-butanol thanks to its best physicochemical properties for inkjet printing deposition conditions, optimized taking into account the plate velocity of the system and the amount of time required for preparing deposited films.

To optimize the solution and the pyrolysis conditions, at first, a complete film prepared by spin-coating with a subsequent thermal treatment (5 ºC/min up to 240 ºC and at 3 ºC/min from 240 ºC to 500 ºC) was carried out. This pyrolysis profile ensured the decomposition of the organic constituents and the formation of nanocrystalline oxides and carbonates (Y_2O_3, $BaCO_3$ and CuO), which are the precursor phases for the YBCO final layer and was optimized in previous works [**70**]. The viability of the prepared films for an additional second high temperature treatment known as TLAG growth is also studied.

The initial prepared solution was a Fluorine-Free propionate-based solution, where the salts used were commercial acetates. The optimized solution for spin-coating uses an organic solvent media resulting in a mixture of methanol and propionic acid. Spin-coating samples of this solution lead to very homogenous films and its transformation to YBCO by the TLAG route, giving rise to very high critical currents (3-5 MA/cm^2) for thin films (100nm). This type of solution is well-known in our group, obtaining very promising results for the TLAG process [**70**].

However, this solution was designed with the purpose to achieve the optimal parameters for thin films deposited by spin-coating deposition. Since the deposition of Fluorine-free solutions by inkjet printing was hardly studied in our group, the optimal ink composition had to be thoroughly studied. The aim of our study was the deposition of thick YBCO films via inkjet printing deposition, with the opportunity to print thick films in one single deposition, so the precursor solution needed to be reconfigured.

Spin-coating depositions were performed over (001) $SrTiO_3$ (STO) and (001) $LaAlO_3$ single crystals. The degree of decomposition of the pyrolized films was determined by FT-IR spectroscopy and XRD. The FT-IR spectra of a just deposited film was used to know the initial state of the film before the pyrolysis. The homogeneity of the films was determined by optical microscopy. The initial thermally pyrolized samples under wet oxygen flow at 500 ºC revealed homogenous films.

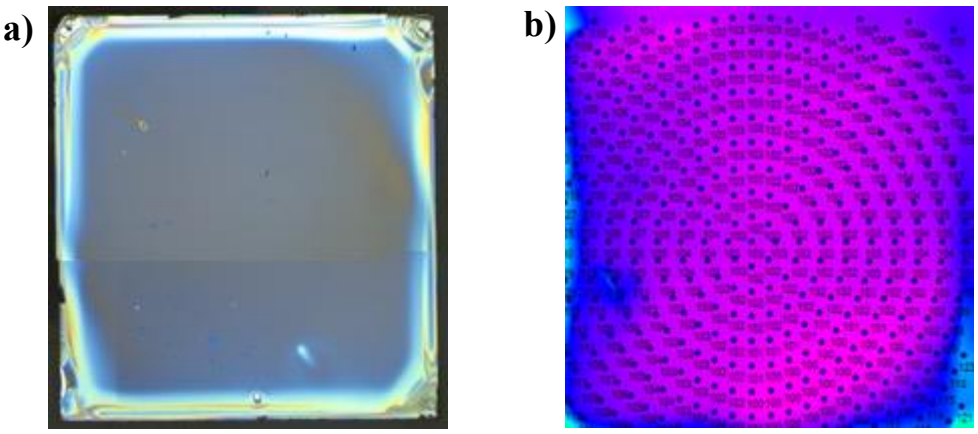

Figure 3.2. *a) 1-layer spin-coating pyrolized sample of 1M solution from acetate precursors using 1-butanol and propionic acid over 5x5 mm2 LAO single crystal. b) Interferometer measurement of the layer, which gives around 100nm thick samples.*

In Fig. 3.2, we observe that the samples prepared using a 1M acetate precursor solution in 1-butanol showed good homogeneity in all cases for the thermal pyrolysis at 500 ºC. Moreover, the results were found to be highly reproducible. The use of 1-butanol greatly helped to smooth the film surface, although in the case of spin-coating, even lower thickness for the pyrolized film was achieved compared to methanol, around 100nm per layer as compared to 200 nm for the methanol case.

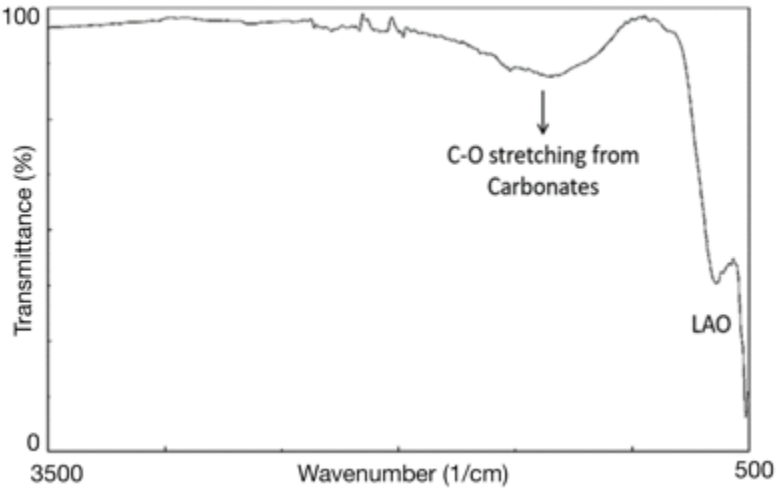

Figure 3.3. *FTIR spectra of a pyrolized film using a Fluorine-free solution consisting of acetate precursors and 1-butanol and propionic acid as solvents (Solution FF-B2).*

Still, the results obtained agree with the earlier results obtained employing the solutions in methanol and propionic acid. In Fig. 3.3, FTIR spectra of the pyrolized samples at 500 ºC only show the characteristic carbonates resonance vibration as a broad band at 1400 cm^{-1} associated to $BaCO_3$. Thus, this treatment leads to the decomposition of all organic matter present in the film. Moreover, the crystalline structure of the pyrolized films was determined by X-ray diffraction. We would expect diffraction peaks from yttrium and copper oxides and from barium carbonate. In the case of barium carbonate, two different crystalline phases can be present: monoclinic and orthorhombic.

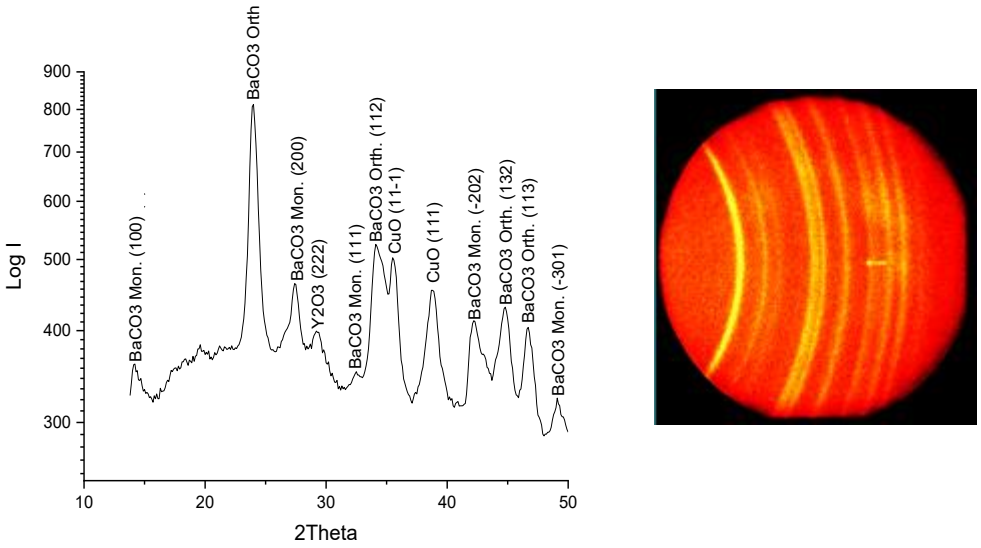

Figure 3.4. *XRD Pattern of a pyrolized sample using multideposition for 3 layers (up to 300nm) of spin-coating with a 1M solution for IJP, using 1-butanol as solvent (Solution FF-B2).*

Following the TLAG method, monoclinic barium carbonate transforms to the orthorhombic phase in order to react with copper oxide to form the Ba-Cu-O phases [**139**]. Thus, it is preferred that there is little to none of monoclinic $BaCO_3$ presence in the pyrolized films because it will slow down the YBCO growth process [**70, 139**]. In our case, since that $BaCO_3$ orthorhombic is the majoritarian in our films, we would not expect that delay during growth.

From all this study, it is concluded the propionate-based solution prepared in this chapter (using acetate precursors, butanol, and propionic acid) gives rise to a similar TLAG scenario than the previously studied FF solutions with methanol, and that this solution could be used for inkjet printing deposition. The use of additives will further be studied to obtain better homogeneity of the films and smoother film densification to avoid the formation of defects on the thicker samples, as seen in the next subchapters.

3.3 Results and Discussion

3.3.1. Fast Mode Inkjet Printing deposition of Propionate-based solutions

Initially, the inkjet printer employed was a home –made system using a commercial lead zirconium titaniate (PZT) piezoelectric head (Microfab Technologies) with a 60µm nozzle diameter to fabricate test pieces on single-crystal (001) $SrTiO_3$ (STO) and single-crystal (001) $LaAlO_3$. The plate velocity of this inkjet printing was of 1 cm/s. In this particular case, the home-made system consists of the use of a 1mL syringe coupled to the piezoelectric MicroFab head [**140**], linked through a Polyethylene tube. In order to create and ensure drop formation, the syringe is connected to a Nitrogen pressure system by a Venturi tube, which stabilizes the meniscus of the liquid. Under certain applied voltages, the piezoelectric head it is able to expand and contract, creating vacuum in the nozzle tip to form drops in the size of the picolitres, if there is enough energy to overcome the surface tension present on the meniscus, found at the tip of the nozzle.

Throughout this section we will apply the described theoretical concepts of the previous chapters together with the knowledge obtained during the whole TLAG-CSD process evaluation of the precursor solution prepared performed in spin-coating samples, by using the home-made inkjet printer located in a clean room type 10000 with a 30% controlled humidity in Nanoquim Laboratories [**141**].

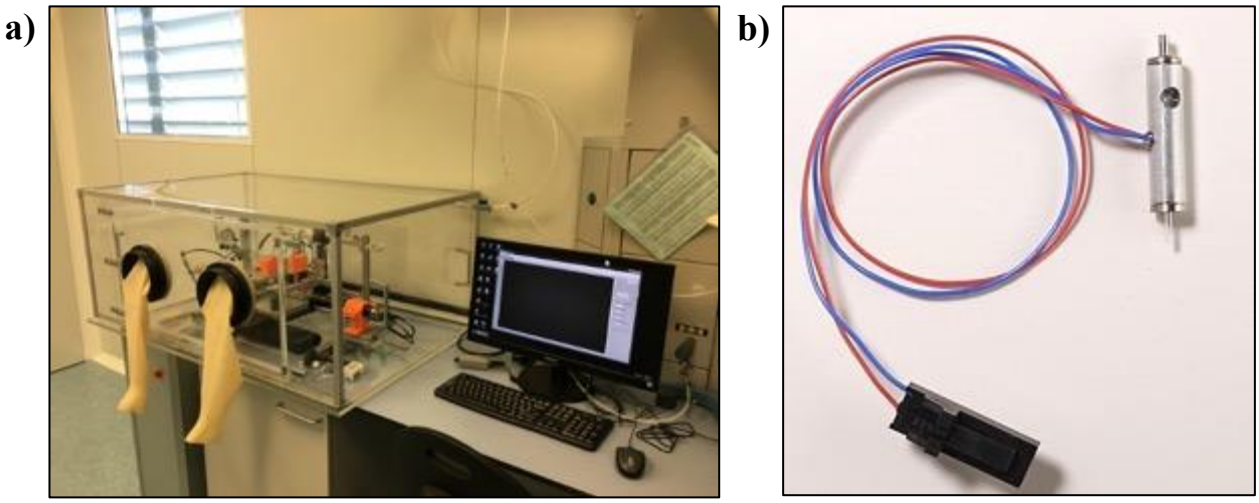

Figure 3.5. *(a) Homemade inkjet printing system in a clean room environment. (b) Microfab Nozzle.*

In Inkjet Printing, a line is a set of drops deposited in the X axis. The drop pitch refers then to the drop distances, in micrometres, for the X axis or horizontal direction of the inkjet set-up, forming a line. On the other hand, the Y axis or vertical direction of the deposition represents the distances between each line deposited, in micrometres, which is known as line pitch. A schematic representation is shown in Figure 3.6:

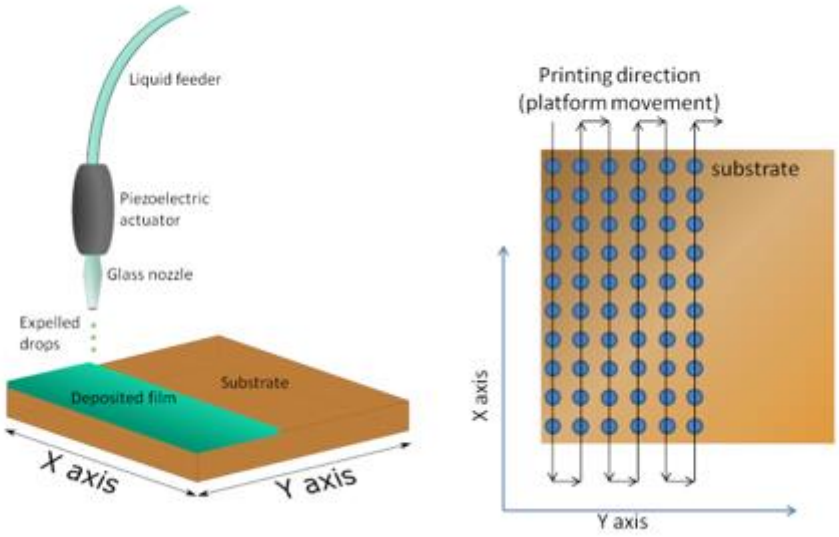

Figure 3.6. *Schematic representation of single nozzle printing motion and of the reference axes [**92**].*

The samples are printed line by line, moving a motorized platform in two perpendicular axes (X and Y) while the nozzle remains fixed. The X axis corresponds to the line printing direction, and it has a movement speed of 1 cm/s. The Y axis is the lateral step that the platform makes once the line in X axis is completed. We use the nomenclature "(XxY)" for the deposition matrix used to prepare full deposited films, being the drop distances in the X-axis in µm and the line distances in the Y-axis in µm. As an example, (80x80µm) represents a deposition matrix with a drop distance of 80µm on X direction and 80µm on Y direction.

Although we work with a drop on demand system, the drops are constantly generated at a certain frequency, which coincides with the rate at which the voltage waveform is applied to the nozzle, resulting in the order of hundreds of drops per second. For that matter, the lines in X direction do not end at the edges of the substrate, but the selected range of deposition of one line is extended to end outside the substrate. This is done to prevent the drops that are being generated in the time-lapse during the lateral step on the Y direction, to be deposited on top of the substrate, and on the other hand guarantees that the platform velocity is constant while the nozzle is over the substrate. As an example, if a LAO 5x5 mm^2 is being used as a substrate for the deposition, usually the selected line range would be 7x7 mm^2.

As seen in Table 3.1 we showed the different rheological properties of the chemical solution prepared as well as its Z numbers, typically used to define the solution printability. As observed from the different ink parameters, some values are out of the range or very close to the Z numbers desirable (Z must be in-between of 4 to 14), as it is the case for methanol solutions or highly concentrated solutions, which will have a higher tendency for satellite formation, nozzle clogging or drop formation inhibition. For that matter, the deposition study was done with the 1-butanol solution using acetate salts as precursors.

For inkjet printing, the chosen concentration of the solution was 1M (∑Metals). 1M solutions present the viscosity to reach proper Z values for film deposition at higher concentrations. In contrast, the other solutions prepared at higher concentrations are out of the printable Z values or very close to the limit, which could affect the jetting stability of the drops. In fact, the higher the solution concentration the less solution volume needs to be deposited onto the substrates to reach a certain thickness in one single deposition, which in turn reduce the sources of inhomogenities arising from the liquid movement that occurs during and after the deposition, such as coffee-ring effects. The aim is to take the highest possible concentration while being in the right Z values.

3.3.2 Drop Merging Study

The first test accounts for the stable deposition of drops at large drop pitches to evaluate its drop impact and compute the required deposition matrix (XxY) to obtain a proper film homogeneity. The ink composition obtained by using 1-butanol as solvent will be tested by inkjet printing in order to obtain better homogeneous depositions while avoiding nozzle clogging.

Since the identification of the best drop pitch combinations is essential to ensure a homogeneous deposition by inkjet printing, an extensive study on how the drop and lines merge was done. Firstly, however, it is needed to tune the waveform to obtain a stable drop formation. A stable drop formation was obtained using the following waveform parameters:

- Pulse Length = 20µs
- Pulse Width = 35V to -25V
- Drop volume = 120 pL
- Frequency = 200 Hz

Moreover, to test the stability of drop formation, 1 mL of the solution was placed on a 1mL volumetric syringe in the printhead nozzle, continuously ejecting drops. The initial volume placed on the printhead was marked, and once the drop diameter was determined by means of a stroboscopic camera, the drops were generated during 2 hours 30 minutes, at a constant drop frequency of 100 Hz, depositing a total of 0,11 mL, subtracting the volume from the syringe. The difference between the theoretical value expected and the calculated one using the stroboscopic camera, differs from a 7pL in each drop during the whole test, implying a good resolution of the diameter measurement, good drop formation and stability, and its suitability for inkjet printing.

In order to understand the mechanism of liquid movement, to test the performance of this solution and to avoid inhomogeneities, we performed a drop merging of drops study. Firstly, a large drop pitch (500 µm) was set to study the drop impact and drying performance on top of a LAO single crystal LAO substrate used for single drops. Later on, several drop pitches were selected to study the proper formation of lines in the X direction. The deposition of the 1M solution which accounts with high boiling point solvents was properly demonstrated as shown in Figure 3.7:

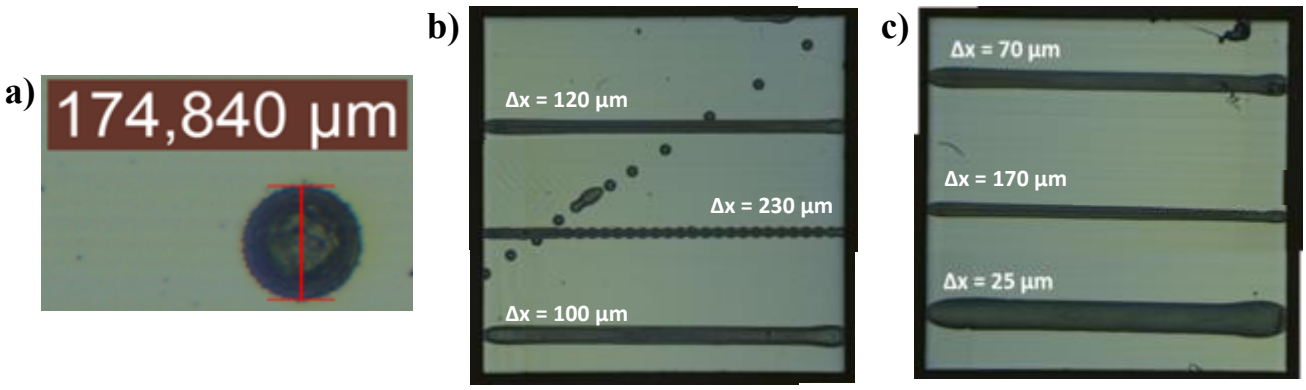

Figure 3.7. *(a) Drop diameter obtained for a 120pL drop; (b) and (c) study of drop merging.*

As observed in Figure 3.7, for the complete formation of lines, less than a 230μm of drop pitch is needed to completely merge the drops in one single X direction. However, very narrow drop pitches form lines of very high widths and more importantly, liquid accumulates at the edges of the substrate, as in the case of 100 μm, 70 μm or 25 μm of drop pitch. To avoid this, in principle, drop pitches with less distances than the observed drop impact diameter should be enough to obtain lines with enough liquid merging. Although several drop pitches could be used, we choose a line pitch between 100-120 μm, where we selected the 120 μm of drop pitch as a reference for the line merging study, since a continuous and straight line is obtained during deposition without much liquid accumulation.

3.3.3 Merging of lines

From the drop merging experiment, we determined the drop distance in order to reach a homogeneous drop merging in X direction. Next, the line distance needs to be determined. Since it is apparent that the source of inhomogeneity will come from both, very short drop pitches and bad merging of the lines in the Y direction, we studied how the lines merge prior to the full deposition of films, because if the lines are deposited very close, liquid dragging may occur.

For the line merging study, the strategy consisted on printing lines (X direction) with a constant drop spacing of 120μm, changing the distance on the Y axis. We used a drop separation in X of 120μm, obtaining thin, well-defined lines when the separation among lines was of >1000μm. When the lines are printed closer, at a Y distance of 500μm, they become spread, even if there is not direct contact among lines, and below 200μm, the line starts to lose its definition due to line overlapping. Clearly, the most important source of inhomogeneity comes from a bad merging of the lines in the Y direction, which requires to be fine-tuned. The spreading flows towards the first printed line, which is dries faster due to an earlier solvent evaporation, as can be observed in the samples with Y distances below 200μm. Such liquid dragging generates a "C" shaped macroscopic inhomogeneity on the film.

Additionally, the very fast rate of deposition of this inkjet printing system (1cm/s) affects on the low solvent evaporation and on the high liquid redistribution, thus increasing the sources of defects. Again, the deposition homogeneity varies depending on the printing conditions (humidity, temperature, solution homogeneity). These factors are important when we want to print defined lines (i.e., patterning) [**142**]. In that sense, to improve the definition of lines and increase film homogeneity, the incorporation of additives in the solution is a good approximation to try to reduce inhomogenities. Thus, making the coffee ring formation a problem during film drying, as observed in Fig. 3.8.

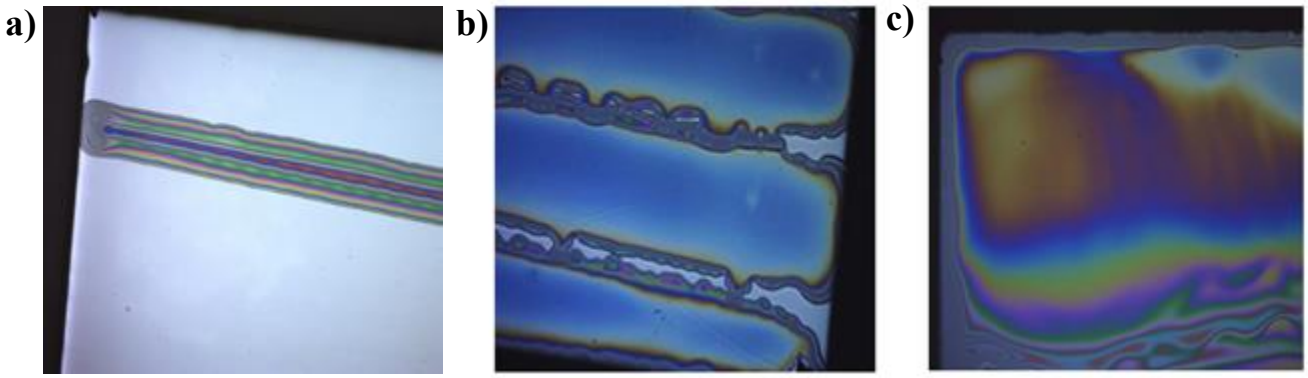

Figure 3.8. *(a) Homogenous line obtained with a 120pL drop and a drop pitch of 120µm; (b) lines printed at a distance of 500µm, they become spread even if there is not direct contact (c) "C" shaped inhomogeneity resulting from the merging of lines at distances below 200µm.*

3.3.4 Film deposition and additive screening

Our main goal was initially to obtain the thickest films as possible in one single deposition, with the aim to have thick films in the range of 1000nm after YBCO growth, with dense epitaxial films. For that matter, several parameters involved in the deposition must be accounted; the drop volume obtained after drop formation, the total surface of the substrate, the number of drops that are deposited onto it, the Yttrium concentration of the solution based on its total metal stoichiometry, the drop and line pitches selected to obtain homogenous depositions and finally, the total volume deposited.

From the total volume deposited we can extract the expected thickness of the films. In order to keep the same deposited liquid volumes, which means the same thickness for each of the samples prepared, the drop pitch must be changed depending on the drop volume. On the contrary, if the drop volume is fixed, drop pitches must be changed in order to increase or decrease the thickness of our samples. In any of the ways, for a 1M solution, the liquid amount required to obtain a specific film thickness after growth, assuming that the film is compact, is calculated from the following expression (equation 3.2), cited from Dr. Bohores Villarejo Thesis [**92**]. Following the equation, we can determine the amount of volume necessary for a given thick film as:

$$\text{Deposited Volume} = \frac{\text{YBCO Volume} * \rho_{YBCO}}{[\text{Y-BCO}] \cdot MW_{YBCO}} \tag{3.2}$$

Where [Y-BCO] is the YBCO precursor solution concentration in Yttrium, $\rho_{Y\text{-}BCO}$ is the YBCO density if it is fully compacted and MW_{YBCO} is the YBCO molecular weight.

If we use the above expression to calculate the liquid required to deposit a YBCO film with a final thickness of 1000nm in a 5x5 mm^2 LAO substrate with a solution 1M in a 1:2:4'66 stoichiometry, required for TLAG growth, we find that:

$$\text{YBCO Volume} = \text{Substrate surface} * \text{Film thickness} = (0.5)^2\ cm^2 * 10 \cdot 10^{-5}\ cm$$

$$[\text{Y-BCO}] = 0.13\ mol/L \text{ for a 1M solution; } MW_{YBCO} = 666.2\ g/mol;\ \rho_{YBCO} = 6.383\ g/cm3$$

$$\text{Deposited Volume} = \frac{0.5^2 \cdot 10^{-4} \cdot 6.383}{0.13 * 666.2} = 1.84 \cdot 10^{-6} L$$

$$\text{Total deposited volume for 1000nm YBCO films} = 1.84 \mu L$$

Based on the information obtained from the above equation, which relates the final thickness of the film to the amount of total volume deposited onto the substrate, to perform inkjet printing depositions of 1000nm thick YBCO films after growth, we had to take into account several factors.

For example, increasing the solution concentration may have an effect on the deposition, since less amount of volume is required to reach the desired values, which in turn may lead to less liquid accumulations and more homogenous depositions. However, higher concentrations on the solution may also lead to jetting instability, taking into account its computed Z numbers. Furthermore, we want to keep a specific range of drop volume that ensures proper jet stability, being 120 pL for our precursor solution, so to maintain constant the total deposited volume onto the substrate, in this particular case of 1.84 µL, the drop and line pitches will have to be adjusted.

Based on the results obtained in both studies, regarding the best drop and line pitches combinations to achieve homogenous layers, especially for the most suitable drop overlapping to obtain straight lines without liquid accumulation at the edges, we looked for the optimal deposition matrix. As seen in figure 3.9, a 120x15µm deposition matrix using the 1M solutions with 1-butanol (FF-B2), resulted in large liquid accumulations and the apparition of macroscopic defects (like cracks) on the sample after pyrolysis.

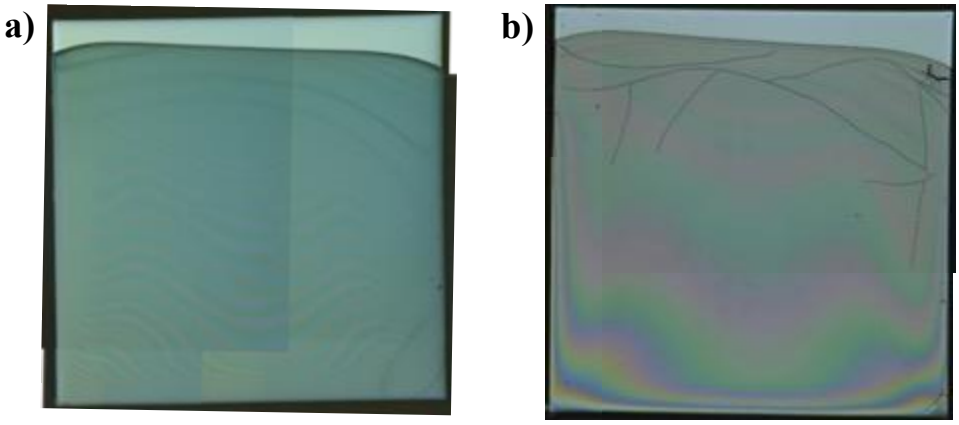

Figure 3.9. *Deposited film (a) and pyrolyzed film with defects using the spin-coating pyrolysis profile (b) made by inkjet printing (120x15µm). Drop volume of 120pL, deposited on a LAO 5x5 mm^2 substrate, using a 1M Fluorine-free solution with an expected thickness of ~1000nm after crystallization.*

As above mentioned, one of the particularities that inkjet printing deposition techniques needs to mitigate is the accumulation of liquid at the edges and at the very first printed line. Such characteristic is a combination of Marangoni flow and coffee-ring stain effects that induces liquid movement [**120, 143**]. During deposition, due to the substrate-liquid interaction, a surface tension gradient occurs inducing the liquid to move towards the edges and the already printed lines, which are drier due to solvent evaporation. Therefore, given the large liquid accumulations occurring during deposition of these thick films, we suggested to reduce the thickness of the films in order to decrease total volume of solution deposited onto the substrate. The desired thickness after growth (700 and 500 nm, respectively) was input to obtain the amount of deposited volume required, according to expression 3.2.

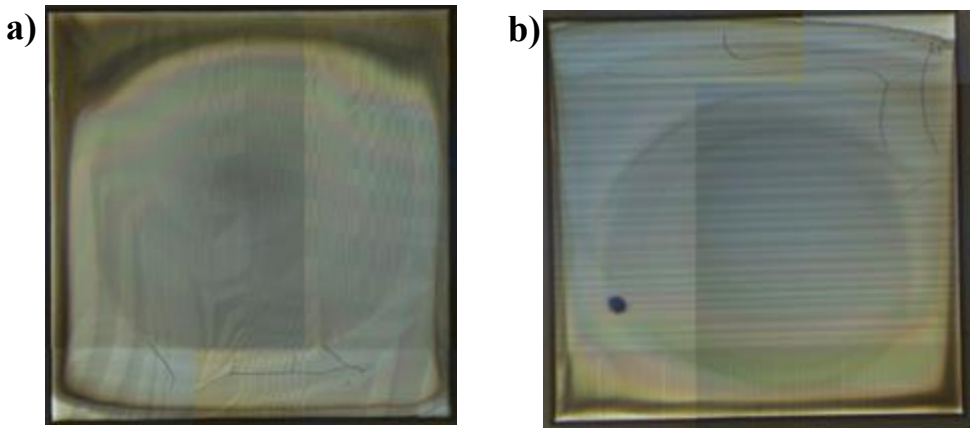

Figure 3.10. *Pyrolized films with defects using a drop volume of 120pL. (a) (120x30µm) matrix and (b) (120x20µm) matrix. The thickness expected for (a) is ~500 nm. and for (b) ~700 nm. for thick YBCO film after crystallization.*

As observed in Figure 3.10, the deposition of 700 and 500 nm films using the same chemical solution still produced liquid accumulation towards the edges, at the fast plate velocity of this inkjet printing system (1 cm/s). In fact, very large coffee-stain effects, together with the formation of cracks occurring during pyrolysis due to the presence of inhomogenities on the sample, suggest that the chemical solution require further optimization. By using additives, we expect to avoid liquid movement and defect formation, by pinning better the liquid.

3.3.4.1 Use of UV-Curable Varnish

Previous works of the group performing inkjet printing deposition of trifluoroacetates solutions had used a photocurable polyacrylic ester-based commercial varnish from Chimigraf-KAO [**92**] as additive to reach films above 1000 nm. The UV-Curable varnish seemed to be the most optimal additive addition to the solution, among the several used (PVP, glycols) [**144-147**]. Therefore, we decided to test the performances of the FF and LF solutions with the varnish additive to compare the results.

We started by replicating first some of the previous work of the group with the LF solution. After the deposition, the films followed a curing treatment with a with a LED lamp (λ = 395 nm), with an input power of 0.7 W, and the curing time was fixed to 10 min. The LED UV-lamp curing process contributed to pin the liquid after deposition and so to optimize the thickness homogeneity [**148**]. Figure 3.11 shows that using the UV-curable varnish for LF solutions, the liquid accumulation and the formation of cracks could be drastically reduced.

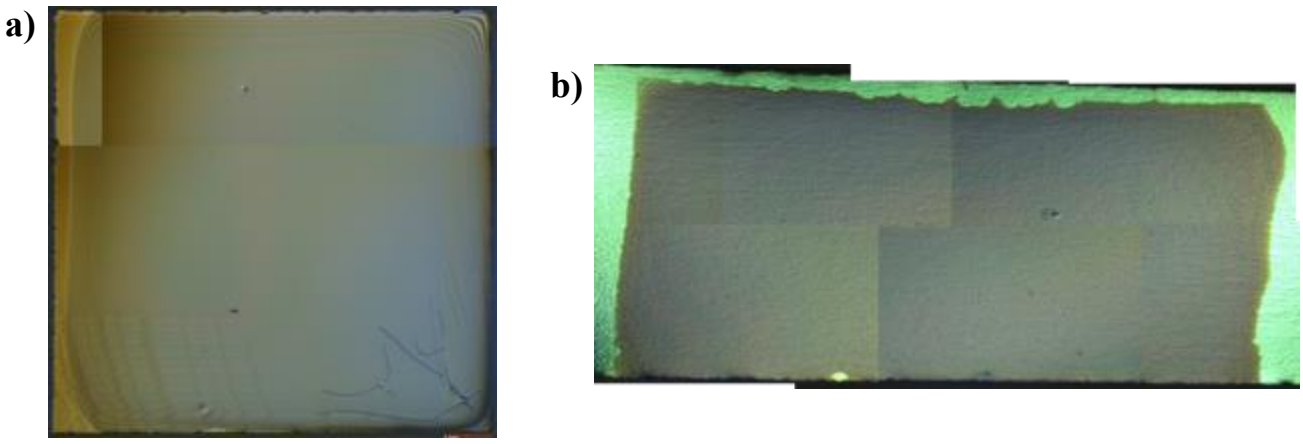

Figure 3.11. *Defect-free pyrolized precursor YBCO film by inkjet printing (120x25) with drop volume of 120pL and UV-curing time of 10 min., on (a) LAO substrate and (b) SuperOx Coated Conductor, using a 1M Low-Fluorine solution with 1-butanol as solvent and 6.6%vol. of UV-curable varnish as additive. The thickness expected is ~700 nm. thick YBCO film after crystallization.*

The implications of using a polymeric additive such as the above mentioned gave rise to a different deposition situation that leads to defect-free homogenous samples at this very fast modality of inkjet printing depositions. By creating a thin film of polymerized material on the surface of the film, the precursor solution did not experiment a fast drying of the solvents avoiding liquid redistribution and coffee-ring effects. Given the good results of the UV-curable commercial varnish in the inkjet printing deposition of the LF-TFA solutions [**92**], we decided to use the same approximation for the FF solutions.

We want to recall that in the case of LF-TFA a total amount of 6.6-10%vol of additive was studied to generate homogeneous depositions while reaching film thickness after pyrolysis in the range of 1.5-2 µm without cracks in a single deposition [**92**]. Therefore, we first checked for the rheological properties of the solution when several percentages of additives are added to the solution, making sure that the Z numbers are kept in the values needed for a proper Inkjet printing deposition and drop formation, as seen in Table 3.2:

Table 3.2: Rheological properties of the precursor solution with % additive.

% additive	0	6.6	10
Concentration	1	1	1
Viscosity (cP)	7	9	11
Contact angle (º)	>10	>10	>10
Density (g/cm^3)	1.01	1.1	1.1
Surface tension (mN/m)	24.2	25.2	25.5
Z	7.4	5.8	4.8

All of the solutions tested were on the range of the stipulated Z values, meaning that all of them can be used for proper inkjet printing depositions, ensuring drop formation. From that, we wanted to test the additive for our Fluorine-free (FF) solutions, since when a 6.6% additive was added in the LF solution, the homogeneity of the depositions clearly improved.

We expected that by adding some percentage of UV-curable varnish additive to our prepared solution, the resulting deposited samples could behave similarly. When a 6.6% additive was used, there was still liquid movement and liquid accumulation at the very first printed lines during deposition, creating thickness inhomogenities. In fact, as the thickness of the films is increased, this C-shape resulting from coffee-stain effects was larger, indicating that more %vol. of varnish is needed to overcome such problems for this FF solution, as seen in Figure 3.12.

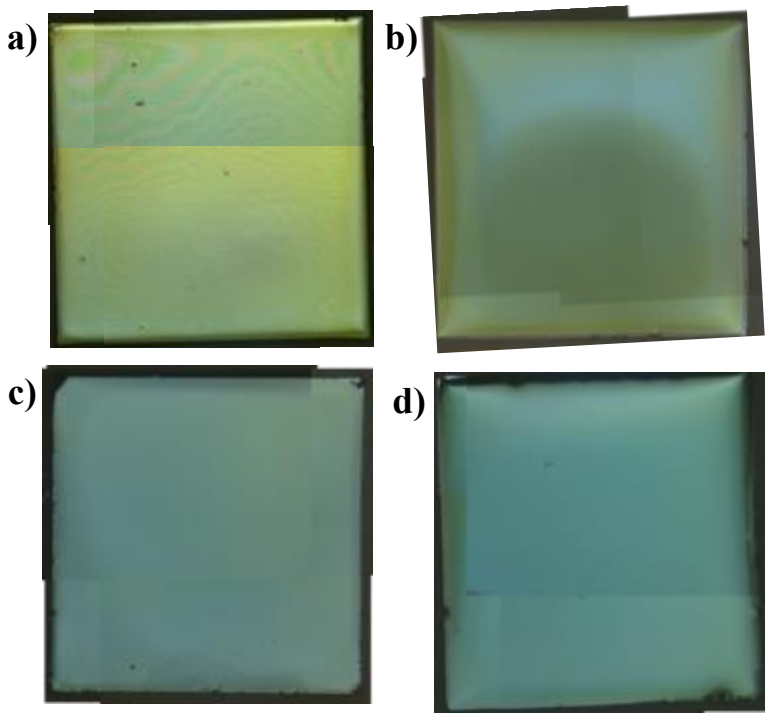

Figure 3.12. *Deposited films by inkjet printing using a 1M propionate-based solution, drop volume of 120pL and UV-curing time of 10 min. on LAO substrates. (a) Deposition matrix of (120x25µm) using 6'6%vol. varnish. (b) Matrix of (75x15µm) using 6'6%vol. varnish. (c) Matrix of (125x15µm) using 10%vol. varnish. (d) Matrix of (75x15µm) using 10%vol. varnish. Expected thickness of ~700nm for a) and c), ~1000nm for b) and d).*

By increasing the amount of UV-varnish from 6.6% to 10 %vol, the homogeneity of the samples improved and we were able to avoid the coffee-ring effects that affect the printed samples as like without using additives. In this sense, this additive improved the homogeneity of the depositions, avoiding liquid accumulation and differences in thickness, ensuring its suitability to continue with the pyrolysis of the layers and later to our TLAG-CSD process.

Once placed under UV radiation, which triggers the photo-polymerization of the polyacrylic ester-based varnish, the 10%vol. amount is able to minimize liquid spreading, contributing to pin the solution onto the substrate. In this study we found that a 10% vol. of UV-curable varnish was better to obtain homogenous depositions, compared to the ones obtained without varnish or using a 6.6% as in the Low-Fluorine case. With the 10%vol varnish, depositions of both expected thickness, of 700nm and 1000nm after crystallization, were obtained without liquid movement, indicating a good ratio of additives for our prepared Fluorine-free solution.

3.3.5 Pyrolysis of thick Inkjet Printing Films

The pyrolysis step is the main complex issue for the development of thick YBCO films due to the strong stresses produced. During deposition, we need to avoid the solution accumulation at the edges which will produce differences in thickness at some parts of the film, affecting the homogeneity and morphology of the films and the generation of inhomogeneous stresses during the pyrolysis which may induce cracks [**48, 149-152**]. At the pyrolysis step of the films during the TLAG-CSD process the decomposition of organic matter present in the films induces an in-plane stress generation to the film, since the vertical thickness shrinkage is accompanied with the film being in-plane clamped to the substrate.

Therefore, strong stresses generated during this densification of the film is released usually in the form of defects on the sample, such as the formation of crack. Analysis of the pyrolysis of functional thin films has shown that the generation of cracks severely degrade the superconducting properties, so the stress release during the pyrolysis becomes a very important aspect to study in thick films [**152**]. By increasing the film thickness, especially in one single deposition as in the case of inkjet printed samples, the tendency to form cracks severely increases.

For instance, it has been previously established [**92,94**] that cracks are formed in films when the film thickness exceeds a critical thickness value (t_c) under a tensile stress applied:

$$t_c = \frac{2G_c E}{Z\sigma^2(1-v)} \quad (3.3)$$

where Gc is the energy per unit area needed to form two-crack surfaces, E is the Young's modulus, v is the Poisson's ratio, Z is a dimensionless geometrical parameter and σ is the biaxial tensile stress of the film.

To develop homogeneous films with large thicknesses through the TLAG-CSD process, it is mandatory to control and fulfil all the requirements required to avoid those defects. Clearly, defect formation derives from a complex relationship between the chemical nature of the precursors, the decomposition during the thermal treatment and the thermo-mechanical properties of the deposited films. To evaluate the main issues controlling this phenomenon, several in-situ analytical methodologies, such as in-situ optical imaging of the pyrolysis will be performed, as well as the usage of different heating ramps that could diminish to certain extent the accumulation of stress in the films.

By in-situ imaging of the pyrolysis profile, we can analyse the major stress-relief mechanisms that the films undergo when the organic moieties present in the film decompose towards the corresponding oxides and carbonate compounds. The objective was to set a pyrolysis profile where the various stress-relief mechanisms that the films undergo during its densification could avoid cracking.

For that reason, as seen in previous figures, the initial pyrolysis profile used was pretty similar to the one that Dr. Villarejo optimized during the pyrolysis of thick IJP Low-Fluorine based films [**92**]:

- From 25ºC to 160ºC at 15 ºC/min. Since only solvent evaporation occurs during this step of the pyrolysis, high heating ramps can be used to avoid time-consuming processes.
- From 160ºC to 300ºC at 1 ºC/min. At these temperatures, the major stress-relief mechanisms occur, i.e., it is the most important part of the pyrolysis profile to avoid crack formation. Therefore, the heating ramp is strongly reduced.
- From 300ºC to 500ºC at 3 ºC/min. Since most of the stress is already released in previous temperature stages of the pyrolysis, the heating ramp can be raised again to avoid time-consuming process and coarsening of the oxide and carbonate phases which would in turn delay its reaction in later stages of the TLAG-CSD process.

In the case of LF precursor solutions, the incorporation of an additive had a relevant role in the decomposition and stress-release process by sustaining the film after all the carboxylate moieties have decomposed, including the TFA ones [**92**]. In fact, TG Analysis of the LF solution [**94**] revealed that TFA moieties, which decompose much later than FF carboxylates, are able to structurally sustain the film skeleton.

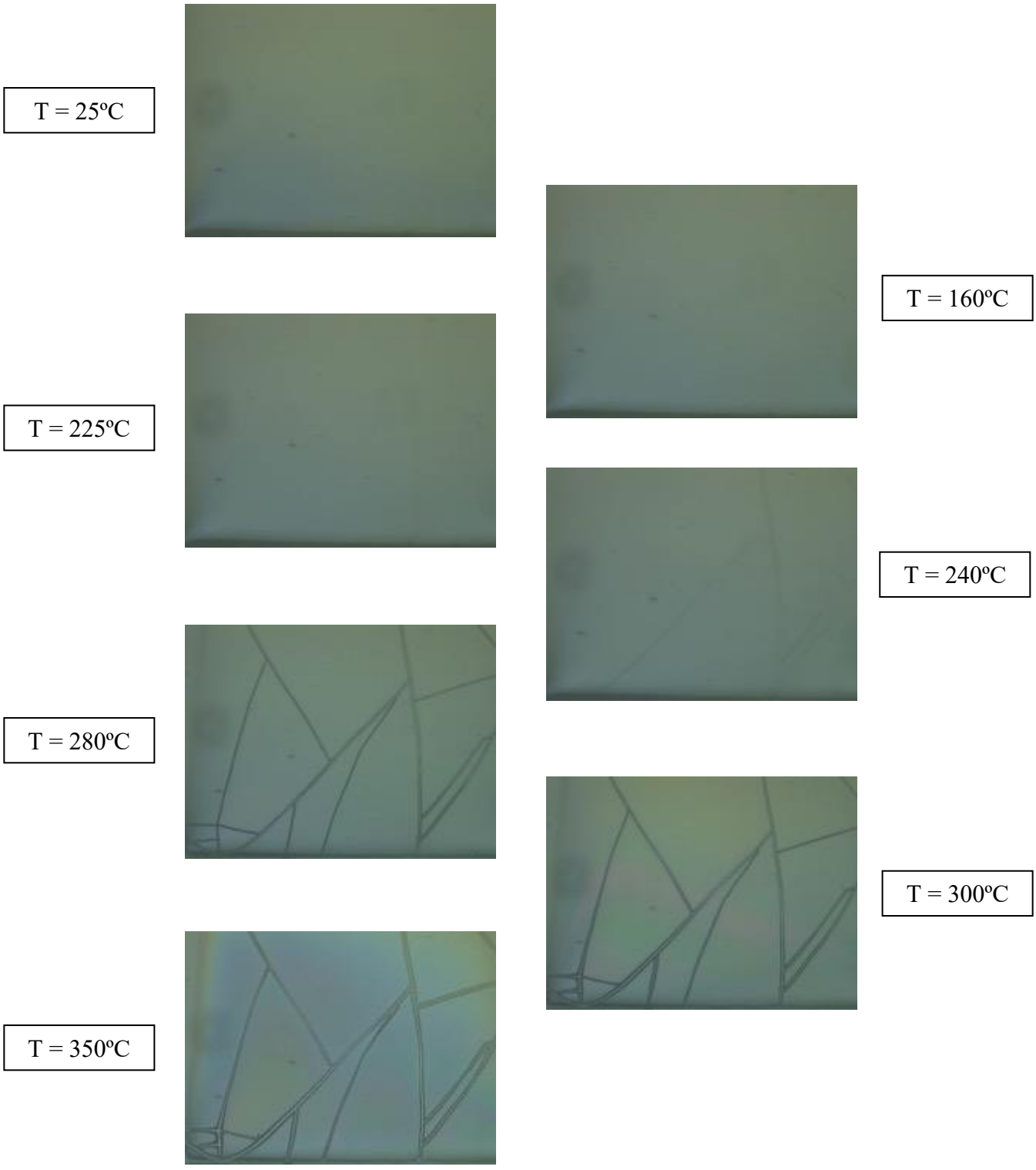

Figure 3.13. *In-situ imaging of a pyrolysis process of a thick film (125x15µm) using a 120pL volume drop, with an expected thickness of 700 nm. after growth with a profile of 15ºC/min to 160ºC, 1ºC/min to 240ºC, 5ºC/min to 500ºC, 5 min dwell under Humid Oxygen atmosphere. The precursor solution was FF-B2 with 10%vol. additive. Notice the appearance of cracks at temperatures around 240ºC. Video 1 in Appendix A.*

However, as seen in Figure 3.13, this pyrolysis profile did not ensure defect-free samples. The fact that in the case of the FF there are no TFA moieties provoke that around 240ºC, a major mass loss occurs, in contrast to the sequential decomposition of propionate-TFA-varnish decomposition, as in the case of the LF solution, leading to huge defects on the samples. This implies that there is a requirement for another additive agent to compensate the stress generated during densification, in order to avoid the cracks of the film during propionate decomposition.

On the contrary, a lot of cracks originate in the slowest heating ramp of the pyrolysis profile, indicating that the decomposition of the metalorganic compounds presents in the film needed further study. In such pyrolysis conditions, under an oxygen atmosphere, carboxylates decompose around 235ºC [**76**], matching well with the crack formation. Indeed, there has to be major correlation with the apparition of defects and propionate decomposition during pyrolysis. Since in our work we are using propionate-based solutions with a specific (3-7) stoichiometry, it means that the major concentration of each individual metal present in the solution comes from Copper, with a concentration of [Cu]=0.608 mol/L, in contrast to the Cu concentration found in the LF route, where the usual stoichiometry corresponded to the (1:2:3) ratio, with a concentration of [Cu]=0.5 mol/L.

Additionally, we know that when using the UV-curable varnish, the thickness of the deposited film is higher (for the LF solution using 10%vol. is around 17000µm, in contrast to 7µm without additives for a final YBCO layer of 1µm [**92**]), so we expect that for this %vol. of additive in FF-B2 solution, the thickness will be very similar, which in turn may surpass the critical thickness of the films, leading to detrimental effects such as excessive film shrinkage and cracks on the samples.

3.3.5.1 Influence of the heating ramps during pyrolysis of thick films

It was clear that using such pyrolysis profiles was not enough to avoid crack formation in the samples. For that reason, several heating ramps were tested in order to evaluate, characterize and determine the reasons behind crack formation and how it could be avoided. As a matter of fact, some observations during pyrolysis in recent years have stipulated that faster heating ramps are beneficial to obtain pyrolized films without defects [**65, 153**].

Moreover, faster heating ramps are also preferred to avoid coarsening of the pyrolized phases, such as copper aggregation [**128**]. In that sense, two possible ways were explored; being a slower ramp in the most problematic step of the pyrolysis and the other to go faster at that stage to avoid crack formation. The pyrolysis profiles used are catalogued in Table 5.

Table 3.3. Heating ramps profiles analysed during pyrolysis studies:

Pyrolysis Profiles	**Temperature**		
	25-160	160-240	240-500
A	5	5	3
B	15	1	3
C	15	0.5	3
D	1	1	1
E	0.5	0.5	0.5
F	15	15	15

With these pyrolysis profiles we would expect to avoid crack formation, either by going slower in the most critical parts of the pyrolysis, or as above mentioned, to go faster to avoid possible coarsening and moreover the accentuation of the formation of defects, as some works state that faster heating ramps could result on more positive outcomes. We made in-situ imaging of all the pyrolysis profiles by using samples with the same deposition characteristics to being comparable.

We replicated the pyrolysis profile used for the trifluoroacetates inkjet-printed samples by reducing the temperature rate on the most critical part, being 15/1/3 ºC/min (pyrolysis profile B) However, we saw a lot of cracks appearing, as shown in figure 3.15:

Figure 3.15. *15/1/3 ºC/min pyrolysis profile (or B). The precursor solution was FF-B2 with 10%vol. varnish using a deposition matrix of (125x15µm).*

As seen in Figure 3.15, with this pyrolysis profile 15/1/3 or B, it was not enough to overcome the crack formation during decomposition. In fact, by going slower a lot of cracks appeared, if compared with the previous samples obtained without varnish additive while following the 5/5/3 or pyrolysis profile A (see Figure 3.9). While with the usage of the UV-curable varnish, much better homogenous depositions were obtained, it becomes apparent that the use of this additive cannot fulfil the requirement to sustain the film during its densification and in addition it incorporates higher thickness in the dried film.

Another pyrolysis profile used with the aim to reduce the heating rate in the most critical part of the pyrolysis was profile C, which reduces the temperature rate from 1ºC/min to 0.5ºC, being 15/0.5/3. We also tried to slow down the whole pyrolysis profile to the same temperature rate of 1ºC/min or 0.5ºC/min, being 1/1/1 ºC/min or 0.5/0.5/0.5 ºC/min, which we called pyrolysis profile D and E.

The aim was that by reducing the temperature gradient of the whole process we could avoid the formation of defects by slowing down the metalorganic decomposition of the precursors, especially the copper carboxylate decomposition in order to avoid a very rapid densification of the film, which in turn would generate very high stresses in the film, producing the cracks. However, as seen in Figure 3.16, with this slow pyrolysis profile neither the crack formation could be avoided.

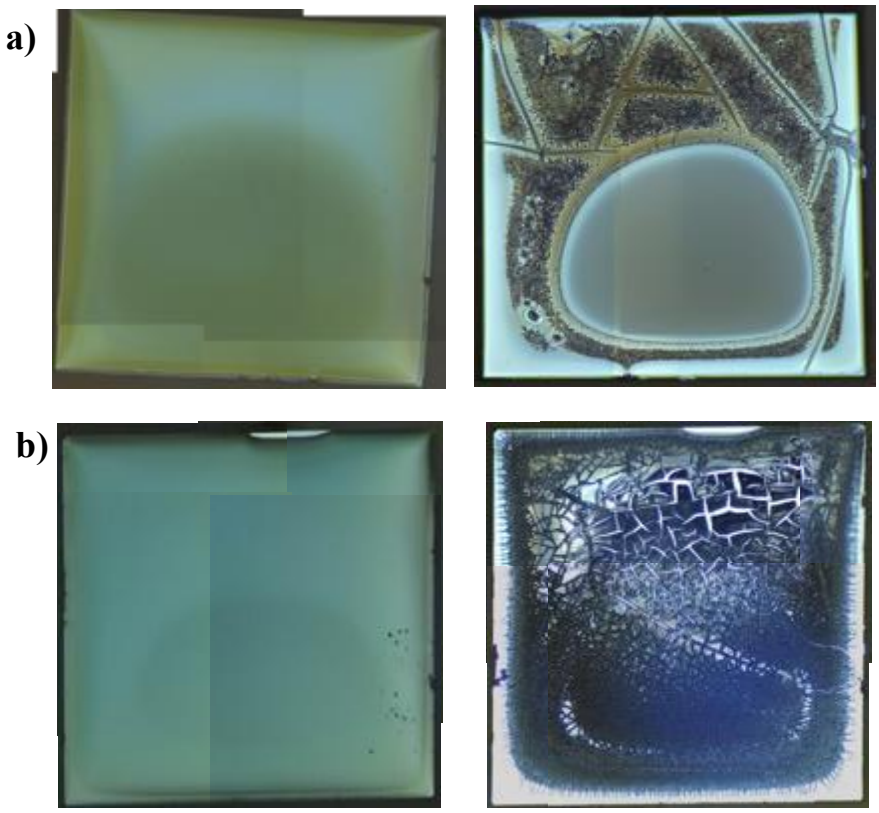

Figure 3.16. *(a) 1ºC/min pyrolysis. (b) 0.5ºC/min pyrolysis (VIDEO). Both samples were prepared using the precursor solution was FF-B2 with 10%vol. varnish and a deposition matrix of (125x15µm).*

By slowing down the decomposition of the precursors we expected that we could avoid a very rapid densification of the film, which in turn would generate very high stresses in the film, producing the cracks. However, as you may see in video (see Appendix A), slowing down the temperature profile was not enough to overcome the stress generated during densification, giving rise to the formation of cracks during Cu decomposition, around 240ºC.

The standard spin-coating pyrolysis profile of 5/5/3 ºC/min was also studied. We wanted to test if by accelerating the decomposition rate of the precursors, we could avoid the generation of strong stresses. However, neither this decomposition profile using UV-curing varnish did not obtain the desired results, as seen in Figure 3.17. We saw that in contrast to the results obtained when not using 10% of varnish, in this case the polymeric film created at the surface of the deposited film resulted in "exploded" samples.

Finally, we also tried to severely increase the temperature rate of the pyrolysis profile by selecting a fast ramp by strongly speeding up the decomposition reactions during the salts decomposition, i.e. 15 ºC/min, calling it pyrolysis profile F. The aim was to reduce aggregation by fastening the whole pyrolysis process. However, this temperature profile ended up by delaminating the film from the substrate, thus breaking it.

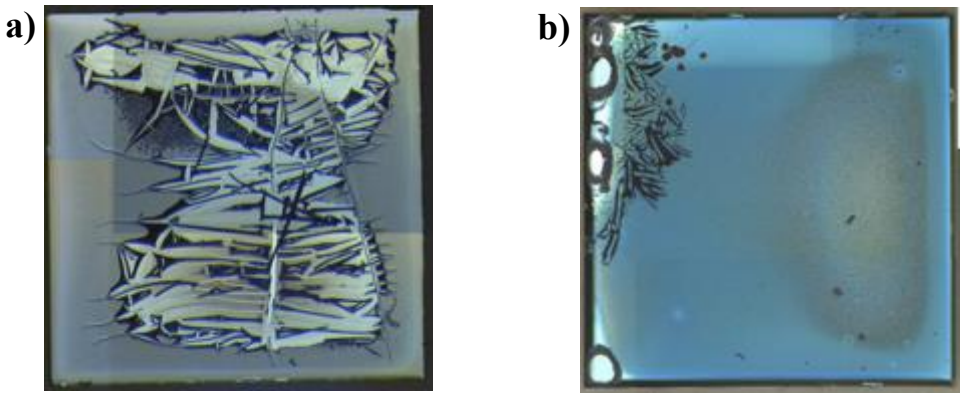

Figure 3.17. *(a) 5-3ºC/min standard pyrolysis. (b) 15ºC/min pyrolysis. The sample is prepared using the precursor solution FF-B2 with 10%vol. varnish and a deposition matrix of (125x15µm).*

With the identification of the most critical parts of the pyrolysis, which involve the formation of defects during the decomposition of the organic components present in the solution, we tried to overcome the stress that it is generated by analysing the process by in-situ imaging and different heating rates. Nonetheless, none of the pyrolysis profiles used were appropriate to avoid the generation of defects.

In fact, as we have seen, the crack formation occurs on a very well identified temperature region of the pyrolysis, that is during the Copper carboxylate decomposition, around 235ºC. This part of the decomposition consists of the elimination of around 25% of the total organic mass present in the film and occurs once all the solvents present in the film have been evaporated, thus when only a "gel-like" film remains.

An estimate thickness of the samples after drying is around 17000µm, measured by interferometry, for the studied case which would give a final YBCO layer of 1µm. We can conclude that this thickness surpasses the critical thickness of the film, leading to defects due to the stress generated during the decomposition of the carboxylates. This pyrolysis is different from the one reached with solutions containing metal-TFA moieties, where TFA remains in the film during the pyrolysis stage of propionate decomposition (around 235ºC), and TFA decomposes around 300ºC, which was seen to be able to sustain the film after the other carboxylate precursors present had already decomposed. Much later, around 420ºC, the UV-curable varnish finally decomposes, once all the other organic moieties present at the film had already transformed to its correspondent nanocrystalline oxides.

In the case of the Fluorine-free solution, since there is no organic moiety able to properly sustain the film after propionate decomposition, although the polymeric additive used decomposes much later (ending at 420ºC), this is not resilient enough to avoid cracking around 240ºC.

This gave insights about the usage of the UV-curing varnish as a non-adequate additive for these types of solutions, as it is not good enough to sustain the film during thermal decomposition in the temperature range after propionates have decomposed. Probably other additives should be used to avoid defect formation while keeping a homogenous inkjet printing deposition. In that sense, other Fluorine-free solutions were prepared to try to overcome the problems associated to the pyrolysis by changing the additive used, as reported in chapter 4.

3.4 Outlook on inkjet printed samples using UV-Curing Varnish

In this work, Fluorine-Free acetate precursors were investigated to produce superconducting YBCO films on LAO substrates by inkjet printing deposition. The rheology of solutions with different solvents and concentrations was thoroughly studied in order to obtain the most homogenous films as possible.

The spin coating solution composition (such as FF-M1) was not suitable for the deposition of thick films by inkjet printing, either in terms of solvent evaporation or Z numbers. The low boiling point of methanol was not optimal for inkjet printing depositions, thus from our study we concluded that a mixture of high boiling point solvents (>100°C) was required to reach optimal homogenous depositions. Otherwise, nozzle clogging occurred. Instead, a solution with 80% butanol and a 20% of propionic acid is presented as effective ink compositions to obtain enhanced homogeneity on the thick film deposition by inkjet printing.

The solution concentration was 1M (ΣMetals) to deposit manageable liquid volumes on top of the substrates utilized, slowing down the evaporation rate of the films while showing full coverage on LAO single crystals, since higher concentrations imply less total volume deposited for a given thick film preparation. From the rheology results, it was shown that the 1M solution in 1-butanol and propionic acid in 80/20 concentration (namely FF-B2) was the most appropriate for inkjet printing deposition to obtain homogeneous film depositions with film thickness between 1400-2000nm after pyrolysis.

The driving waveform of the inkjet piezoelectric actuator was adapted to the solution parameters, achieving stable and reproducible drops. We studied different drop volumes to test the effect on the film deposition homogeneity and an optimized drop and line pitches to avoid liquid accumulation on the substrates. To obtain a continuous drop formation, a fixed selected drop volume to reach the desired thickness was set.

Still, we observed that without a proper screening of an additive a liquid dragging phenomenon occur; the ink presented a liquid movement towards the first printed line during the deposition process creating C-shape and coffee-ring effects, originated from the low solvent volatility. To avoid such phenomenon, we add a commercial UV-curable varnish previously used in our group (a photocurable polyacrylic ester-based commercial varnish from Chimigraf-KAO Co.). We found that by the photo-polymerization reaction triggered by the UV radiation on films, the film's homogeneity was much further improved thanks to the effects of the polymerization in avoiding liquid dragging and better fixing the solution to the substrate.

Nonetheless, for inkjet printing depositions the substitution of TFA molecules to fully Fluorine-free precursors implied a strong modification of the pyrolysis process and stress release, so a lot of defects (film cracking and/or delamination) were generated during pyrolysis, even when using a UV-Varnish additive to increase the deposition homogeneity. It is known that the acrylate precursors of the varnish additive modify the temperature ranges of the decomposition reactions, reaching higher temperatures than using solely propionates or TFA precursors, contributing to relax the in-plane stress generated during densification. However, it also contributes an increase of the thickness of the films after deposition.

While lower amounts of additive led to inhomogenous depositions, we found that when using a 10% vol. of UV-curing varnish to obtain homogenous deposited layers, its high film thickness after deposition (around ~17000µm for an YBCO layer of ~1µm) surpassed the critical thickness leading to strong defects formation in the samples. Indeed, the presence of TFA moieties on the film is beneficial to achieve crack-free layers when such a varnish additive is used, since the sequential decomposition reactions of propionate-TFA-varnish series can release the generated stress in the film.

During pyrolysis, the decomposition of the carboxylates induces a densification of the film, generating a lot of stresses on the film, which tend to generate cracks above a critical film thickness. For our FF precursor solution, we specially identified a correlation between the formation of defects and the decomposition of mostly Cu carboxylate around 235ºC. While the UV-curing varnish allowed us to obtain much better homogenous deposited samples, its role during pyrolysis was not enough to suppress the tension forces that are being generated during the densification and subsequent strains, creating cracks and other defects along the sample.

Even though several changes in the heating ramps were made, and the pyrolysis stress relief mechanisms were identified by means of in-situ optical imaging in the pyrolizer, these changes were not enough to overcome the problems that occur during the pyrolysis. This suggests us to explore different precursors and additives, as it will be explained in the next chapter, with the aim to solve the intrinsic stress behaviours of the films during its densification. For this reason, although a precursor solution made from commercial acetate powders together with the use of a UV-curing additive resulted on homogenous deposition of thick films, it was not enough to avoid defect formation during pyrolysis, and it was discarded as a suitable chemical solution candidate to be used in Inkjet Printing due to the above-mentioned studies.

4.

Discrete Mode Inkjet Printing deposition of thick films using Fluorine-Free solutions with Ethanolamine as additive

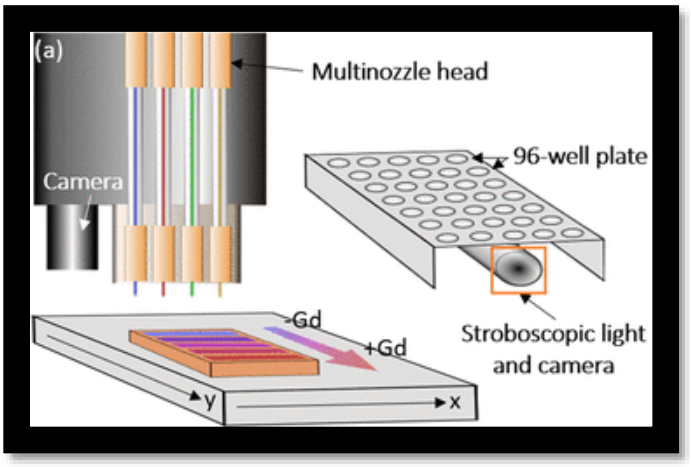

In this chapter we will explore the discrete deposition mode that accounts for the new inkjet printing system, upon the arrival at the group of a Drop-on-demand piezoelectric inkjet printing (DoD IJP) from Microdrop Technologies GmbH, with a more sophisticated software and moving/heating plate, allowing us to obtain samples in a more reproducible manner. We will evaluate the use of metal propionate salts and ethanolamine as additive. Additionally, the versatility of such drop-on-demand inkjet printing (IJP) modality allows to perform combinatorial studies, through fabrication of compositionally graded materials with high spatial precision, by mixing precursor solutions with different rare earth (RE) elements.

Adapted in part from: *Queraltó, A., Pacheco, A., Ricart, S., Puig, T. et al. Combinatorial screening of cuprate superconductors by drop-on-demand inkjet printing. ACS Applied Materials and Interfaces, 13(7), 9101–9112 (2021).*

4.1 Introduction

In the last chapter we saw that while the usage of a polyacrylic additive ensured good homogeneity during the deposition, its role during pyrolysis was not enough to suppress the tension forces that are being generated during densification, creating cracks on the pyrolized sample, and therefore it was discarded as a suitable candidate to be used in Inkjet Printing depositions of Fluorine-Free solutions for TLAG YBCO films growth. This suggested us to explore an alternative combination of precursors and additives, with the aim to solve the defect formation during the pyrolysis of the metalorganic precursors. Here, we present a novel and versatile inkjet printing deposition while using an amine additive to achieve defect-free thick pyrolized layers. In addition, the fact that we got a new IJP machine with additional capabilities enabled us to explore parameters that could not be studied in chapter 3.

Amine additives have been widely used in CSD solutions due to its enhancement of precursor salt solubility and increase in-solution viscosity [**154-155**]. In this chapter, we study one of the short carbon chain amines, the ethanolamine, as a possible additive to obtain more robust, soluble and stable solutions. We investigated the capacity to increase the homogeneity of the depositions by facilitating drop formation, which in turn could as well prevent excessive drying of solvents and nozzle clogging during inkjet printing depositions. But more importantly, we wanted to analyse the amine additive, acting as a chelating agent, for the improvement of the physicochemical properties of the solution. We expected to form a coordinated complex with some of the precursor salts that could help on reducing the stress during the pyrolysis.

Contemporarily, in our ICMAB group we started to evaluate a reproducible synthetic process for the improved preparation of the precursor solution using propionate salts. While the butanol solution was used for inkjet printing, the new solution was optimized for our current spin-coating depositions of the TLAG growth studies.

In this regard, the use of highly concentrated solutions with ethanolamine (EA) as additive gave impressive results regarding the good homogeneity, high thickness, and low porosity of the films [**155**]. High current density values (Jc >2 MA/cm^2, at applied H=0) have been achieved using the TLAG growth methodology with even further promising results [**75**]. Therefore, this chapter is devoted to analysing the opportunities of the EA additive and propionate salts for ink jet printing deposition, considering that some modifications on the solutions will need to be considered to adapt to the inkjet printing process.

4.2 Experimental Section

4.2.1 Solution preparation

In this approach, Fluorine-Free solutions were prepared with propionate salts synthesized in our laboratories, which are studied and thoroughly described in a parallel PhD Thesis (L. Saltarelli). The aim was to start from the metal propionates to avoid the ligand exchange reaction that occurred in the solutions used in the previous chapter 3. In particular, the formation of Barium-acetate-propionate mixed compounds, coming from the corresponding commercial acetate salts and propionic acid. Additionally, it further reduces the cost of the prepared solution by preparing ourselves the carboxylate salt precursors from their respective low-cost oxides and carbonates, as well as we can control the purity. Since the propionates prepared solutions must behave similarly, it was concluded that a similar TLAG-CSD scenario could be found by using our prepared propionate-based solutions, with the benefit of starting from precursor metalorganic salts in which we could properly control its synthetic process, ensuring high yields of the reaction, no impurities and small grain sizes to further increase solubility. Therefore, making it a more controlled and reproducible synthetic methodology. To make it a very reproducible process, all the steps and synthetic procedures for the correct preparation of the solution were stipulated in agreement with the whole research group.

Home-made Yttrium (III) propionate $(CH_3CH_2COO)_3Y$, Barium propionate $(CH_3CH_2COO)_2Ba$ and Copper (II) propionate $(CH_3CH_2COO)_2Cu$ were sequentially dissolved at 35 ºC (Cu→Ba→Y), with its appropriate total metal concentration, using a 50/50 volumetric ratio of 1-butanol (Alfa Aesar, 99.4 %) with propionic acid (99 %, Sigma-Aldrich) under Argon atmosphere. The mixture is left stirring for 1 hour until, by turning off the heating plate, it reaches room temperature resulting in a clear deep blue solution without precipitates. The total cation concentration was adjusted by controlling the amount of volume in a volumetric flask and filtered with a PTFE filter. All solutions possessed a 3:7 (Ba:Cu) stoichiometry, which is the most suitable stoichiometry found so far for the TLAG method.

During the screening of the appropriate amount of amine additive for proper inkjet printing depositions, ethanolamine is added first into the flask, by weighting it in the vial considering its density (1.012 g/cm^3), prior to add the solvents. Then the solvents are added in its appropriate volumetric ratio under Argon atmosphere, starting with propionic acid. The total cation concentration was adjusted by controlling the amount of volume in a 5mL volumetric flask and then filtered in the same manner as described above.

Here, a 50/50 volumetric ratio was used to ensure a proper dissolution of the metal precursors, because previous attempts have shown that lower amounts of propionic acid led to precipitation of the salts, since the propionate precursor salts seems to have lower solubility than the acetate precursor ones, especially when less polar solvents, like 1-butanol, are used in the solution preparation procedure. More acid presence ensures more stability of the solution. In fact, for the preparation of 1M inkjet printing precursor solutions using 1-butanol, having the same total metal concentration of the precursor solutions prepared in chapter 3, Cu propionate was not able to be properly dissolved, leading to precipitation of the salts in the next few hours. Although several attempts were made to achieve stable full propionate precursors solutions, Cu propionates were not properly dissolved at the required concentrations.

For that reason, we selected Yttrium and Barium propionates salts as precursors, which could be easily dissolved, together with a commercial Copper (II) acetate $(CH_3COO)_2Cu$ (99.99 %, Sigma-Aldrich) precursor salt for the preparation of inkjet printing inks. Our expectation is that, due to the excess of propionic acid, formation of the mixed barium acetate propionate salt was drastically reduced, as will be shown in the IR study.

Although ethanolamine and other amine additives are known for enhancing precursor salt solubility [**75**], the nature of the solvents made it impossible to achieved soluble solutions at the high salt concentrations required. In contrast, for the methanol solution, we could reach up to 2M concentrations with the 3 prepared metal-propionates. The latter has shown very promising results thanks to the viscosity and solubility enhancement of the ethanolamine additive, reaching thick films with low porosity by using the spin-coating technique [**75**]. In the present case of this thesis the required concentration corresponds to 1M (∑Metals).

4.2.2 Solution Characterization

There are some ink parameters that allow us to interpret if a particular solution is able to perform reproducible depositions by Inkjet printing. We have already seen that some solutions do not fulfil some of the requirements for proper drop ejection in inkjet printing, as in the case of methanol solutions, which eventually leads to the generation of satellites and nozzle clogging. On others, its high concentrations and very high viscosity inhibits drop formation. From the rheological parameters of the prepared inks, the Z number between 4 and 14 is set to stablish the defined range for the generation of stable drops [**96**]. To identify the suitability of ethanolamine as a correct additive for inkjet printing inks, the measurement of the rheological properties of the prepared solutions was done. Results are summarized below, taking special consideration to the viscosity parameter, known to be enhanced when amine additives are used.

4.2.2.1 Solution Rheological Properties

An appropriate screening of the EA additive was made to obtain the rheological values of the solution and evaluate the Z values needed for a stable drop ejection. Upon definition of %EA values for proper inkjet printing ejectability, the functional margins for an adequate homogenous liquid merging had to be evaluated. From that, we wanted to test the additive performance in our Fluorine-free solutions on the depositions made by inkjet printing and analyse its resultant pyrolysis microstructure.

Table 4.1. Rheological properties of the precursor solutions prepared with %EA:

Nomenclature	EA (%vol.)	Viscosity (cP)	Contact angle (º)	Density (g/cm3)	Surface tension (mN/m)	Z	Ejectability
FF-E0	0	5.5	10	1.04	24.8	9.2	Ejectable
FF-E1	1.14	6.8	10	1.04	25.4	7.9	Ejectable
FF-E2	1.8	7.9	10	1.05	25.4	6.5	Ejectable
FF-E3	2	8.2	10	1.05	25.4	6	Ejectable
FF-E4	3.66	15.2	10	1.06	25.8	3.1	No ejectable

As observed in Table 4.1., the addition of ethanolamine produces only changes in viscosity keeping constant all the other rheological parameters. This is an interesting feature for inkjet printing depositions, because as already mentioned in chapter 1.4, changes on the rheological properties can affect drop formation. Since the only value that ethanolamine modifies is mostly the viscosity, thus being the only parameter that changes the Z values, allow us to fine-tune the solution to find the most optimal values.

High EA contents in the solution, as in the case of 3.66% vol. (FF-E4), severely increases the viscosity of the solution, giving rise to high Z-values and thus hindering drop ejection for IJP deposition. In fact, 3.66%vol. corresponds to the exact stoichiometry of Cu:EA in 1:1 ratio, which leads to the formation of its corresponding metalorganic compound by ligand exchange.

Such compound severely increases the viscosity, which give rise to very thick films difficult to pyrolize without generating defects. All the other solutions, however, are on the range of the stipulated Z values, ensuring proper drop formation.

We also checked the rheological properties of the solution over time, from different precursor solution prepared throughout the thesis. Since the reproducible and continuous jetting of drops is detrimental for the correct deposition and homogeneity of the films, we made continuous viscosity measurements of the solutions prepared, ensuring that the values are not out of the range of the stablished Z numbers for optimal ejectability, and that such values do not change over time. These studies could give us information too on the reproducibility and stability of the solution and synthetic method.

The results of viscosity over time, for solutions prepared at different dates among years, with different content of EA, are shown in Figure 4.1, where a very slight increase of viscosity is obtained over time. Additionally, from the study of stability we could conclude that no precipitates are observed in the course of months. Therefore, the solution with EA seem to fulfil all of the stated requirements.

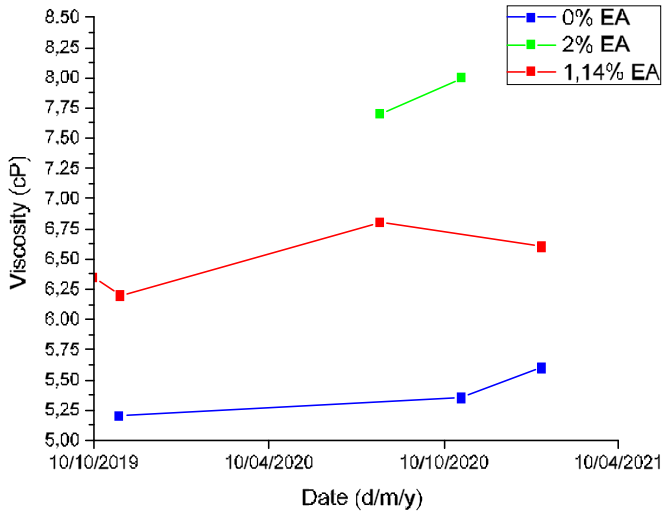

Figure 4.1. *Viscosity evolution of different precursor solution FF prepared as a function of time.*

4.2.2.2 FTIR Analysis

The FTIR spectrum of the as-prepared solution (FF-E1) accounts for the presence of propionate ligands, which exhibit the characteristic C-sp3 absorption peaks at 2978, 2944, and 2876 cm^{-1}, and absorption peaks at 1466, 1431, 1371 and 1299 cm^{-1}, all characteristic fingerprints of such particular ligands [**130-138**]. Notice the presence of the intense Cu band at 1585 cm^{-1}, corresponding to the C=O stretching mode, next to their equivalent bands for the Ba-Prop and Y-Prop salt at 1530 cm^{-1} (the absorptions of both salts overlap).

We do not observe the shifting to 1546 cm^{-1} for the C=O stretching mode characteristic of the Ba-Prop-Ac salt as in the chapter 3 [**132**]. Since only Cu acetates have been used in the preparation of the precursor solution, and propionic acid was in excess, a band at 933 cm^{-1} resulting from Ba-Prop-Ac salt presence is not observed [**132, 135**]. Two broad peaks appear at 3438 and 656 cm^{-1}, corresponding to 1-butanol characteristic infrared peaks, used as solvent. We can thus verify that that the metal precursors are propionates.

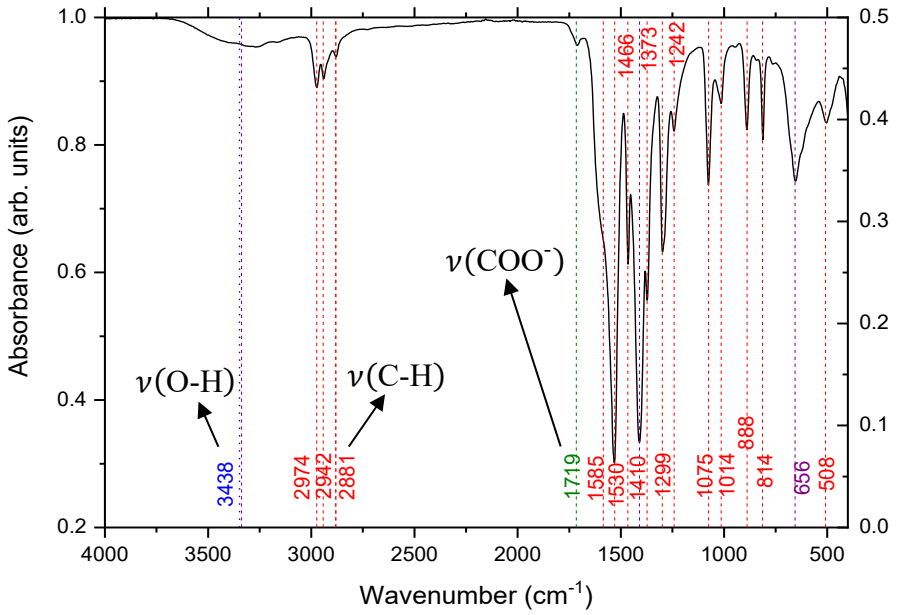

Figure 4.2. *FTIR spectra of the as-prepared solution using 1-butanol as solvent with 1.14%EA (FF-E1).*

It has been stated that the separation between the asymmetric and symmetric carboxylate bands $\Delta\nu = \left[\nu_{as}\left(\mathrm{COO^-}\right) - \nu_s\left(\mathrm{COO^-}\right)\right]$ can be used to determine the type of carboxylate-metal complexation. It has been proposed that chelating coordination exists when ($\Delta\nu$ < 134.6 cm^{-1}) bridging coordination exists when ($\Delta\nu$ > 134.6 cm^{-1}) and monodentate coordination appears when ($\Delta\nu$ > 180 cm^{-1}). In Figure 4.2, we observe that the initial asymmetric and symmetric carboxylic bands are located at 1530 and 1410 cm^{-1}, respectively. Thus, $\Delta\nu$ ~120 cm^{-1} (a very similar value was obtained for hydrated yttrium propionate) can be attributed to a bidentate chelating coordination mixed with a bridging coordination type.

4.2.2.3 Water Content

One of the factors that is involved on the precursor solution stability and robustness is the percentage of water that can be found after the synthetic process. Our group found that more than 2% volume of water content in the FF solutions was detrimental in the achievement of good textured YBCO films [**75, 128**]. To check the water content, continuous evaluations of the solution were made in order to ensure its good quality.

Special control is taken during solution preparation and deposition to minimize environmental water contamination and keep its initial water content as possible. However, since our solutions are composed by a carboxylic acid and an alcohol, esterification reactions can occur, being water a sub-product of the following equation:

$$CH_3CH_2COOH + CH_3(CH_2)_3OH \rightarrow CH_3CH_2COO(CH_2)_3CH_3 + H_2O \qquad (4.1)$$

Since 1-butanol has a lower reactivity if compared to methanol, we found that all solutions had very low water volume percentages after its synthesis, of around ~0.5 %wt., with an increased rate of ~0,06%wt/day.

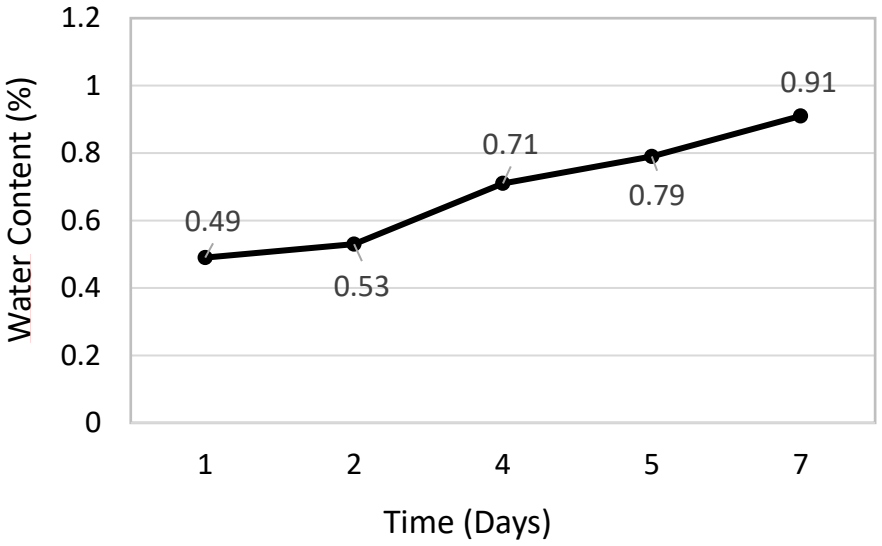

Figure 4.3. *Water content of the precursor solution prepared among time for a solution with 1.14%EA (FF-E1).*

In conclusion, we demonstrated that this class of solution had good stability over time, without precipitation of the metal salts over months. Additionally, all solutions had very low water volume percentages after its synthesis, with little increase due to esterification reaction among time. We know that ethanolamine inhibits the esterification reaction, but we could control the amount of water confirming the robustness and stability of the solution. In fact, our group has shown that the %vol. of water in the methanol-based solutions, if well-kept sealed, does not surpass the critical value of 2%vol. for months [**75**].

As seen earlier, the butanol-based solutions prepared are very stable with time. Regarding the esterification reactions that occur between propionic acid and butanol, in a matter of 7 days, the presence of water is small, around 0.9% in weight, indicating very low yields of the reaction. Moreover, Ethanolamine have shown to be a suitable additive for the preparation Fluorine-Free film regarding the mechanical resistance avoiding crack formation and helping to densify the film (achieving thicker films with less porosity) [**75**]. However, too much EA content could lead to aggregation of the oxides and carbonates and may even act as a reducing agent [**75**].

4.2.3 Precursor Solution Evaluation for the TLAG method

To test the viability of the solutions with ethanolamine (FF-E1) for the TLAG-CSD method, we deposited few films by spin coating on STO substrate. Afterwards, the sample was placed in a tubular oven for its correspondent pyrolysis of the organic components of the solution, using the standard pyrolysis profile of 5ºC/min up to 240ºC and 3ºC/min up to 500ºC to ensure the complete firing of the organic moieties. Films of ~120nm were obtained, measured by interferometry.

The degree of decomposition of the pyrolized films was determined by FTIR and XRD, while the homogeneity of the films was determined by optical microscopy. The initial thermally pyrolized samples under wet oxygen flow at 500 ºC revealed good homogenous films. In Fig. 4.4, we observe that the samples prepared using the FF-E1 precursor solution in spin-coating showed good homogeneity and no defects in all cases after the thermal pyrolysis at 500 ºC. Moreover, the results were found to be highly reproducible. While the use of 1-butanol would help on the depositions made by inkjet printing, lower film thicknesses were achieved in spin-coating if compared to the highly concentrated methanol solution, optimized in our group for such deposition technique.

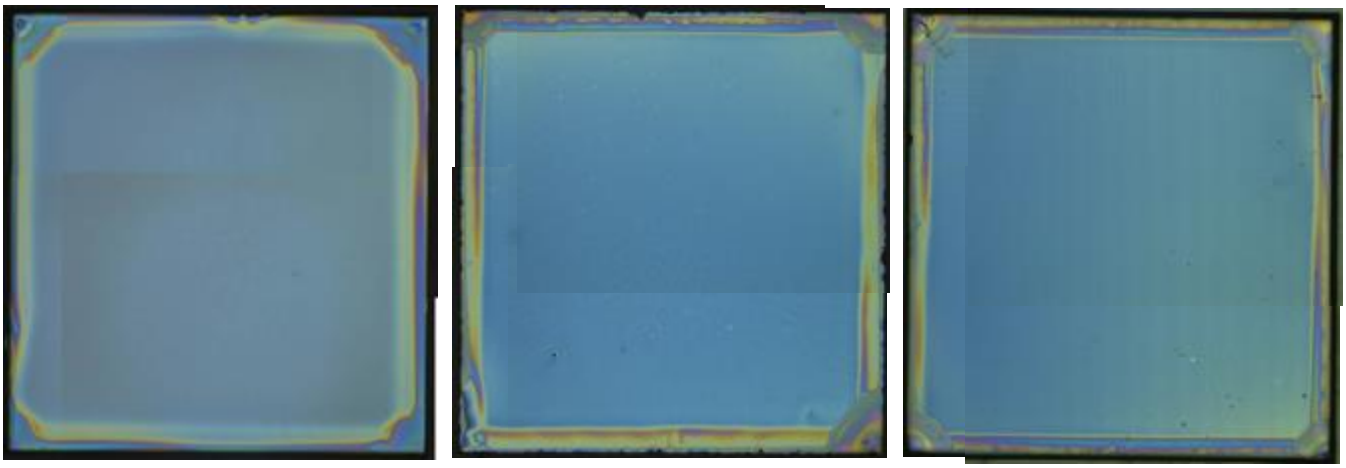

Figure 4.4. *Examples of 1-layer spin-coating deposited samples of 1M+1.14% vol.EA solution using 1-butanol (FF-E1). One pyrolized layer gives around 100 nm. thick samples.*

The effect of the ethanolamine additive not only have shown better performances in terms of solution stability, additionally, but analysis on the prepared films have also revealed a better performance during the decomposition of the carboxylates [**75**]. Thickness measurements and TEM images have shown the capacity to obtain homogenous depositions by spin-coating, with high thickness above 400 nm per layer, and very low porosity (1%) for solutions in 2M concentration in methanol and a 4% of EA, in contrast to the thinner films obtained previously by our group, mentioned in chapter 3. All the above-mentioned aspects suggest us that ethanolamine can be a suitable additive for inkjet printing depositions.

The crystalline structure of the pyrolized films were determined by X-ray diffraction. Samples pyrolized at 500ºC showed peaks corresponding to copper oxide (II), whose formation was expected. As for the barium carbonate, both monoclinic and orthorhombic phases are present in the XRD pattern, being the orthorhombic phase its major contribution. In this respect, the pyrolyzed film fulfils the requirements to provide a high-quality YBCO film after growth. In the next section, the effort undertaken to validate if this solution can reach homogeneous IJP deposition and also ensure homogeneous thick pyrolyzed layers is presented.

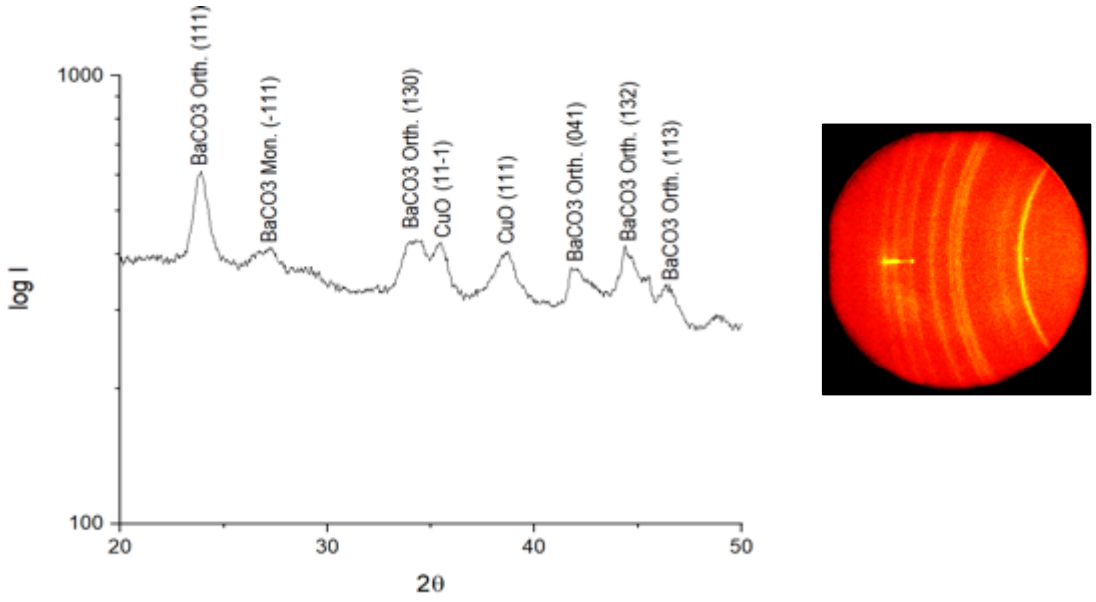

Figure 4.5. *XRD Pattern of a spin-coating pyrolized film using the FF-E1 solution.*

4.3 Results and Discussion

On the arrival of a Drop-on-demand piezoelectric inkjet printing (DoD IJP) from Microdrop Technologies GmbH [**156**], it was used to fabricate test pieces on single-crystal (001) $SrTiO_3$ (STO), single-crystal (001) $LaAlO_3$ and LSMO-SUNAM coated conductor tapes (CC) as substrates. A piezoelectric (PZT) head supplied by Microdrop Technologies GmbH [**157**], with a 50µm nozzle diameter was used. The later IJP system possesses a 96-well plastic plate array, where the precursor solution is placed, with the addition to use different precursor solutions at the same time in discrete deposition modes.

The deposition studies began on this system especially due to its more sophisticated software and moving/heating plate, which allow us to obtain samples in a more reproducible manner. Moreover, with the opportunity to use more than one nozzle in one single deposition, by its capability to operate with a multinozzle head with up to four nozzles, it created an interest for high-throughput experimentation by chemical solution deposition on combinatorial studies.

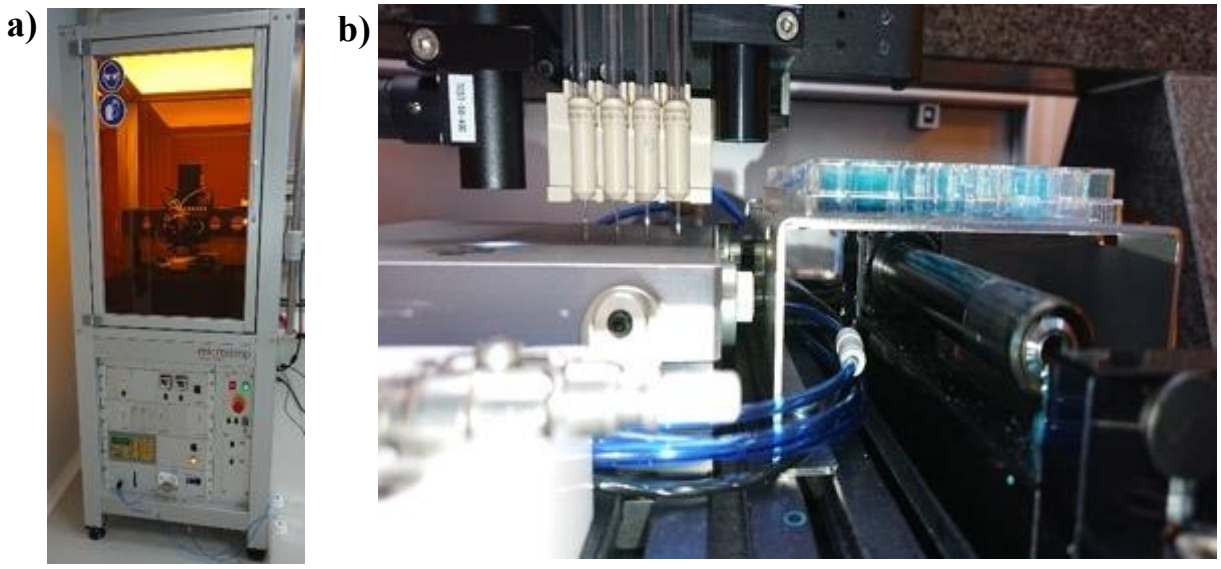

Figure 4.6. *a) Whole Inkjet Printing system coupled to a computer. b) DoD IJP setup, consisting of a 96-well plate array, a multi-nozzle head with four independent nozzles, a stroboscopic light/camera for drop inspection and a camera for surface inspection.*

4.3.1 MicroDrop Inkjet Printing deposition modes

There are mainly two different types of deposition procedures in our Inkjet Printing systems. On one hand we have a drop on demand technique whose procedure accounts for specific printing positions, automatically generated through a Python interface, that outputs a (x,y)-coordinate file with the desired pattern dimensions and drop/line pitches, giving rise to a discrete deposition technique. This procedure is what we called Slow Mode, only available at the MicroDrop apparel. On the other hand, a more continuous deposition mode is also available, where the frequency of ejection is automatically determined by the plate velocity, with the possibility to change it in order to increase the rate of deposition, from 0.5 mm/s to 1 cm/s. While the home-made inkjet printing has a predefined move plate speed of 1 cm/s, the MicroDrop printer has then different speed configurations with the possibility to change the plate velocity. The process will be called Fast Mode, usually with a constant plate velocity of 0.5 mm/s in the MicroDrop system. This deposition approach will be the main deposition technique used, not only to avoid time-consuming processes, but also due to its greater similarity to reel-to-reel industrial systems (see Videos 2&3 in Appendix A).

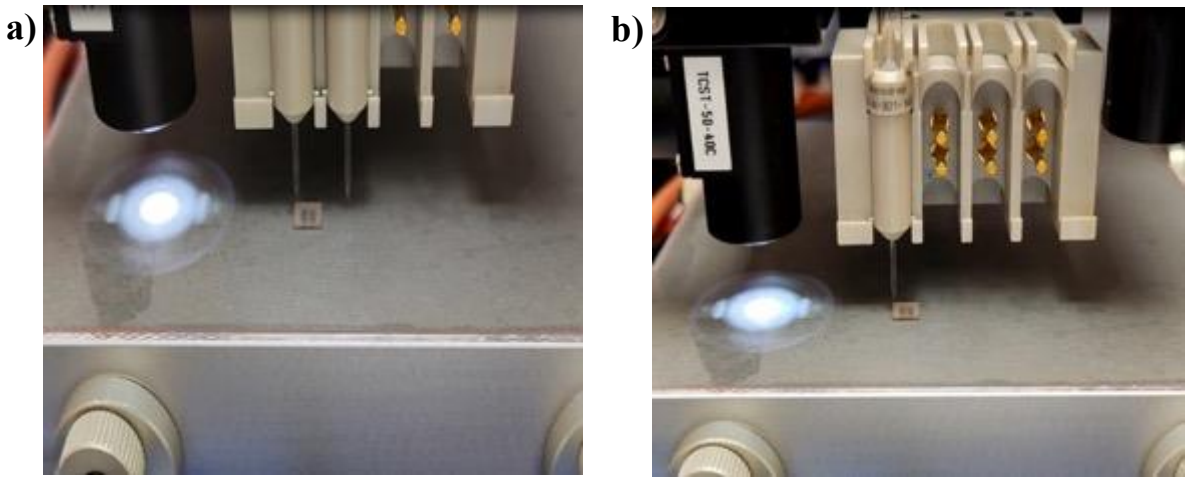

Figure 4.7. *(a) Drops are deposited in a discrete manner on a determined place of the substrate (x & y coordinates). Deposition time increases due to the nozzles specific movement at a selected point. (b) Drops are ejected continuously following the plate movement. Switchable plate velocity (from 0,5 mm/s to 10 mm/s) so the deposition can be very fast.*

As can be observed, these two different modalities had to be different approaches regarding its proper deposition of drops, drop merging, drop overlapping and liquid pinning to the substrate due to solvent evaporation, which implies different setup configurations in order to achieve the desired homogenous printed films.

Obviously both deposition modalities of the inkjet printer required different deposition parameters for its proper homogenous deposition of the solutions. The deposition matrix, being drop pitch and line pitch for proper drop merging, the drop volume, the evaporation rate of the solvents, the overall rate of deposition and the rheological properties of the solution, all of them playing a role on how the chemical solution will be deposited, which will have an impact on the resulting sample morphology, microstructure and properties.

As an example, a deposition matrix used for homogenous depositions in Slow or Discrete Mode could produce large liquid accumulations if the plate velocity is very high, as it is in the case of the Continuous or Fast Mode, as seen in Figure 4.8, which imply that in each mode used, there should be a proper optimization of the deposition parameters, such as drop volume and/or the predefined patterning.

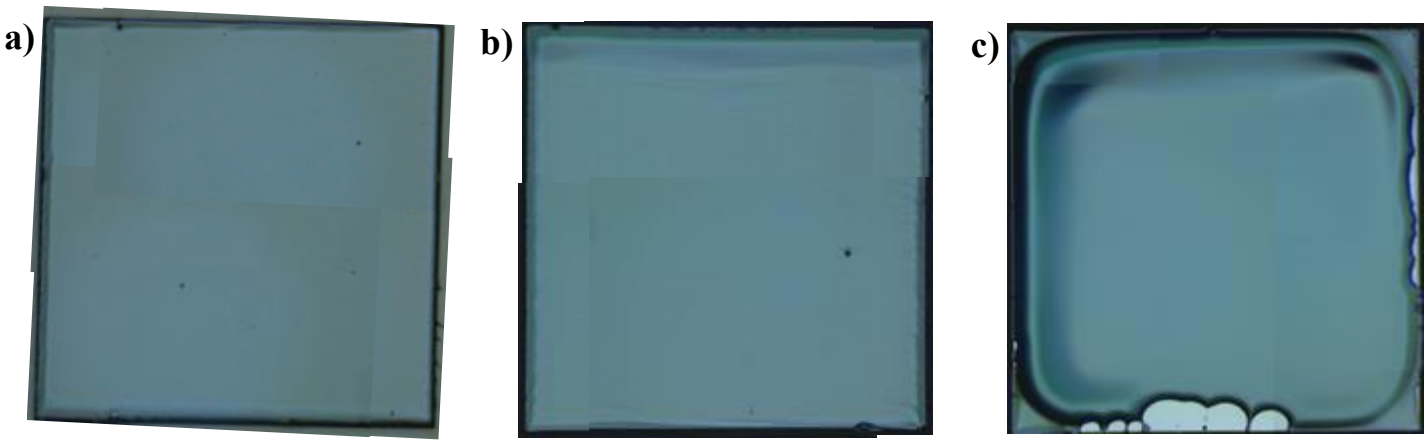

Figure 4.8. *Optical Microscope images of the deposited films using different inkjet deposition modes, with the same deposited volume, same deposited grid and drop volume; (a) Slow Mode; (b) Fast Mode at 0.5 mm/s and (c) Fast Mode at 1 cm/s.*

Throughout this section we will apply the theoretical concepts described, together with the knowledge obtained during the evaluation of the precursor solution prepared using ethanolamine as additive. Here, we will evaluate the capacity of the solution designed to perform inkjet printing depositions with the desired thickness to achieve good homogeneity for the preparation of defect-free samples. In this case, the preparation of thick films will be carried out in the MicroDrop inkjet printer system, a Drop-on-Demand (DoD) system, which was acquired during this PhD thesis, where the printhead dispenses ink only when specified. The system was in a clean room type 10000 with a 30% controlled humidity (See Figure 4.6). In the next section, this discrete mode is summarized.

The Slow Mode deposition technique, available in the MicroDrop Inkjet printing system, is a discrete deposition mode that rely on the deposition of a determined number of drops for each specified position of the nozzles used. The positions of each nozzle is determined by a generated x,y-coordination file containing the desired pattern. Such pattern involves the drop pitches and line pitches selected (μm), the dimensions of the matrix (mm^2), the number of nozzles involved in the deposition (up to 4 nozzles can be used in this deposition mode), and the number of drops to be ejected on each defined position.

As an example, to deposit a film on a 5x5 mm^2 LAO or STO substrate, placing one drop on each specified position, the initial point of the deposition matrix would account for one deposited drop from nozzle 1 at (0,0 mm) position, while the last point of the deposition matrix will involve the deposition of a single drop for nozzle (2 to 4) at (5,5 mm) position. Since the motorized plate during the deposition moves towards the specified points selected for each nozzle used, this deposition modality has a slow rate of deposition, being 0.21 mm^2/min. So, for a 5x5 mm^2 substrate, the deposition can last up to 2 hours.

The slow rate of deposition differ much from the other inkjet printer system previously used in chapter 3, since the deposition is discrete, implying that the nozzles move towards the end of the substrate to come back again at the specified position of the x,y-coordination map, for only one deposited drop in each position. Moreover, since the deposition of the drops are very slow, the drying effect of the solvents and the precursor solution once deposited over the sample will play a very relevant role, contrary to the case of chapter 3. Therefore, the drying process is anticipated to be critical to achieve homogenous depositions. For a more detailed visualization of the plate movement and the Slow Mode deposition technique we hesitate to watch its correspondent video on Annex A.

For that matter, the parameters involved in the depositions must also be fine-tuned, including the drop volume obtained after drop formation, the number of drops that are deposited as the total volume deposited, the drop diameter impact on the substrate and its subsequent drop and line pitches for proper drop merging [**158-165**]. In our study, in addition, we will also consider small modifications on the amount of ethanolamine additive, as a parameter to control homogenous depositions and defect-free pyrolyzed films.

The versatility of such drop-on-demand inkjet printing (IJP) mode allows performing combinatorial studies, even at our group [**166-167**]. Nowadays, high-throughput experimentation (HTE) is achieving more and more relevance in material design as a way of accelerating the optimization of materials. Additionally, the advancement on machine learning algorithms enables fast analysis of HTE results. Altogether, is then seen as complementary methods for data-driven materials approaches.

4.3.1.1 Drop and Line Merging Study

The identification of the best drop pitch combination is essential to ensure a homogeneous deposition of the ink. Firstly, it is needed to tune the waveform to obtain a stable drop formation. Once the drop formation is stabilized, an average deposited drop size is also needed. Measuring the diameter of several drops deposited on single-crystalline (001) STO substrates with a separation of 500μm between them, at ambient temperature, will give us the independent drop impact diameter necessary to study the proper drop merging, and the required separation among them, to obtain homogenous layers.

Depending on the nozzle used, the waveform parameters need to be tuned to achieve stable drop formations for each particular nozzle characteristics. Still all the nozzle utilized here consisted of a piezoelectric printhead (PZT) with 50μm diameter (AD-K-901, microdrop Technologies GmbH) [**157**]. We have defined a range where stable drop formation can be obtained, by using the following waveform parameters:

- Pulse Length = 20 to 30 μs
- Pulse Width = 130 to 150 V
- Drop volume = 180-200 pL

The drop volume can be modulated by both the pulse length and the pulse width. As these values increase, the drop volume will also increase. Based on our studies, drop volumes in the ranges of 180pL to 200pL are jetted in a reproducible continuous manner. Values around 180-190pL are preferred, since as higher is the voltage applied, more changes on the drop occur, even with satellites at some instances. In order to understand the mechanisms of liquid movement and accumulation for this particular deposition mode, a merging of drops study was performed. A large drop pitch (500 μm) is selected to study the drop impact and drying performance on top of a single crystal STO substrate for each drop.

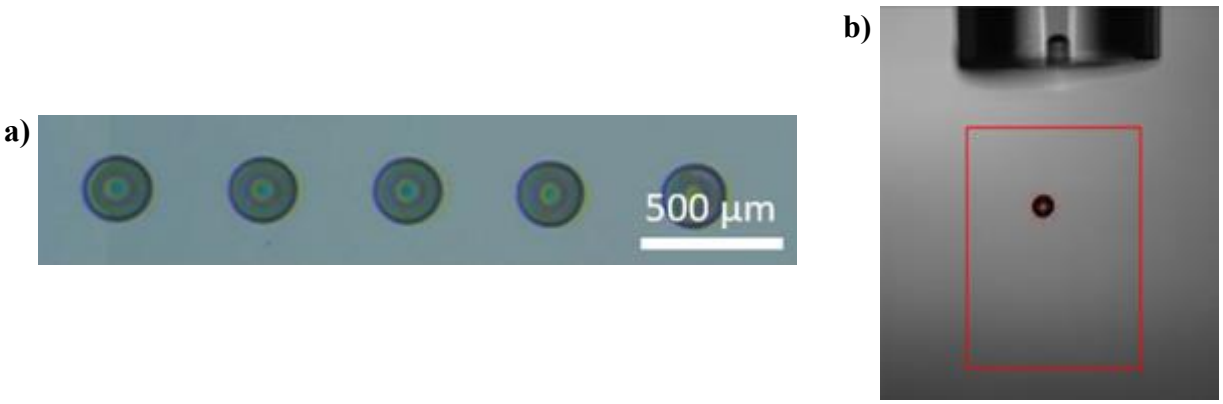

Figure 4.9. *(a) Drop diameter obtained with a Data Grid with 2 nozzles using 180pL of drop volume. Giving an average drop impact diameter of 241±4µm. The ink is FF-E0 (0%EA). (b) Stroboscopic camera image during drop formation used to determine the drop volume via software analysis.*

Since our x,y-coordination files are generated through python interface, we are able to estimate the drop merging interaction to measure the degree of drop overlapping, in both X and Y directions. We have calculated experimentally the average drop impact diameter via optical microscope, which enable us to compute approximations on how the drops and lines will merge, and which will be the shape of the deposition matrix computed in the x,y-coordination file. The degree of overlap can be calculated by using the following expression:

$$\frac{O}{D} \times 100 \qquad (4.2)$$

where *O* is the overlapping distance between two drops (*D-dx* or *D-dy*) and *D* is the diameter of the drop impact.

The resultant film morphology largely depends on such overlapping degree. By preparing the coordination files and analysing its degree of overlapping, it presents the opportunity to estimate the deposition parameters needed to obtain homogenous depositions, based on the theoretical scheme of distribution of the drops to be homogeneous. However, this does not imply that the resultant deposition will be homogeneous, since it does not take into account liquid movement.

Once compared with the experimental depositions, via optical microscope, the different drop and line pitches selected could vary in order to obtain better drop merging while reducing liquid accumulation.

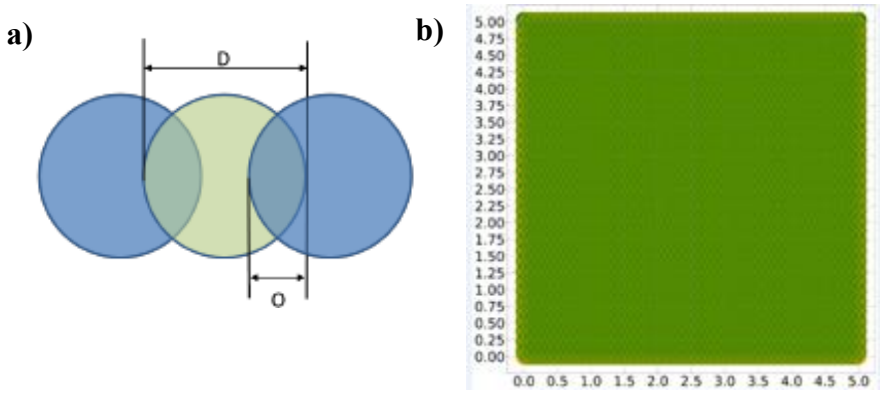

Figure 4.10. *(a) Schematic representation of drop overlapping. (b) Example of a x,y-coordination file for a drop of 180pL using drop and line pitches of X = 50 µm and Y = 85 µm. These drop pitches result in degrees of overlap in x = 80% and for y = 65%.*

In order to understand the mechanism of liquid movement, to test the performance of this solution and to avoid inhomogeneities, we performed a drop-line merging study for Slow Mode. Several depositions were performed experimentally where different drop pitches were used in order to fine tune the best deposition conditions for drop merging and line formation for this particular deposition technique.

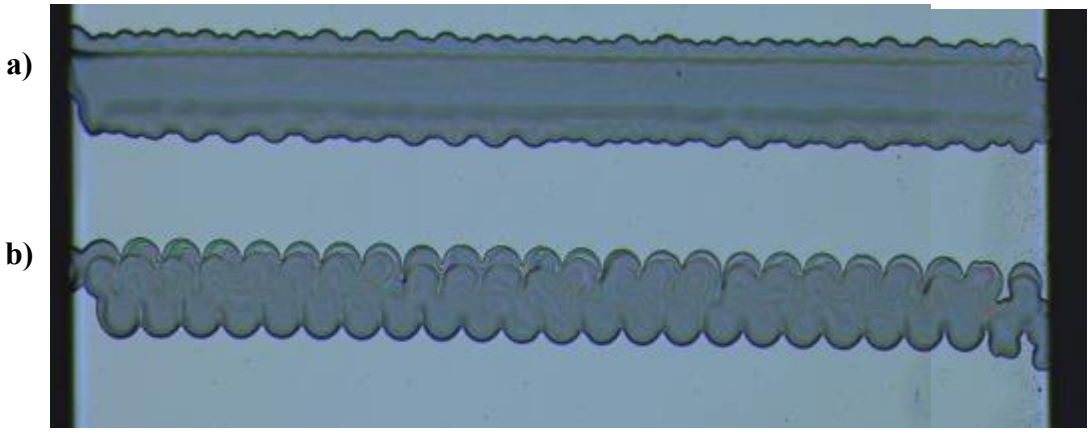

Figure 4.11. *Drop merging analysis, creating 2 deposited lines with FF-E0 (0%EA): (a) Drop Spacing = 50 µm; Line spacing = 75 µm; 2 lines. (b) Drop Spacing = 100 µm; Line spacing = 37,5 µm; 2 lines.*

As observed in Figure 4.11, for the complete formation of lines (complete merge of drops in x-horizontal direction), less than a 100 μm of drop pitch is required. However, drop pitches smaller than 50 μm also have shown larger liquid accumulation which led to inhomogeneities due to liquid movement. On the contrary, if larger drop pitches combinations are selected, drops will not merge continuously leading to unconnected patterns. Although several drop pitches could be used, drop pitches of 50 μm were selected as the reference drop pitch for the line merging study, due to the fact that a more continuous and straight line is obtained during deposition, without much liquid accumulation. Once the drop pitch is already selected, different line pitches were tested in order to avoid liquid accumulation.

For the proper merging of printed lines, we selected a serial of patterns in both X and Y directions from the already evaluated line merging parameters, using mostly a drop separation in X of 50μm, while changing the length of the Y direction.

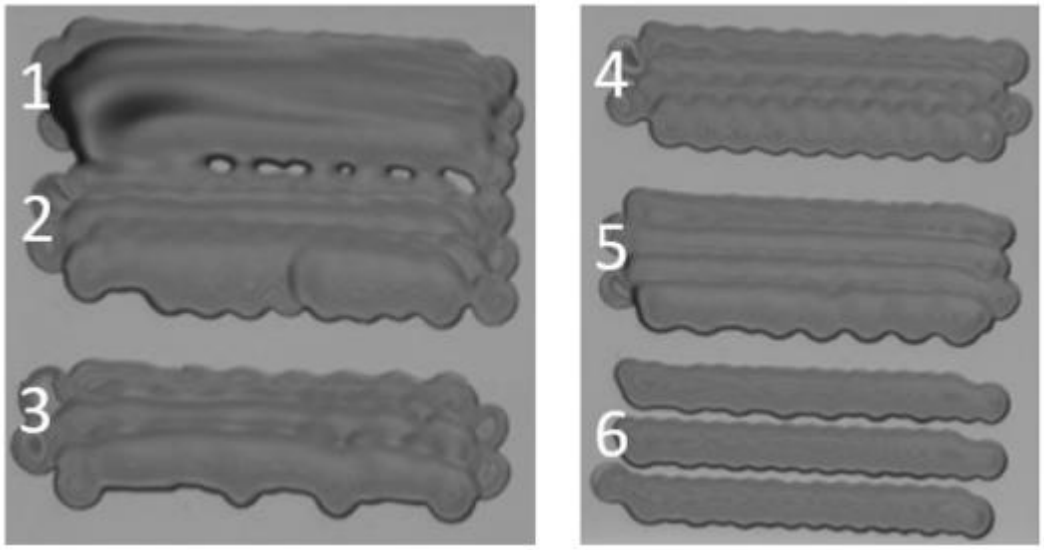

Figure 4.12. *Optical microscope images of several patterns with different drop and line pitches as indicated (XxY): 1) 50×50μm, 2) 75×75μm, 3) 100×75μm, 4) 75×100μm, 5) 50×125μm, and 6) 50×250μm. Note that no additives were added to the chemical solution used, accentuating the liquid accumulation at the edges and the first printed lines. The deposited solution was FF-E0, with no EA content. Extracted from Queraltó A., Pacheco A. et al [**166**].*

As seen in Figure 4.12, as the printed lines are deposited at lower line pitch values, they start to lose their definition, resulting in large accumulations of liquid, as in the case of 50x50µm (1), where the liquid moves towards the first printed line. From the optical microscope images, we were able to stipulate the best deposition matrices for proper drop and line merging. We found that a scenario using a drop pitch of 50-75µm (2 and 5) in the X direction and a line pitch of 75-125µm (4 and 5) in the Y direction could lead to the deposition of homogenous films. The degree of overlapping between lines is what will redefine the shape of the film, whether there are large accumulations of liquid or not, whether the lines merge well together or conform to shapes with considerable differences in thickness on the surface of the film. On the other hand, if the degree of overlap between lines is too high or non-existent, the lines will not be able to merge properly, resulting in unconnected patterns (50x250).

4.3.1.2 Film deposition and additive screening

Our main goal was to define the thickest YBCO films reachable by one single deposition using IJP. Previous results from the homemade inkjet printer however, have shown that the thickness is limited by the appearance of defected films after pyrolysis. In this chapter, we concentrated in attempting to deposit films in the range of 1000 nm after pyrolysis (500 nm. after growth). and subsequently keep increasing the thickness.

Here we explore the inclusion of additives in the ink to enhance the solubility of the metalorganic precursors, increase homogeneity, facilitate drop formation as well as to prevent excessive drying of solvents and nozzle clogging. To do so, several $\%_{v/v}$ EA were tested to find a compromise between the increase of ink viscosity with the amount of EA and the increased difficulty for drop ejection. Several samples prepared with inks containing from $0\%_{v/v}$ to $2\%_{v/v}$ of ethanolamine. Remind that we cannot use methanol-based solutions since the low boiling point of the solvent leads to nozzle clogging very easily.

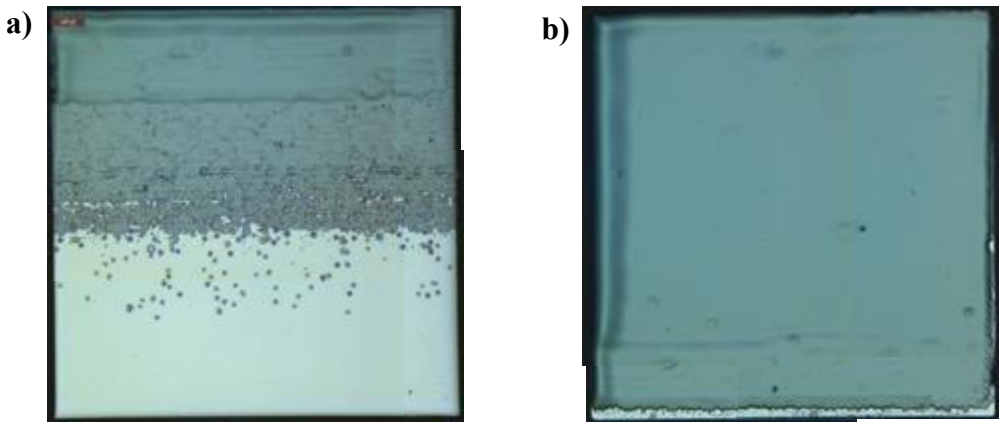

Figure 4.13. *Optical microscope images of as-deposited samples using (0% EA) showing: (a) Nozzle clogging by using a 1M solution with methanol. (b) Homogenous morphology for inks containing 1-butano (FF-E0). Drop pitches of 50 µm and 95 µm along the x and y directions were employed.*

The addition of ethanolamine clearly shows a qualitative improvement in the homogeneity of the printed lines, in which liquid movement is greatly reduced, being the edges better confined into the printed dimensions. The slow deposition rate, together with the viscosity enhancement produced for the inclusion of ethanolamine as additive induces a better pinning of the liquid into the substrate.

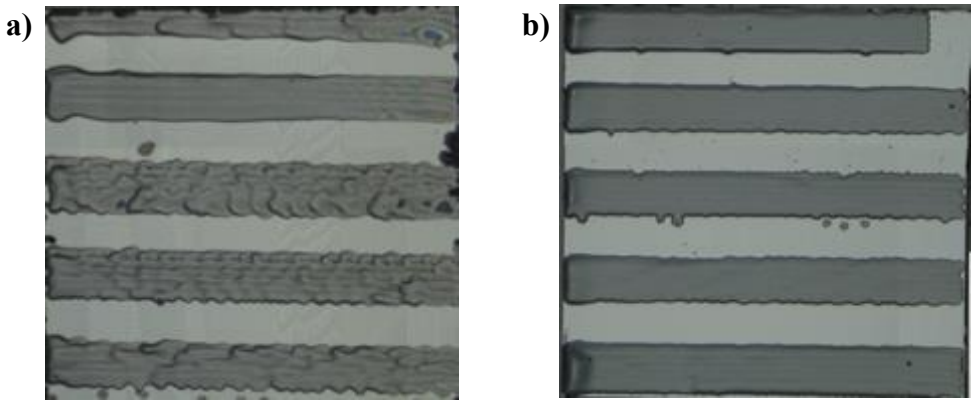

Figure 4.14. *Optical microscope images of as-deposited samples showing the morphology for inks containing (a) 0% (FF-E0) and (b) 1.14% of EA (FF-E1). Drop pitches of 50 µm and 95 µm along the x and y directions were employed.*

Our results suggest that the ethanolamine used in this study, not only allows for better depositions regarding its homogeneity due to viscosity enhancement, but also affects the drop jetting. As observed in 4.13 and 4.14, the slow rate of deposition of this mode can lead to nozzle clogging, even when high-boiling points solvents are used on the inks. Ethanolamine prevents such nozzle clogging to a certain extent.

Additionally, the deposition of chemical solutions at very slow deposition rates allow the solution to pin better into the substrate thanks to solvent evaporation. Once the deposited drops are allowed to evaporate the solvents, the resultant gel-like fluid is pinned into the substrate while is merging with the other surrounding drops avoiding liquid redistribution. Once a fully printed line is deposited, the next printed line is able to merge without further liquid movement.

Ethanolamine has shown a huge improvement in the liquid pinning to the substrate by increasing the viscosity of the solution. Together with the slow deposition mode used, the drying of the drops and lines allow for a better evaporation of the solvents present in the solution, jellifying the deposited material and fixing it to the substrate, thus avoiding liquid movement and coffee-ring effects.

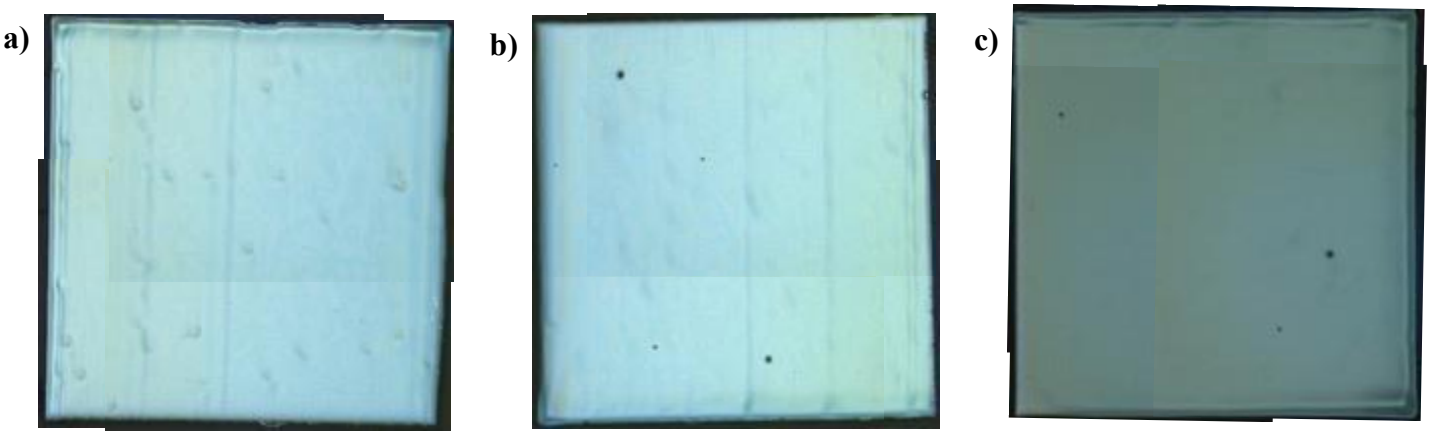

Figure 4.15. *Optical microscope images of as-deposited samples showing of homogenous depositions using a 1M+1%EA ink (FF-E1): (a) Deposition matrix of (50x95) with a drop volume of 180pL. (b) Deposition matrix of (50x85) with a drop volume of 180pL. (c) Deposition matrix of (50x75) with a drop volume of 180pL.*

Finally, we have reached an equilibrium between the drop and lines pitches required to obtain proper drop merging and homogenous depositions. A certain percentage of ethanolamine additive (1%vol.) is able to overcome the problems related to the liquid inhomogeneities during deposition. In combination with the slow rate of deposition of the IJP mode, which enhances solvent evaporation, allow us to obtain deposited films with good homogeneity. The next step will be to study its suitability to reach defect free pyrolyzed films.

4.3.2 Pyrolysis Analysis of Discrete IJP deposited Films

Major issues during the pyrolysis of inkjet printed films had to be solved, especially regarding the crack formation that appears during the decomposition of organic matter present in the solution. Previous attempts to avoid the crack formation were not properly achieved, even when reproducible homogenous depositions were performed. As the solvents dry and the metal carboxylate salts start to decompose, a coarsening and densification effects occurs, which induces stress on the films released in the form of defects on the sample, such as crack formation. Defect formation was evaluated by in-situ imaging of the pyrolysis, matching well with the decomposition of Cu carboxylate, around 235ºC.

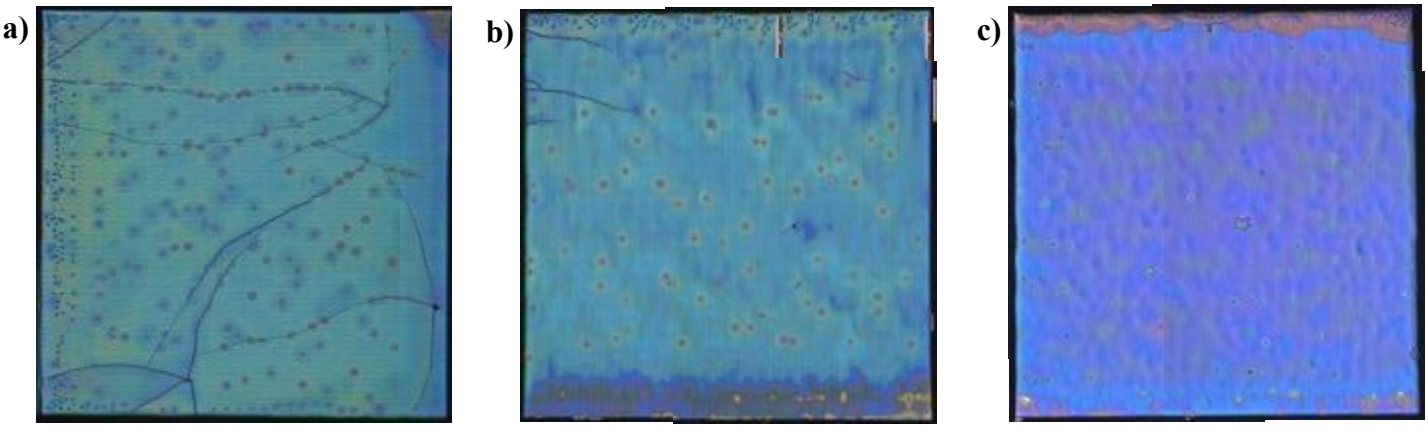

Figure 4.16. *Optical microscope images of pyrolized samples (75x75) under standard pyrolysis conditions (5ºC/min to 240ºC and 3ºC/min to 500ºC, 0.12L humid O_2): (a) 1M+1%EA solution (FF-E1). (b) 1M+1.5%EA solution. (c) Crack-free pyrolized film using 1M+2%EA (FF-E3).*

As it is shown in the previous section by using a certain percentage of ethanolamine (1-2%), we could start printing full deposited films and study the stress-release mechanisms of the films during the pyrolysis. We started by depositing films to study its behaviour under the standard pyrolysis profile conditions used in spin-coating samples (see section 4.2), while screening the %v/v of ethanolamine required to avoid crack formation.

The crystalline structure of the pyrolized films were determined by X-ray diffraction. Samples pyrolized at 500ºC showed peaks corresponding to Yttrium and Copper oxides, together with a mixture of BaCO3 with orthorhombic and monoclinic phases, whose formation were expected considering the thickness of the film, being the orthorhombic phase its major contribution. In this respect, the pyrolyzed film fulfils the requirements to provide a high-quality YBCO film after growth. In this case, it validates IJP depositions as a possible CSD technique to achieve homogeneous thick crack-free pyrolyzed layers.

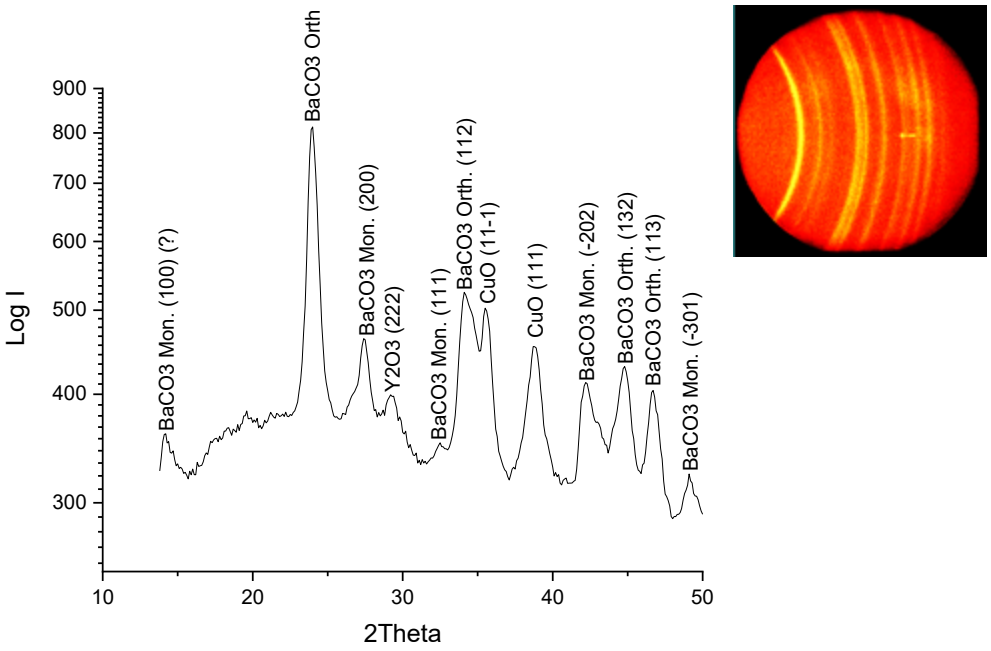

Figure 4.17. *GADDS diffractogram from a Slow Mode deposited sample (75x75µm) under standard pyrolysis conditions (5ºC/min to 240ºC and 3ºC/min to 500ºC, 0.12L humid O_2 using 1M+2%EA (FF-E3).*

From these preliminary results we observed that whereas a 1%v/v of EA is enough to obtain homogenous depositions, the avoidance of crack formation can only be accomplished when a 2%v/v of ethanolamine is used in the IJP ink. During pyrolysis, EA is able to minimize phase segregation and decrease film porosity, if the appropriate amount is properly fine-tuned [**75**]. Our assumption is that EA, acting as a chelating agent is able to bind to the metals, displacing some propionate moieties, to change the transformations of the metal intermediates, thus inhibiting phase segregation and CO_2 release at the end of the pyrolysis synthetic route, thus avoiding crack formation.

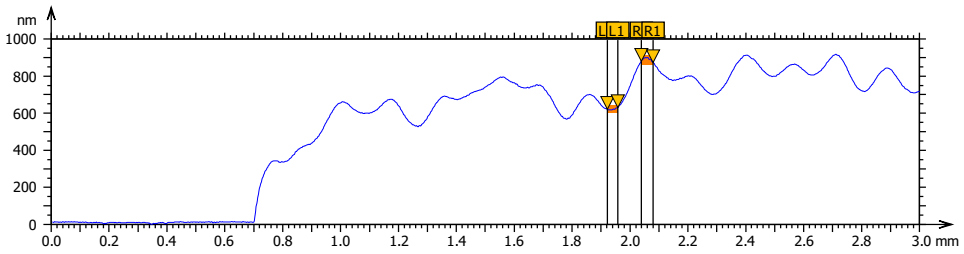

Parámetros	1	Unidad
StpHt	270	nm
TIR	259	nm
Avg	696	nm
Slope	0.123	°

Figure 4.18. *Profilometry measurements of a (75x75) pyrolized sample using 1M+2%EA, notice the 270 nm thickness inhomogenities at the surface in an average thickness after pyrolysis of 700 nm.*

The profilometry measurements of the samples have shown that by using a squared matrix deposition, in which the drop pitch used is the largest to obtain continuous deposited lines, and the line pitch has shortened to the values that could lead to liquid accumulation, results in huge thickness inhomogeneities on the range of 250-300nm in height, which implies also a difference in thickness after TLAG growth, which may effect on the superconducting and current percolation properties of the final YBCO layer.

We repeated the measurements when using different deposition matrices. By using a 2%$_{v/v}$ of ethanolamine and a 50x85µm matrix we could avoid crack formation and obtain defect-free films while films with homogeneous thickness were obtained, as detected by interferometry and profilometry measurements.

The most possible outcome is that we can still produce thicker films while using ethanolamine, since we do not have reached the critical thickness value of the film (t_c) for this type of solution, implying that up to 1000nm thick films after pyrolysis, the stress-relief mechanisms can be avoided with this combination of ink, matrix, substrate and pyrolysis.

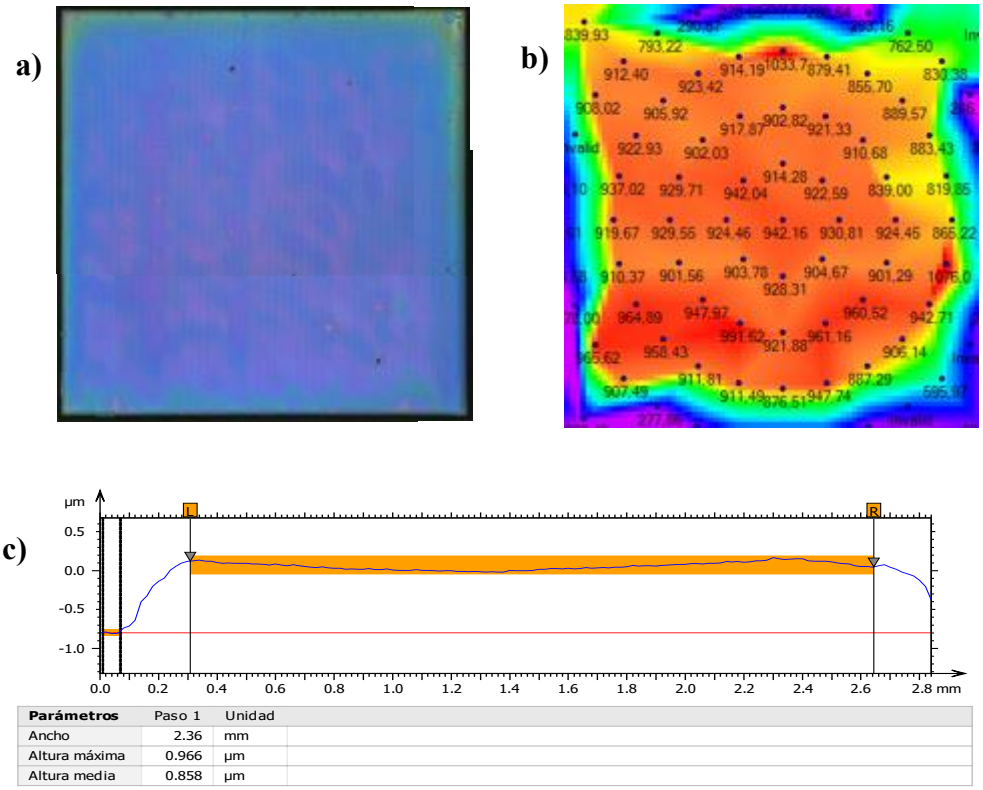

Figure 4.19. *(a) Optical microscope images of pyrolized samples (50x85µm) under standard pyrolysis conditions (5ºC/min to 240ºC and 3ºC/min to 500ºC, 0.12L humid O_2) with 1M+2%EA solution. (b) Thickness Interferometry Map of the sample with an average thickness of 920nm (c) Profilometer measurement of the sample, without thickness inhomogenities and an average thickness of 860nm with a maximum thickness of 960nm.*

Considering the amount of the deposited drops in the substrate, taking into account the computed drop and line pitches of the Python x,y-coordination files, the drop volume and the dimensions of the substrate, we are able to compute the total deposited volume in each given sample.

The distribution between the total volume deposited and the measured thickness through interferometry and profilometry techniques have shown, interestingly, a linear relationship between them, implying that the total deposited volume on each deposited sample will be translated into the thickness of each given samples, giving rise to very reproducible results, especially in the latter case when using a deposition matrix of (50x85µm).

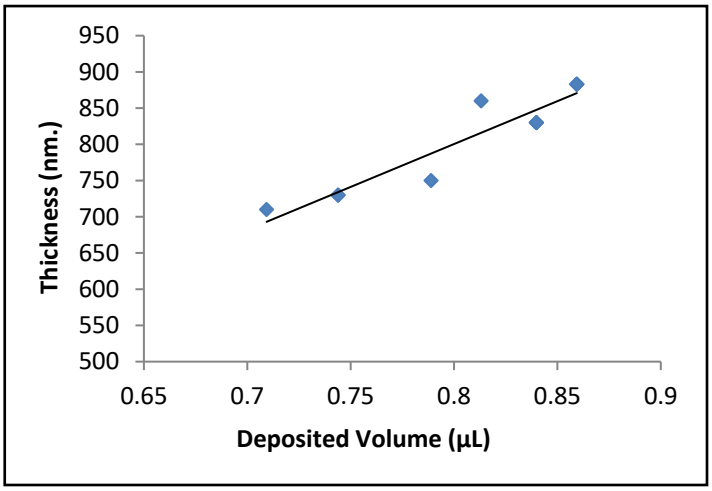

Figure 4.20. *Thickness Distribution of Slow Mode Inkjet Printed samples based on Profilometry measurements against the total volume deposited.*

Summarizing, we have found a reproducible way to obtain thick films using the discrete deposition mode by using a certain deposition matrix that allows for homogenous layers without cracking and a solution based on FF-E0 with an addition of 2%vol. of EA as additive (FF-E3). This has enabled us to obtain layers beyond 1000nm in thickness after pyrolysis without any defects and smooth surface. For such discrete deposition mode, we recommend using a drop pitch of 50µm and line pitches of 80-95µm, depending on the desired thickness, to obtain pyrolized layers with good performances. This methodology can also be used in combinatorial studies, as it will be shown on the next section.

4.4 In-situ characterization of the pyrolysis process by advanced thermal analysis

Since for this new solution (FF-E3) the optimal pyrolysis profile was already determined in such discrete deposition methodology, by obtaining thick films with no structural defects such as delamination or cracks, the objective in this section is to undertake a thorough analysis to determine the different stages of the pyrolysis, regarding the sequential decomposition of the precursor salts, to know the range of temperatures in which a specific precursor or additive is decomposed.

4.4.1 In-situ analysis of the decomposition pathways

To fully disclose the decomposition pathway, described at the beginning of the chapter, we will use different in-situ characterization techniques to monitor and determine the mass evolution as well as evolved volatiles during the pyrolysis process: thermogravimetric analysis (TGA) for the mass evolution and Evolved Gas Analysis (EGA) to determine the volatiles released during the pyrolysis, together with FTIR analysis of quenches. These measurements were performed using films which were deposited by drop coating, utilizing our optimized precursor solution with ethanolamine (2%vol. EA or FF-E3) and without it (FF-E0). We expect to determine the major decomposition steps of the reaction and the effects that ethanolamine has over it.

The deposition homogeneity may differ from the inkjet printing deposited films, since the kinetics depends on the morphology and sample thickness. The kinetic results obtained from drop casted films may slightly differ from the actual kinetics of films obtained from inkjet printing. The films may also absorb water, from the ambient atmosphere, which is not so much controlled as in a clean room environment. If the water mass is not properly considered, it can lead to errors on the weighted mass, or unexpected chemical transformations due to the hygroscopic nature of the solution.

4.4.1.1 Thermogravimetric analysis (TGA) of the precursor solution

The TG curves are normalized to the mass of the dried film. The mass of the dried film is obtained from the EGA analysis; from the volatiles we determine the temperature at which the evaporation of solvents and water ends. For a dried film, the expected final mass when the propionate precursor salts decompose to form CuO, Y_2O_3 and $BaCO_3$ is 47.5% (43.8% if a 2% EA was added). In Fig. 4.18 we have plotted the expected final mass as a horizontal dashed line and we can see that at 500ºC the final mass approaches the expected one. From the dTG curves we observe that the first stage is more intense than the second one, indicating a major organic mass decomposition rate.

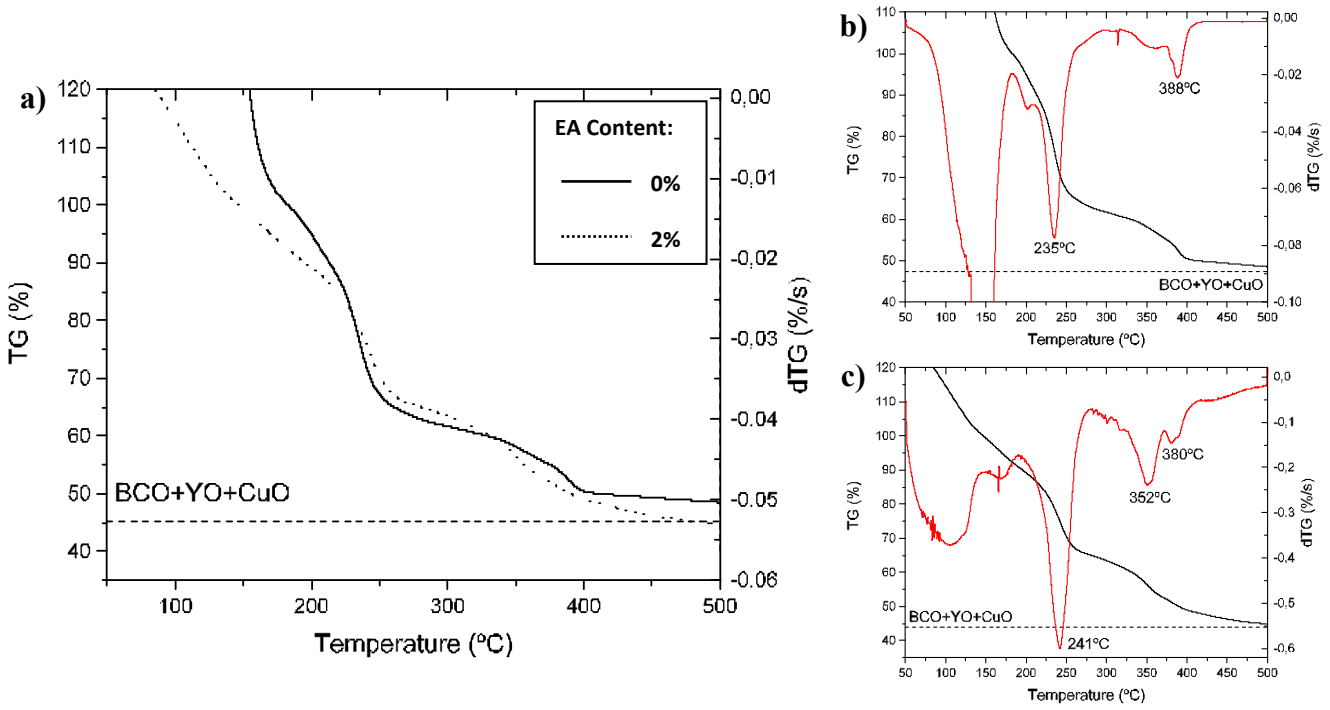

Figure 4.21. *(a) TGA comparison of a precursor solution with no additives vs. 2%EA. (b) DTG+TG of the precursor solution with no additives. (c) DTG+TG of the precursor solution with 2%EA.*

This analysis shows similar results for all the precursor solutions (FF-E0 and FF-E3), but with some variations on the temperature of the salts decomposition. From the TG curve (Fig. 4.18) we observe a continuous mass loss from 100°C until 410°C. The mass lost before 180°C corresponds mainly to the solvent and absorbed water evaporation. From the time derivative of the TG curve, we obtain the dTG curve, related to the decomposition rate. From the dTG curve we observe three main stages. The first one centred at 150ºC corresponds to solvent evaporation, a second one with a peak temperature at 240°C is mostly related to propionate decomposition. The third, with two peaks, starting at 300°C with a maximum at 390°C is mostly related to the decomposition intermediate oxycarbonates and ethanolamine.

Below 290ºC there are no significant differences between both precursor solutions (FF-E0 vs. FF-E3), the only difference is that the sample with no additives shows a more pronounced dTG peak at low temperature. This more pronounced peak indicates that a large amount of solvent evolves at low temperature, the reason being that the film is thicker and the drying step was shorter. Therefore, at lower temperature and shorter time, the solvent removal is lower, so more solvent is evolved during the early stages of the TG measurement.

Above 300ºC there are relevant differences between the films, that are probably related to the presence of the EA additive. Above this temperature there are two peaks at 351ºC and 390ºC that are related to the decomposition of propionates and inorganic intermediates (i.e., yttrium oxycarbonate), releasing CO_2 above 350ºC up to 450ºC [**134, 168**]. The presence of EA may alter the formation of these intermediate compounds and thus the release of CO_2. From the previous Figure 4.18 we can see that with 2% of EA dominates the process at lower temperature, so most CO_2 evolves around 351ºC, while with 0% EA, most CO_2 evolves around 390ºC.

The sample with 0% EA shows by far the lowest decomposition at 351ºC, resulting in a very broad peak in contrast to the inclusion of EA as additive. These differences in the dTG of the samples are an indication that EA is indeed acting as a chelating agent, thus modifying both the reaction pathways and the microstructure of the films, in terms of physical and chemical properties.

During the pyrolysis of the precursors CO is formed, and as a result, copper oxide may reduce to form Cu_2O or even metallic copper. We have observed that the amount of EA affects the reduction of copper. Indeed, the amount of Cu_2O is reduced when a proper amount of EA is added into the solution. The amount of EA affects the formation of Cu_2O in two different ways.

On one hand, EA has an effect on the morphology, the higher the amount of EA the lower the porosity. A more compact film reduces the gas transport making the CO removal and the incorporation of O_2 more difficult, therefore enhancing copper reduction. In addition, crack formation is inhibited so gas renewal is further impeded. In very thick films such in the inkjet printed ones, limitations in the gas transport during pyrolysis creates local atmospheres within the bulk of the film, so that Cu (II) species reduce to Cu (I) and Cu (0) counterparts [**171-172**].

On the other hand, the presence of an amine reduces CO formation, thus copper reduction is hindered; in a ternary solution without additives under humid O_2 atmosphere, Rasi et al [**133**] observed the formation of Cu reduced species, such as Cu_2O and Cu, around 300ºC, which further re-oxidizes to form CuO. With the addition of amines, an intermediate ester is formed [**155**], and the amount of Cu_2O is significantly smaller when compared to the solution without additives. Thus, it seems that a larger amount of EA reduces the amount of CO released above 350ºC. It has been found that in inert atmosphere Cu reduction is prevented; in inert atmosphere the formation of an ester may be the reason why oxygen remains to form CuO.

Conversely, in oxidative atmospheres the decomposition of yttrium propionate is shifted down, so it happens before the decomposition of EA and as a result, the copper oxide reduces around 250ºC, coinciding with the first stages of yttrium propionate decomposition (carbon monoxide (CO) is formed during the decomposition of propionates as a by-product).

4.4.1.2 Ex-situ FTIR analysis of quenches

At low temperature the stable $BaCO_3$ phase is the orthorhombic one. However, the reduction of copper results in the formation of monoclinic $BaCO_3$ [**173**]. To analyse the formation of monoclinic $BaCO_3$ we have performed different quenches at selected decomposition stages. Then, the quenched samples are analysed by FTIR to determine the solid phases. We have performed a series of quenches (150, 300, 350 and 380ºC) of the sample with a 2% of EA to check the formation of copper, coper oxides and phases of barium carbonate.

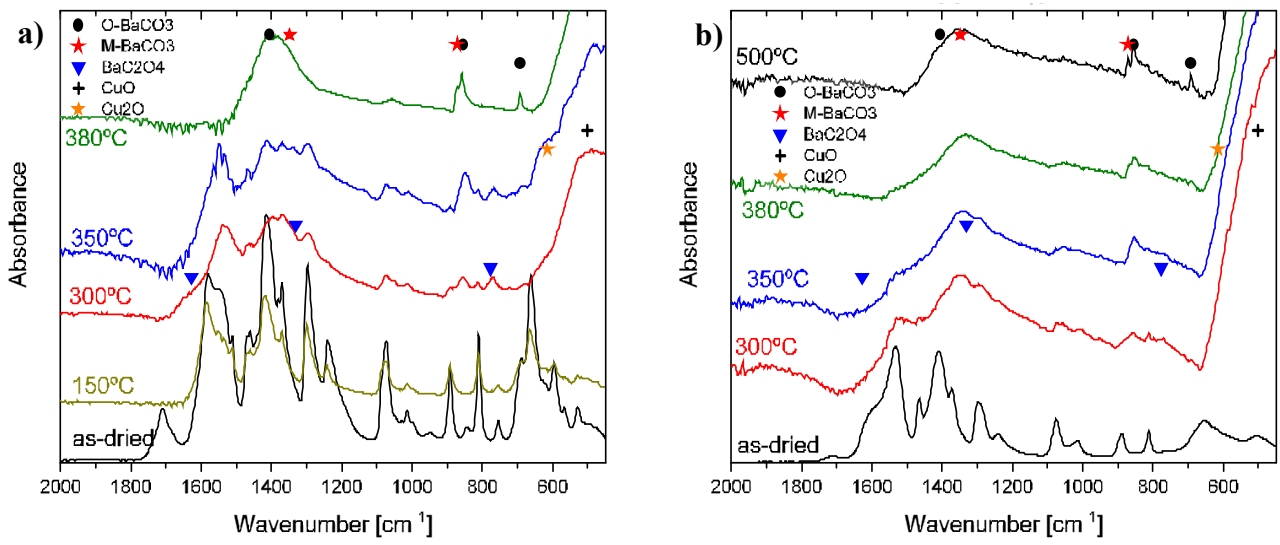

Figure 4.22. *FTIR analysis of quenches at room T, 150ºC, 300ºC, 350ºC and 380ºC for (a) Precursor solution with no additives (FF-E0). (b) Precursor solution with 2%EA (FF-E3).*

It seems that when the amount of EA is incremented, the decomposition of yttrium and barium propionates is enhanced, at 350ºC less organic fraction remains when a 2% of EA is present. When no EA is added only CuO is observed at 300ºC but at 350ºC a significant amount of Cu_2O is formed. The formation of Cu_2O is related to the decomposition of yttrium and barium propionates. Conversely when a 2% of EA is added, decomposition of yttrium propionate is advanced and Cu_2O is already present at 300ºC together with CuO. However, in both cases at 500ºC Cu and Cu_2O are oxidized and only CuO is observed (see Chapter 4.3).

We also observe that, in both samples, the formation of Cu_2O is linked to the formation of monoclinic $BaCO_3$. This can be clearly seen for the 2%EA sample, at 350ºC and 380ºC we observe the presence of Cu_2O and $BaCO_3$, and more interestingly most $BaCO_3$ is in the form of the monoclinic phase. Afterwards, at 500ºC we observe both phases monoclinic and orthorhombic $BaCO_3$.

Thus, around 350ºC when copper reduces barium carbonate crystallizes as monoclinic, at higher temperatures Cu oxidizes to form CuO and the stable monoclinic $BaCO_3$ phase is also formed. Eventually, at 500ºC both monoclinic and orthorhombic phases coexist. Since FTIR is not a quantitative technique is hard to tell which sample has a larger amount of monoclinic $BaCO_3$, still it can be seen that relatively similar amounts of monoclinic $BaCO_3$ are obtained for the samples with 0% and 2% of EA.

As an interesting feature, the formation of different intermediates while using EA enhances the overlapping of the different decomposition stages, thus, preventing the segregation of the final products. Such behaviour has also been observed in the usage of other amine additives [**155**], so it seems that the use of chelating or coordinating agents minimizes phase segregation.

4.4.1.3 In-situ Evolved Gas Analysis (EGA) of the decomposition reactions

In addition, coupled to TGA, FTIR Evolved Gas Analysis (EGA) was also performed. In-situ EGA is used to identify the volatiles evolved when the mass of the sample diminishes, in our case to identify the volatiles evolved during film dehydration, solvent evaporation and during thermal decomposition.

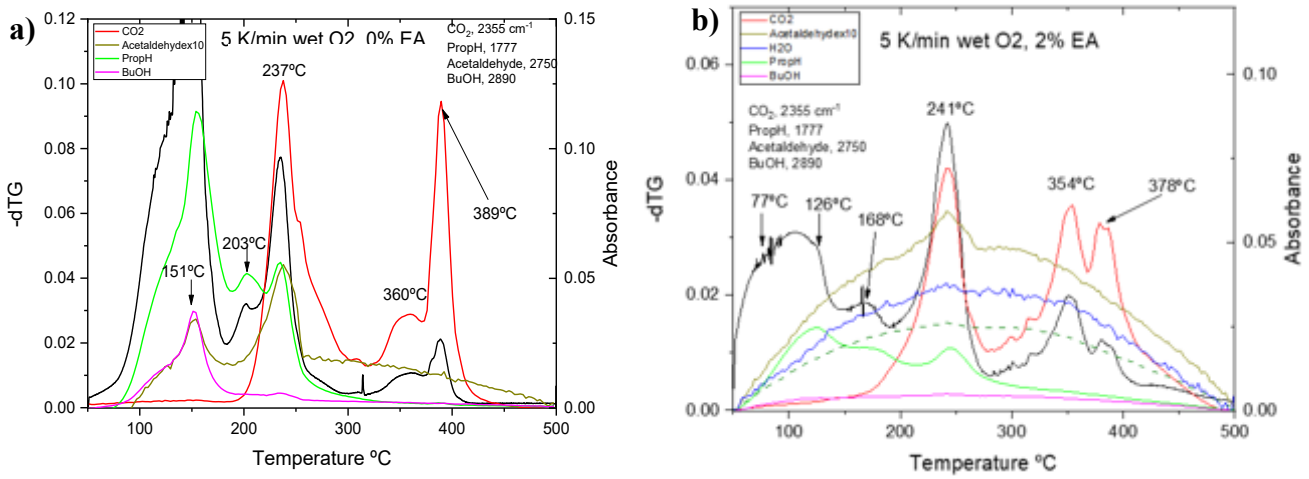

Figure 4.23. *FTIR-EGA of (a) Precursor solution with no additives. (b) Precursor solution with 2%EA.*

The EGA analysis without additives or with 2% (Fig. 4.20) shows the next results:

- A broad peak, with a maximum at 151ºC is observed. This peak is related to solvent evaporation, as we already mentioned from TGA curves. The main volatiles observed are propionic acid and BuOH, the solvents used in the preparation of the solution. Little amount of water is released, indicating either low water absorption during solution preparation or that water is efficiently removed during film drying.

- From 160°C to 275ºC, a first decomposition peak appears, with two maximums at 203ºC and 237°C, respectively. At 203ºC we observe the formation of propionic acid resulting from the hydrolysis of copper propionate, reaction (4.3).

At 237ºC we observe acetaldehyde, water and CO_2, volatiles formed during the reaction of Copper and Barium propionates with oxygen, reactions (4.4 & 4.7). We also observe the formation of propionic acid that can be attribute to the decomposition of yttrium propionate, reactions (4.5 & 4.6).

- From 300°C to 410ºC, two decomposition peak are detected, with a maximum at 360ºC and 389ºC, respectively. The main volatiles detected at this last stage of the decomposition are CO_2 and water. They are related to the decomposition of intermediates, such as yttrium oxycarbonate, reaction (4.8) and of the complete oxidation of the remaining organic moieties.

- From 410ºC to 500ºC, there are no more dTG-DSC peaks, indicating that the decomposition of the metalorganic precursors has been finished.

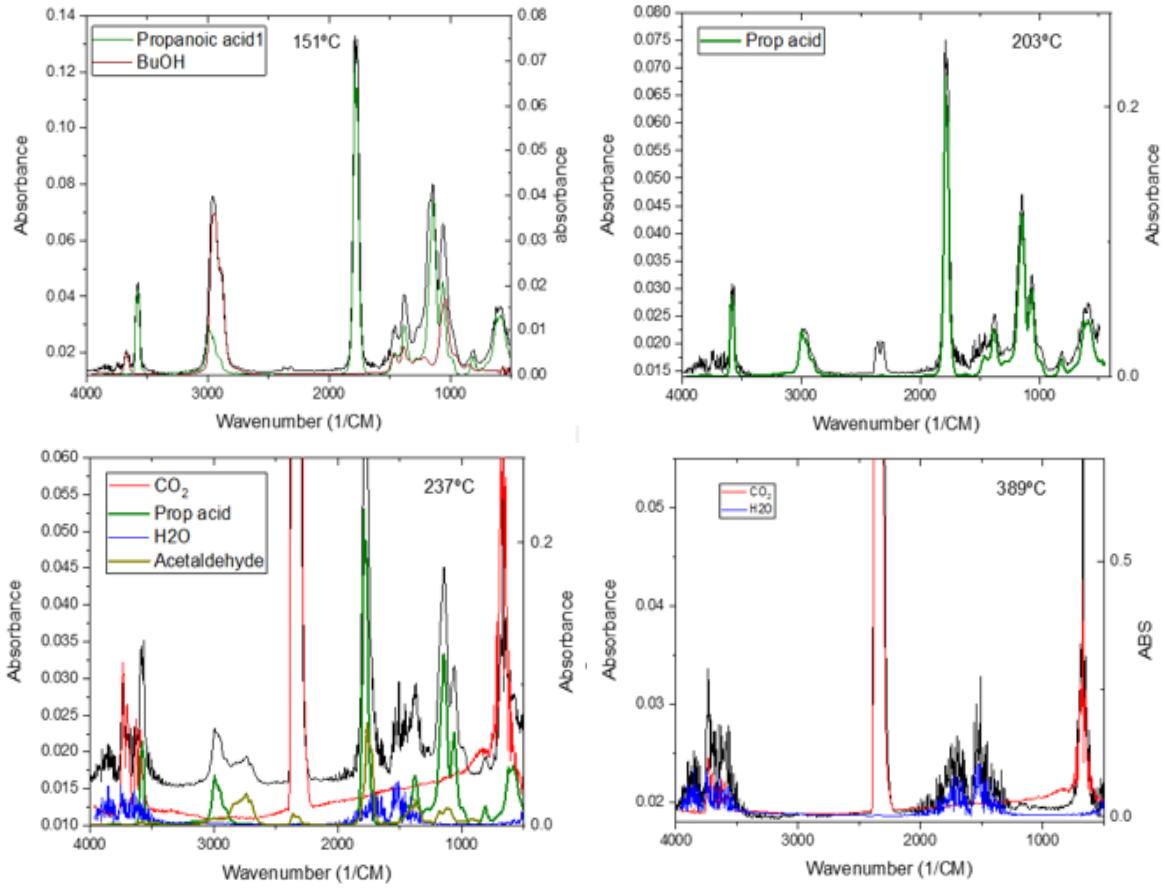

Figure 4.24. *FTIR-EGA of FF-E3 precursor solution at different stages of the pyrolysis: a) 151ºC, b) 203ºC, c) 237ºC and d) 389ºC.*

4.4.2 Summary on Thermal Analysis

When ethanolamine additive is added in the solution, the separation of the with two intense peaks at 354ºC and 378ºC, respectively, became more pronounced. This imply that ethanolamine is increasing the decomposition rate of the molecules at lower temperatures. Our assumption is that EA, acting as a chelating agent is able to bind to the metals, displacing some propionate moieties, to change the transformations of the metal intermediates, thus inhibiting phase segregation and CO_2 release at the end of the pyrolysis synthetic route. From the analysis of the released gases, we were able to define the mass evolution during the pyrolysis stage in two zones around 160-270°C and 300-400°C.

These zones properly match with the ones observed in the in-situ imaging of the pyrolyzer study (see chapter 3), being the first zone the decomposition of propionates and the highest mass loss that occur to the film, related to the formation of defects such as cracks. While the second zone being related to the decomposition of intermediates and the possible appearance of pores due the release of CO_2 at higher temperatures. In general terms our pyrolysis profile, under wet oxygen flow (120 mL/min) to avoid sublimation of copper species, can be described as follows:

1. From 25ºC to 180ºC at 5 ºC/min. At stage, only solvent evaporation occurs as it is shown in section 4.4.1.

2. From 180ºC up to 300ºC the mass evolution is dominated by the decomposition of the precursors. At 180ºC the end of evaporation overlaps with the onset of Cu propionate decomposition. As it is shown in section 4.4.1, around 200ºC we reach the maximum of the decomposition of copper. Two different mechanisms are involved in the decomposition of copper propionate [**133**]. As it is shown in section 4.4.1, at low temperature (around 200°C) the dominating mechanism is hydrolysis:

$$Cu(CH_3CH_2COO)_2 \xrightarrow{H_2O} CuO + 2\,CH_3CH_2COOH \qquad (4.3)$$

While at higher temperature (around 210ºC) the mechanism that dominates copper propionate decomposition is the reaction of the precursor with O_2:

$$Cu(CH_3CH_2COO)_2 \xrightarrow{2O_2} CuO + 2CH_3COH + H_2O + 2CO_2 \quad (4.4)$$

At around 250°C we have the maximum mass loss rate related to the end of the decomposition of copper propionate together with the main decomposition of yttrium and barium propionates, i.e., the greatest removal of organic moieties takes place around 240ºC (see section 4.4.1). At this temperature occurs the main stress relief mechanisms occur, as at these temperatures the greatest mass loss and shrinkage of the film volume takes place [**94**]. Thus, around 240ºC the major stress-relief mechanisms such as crack formation may occur. For this reason, 5ºC/min seems an appropriate heating ramp, in a compromise between being fast enough to avoid aggregation, but not so fast to induce delamination of the films.

Two mechanisms compete for the decomposition of yttrium propionate. At low temperature, the hydrolysis of yttrium propionate was detected to be the main decomposition mechanism [**134**]:

$$2\,Y(CH_3CH_2COO)_3 \xrightarrow{H_2O} Y_2O_3 + 6\,CH_3CH_2COOH \quad (4.5)$$

While at higher temperature the reaction with oxygen is the main mechanisms to yield yttrium oxycarbonate:

$$2\,Y(CH_3CH_2COO)_3 \xrightarrow{O_2} Y_2O_2CO_3 + 3\,CH_3CH_2COOH + 3\,CH_3COH + 2\,CO_2 \quad (4.6)$$

Finally, oxidation is the main mechanism for the decomposition of barium propionate to yield barium carbonate [**132**]:

$$Ba(CH_3CH_2COO)_2 \xrightarrow{O_2} BaCO_3 + 2\,CH_3COH + CO_2 + H_2O \quad (4.7)$$

3. Finally, from 300ºC to 500ºC the correspondent intermediate species start decomposing too [**134, 168**]. At these temperatures yttrium oxycarbonate was observed to decompose to form yttrium oxide:

$$Y_2O_2CO_3 \rightarrow Y_2O_3 + CO_2 \quad (4.8)$$

As a conclusion, there has to be a proper compensation of the EA amount added in the solution. In high amounts, EA could act as a reducing agent, by both the reductor nature of the amine groups as well as the formation of CO during its decomposition, regarding the reduction of CuO species. Whereas if a proper amount of EA is added, copper is able to re-oxidize again at higher temperatures.

EA also inhibits the transformations of some intermediate phases, reducing the amount of CO_2 released above 350ºC. On the other hand, EA is able to minimize phase segregation and decrease film porosity, one important feature that increase the superconducting performance films.

The usage of EA as an additive for fluorine-free propionate-based solutions seems adequate in some cases, if an appropriate amount is properly fine-tuned. Amine additives, and specifically ethanolamine, will further help on the pyrolysis of thick films prepared thorough the IJP-CSD methodology presented throughout this thesis.

4.5 Combinatorial Chemistry: a case study for DoD IJP

Combinatorial chemistry approaches are pushing forward for the development of inorganic functional materials. The strategy relies on the fabrication of large arrays of samples that are treated together or individually and characterized, allowing a faster evaluation of the processing parameters. The produced data is stored on large relational databases that can be later analysed using computational methods to find the optimal compositions and processing conditions.

Combinatorial chemistry approaches allow to speed up the discovery of materials and focus on the interpretation of the best possible outcome results. Nowadays, this strategy is starting to flourish, thanks to the development of data-driven methods based on big data analysis tools, machine learning algorithms, and other computational methods. High-throughput experimentation (HTE) strategies, based on the combinatorial chemistry approach, are currently being researched in many diverse fields such as solar cells, lithium-ion batteries, electronics, water splitting and superconductivity [**174-176**].

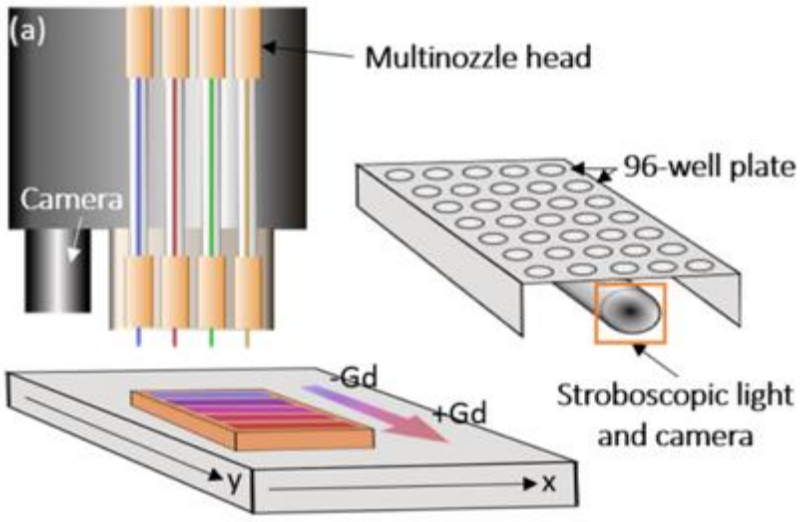

Figure 4.25. *(a) DoD IJP setup, consisting of a 96-well plate array, a multinozzle head with four independent nozzles (two are used in our experiments), a stroboscopic light/ camera for drop inspection, and a camera for surface inspection [**166**].*

From several deposition techniques available for the assembly of combinatorial test pieces, drop-on-demand inkjet printing appears as an ideal technique, since it allows the fabrication of complex-shaped samples suitable for high-throughput measurements, thanks to the development of uniform and graded compositions. In this particular case, the Slow Mode present on our inkjet printer system allow for the deposition of more than one precursor solution at the same time, making it interesting for these studies.

Despite the good properties exhibited, the exploration of rare-earth (RE) metals other than Yttrium to produce superconductor REBCO films has acquired much interest in recent years specially regarding the mixing of different RE metals, such as in the case of Y/Gd, to stablish the suitable stoichiometry combinations to find the best superconducting properties. For instance, values of $J_c > 7$ MA cm^{-2} (77 K, B = self-field, on STO) have been reported for $Y_{0.77}Gd_{0.33}Ba_{1.5}Cu_3O_{7-x}$ [**177-182**].

In this case, a combinatorial chemistry approach using ink jet printing is a very appealing strategy to mix different REBCO precursor solutions. In our case, the two prepared solutions account for YBCO and GdBCO precursor solutions. Additionally, this approach may contribute to the full disclosure of optimal processing conditions for our TLAG-CSD method. Specially, by exploring the non-equilibrium kinetic phase diagram of REBCO films, contributing to the understanding of the kinetic influence of the growth process for the different compositions and eventually, leading to the optimal growth rates and functional properties of superconducting coated conductors.

4.5.1 Combinatorial Chemistry Stripes Deposition

Drop positions and solution mixing upon deposition, are key parameters to define combinatorial patterns. In our case, we selected a set of five equally separated stripes of different compositions, starting from fully YBCO stripes up to fully GdBCO stripes and its various combinations, being $Y_{1-x}Gd_xBa_2Cu_3O_7$. The precursor solution used was the optimized for full YBCO films, being 1M+2%EA (FF-E3).

The validation of the composition homogeneity within one stripe is essential to demonstrate the capabilities of stoichiometry tuning. The (x,y) coordinates were automatically generated using a self-made Python interface, which allowed us to find a suitable deposition matrixes for the stripes, computing its proper drop overlapping. Nevertheless, we already set the best possible combinations for the Slow Mode available in our inkjet printer system, based on the drop and line merging studies already made, and we performed the deposition of stripes based on the best drop overlapping found, that is a drop pitch of 50µm.

Thanks to the prior film homogeneity and pyrolysis studies, the use of ethanolamine together with the slow deposition rate of the Slow Mode, crack-free homogenous stripes in different metal composition were easily obtained in a reproducible way. The visual representation of the printing positions and drop overlapping, considering a drop diameter of 240µm and a grid size of 50×95µm is found in Figure 4.26.

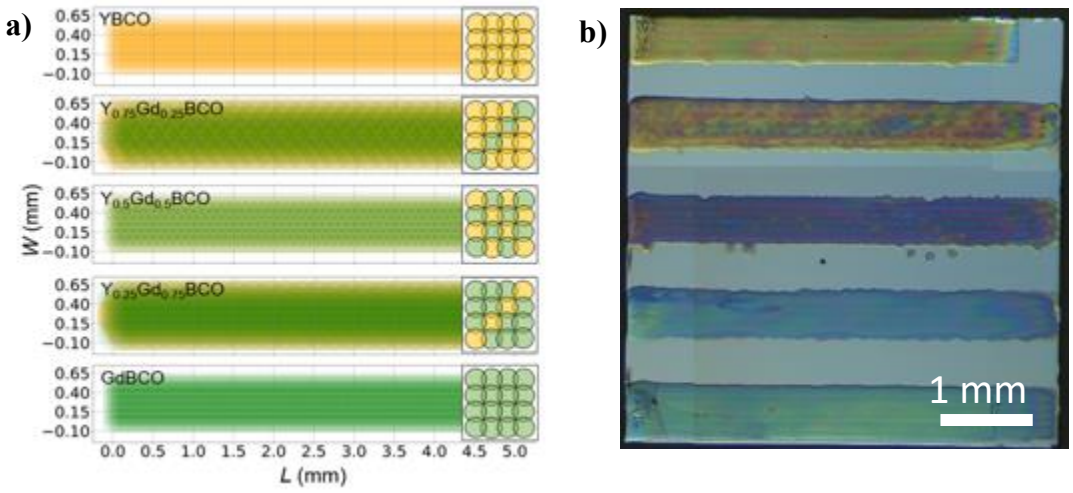

Figure 4.26. *(a) Plots that illustrate the printed patterns for $Y_{1-x}Gd_xBa_2Cu_3O_7$ composition ratios of (1) x = 0, (2) 0.25, (3) 0.5, (4) 0.75, and (5) 1, with a grid size of 50×95µm. The graphs on the right side show the drop alternation between the two inks, being yellow and green the drops of the two different solutions used. (b) Crack-free pyrolized stripes made with the patterns designed. The solution used was FF-E3.*

4.5.2 $Y_{1-x}Gd_xBa_2Cu_3O_7$ deposited stripes characterization

The homogeneity of combinatorial $Y_{1-x}Gd_xBa_2Cu_3O_7$ samples was designed with computational methods and confirmed by profilometry measurements. We reveal the advantages of this strategy in the optimization of the epitaxial growth of high-temperature REBCO superconducting films using the novel transient liquid-assisted growth method (TLAG) by evaluating the composition of combinatorial samples by energy-dispersive X-ray spectroscopy (EDX) and X-ray diffraction.

Profilometry measurements have shown a homogenous deposition, where inhomogenities do not appear on the surface. Very low roughness, as stated in the RMS values, are achieved after the pyrolysis of the stripes. Profilometer measurements of the thickness shown an average thickness of 750-600 nm. in one single deposition, with much higher values if compared to samples using other related CSD methods, which in turn can help to reduce noise on other characterization techniques. Although thicker values could be designed, the aim of this study to obtain different metal stoichiometry.

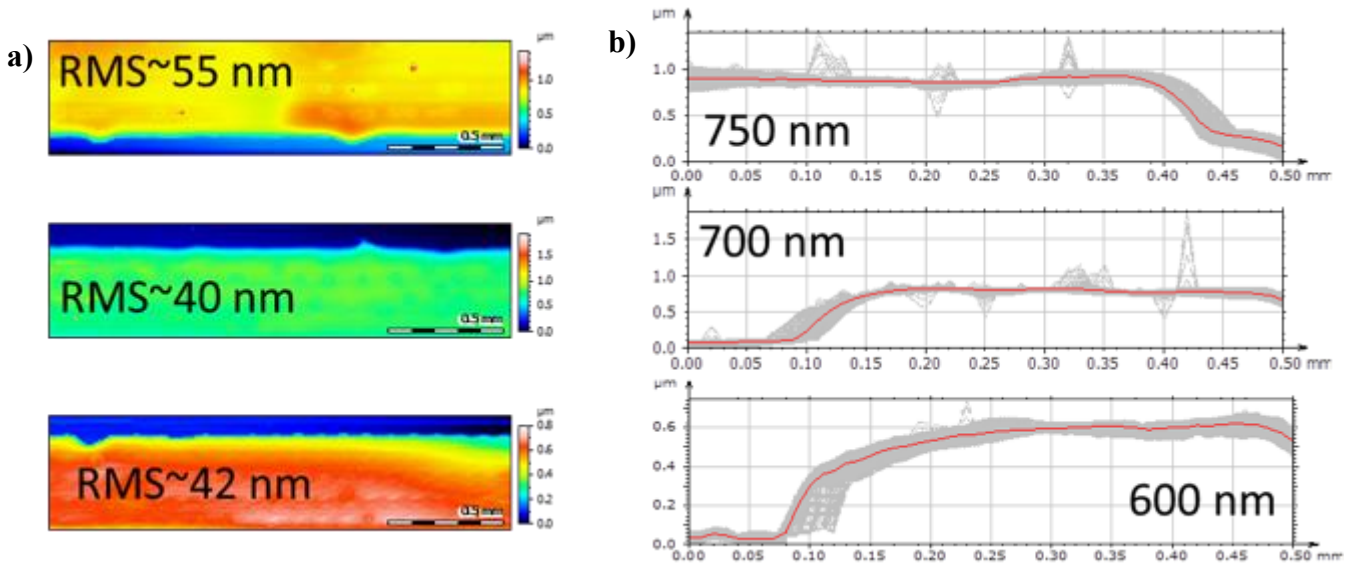

Figure 4.27. *(a) RMS values obtained on the printed patterns for $Y_{1-x}Gd_xBa_2Cu_3O_7$ with a grid size of 50×95µm. (b) Profilometer thickness measurements of the crack-free pyrolized patterned stripes.*

In our study, we used EDX for several combinatorial samples to evaluate the composition accuracy of each stripe and validate the Slow Mode approach. The elemental analysis performed by EDX of a typical area of approximately 250×250µm, where the acquisition was conducted for each stripe, in stripes with $Y_{1-x}Gd_xBa_2Cu_3O_7$ compositions of x from 0 to 1. Figure 4.28 shows the EDX elemental analysis and SEM images of selected areas from stripes with $Y_{1-x}Gd_xBa_2Cu_3O_7$ compositions of x = 0.5 as an example. After measurement of several stripes, we performed a statistical analysis that shows the average values obtained and their standard deviation for each theoretical desired composition.

Focusing on compositions with different percentages of $Y_{1-x}Gd_xBCO$ inks, we confirm on samples annealed though the TLAG method, that the desired composition values and measured ones do not deviate much from each other. Nevertheless, there is a slightly large dispersion of values with a maximum variation of ±15% for different samples with $Y_{0.5}Gd_{0.5}BCO$, which might be influenced by the fact that growth at 50/50 was the most complicated over the full range explored.

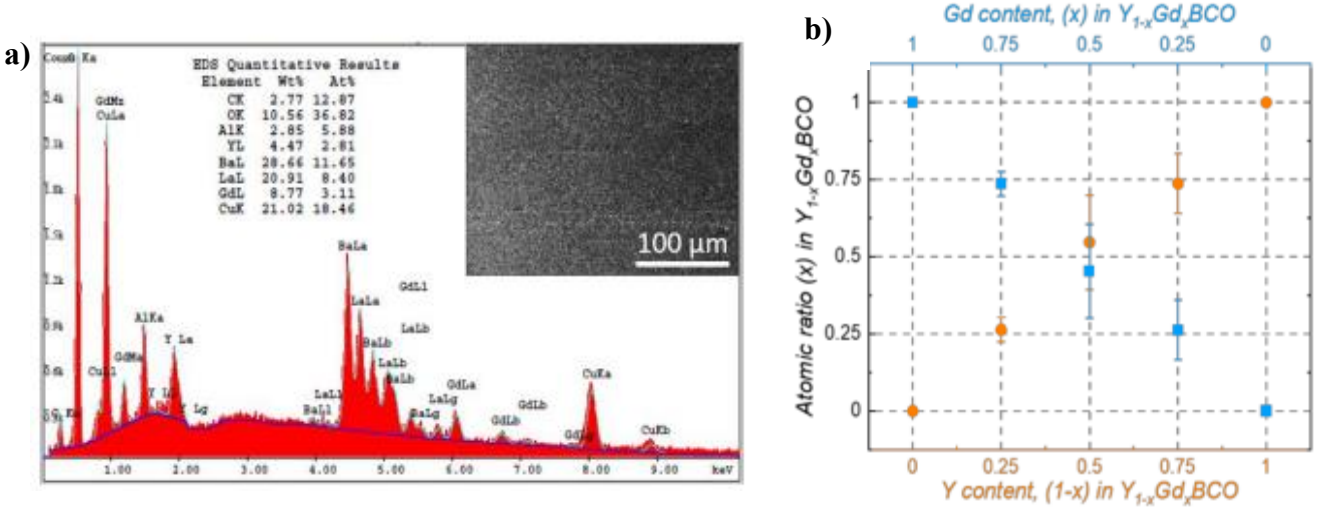

Figure 4.28. *(a) EDX elemental analysis and SEM images of selected areas from stripes. (b) Statistical analysis with the average values for composition.*

4.5.3 Combinatorial chemistry outlook

The potential of combinatorial and high-throughput experimentation, for a fast identification of the experimental conditions, to grow different compositions by the TLAG-CSD approach was demonstrated. Drop-on-demand inkjet printing was successfully used to deposit combinatorial samples in the form of stripes of different composition, obtaining a homogeneous surface distribution during the pyrolysis step after the optimization of the ink composition and printing positions.

The desired compositions could be successfully implemented and confirmed through the combined use of computational methods and characterization techniques such as EDX, as evidenced by elemental rare earth ratio. The results obtained are being used by other members of the group for the fabrication of continuous compositional gradients. This should enhance the mapping of the best growth conditions, by a faster screening of functional properties, the construction of libraries, that could include other RE ions or liquid composition changes, as well as the implementation of machine learning algorithms for a swift and smart optimization of TLAG-CSD REBCO film growth [**167**].

Moreover, the methodology developed here may be extended to many different functional materials with different needs of fast screening and optimization. Combinatorial screening will also help on new design strategies of novel material based on “big data” (i.e., data-driven approach), aiming not only to accelerate the innovation throughput in the field of superconducting films and coated conductors, but also in other fields of materials science.

4.6 Conclusions on the Inkjet Printing Discrete Mode

The Slow Mode available at the MicroDrop Inkjet Printer system has shown its competitiveness as a possible Chemical Solution Deposition method for the preparation of YBCO thick films with homogeneous pyrolysis, upon its proper optimization for the TLAG-CSD methodology. As a drawback, the slow deposition mode has very large deposition times, even up to 2 hours for deposition of 5x5 mm^2 films due to the discrete deposition and the movement of the nozzles, which may be difficult to implement at reel-to-reel industrial processes. However, this technique has demonstrated very promising and appealing results for lab-scale and combinatorial chemistry studies.

The Slow Mode rely on the deposition of a determined number of drops for each specified position on the substrate. The positions of each nozzle and its associated deposited drop is determined by a Python coordination file that allow us to obtain homogenous depositions once properly optimized. We have used the drop volume and the drop impact dimeter to calculate the degree of overlapping of drops and lines to select the adequate deposition matrixes to obtain homogenous films.

Through these studies, Fluorine-Free precursor solutions based on propionate salts and ethanolamine as additive were investigated for the deposition of YBCO precursor films by inkjet deposition. The rheology of the solutions with different %vol. of ethanolamine was thoroughly studied in order to obtain the most stable composition for inkjet printing, to achieve the most homogenous films as possible and to avoid nozzle clogging or drop formation inhibition based on its Z numbers. The driving waveform of the inkjet piezoelectric actuator was adapted to the solution parameters, achieving stable and reproducible drops in all solutions with an EA content up to 2%v/v (FF-E3). Higher EA values however, resulted on the inhibition of the drop formation due to its very high viscosity nature.

A solution with 50%v/v butanol and 50%v/v of propionic acid is presented as effective ink composition to obtain enhanced homogeneity in the thick film deposition by inkjet printing. The solution concentration was kept at 1M in order to deposit fewer liquid volumes, enhancing the evaporation rate of the films while showing full coverage on single crystals.

During the decomposition of the metal precursors, ethanolamine influences the densification of the films, achieving a dense microstructure after pyrolysis. No cracks are observed after the thermal treatment. More specifically, by using a specific drop and line pitches together with a 2%$_{v/v}$ of ethanolamine (FF-E3), we could achieve reproducible and homogenous depositions while avoiding crack formation.

Based on the profilometry measurements made on the pyrolized samples, we have shown a linear relationship between the total deposited volume and the final thickness after pyrolysis for each sample. In addition, we found that by using a deposition matrix of 50x85µm, we can obtain thick and homogenous depositions in a reproducible way for films around 1000 nm after pyrolysis.

From our understanding, the deposition of chemical solutions at very slow deposition rates allows the solution to pin better into the substrate thanks to solvent evaporation. Once the deposited drops are allowed to evaporate the solvents, the resultant gel-like fluid is pinned into the substrate while is merging with the other surrounding drops. Once a fully printed line is deposited, the next printed line is able to merge without liquid redistribution, allowing for a homogenous deposition without liquid movement and accumulation on the edges.

Our observation is then, that the evaporation rate is critical for the homogeneous dispersion of the liquid, avoid liquid dragging to obtain crack free layers. In this case the use of ethanolamine as additive does not only ensure a stable, robust precursor solution being able to jet drops continuously but also helps during the pyrolysis process.

If the appropriate amount of ethanolamine is fine-tuned, it could minimize phase segregation and decrease film porosity. Excessive amounts of EA can act as a reducing agent, however, if properly controlled, EA acts as a chelating agent, binding to the metals while displacing some propionate moieties. It changes the transformations of the metal intermediates during decomposition, inhibiting phase segregation of the Cu species and CO_2 release at the end of the pyrolysis synthetic route. As a direct outcome, it is avoiding crack formation after most of the propionate moieties have already decompose, which is the most critical part of the process.

Finally, to achieve thick homogenous layers, our assumption also relies on the specific plate velocity of the Slow Mode. However, due to the slow deposition rate of the mode, further implementation to industrial scale of this technique and the achievement of very thick films is limited. We expect that by using ethanolamine at faster rates of deposition thick films production can also be achieved, as seen in the next chapter 5.

In addition, the potential of combinatorial and high-throughput experimentation for a fast identification of the experimental conditions to grow different compositions by the TLAG-CSD approach can be demonstrated. Drop-on-demand inkjet printing was successfully used to deposit combinatorial samples in the form of stripes of different composition, obtaining a homogeneous surface distribution during the pyrolysis step, once the optimization of the ink composition and printing positions have been performed. The compositions were confirmed through the combined use of computational methods and characterization techniques such as EDX, as evidenced by elemental rare earth ratio. The results obtained are being used by other members of the group for the fabrication of continuous compositional gradients. This should enable enhanced mapping of growth conditions and faster screening of functional properties for a swift and smart optimization of TLAG-CSD REBCO film growth, with much potential for other applications.

5.

Fast Mode Inkjet Printing deposition of Thick YBCO Films using Fluorine-Free Solutions with Ethanolamine additive

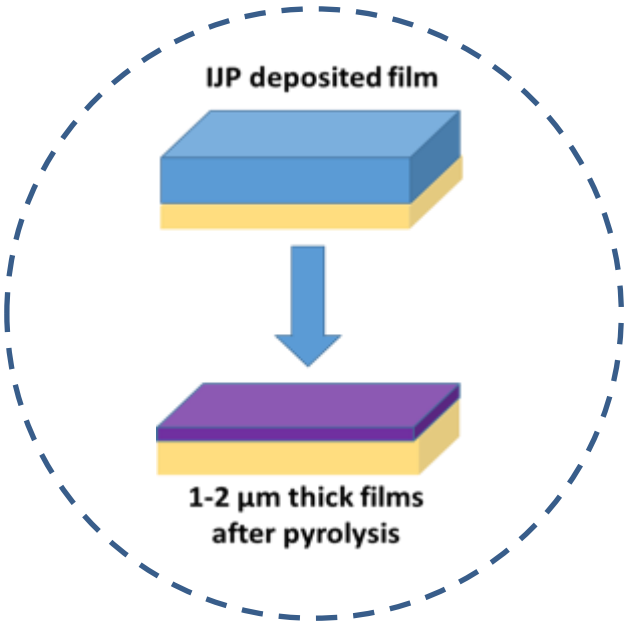

In this chapter, we present a more continuous Drop-on-demand deposition modality, or Fast Mode, of the inkjet printing system from Microdrop Technologies GmbH, which resembles more to the deposition procedure of the homemade inkjet printing system of chapter 3. We will present the preparation of homogenous deposited layers on both single crystals and metallic substrates. We will evaluate the optimized precursor solution FF-E3 used in the above chapter 4, while using faster deposition rates. We will discuss the effect of solvent evaporation by performing depositions with substrate heating, and we will validate the method by fabricating YBCO layers by means of TLAG for thick films in the range of 1µm.

5.1 Introduction to MicroDrop Fast Mode

The MicroDrop IJP also accounts for a continuous drop-on-demand deposition, or Fast Mode, which behave very similarly to the homemade inkjet printer system of Chapter 3. This mode of deposition relies on the deposition of predefined patterns by using one single nozzle. By selecting the appropriate deposition matrix in the software, i.e., the drop and line pitches (XxY μm), together with the number of points required in both X and Y direction (total nº of drops), computing the total deposited surface (mm^2), the software automatically set the parameters such as the frequency of ejection required for the deposition of one single drop in each specified point value of the desired pattern. We will perform depositions on both 5x5 mm^2, 10x5 mm^2 LAO and STO single crystal substrates, but also on 6x6 and 10x20 mm^2 metallic substrates from SUNAM, with a buffer layer of LSMO. We will also discuss multifilamentary depositions.

In this case, the motorized platform moves in two perpendicular axes, similarly to the homemade inkjet printer previously used in Chapter 3. However, it also has the possibility to change the plate velocity from 0.5 mm/s to 10 mm/s. In contrast to the deposition rate of Data Grid mode (0.21 mm^2/min), the deposition rate of the continuous mode spans from 0,84 mm^2/min up to more than 1,68 mm^2/min, by which the time required to prepare a 5x5 mm^2 film is reduced down to less than 30 min.

For the fast mode deposition of thick films, we have used the same precursor solution designed for the Slow Mode of chapter 4, that is a 1M of Y, Ba propionate, Cu-acetate precursors in a 50/50 propionic acid/1-butanol solution with a 3:7 stoichiometry and 2%vol. ethanolamine (FF-E3). Therefore, we expect a similar behaviour in terms of jetting. However, since the rate of deposition is much faster than the other deposition mode, we expect that the deposited solution will behave differently in terms of solvent evaporation, which can modify the liquid distribution and pyrolysis outcome.

Since the deposition rate of the continuous mode is much faster, in contrast to the discrete mode, the depositions matrixes used to obtain homogenous depositions will have to be modified. From the results obtained in Chapter 4, we concluded that if the solvent evaporation rate is high enough there is a better pinning of the liquid onto the substrate, avoiding liquid movement.

Therefore, we expect to change the drop and line pitches in this deposition mode, to allow for the best solvent evaporation rate to better pin the liquid, avoiding liquid accumulation on the edges. In fact, if the grids optimized in chapter 4 are used, liquid accumulation occurs leading to huge inhomogenities as shown in Figure 5.1.

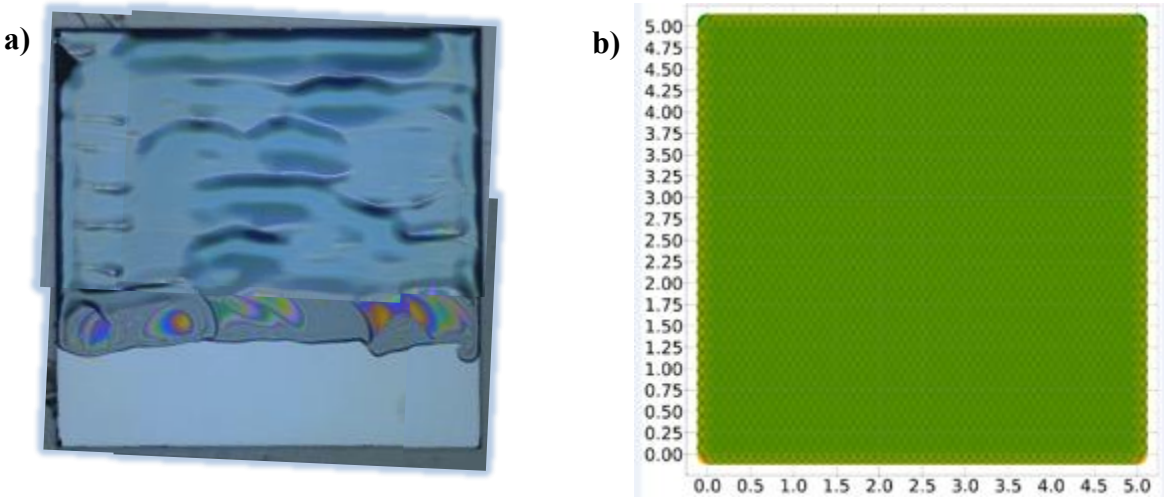

Figure 5.1. *(a) Optical microscope images of as-deposited samples showing a non-homogenous deposition using a 1M+2%EA solution with a (50x80) deposition matrix of with a drop volume of 190pL. (b) (x,y)-coordinate map of the pattern generated using a self-made Python interface.*

To avoid this liquid movement, the several parameters affecting the deposition must be accounted, such as the drop volume, the drop diameter impact, the deposition matrix and the plate velocity will have to be properly tuned. Furthermore, it was concluded in chapter 4 that the enhancement of the evaporation rate of the solvent once deposited was very beneficial for avoiding liquid dragging. We will also evaluate the deposition of our precursor ink at different temperatures to evaluate its homogeneity.

5.2 Fast Mode Drop and Line Merging Study

For the identification of the best drop and line pitch combinations, an average drop size is needed once a stable drop formation is achieved. We will measure the drop impact diameter by measuring the diameter of several drops deposited on single-crystal substrates at ambient temperature (21ºC). First, we must obtain a proper waveform to obtain a continuous jetting of drops without clogging or satellite formation. Once the waveform is obtained, the stable drop formation needs to be parameterized. In this case, for continuous grid modes, the stable drop formation has a larger volume to avoid possible clogging during movement, and can be obtained by using the following waveform parameters, without any drop formation inhibition, nozzle clogging due to speed or formation of satellites:

- Pulse Length = 25 to 28 µs
- Pulse Width = 135 to 145V
- Drop volume = 190-200 pL

In order to understand the mechanisms of liquid redistribution for this particular deposition mode, a drops merging study was performed. A large drop pitch (500 µm) was selected, with a plate velocity of 0.5 mm/s, the lowest plate velocity of this mode, to study the drop impact and drying performance on top of a single crystal LAO substrate for each single drop.

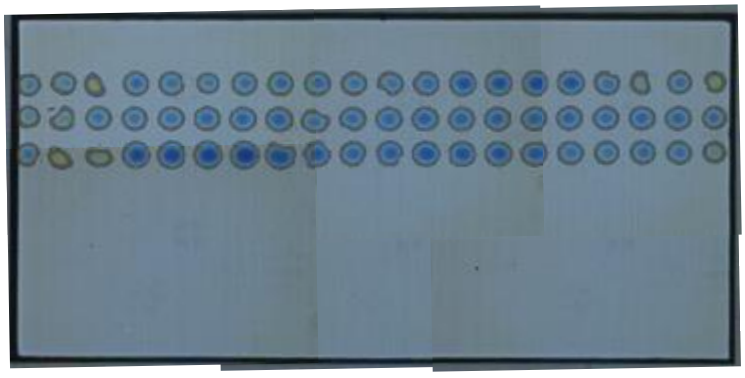

Figure 5.2. *Drop diameter obtained with Continuous Grid using 190pL of drop volume using the FF-E3 ink. Giving an average drop impact diameter of 360±4 µm, on a 10x5 mm^2 LAO substrate.*

Notice that the shape of the drop impact diameter differs slightly from one to the other, giving rise to different drop shapes. This could imply different drop merging behaviours and liquid accumulation if not a proper drop pitch is selected. Taking into account the average drop diameter of 360±4 µm, the span of the drop pitch screening has to be below that value, possibly in a range of 100-350µm for proper drop merging.

Thanks to the faster deposition rate of the Continuous Deposition Mode, several full films were deposited and examined, via Optical Microscope, to check for the resultant morphology of the deposition. We performed an experimental screening of the drop pitches first, by finding the best drop merging conditions, considering that smaller values or equal to 50µm have shown large liquid accumulations, and that large drop pitch values will lead to unconnected patterns.

We kept the same total deposition volume (1 µL) for each deposited sample, in a way that the results obtained could be better compared by fixing some of the parameters (drop volume, total volume, precursor ink, plate velocity, temperature) for each deposition matrix used.

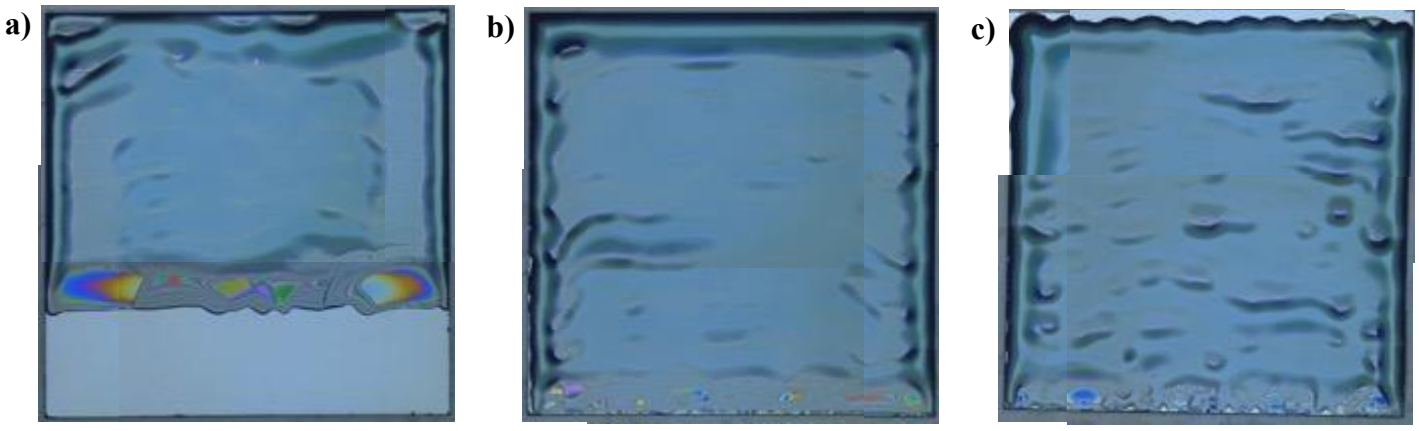

Figure 5.3. *Optical microscope images of several patterns with different drop and line pitches as indicated (XxY) on 5x5 mm² STO substrates: (a) 100×40µm, (b) 200×20µm, (c) 400×10µm. The deposited volume for each sample is maintained, being 1µL in total using the FF-E3 ink.*

As seen in Figure 5.3, the values of drop pitches obtained during the first screening to reach a drop merging situation is between 200-400µm. This has to be compared with the 50µm selected for the slow mode. Therefore, we conclude that the drop pitch for this deposition mode has to be much larger that of the slow mode, which we ascribe to the faster movement of the moving plate. From the degree of overlapping between lines, we can define the shape of the film. In this case remains constant, factoring the total deposited volume in the sample. Nonetheless, to continue the screening of the deposition parameters, in narrowed range, several films were printed to find the best line pitch values for homogenous depositions. New deposition matrixes were prepared by changing the drop and lines pitches according to the total deposited volume, in this case being the drop pitch in a selected range between 200-300µm, keeping in mind that in this range the film homogeneity should increase.

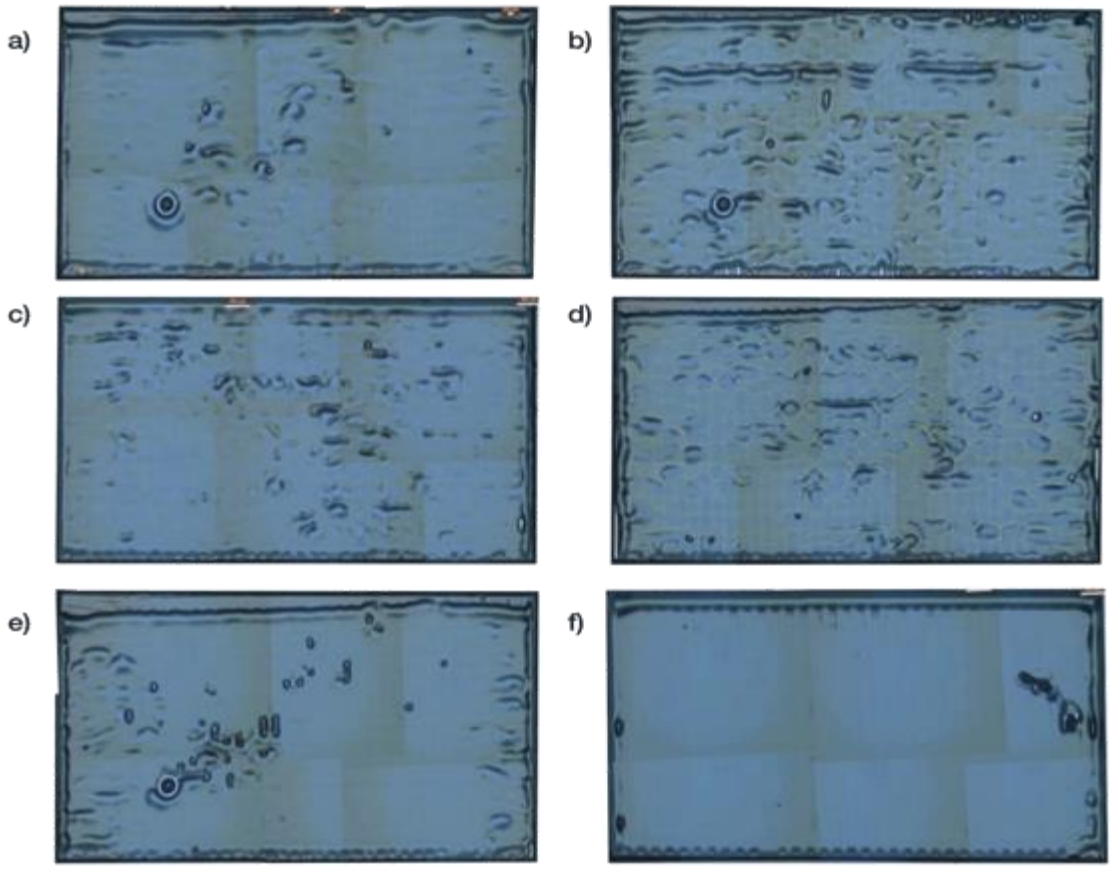

Figure 5.4. *Optical microscope images of the several deposited patterns on 10x5 mm² LAO substrates, with different matrices (XxY): (a) 200µm×25µm, (b) 225µm×22µm, (c) 245x20, (d) 250×30µm, (e) 250×25µm, (f) 280×16µm. The deposited volume for each sample is maintained, being 1µL in total.*

As observed in Figure 5.4, if shorter drop pitch values are used (200x25µm) (A), more liquid accumulation is observed at the edges, while for larger drop pitch values such as (280x16) (F) almost an unconnected pattern is obtained due to a bad drop merging in each deposited line (observe the upper part of the deposit). In both situations, the homogeneity of the films is affected; either by larger accumulations at the edges or unconnected drop merging, in which large surface roughness on the film occurs. Relevantly, the best combination conditions that showed very little liquid movement and smooth surfaces were obtained when the drop pitch selected was 250µm (D & E) and the line pitch values were around 15−30µm (see Figure 5.4). Finally, we could conclude that the best pitches combinations resulted in a deposition matrix of (250x19), as seen in Figure 5.5, with the best homogeneity achieved in this mode.

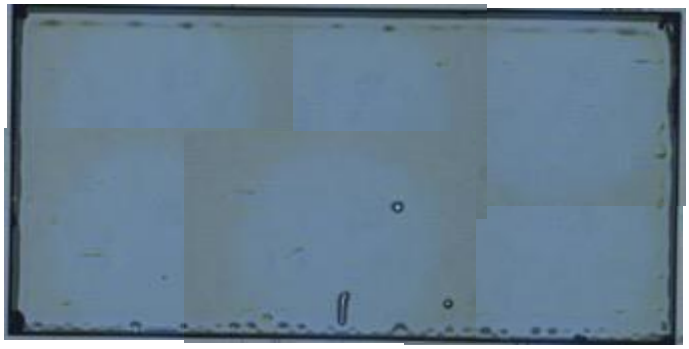

Figure 5.5. O*ptical microscope image of the deposited pattern of 250µm×19µm on 10x5 mm^2 LAO substrate.*

These drop and line pitches selected resulted in degrees of overlap of x = 30% and y = 95%. These overlapping values highly differ from the overlapping values obtained in homogenous depositions using the Slow mode (86% and 75%, respectively). Here, the deposition is at much faster rate, so the optimum values are reached by depositing less amount of drops per line to increase the evaporation rate of the solvents, thus pinning the liquid better into the substrate and resulting in less liquid accumulation. With such deposited films, which had the same total deposited value as those from the slow mode samples, we started the evaluation of the decomposition process during the pyrolysis, trying to avoid cracks.

5.2.1 Pyrolysis for Fast Mode IJP deposited films

The reproducibility on the depositions for the Fast Mode resulted to be much higher than that of the Slow Mode due to the avoidance of nozzle clogging in the Fast Mode, which allow us to create more deposited films to study the pyrolysis process on a more properly way. This can be explained by the higher tendency to nozzle clogging reached by very slow deposition rates (which in some cases could last up to 2 hours in contrast to the 30 minutes of the Fast Mode).

Thanks to its higher deposition rate, the resulting deposited samples appear all with similar shape, homogeneity and thickness. We were also able to dry the deposited samples at 120ºC for 10 minutes, close to the boiling point of propionic acid and 1-butanol, in order to evaporate all the solvents left after the deposit, leaving a gel-like film structure, without delamination or other defects. From that, we were able to calculate the thickness of the dried film and estimate the thickness reduction after pyrolysis. The dried film thickness was calculated by profilometry and compared to the resultant thickness after the pyrolysis.

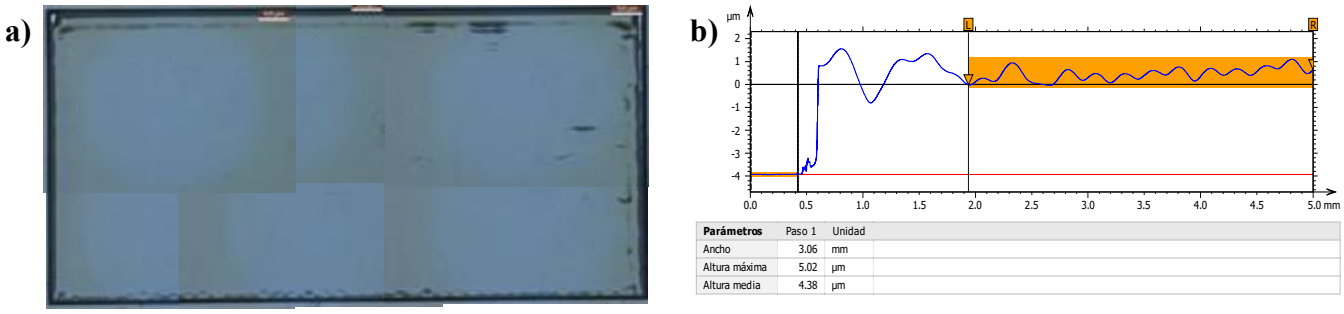

Figure 5.6. *(a) OM images of a dried sample at 120ºC (b) 2D profilometry analysis, with an average height of 4400 nm. after drying.*

Notice that the thickness of this films after drying is very similar to that obtained for slow mode samples in chapter 4, and that it is a regression of the theorized value of 7000nm for a 2000nm pyrolized film made in chapter 3, this time for a pyrolized film of 1200nm.

For the pyrolysis process of the films, the printed samples were submitted to the same stipulated optimized conditions of the previously described pyrolysis treatment in Chapter 4, made in either spin-coating or Slow Mode samples. The only difference here relies on how the deposition was made. In particular, the pyrolysis takes place in a tubular oven using a heating ramp of 5ºC/min from room temperature to 240ºC and 3ºC/min ramp up to 500ºC under humid oxygen atmosphere in a 120 mL/min flux. Thanks to the content of EA present in the solution (FF-E3), the resultant pyrolized layers were not expected to have apparent macroscopic defects (like cracks or delaminations).

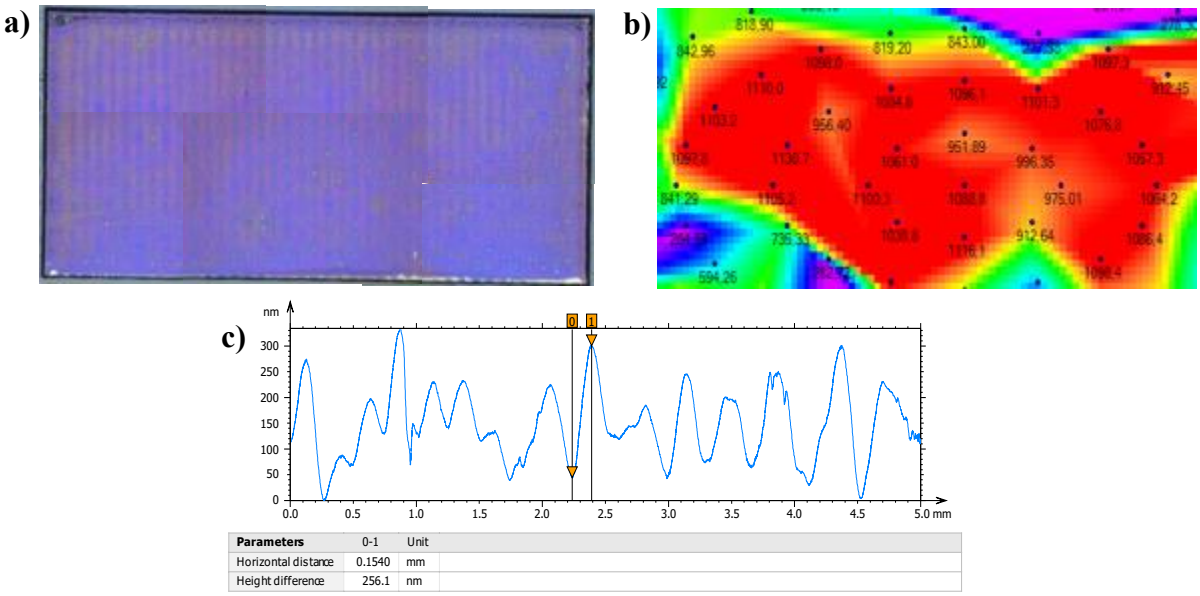

Figure 5.7. *(a) OM images of a pyrolyzed sample (b) Interferometry map. (c) 2D profilometry surface map. From b) an average height of 1100nm has been calculated from different samples.*

We calculated the film thickness of our inkjet printer pyrolized using profilometry and interferometry images from the surface of the layers (Fig. 5.7). By measuring several samples, we obtained an average thickness of 1100nm after pyrolysis, which is about 200nm thicker than that obtained for the discrete Slow Mode, due to a higher drop volume. In this case, we found a thickness reduction between the dried film and the fully pyrolized film of 75%. However, a profilometry study of the surface topography showed inhomogeneities spanning from 50 to 300 nm after the pyrolysis, as shown in Figure 5.7 c).

We ascribe this behaviour to the fact that drop merging was not fully achieved in the films, thus forming some bugling on the surface, shown as ridges and valleys of the films surface after pyrolysis [**183-187**]. The thickness inhomogeneities arising from an unappropriated liquid merging, leads to inhomogeneities in the whole film in the form of vertical mountains and valleys. However, as already mentioned, this was the best deposition matrix achieved without liquid movement, in a compromise between drop overlapping and solvent evaporation. The use of other deposition matrixes resulted in crack formation due to the presence of more inhomogenous deposited patterns, similarly to what we showed in chapters 3 and 4.

5.2.2 Characterization of pyrolized samples using the Fast Mode

Transmission Electron Microscopy (TEM) has been a very powerful characterization tool for pyrolized and TLAG grown samples in our group [**75**], giving additional information regarding the homogeneity and composition of the microstructure, grain size, porosity and thickness. TEM analysis on thickness and microstructure composition of the IJP deposited films are presented. Since the profilometer revealed the presence of thickness variations of 200 nm., detailed images of the case could reveal additional parameters unseen on conventional characterization techniques.

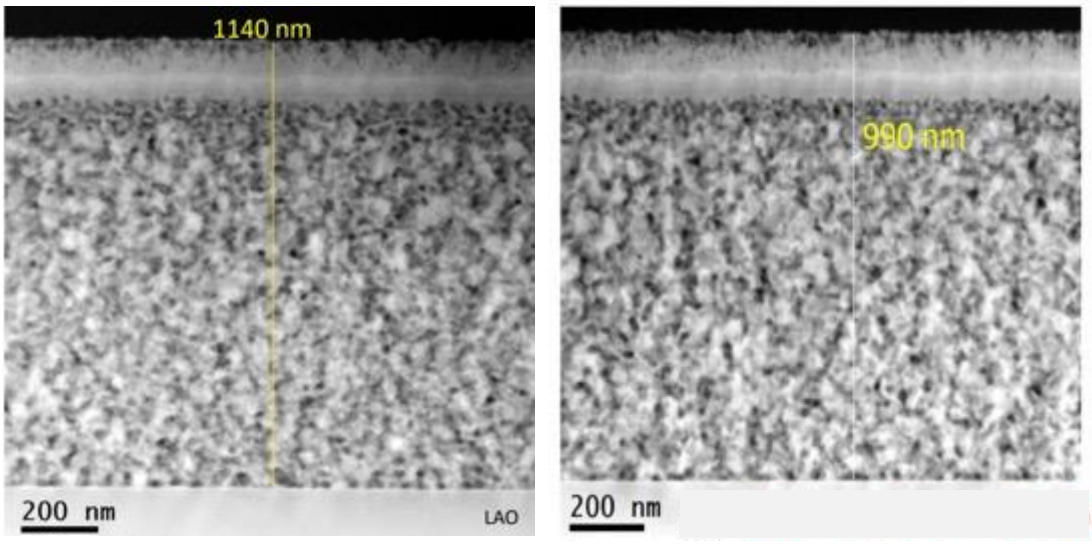

Figure 5.8. *TEM images of a printed pyrolized layer showing difference in thickness due to bad drop merging.*

TEM images revealed a very homogenously distributed microstructure, both in composition and grain size through the layer, being a full dense layer of nanocrystalline oxides and carbonates. Thus, demonstrating that the thickness inhomogeneities do not translate to microstructure inhomogeneites. Interestingly, a very dense interlayer, rich in Cooper, can be observed in the last 200 nm below the surface. These layers are not observed in multideposited spin coated layers of these type of FF solutions. However, these types of Cu-rich layers were often observed with pyrolyzed layers from LF solutions, and ascribed to Cu-TFA and Cu-Ac sublimation during the pyrloysis [**128**]. The presence in our FF solution of Cu-Ac instead of Cu-Prop used in the multideposited spin coating layers, could be the origin of this explanation.

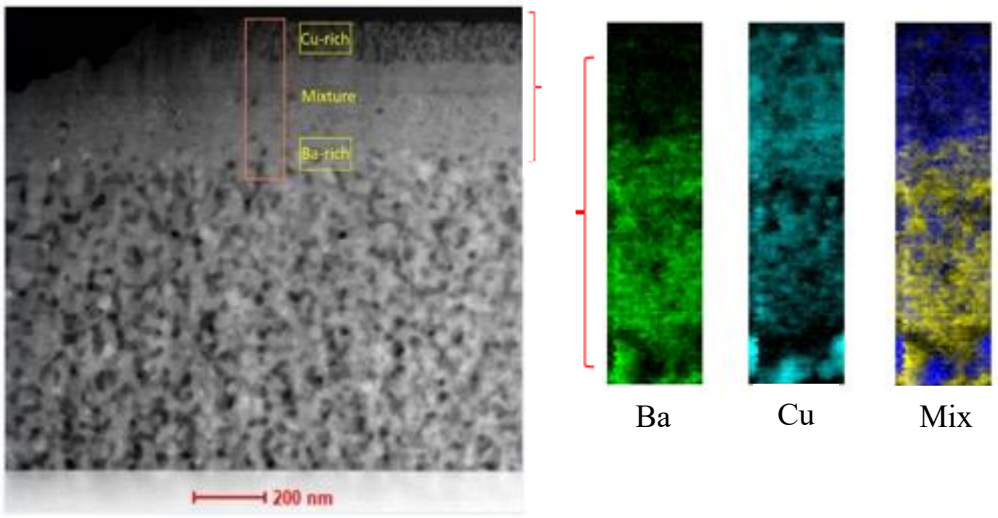

Figure 5.9. *TEM image together with EELS map for the several atoms forming the film: Oxygen, Copper, Barium and mixed Barium(yellow)-Copper(blue) maps.*

From the rest of the film, a low porosity 4.15±0.45% was calculated using the software ImageJ from the black holes inside the structure. This is to be contrasted with the ~2% porosities [**75**] encountered with the multideposited spin coating layers using the full propionate solution with EA and the 15% porosities usually existing in the TFA-based solution.

From Saltarelli L. et al [**75**], it was concluded that EA was the main driver for this porosity decrease and increase in microstructure homogeneity. The differences in thickness, observed during the profilometer measurements of the layer, are confirmed through TEM images, revealing differences in the range of 150 nm.

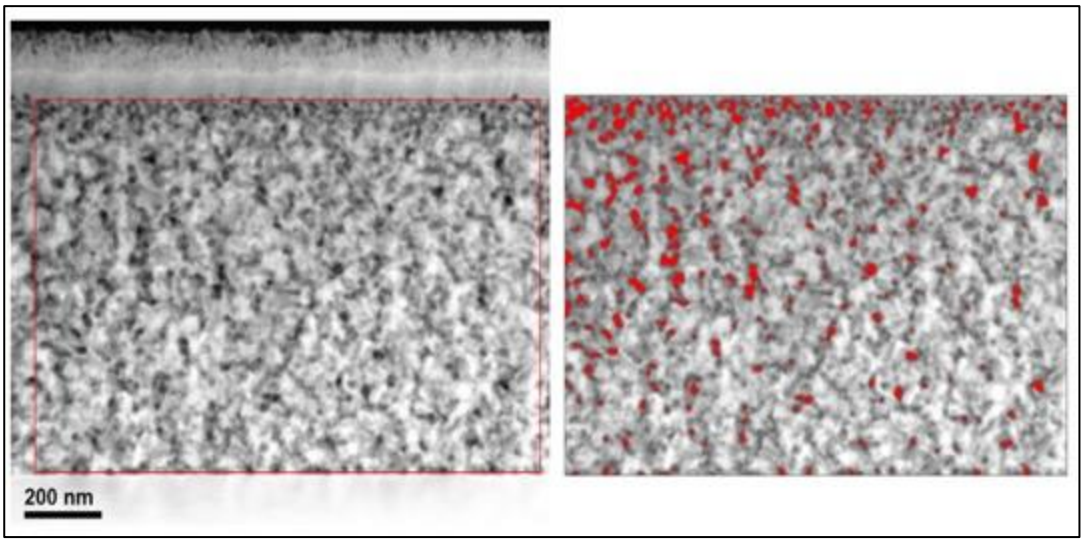

Figure 5.10. *Porosity analysis of the IJP pyrolized samples using ImageJ software.*

Unexpectedly, some XRD patterns of the pyrolized films using such deposition conditions revealed a majoritarian contribution of monoclinic $BaCO_3$, in contrast to the other samples obtained in both spin-coating and Slow Mode samples, suggesting that the thickness of the films was actually very high and the decomposition of the carboxylates, occurring under these thick values, resulted on different decomposition reactions that lead to the formation of monoclinic barium carbonate ($BaCO_3$ monoclinic). The presence of monoclinic $BaCO_3$ is understood as a consequence on the difficulty to eliminate CO and CO_2 gases, due to the high thickness and low porosity of the samples. We observe a correlation between the reduction of Cu and the presence of BCO monoclinic phase, which was also previously described.

Since the decomposition of carboxylates lead to the formation of carbon monoxide and carbon dioxide, among other gases, its trapping on the bulk of the film causes a more reducing atmosphere that affects the transformation to the correspondent nanocrystalline phases, which could explain the results obtained if Figure 5.11. Moreover, our ethanolamine additive, reduces the porosity of films and can difficult the release of gases. The trapping of released gases together with the reduction of porosity have an influence on the resulting oxides and carbonates.

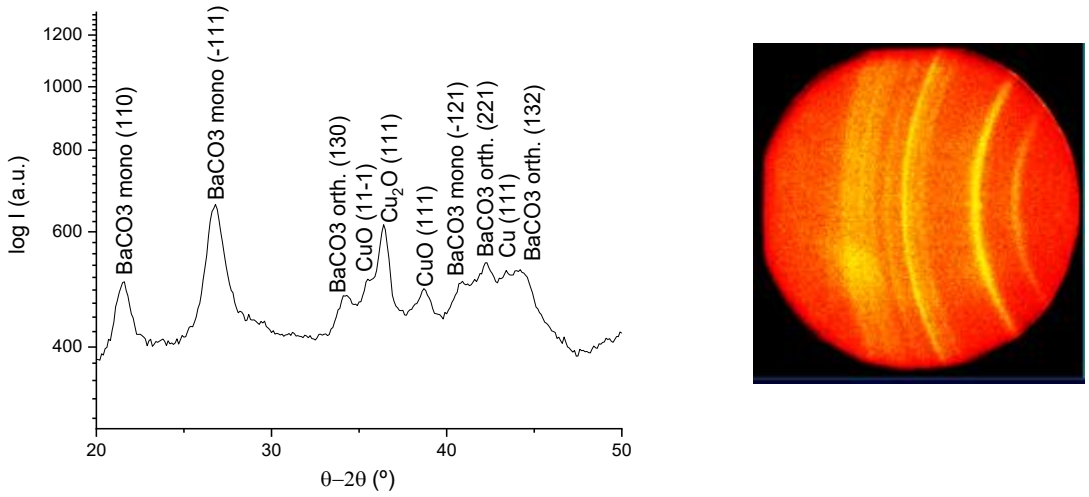

Figure 5.11. *XRD pattern for a pyrolized Continuous Mode (250x19) film with its GADDS diffractogram image.*

It is worth to mention, that while Cu reduction was not observed by XRD in all the pyrolized layers, some monoclinic Barium carbonate did appear in all cases. For that reason, a thoroughly study on the heating ramps together with oxygen flux variations could help in the understanding of the pyrolysis profile. Our idea relied on the combination of using slower heating ramps after Cu propionate decomposition, that is at temperatures higher than 240ºC, and by passing more oxygen gas flux to obtain a more oxidant atmosphere and avoid gas trapping, as higher fluxes could carry the gases produced during decomposition at faster rates. The designed pyrolysis profiles are shown in the following table.

Table 5.1. *Experimental settings of the pyrolysis conditions analysed on the inkjet printed samples with Fast Mode.*

Heating Ramp	25-300 (ºC)	300-400 (ºC)	400-500 (ºC)	Humid O_2 flux (mL/min)
A (conventional)	5 ºC/min	3 ºC/min	3 ºC/min	120
B	5 ºC/min	3 ºC/min	3 ºC/min	60
C	5 ºC/min	3 ºC/min	3 ºC/min	240
D	5 ºC/min	1 ºC/min	3 ºC/min	120
E	5 ºC/min	1 ºC/min	3 ºC/min	240

This study was made with different samples prepared with the same precursor solution, the same jetting parameters and same substrates in order to obtain the closest comparison between them. Obviously, we have used the optimized deposition matrix to achieve the best homogeneity as possible. From these results we expected to see differences in the microstructure composition of the films after pyrolysis.

By achieving a more oxidant atmosphere, we expect to overcome the possible Cu reduction [**172**] and to reduce the amount of monoclinic barium carbonate, which could severely affect the YBCO crystallization in the ulterior TLAG growth method. While in the case of monoclinic barium carbonate is not so critical, it could change the conditions for an optimal growth and delay the reactions to form the Ba-Cu-O liquid, for Cu reduced species could be a major issue for the YBCO overall performance. A comparison between the different layers obtained was made through XRD diffraction studies. We have observed the decrease of the reduced Copper species when higher oxygen fluxes are introduced into the system.

Our interpretation is that under higher fluxes of oxidizing atmospheres, the oxygen is able to easierly be transported favouring the formation of stable Cu (II) oxides. On the contrary however, even with higher fluxes, when the heating ramp of the pyrolysis step is reduced to 1ºC/min, more reduced Cu species are observed. We believe that slower ramps favour the aggregation and coarsening of the Cu species, especially that of metallic Copper, being unable to re-oxidize at higher temperatures due to the larger sizes. Figure 5.10 shows some of the obtained pyrolized samples as an example of the study:

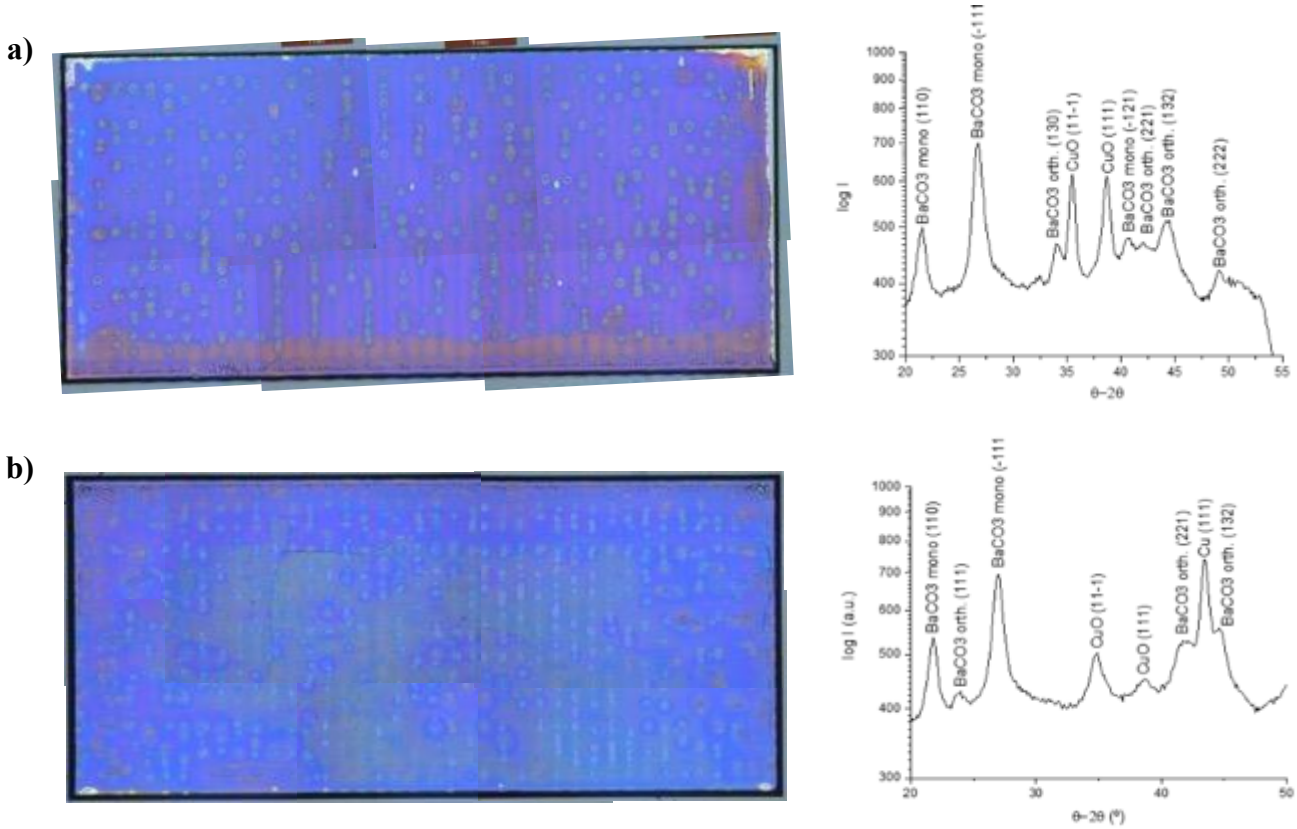

Figure 5.12. *(a) OM image and XRD pattern for a pyrolized Continuous Mode (250x19) film using 240 mL/min of humid O2 gas. (b) XRD pattern for a pyrolized Continuous Mode (250x19) film using 240 mL/min of humid O2 gas, with 1ºC/min from 300ºC up to 400ºC.*

If we compare the XRD patterns obtained in Figure 5.10 with Figure 5.9, we have the certainty that due to the high thickness of the layers, the majoritarian contribution of $BaCO_3$ is monoclinic during the pyrolysis. Besides that, we have found that Cu oxides can be reoxidized if a proper renewable oxidant atmosphere is set during the decomposition of the organic moieties.

5.3 Summary on Fast Mode deposition of thick films

Here, we have evaluated the deposition of thick films at fast rates of deposition by using the Fast Mode of the MicroDrop inkjet printing system. We observed that there is a compromise between the deposition matrix and solvent evaporation which strongly depends on the deposition rate. The drop and line pitches selected resulted in overlapping values that highly differ from the values obtained using the Slow mode depositions. Since the deposition is at fast rates, we demonstrated that we need to decrease the amount of drops in one single line to enhance the evaporation rate of the solvents, so that pinning of the liquid on the substrate is more favourable.

We found the best possible deposition matrix achieved, without liquid movement and defect-free layers. The use of other deposition matrixes resulted in crack formation. Shorter drop pitch values lead to liquid accumulation at the edges, while larger drop pitch values showed unconnected patterns. In both situations, the thickness homogeneity of the films is affected giving rise to films with large surface roughness.

We have reached the best compromise resulting from deposition matrices of 250x19µm. These conditions showed very little liquid movement and smooth surfaces. However, profilometer measurements, later confirmed through TEM images, concluded the existence of large bugling in the films. Surface roughness variations in the scale of 150nm have been observed, which can influence the transient liquid formation and epitaxial crystallization during TLAG growth, specially affecting the superconducting performance.

Since this surface roughness can affect the performance of the whole TLAG-CSD methodology, in the next section a modified approach using the Fast Mode will be presented in the line of enhancing solvent evaporation by substrate heating.

5.4 Fast Mode Inkjet Printing depositions with substrate heating

We have demonstrated that we can develop thick films through inkjet printing depositions at fast deposition rates when using a propionate-based solution with ethanolamine as additive. However, we have also observed bugling of the surface with differences in thickness around 150nm, while using the best deposition matrix that could achieve good homogenous films at room temperature. To avoid bugling, we considered another approach that provides a better drop merging together with a better solvent evaporation procedure to avoid liquid dragging. For this purpose, we investigated the effect of heating the moving plate of the inkjet printer system. Substrate heating has already reported to be a suitable solution to pin the liquid into the substrate [**188-190**].

When a jetted drop impacts into the heated substrate, the solvent is removed (evaporated) at faster rates. Once a drop impacts onto the substrate, is a gel-like material containing mostly the metal precursors with the solvents embedded inside. Once the next ejected drop impacts the substrate, it merges with the already deposited drop, which at that time it should already be fixed onto the heated substrate. Considering this assumption, we expect to obtain a reproducible method for the development of crack-free thick YBCO layers at faster rates of deposition with good homogeneity.

The use of temperature to heat the substrate will have a direct impact on the drop impact diameter, thus, the depositions matrices used to obtain homogenous depositions will have to be reconsidered. A study on the substrate temperature was made expecting favourable changes on the evaporation rate of the solvents, enhancing solvent removal and liquid fixation.

5.4.1 Fast Mode Drop and Line Merging Study with Substrate heating

For the identification of the best drop and line pitch combinations we must take into account not only the influence of the temperature on the substrate, such as the decrease of the drop impact diameter values, but also the effect that would have on the tip of the nozzle located at 1 mm above the substrate, which could clog due to the drying of the meniscus. Measuring an average drop size once a stable drop formation is achieved at different temperature will give some insights.

We utilize the same precursor solution previously described (chapter 4.2), 1M precursor solution using the 3:7 stoichiometry and 2%vol. of ethanolamine as additive (FF-E3). In order to understand the mechanisms of liquid movement for this particular deposition mode, a large drop pitch (500µm) was selected. To study the drying performance, we selected a set of substrate temperatures spanning from room temperature (21ºC) up to 70ºC, increasing 10ºC at each point. It is worth to mention that at temperatures higher than 70ºC, drop formation could not be achieved due to nozzle drying.

We stabilized the temperature on each single crystal LAO substrate, ensuring a well-distributed temperature along the whole surface to obtain an average diameter for each single drop. Here, in order to obtain the most reproducible results as possible, only one particular nozzle was used on the deposition of drops and full films, implying that the parameters necessary for drop formation were always the same. For a continuous stable drop, without nozzle clogging or the formation of satellites, could be obtained by using the following waveform parameters:

- Pulse Length = 25 µs
- Pulse Width = 135V
- Drop volume = 190 pL

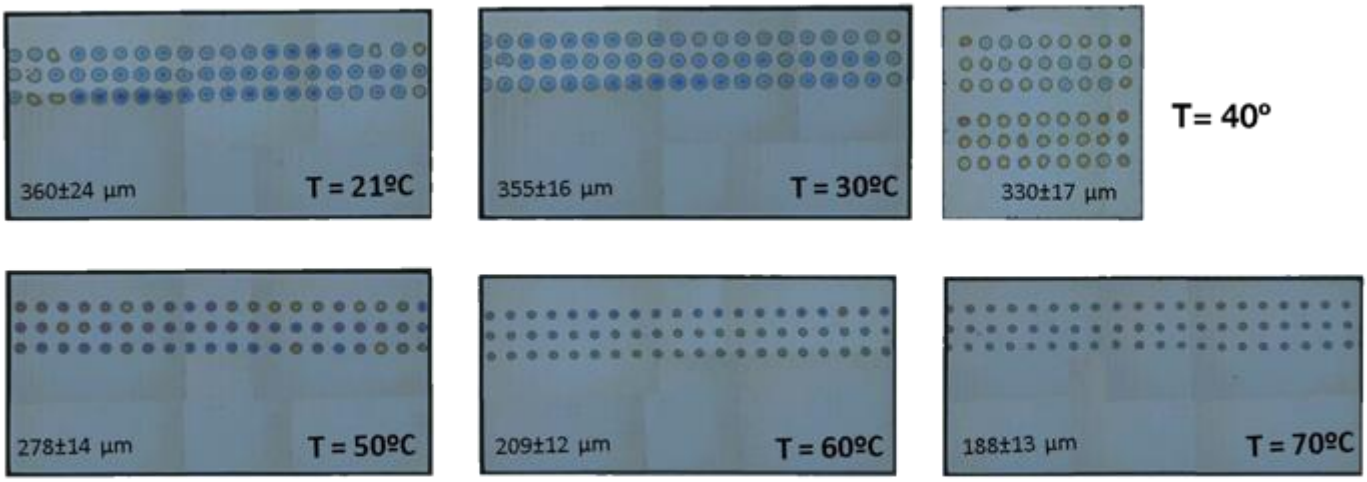

Figure 5.13. *OM images of the ejected drops at distances of 500 micrometers for each selected temperature, together with the average drop impact diameter measured with a drop volume of 190pL using the FF-E3 ink.*

As observed in Figure 5.13, as the temperature of the heating plate increases, the diameter of the deposited drops decreases. The temperature already reduces the volume of the drop by evaporating some solvent before the impact, and it is further reduced while it remains on the heated substrate. Due to the decrease of the drop diameter, drop and line overlapping are affected, thus new grids have to be found to obtain a proper merging.

Notice that as temperature increases, the drop impact diameter shrinks from 360µm to 188µm, which is practically a reduction of a factor two. Indeed, since the drop diameters are smaller, the drop pitch selected for homogenous depositions must be decreased. In addition, at room temperature the shape of the drop impact diameter slightly differs from that of the other drops deposited at higher temperatures. We observe that as the temperature increases, the drop shapes get more regular, also shown in the computed error for the drop impact diameter at high temperatures (>50ºC), reaching higher drop symmetries (Figure 5.12).

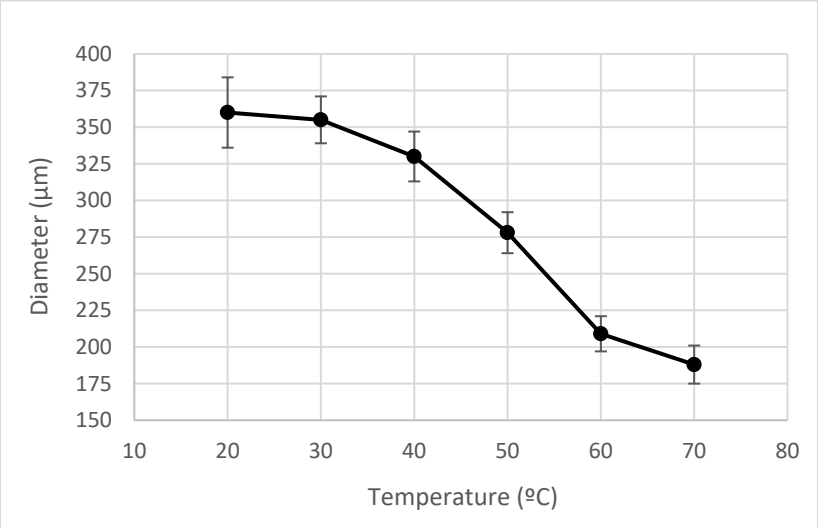

Figure 5.14. *Drop diameter evolution of each deposited drop at a certain temperature, with its associated error.*

Similar to the depositions at room temperature, the drop pitch has to be large enough to overcome the liquid movements related to the fast motion of the substrate plate. In that sense, from the experience obtained in the deposition with Fast Mode at room temperature, values of drop pitches obtained during the first screening demonstrated that a range between 180-300µm was the best to obtain a good drop merging. Thanks to the fast deposition rate (either with the Fast Deposition Mode), 5x5 mm^2 substrates can be printed in 30 minutes. We kept the same deposition volume for each deposited sample, in a way that the results obtained can be better compared.

New deposition matrices were prepared by changing the drop and lines pitches accordingly to the drop impact diameter and the total deposited volume, in this case being the drop pitch in a selected range between 200-300µm, keeping in mind that in this range the film homogeneity should increase due to less drop overlapping. We started by replicating the deposition matrix that was the best situation at room temperature, that is 250x19µm.

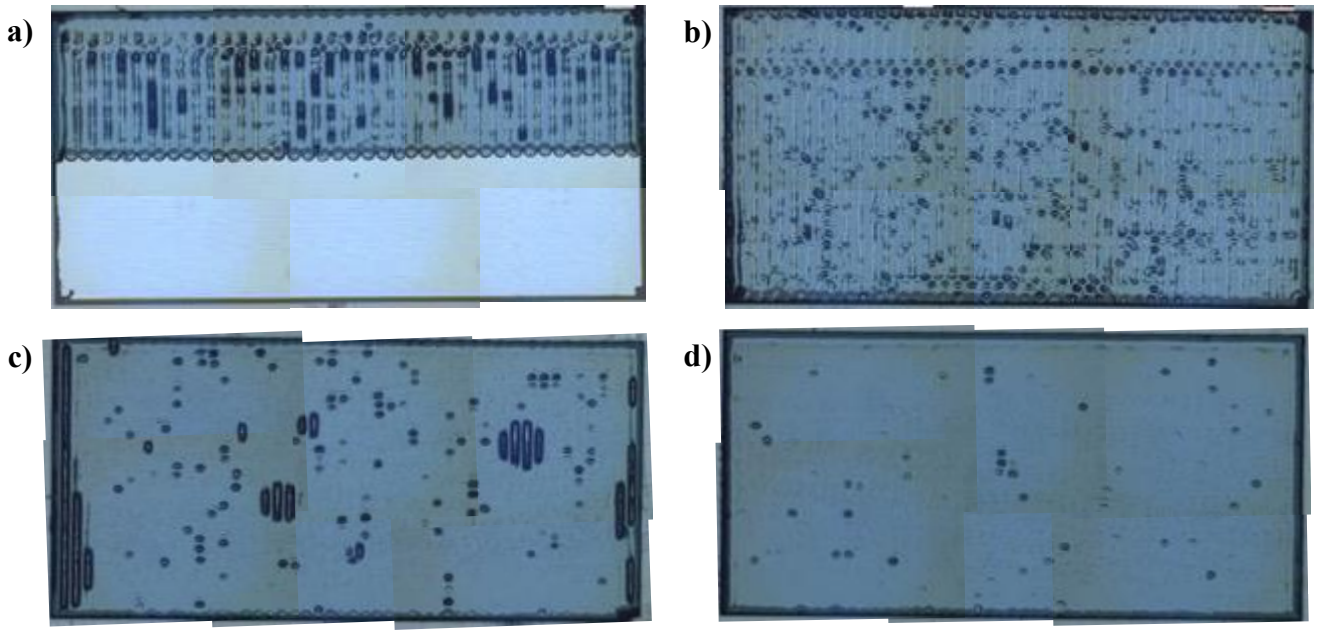

Figure 5.15. *Optical microscope images of the several deposited patterns on 10x5 mm² LAO substrates, with different drop and line pitches as indicated (XxY): (a) 250×19µm, (b) 225×21µm, (c) 200×25µm, (d) 200×22µm. The deposited volume for each sample is maintained, except for case 4.*

But as observed in figure 5.15, the inhomogenities obtained at room temperature (A) were even more accentuated in this case, giving rise to almost unconnected patters due to deficient drop overlapping. As shown, the drops did not merge properly generating surface roughness in the shape of vertical lines from top to the bottom of the substrate. Since we wanted to keep the same deposition volume for each deposited sample, we decreased the drop pitch of the serial deposited films.

We observed via optical microscope, that by decreasing the drop pitch the homogeneity of the depositions increased. When we changed the drop pitch from 250µm to 225µm (B), we still see some inhomogneities on the surface, suggesting that the full drop overlapping has not yet been achieved. However, by using a drop pitch of 200µm (C & D), we have seen a huge improvement on the homogeneity of the samples. However, keeping the total deposited value while using a drop pitch of 200µm, lead to some unconnected patters on the sample.

In this case the line pitch was rearranged to fit well with the drop overlapping, changing from 25µm to 22µm in the Y direction. The realignment implied that the total volume deposited changed from 1 to 1.1 µL, so we expect up to 200nm thicker pyrolized films (i.e., an overall thickness of 1600 µm). We want to remark that by substrate heating deposition, no liquid dragging or accumulation has been observed. This is in agreement with our hypothesis that a faster solvent evaporation should immediately fix the liquid onto the substrate, avoiding thickness differences on the sample, thus avoiding also the formation of defects related to it. For that purpose, we wanted to compare the obtained homogenous deposition at 50ºC, by using the same deposition matrix optimized at room temperature.

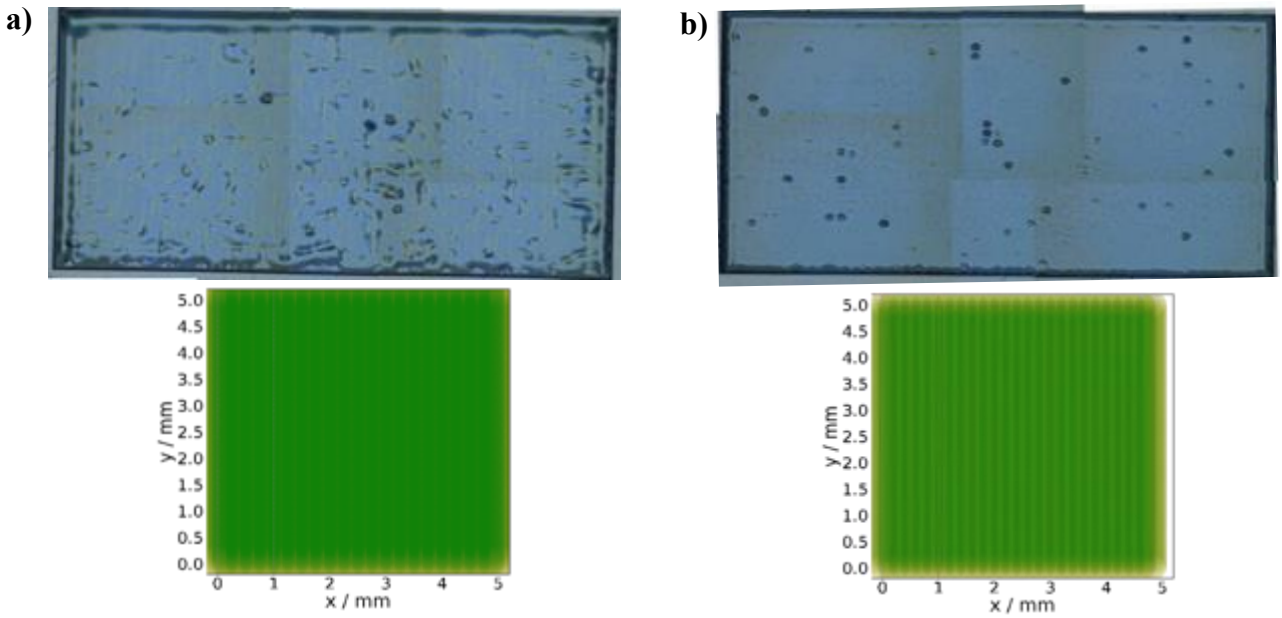

Figure 5.16. *Optical microscope images and its associated deposition matrix map for (a) 250×19µm at room temperature and (b) 200×22µm at 50ºC.*

Consequently, in figure 5.16, we observe a huge liquid accumulation on the first printed lines, and liquid dragging on the edges of the substrate, in contrast to the smooth surface obtained using the Fast Mode deposition with substrate heating. It is noteworthy to say that we compute the deposition matrix in our python interfaces to check for the drop and lines overlapping values, however, the computed values do not consider the effect of temperature that the substrate is submitted to.

Next, we wanted to compare the deposition matrix obtained at 50ºC with other different temperatures. As mentioned, the depositions at higher temperatures (60ºC or 70ºC) lead to nozzle clogging, in which some of the drops were not ejected along the whole deposition or even stopped, due to fully nozzle clogging and drop formation inhibition.

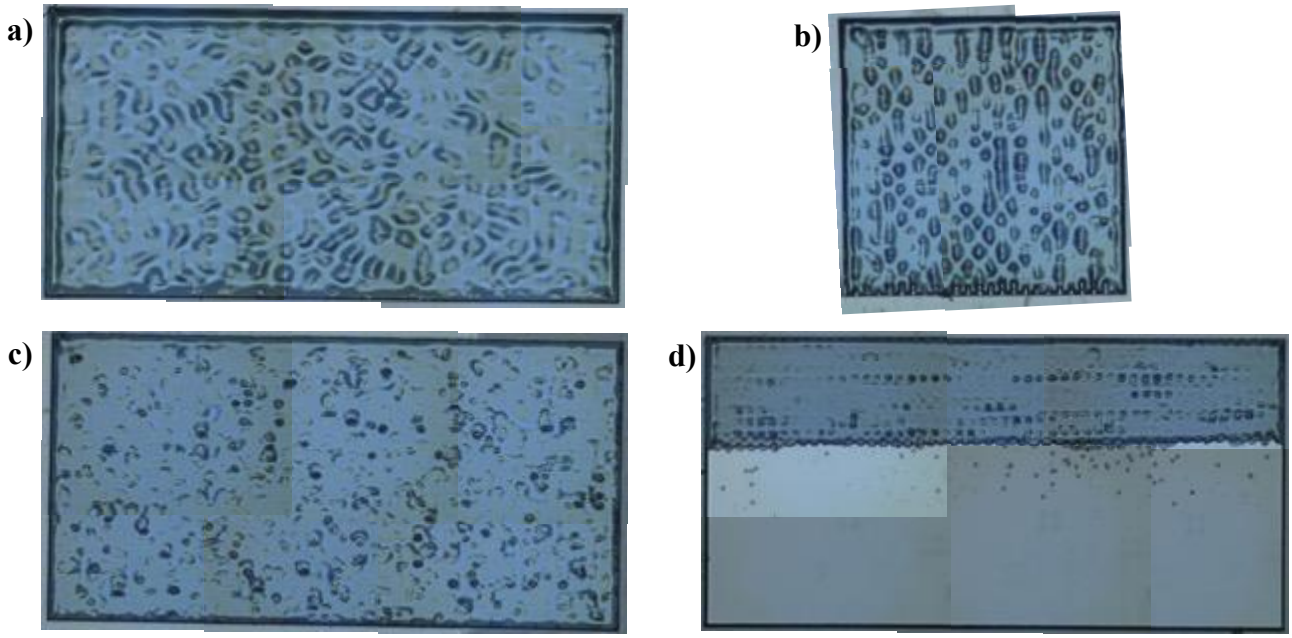

Figure 5.17. *Optical microscope images for 200×22µm samples at (a) 30ºC, (b) 40ºC, (c) 60ºC and (d) 70ºC.*

On the other hand, although the deposition of films was more optimal, in a way that drops could be continuously ejecting in a reproducible way, being able to obtain full films, the temperature was rather low, being the drop impact diameter similar to the samples deposited at room temperature, thus an average value such as (225x21µm) could well probably work.

However, since each temperature need a fine-tuning of the parameters, and that was a time-consuming costly process, we kept as standardized temperature to be 50ºC since it allowed to obtain reproducible smooth surfaces without additional complications.

With these deposited films, using the Fast Mode with substrate heating at 50ºC and a deposition matrix of 200x19µm, we could start to evaluate the decomposition process during the pyrolysis, because we found it the most adequate set-up.

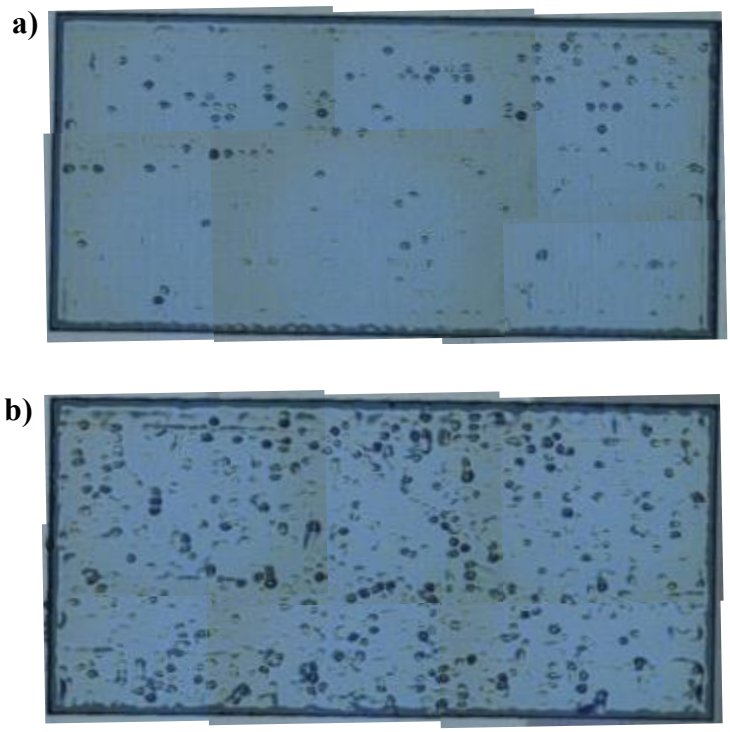

Figure 5.18. *(a)* O*ptical microscope image of the deposited pattern of 225µm×21µm on 10x5 mm² LAO substrate at 40ºC. (b)* O*ptical microscope image of the deposited pattern of 150µm×29µm on 10x5 mm² LAO substrate at 60ºC.*

For example, as Figure 5.18 shows, it is possible to deposit other kind of deposition matrices depending on the temperature set for the deposition. Still, our interpretation is that as higher the temperature is, higher the solvent evaporation will be. Since in temperatures higher than 50ºC, the nozzles start to clog, affecting the matrix positions and possibly inhibiting its proper jetting, while at lower temperatures the solvent evaporation will be minimized, we confirm that 50ºC is the best setup to deposit films, evaluate its proper drop merging and study its outcoming pyrolysis microstructure, as will be discussed in the next subchapter.

5.4.2 Pyrolysis of Fast Mode deposited films with substrate heating

For this study, the samples were submitted to the same pyrolysis treatment described (see chapter 4). The resultant pyrolized samples were characterized via optical microscope and XRD diffraction. In this case, we wanted to pay more attention to the role of ethanolamine, the densifying and homogeneity enhancer capacity so we slightly modified its content, knowing from contemporary works in the group that very small changes of % could strongly influence the pyrolysis results [paper Lavinia].

We changed the ethanolamine content from 2% to 1.8% to check for the performance of the samples during the pyrolysis. This reduction of 0.2% in volume did not practically change the rheological contents of the solution, which are inside the stipulated Z numbers (6 vs. 6.5, Table 4.1). We printed several samples by utilizing the same optimized grid of 200x22µm, with the same drop volume of 190 pL and substrate temperatures of 50ºC, using 1.8% vol. of ethanolamine content.

Visually, the samples were different from the previous obtained samples, transitioning from purple blueish colours to orange, suggesting differences in thickness, porosity or phases due to light reflection. Also, some defects on the sample (shown in Figure 5.17 as black dots) appeared along the surface. Two possible outcomes on the origin of the defects were theorized, being small pieces of dried material jetted from the nozzle during deposition or presence of pores due to effects produced during the releasing of gases along the pyrolysis, as we argued in chapter 4.4.

The XRD diffraction patterns (Fig 5.19) also revealed the appearance of undesired secondary phases such as reduced Copper species, as in the case of the pyrolized samples at room temperature. Mostly due to the high thickness of the film during pyrolysis. The copper reduction could be almost avoided, and the resultant images of the samples gave a similar purplish colour if compared to the other samples analysed.

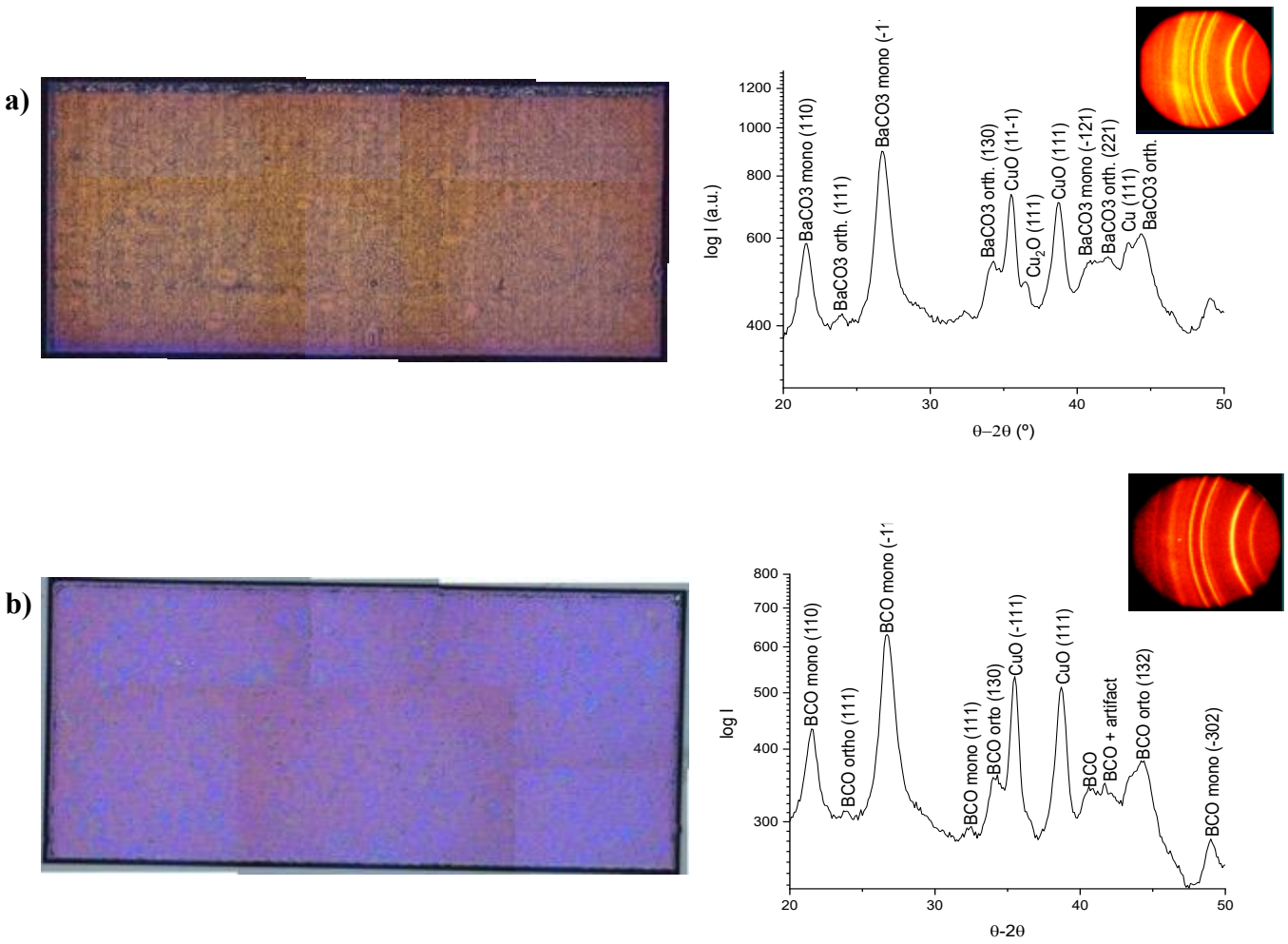

Figure 5.19. *(a) Optical microscope image for a 200×22µm pyrolized sample using 2%EA (FF-E3) and XRD diffraction pattern of the sample. (b) Optical microscope image for a 200×22µm pyrolized sample using 1.8%EA (FF-E2) and XRD diffraction pattern of the sample.*

Since the changing in content of ethanolamine gave the desired results, in-situ imaging of the pyrolysis was performed, where we identify the major stress-relief mechanisms if the organic moieties present in the film decompose towards to its proper oxides and carbonate compounds. In this case, when ethanolamine content was reduced to 1.8% the performance of the process gave very good results in terms of reproducibility, thickness and microstructure composition.

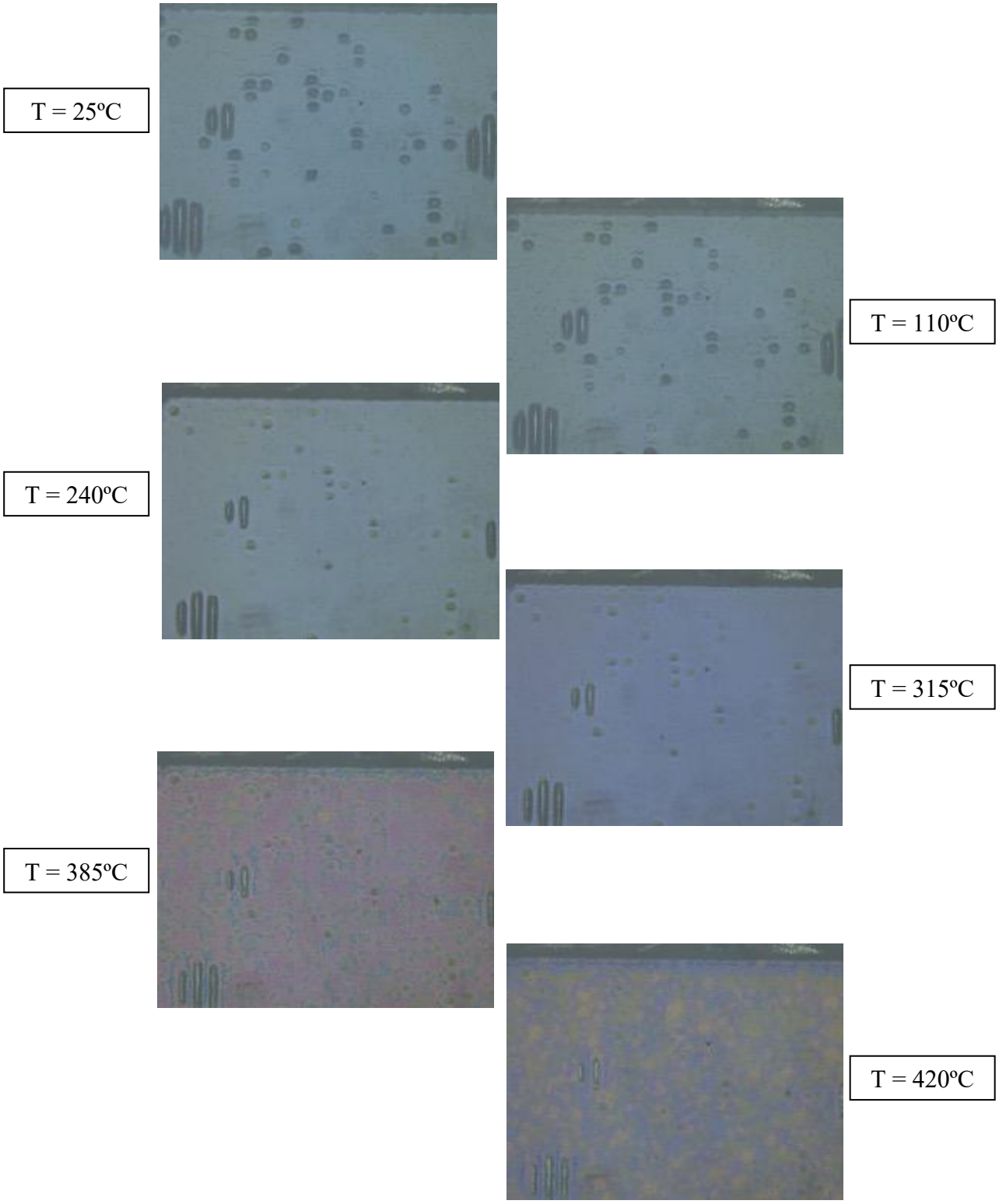

Figure 5.20. *In-situ imaging of a pyrolysis process of a thick film (200x25µm) using a 190pL volume drop, with an expected thickness of 1700nm after pyrolysis. With a profile of 5ºC/min to 240ºC, 3ºC/min to 500ºC, 5 min dwell under Humid Oxygen atmosphere (120 mL/min). Notice that no apparent defects appear on the sample. Video 4 in Appendix A.*

Clearly, as revealed through the in-situ imaging of the pyrolysis process (Fig. 5.20), this pyrolysis profile did ensure defect-free samples. Interestingly, from room temperature (21ºC) to 240ºC, there is some densification of the film. Apparently, it seems that the solvents remaining on the deposited film start to evaporate, which left a gel-like film structure by which all the issues related to drop overlapping are being compensated and decreased.

Figure 5.20 shows the results of a sample with a deposition matrix of 200x25µm, which has in fact less total deposited volume as the other prepared samples, about 0.95L in contrast to 1.1L. We did the in-situ imaging of the pyrolysis of this sample, firstly because it was done during the optimization of the grid for proper liquid merging, but also due to the 'defects' originated during deposition, where some drops did not properly overlap, creating blank spaces where the substrate can be seen, for example on the left part of the images. We expected to see some crack formation at this blank parts of the film due to the tension that could experiment the film directly in contact with the solid substrate, and that could even propagate to other blank spaces of the film.

We did not find neither of the expected cases. The precursor solution with 1.8% content (FF-E2) had shown very good performance in both deposition and pyrolysis, by sustaining the films even on cases that could induce defects on the sample. What we found however, is how the film is densifying, changing its colour due to reflection of light, from deep blue to purple and orange, and the appearance of some 'black dots', especially around the defects during deposition, which appeared around 385ºC, which could be related to the release of the volatile gases during the decomposition of the precursor salts, especially CO_2 (see chapter 4.4). Later on, those black dots seem to disappear, or at least compress to very small sizes, since most of them have already disappeared at temperatures above 420ºC. We hesitate to explain that this sample was not the most optimized of the process, and that this could give rise to undesired patterns that seem to not happen in other samples already explained.

The pyrolizer oven has also different parameters if compared to a tubular oven, so also some discrepancies in respect to the morphology could appear. Still, profilometer analysis of the sample gave very interesting results in both thickness and surface roughness. In fact, roughness was very minimal considering the high thicknesses of the sample (1750nm). This imply that the designed deposition matrix, based on the proper drop merging of the jetted solution was the correct one to obtain reproducible, homogenous films in one single deposition.

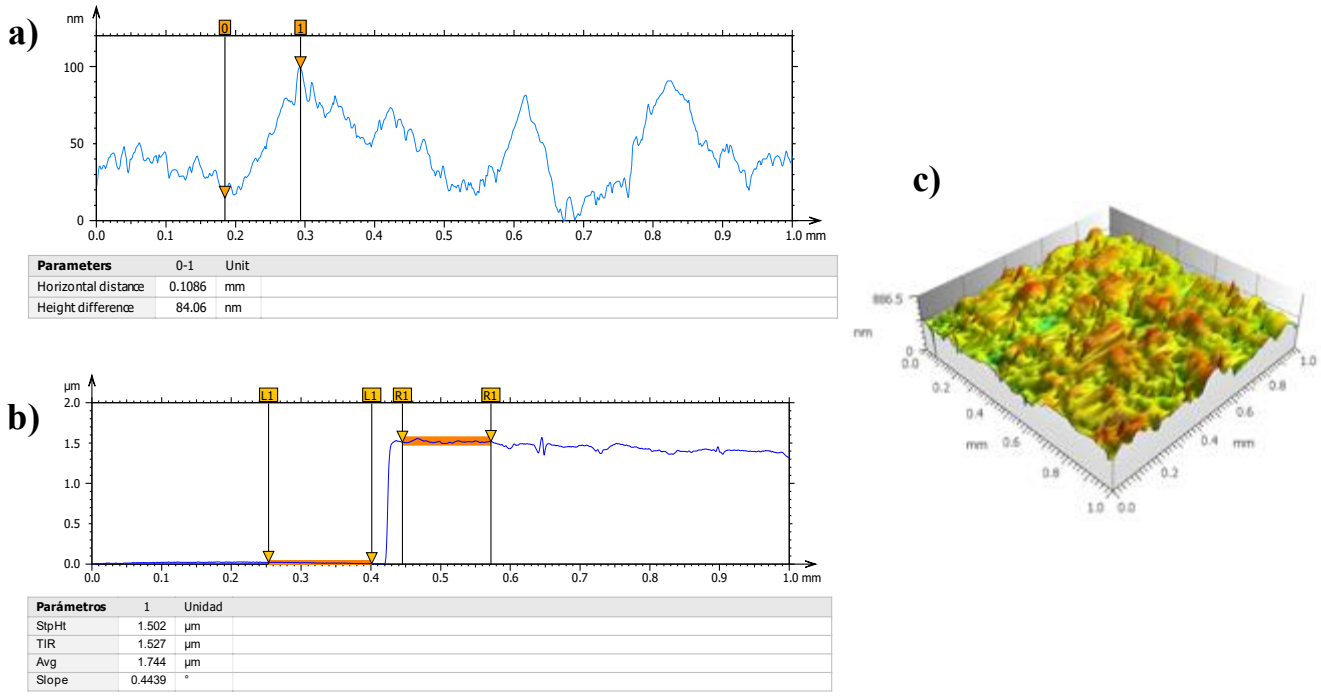

Figure 5.21. *Profilometry measurements of a 200x22µm. (a) 2D surface roughness analysis. (b) 2D profilometer measurement of the thickness. (c) 3D map of the analysed samples.*

What we see in this case is that the RMS gives an approximate value of 65 nm. Considering that the sample has a thickness of approximately 1750nm after pyrolysis, we can confirm that the deposition was very successful. In addition, the thickness of the sample is also very high. This may be due to the total volume deposited during the preparation of the sample, or also a gelling effect due to the heating of the substrate, which results in a lower densification of the film while maintaining the structure.

Thanks to these values obtained, which shed light to the process, we prepared other samples to study the pyrolysis process in more depth, such as in-situ images or effects of the temperature ramp and oxygen flux. A thoroughly study on the heating ramps together with oxygen flux variations could help in solving the problem. Our idea relies on the combination of using slower heating ramps after Cu propionate decomposition, that occurs at temperatures above 240ºC, and an increase of oxygen gas flux to enhance gas transport. The designed pyrolysis profiles are shown in the Table 5.1.

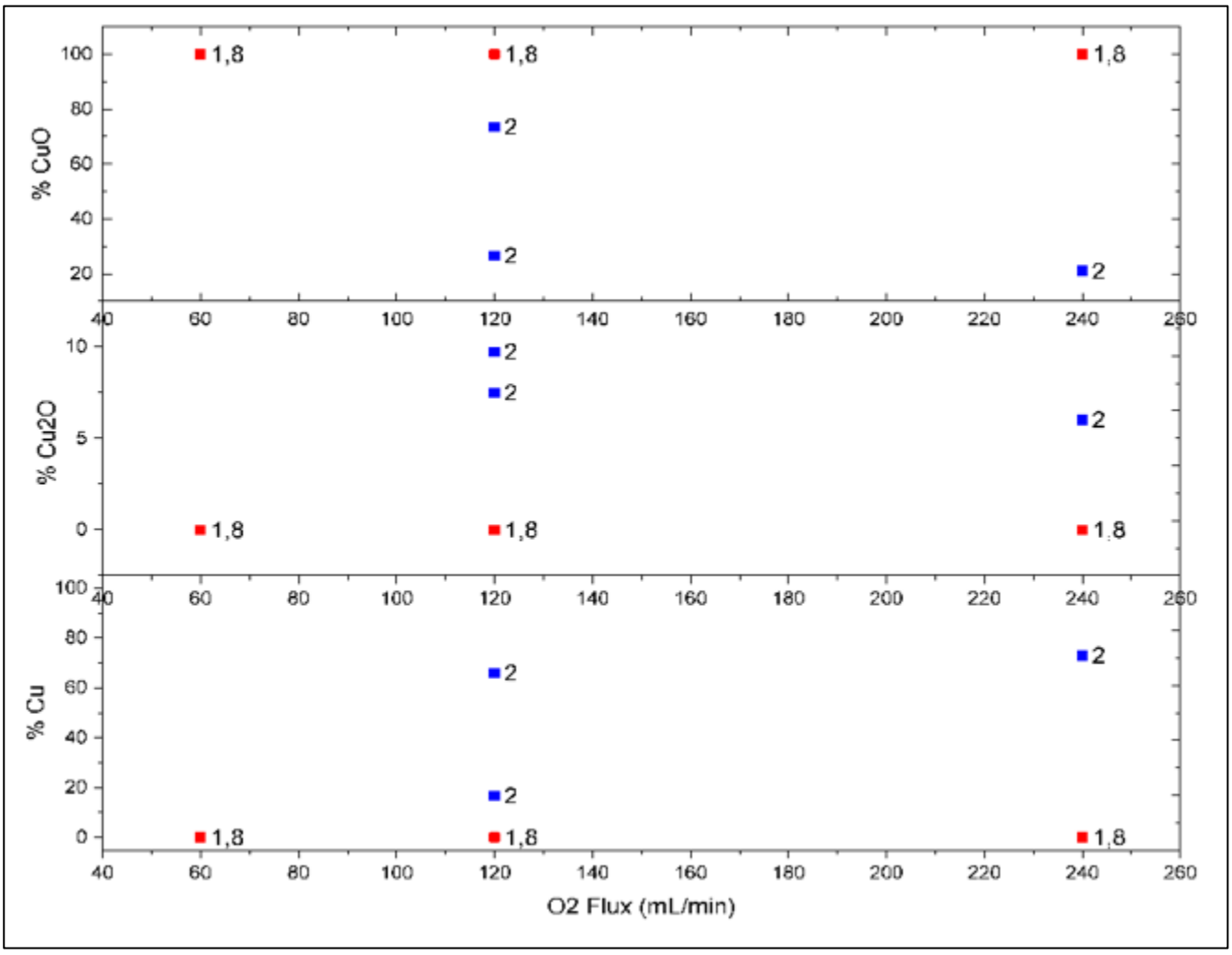

Figure 5.22. *Graph containing the percentage of Cu, Cu_2O and CuO in % for different O_2 fluxes applied and the ethanolamine content of the solution, 1.8%EA (red) and 2%EA (blue).*

As a guidance to interpret the resultant pyrolysis profiles studied, depending on the O_2 flux, ethanolamine content and utilized ramps, a qualitative average was computed. To do so, an %average of each oxidation state of Cu species on the samples, which is not representative of the real %volume of such species was calculated by means of the integrated areas of the peaks found in the XRD measurements, taking the most intense peak for each correspondent Cu species. The area was calculated based on the fitting curves of each related peak. Then, to compute the average, the following equation was used to determine the percentage of each Cu species. Using Cu (II) species as an example:

$$\%Cu(II) = \frac{Area\ (CuO)}{\Sigma\ Area\ (CuO), Area\ (Cu_2O), Area\ (Cu)} \cdot 100 \qquad (5.1)$$

As observed in Figure 5.22, all the samples pyolized when using 1.8% of ethanolamine as additive (red symbols) did not show reduced Cu species, independently of the flux of oxygen applied. Comparing it with the previous results with 2%EA (blue symbols) results in the same CuO content, seems to match well with the results obtained through XRD diffraction (chapter 5.3). High EA content could have negative effects during the pyrolysis since being an amine, it can act as a reducing agent, thus undesirable secondary phases may appear.

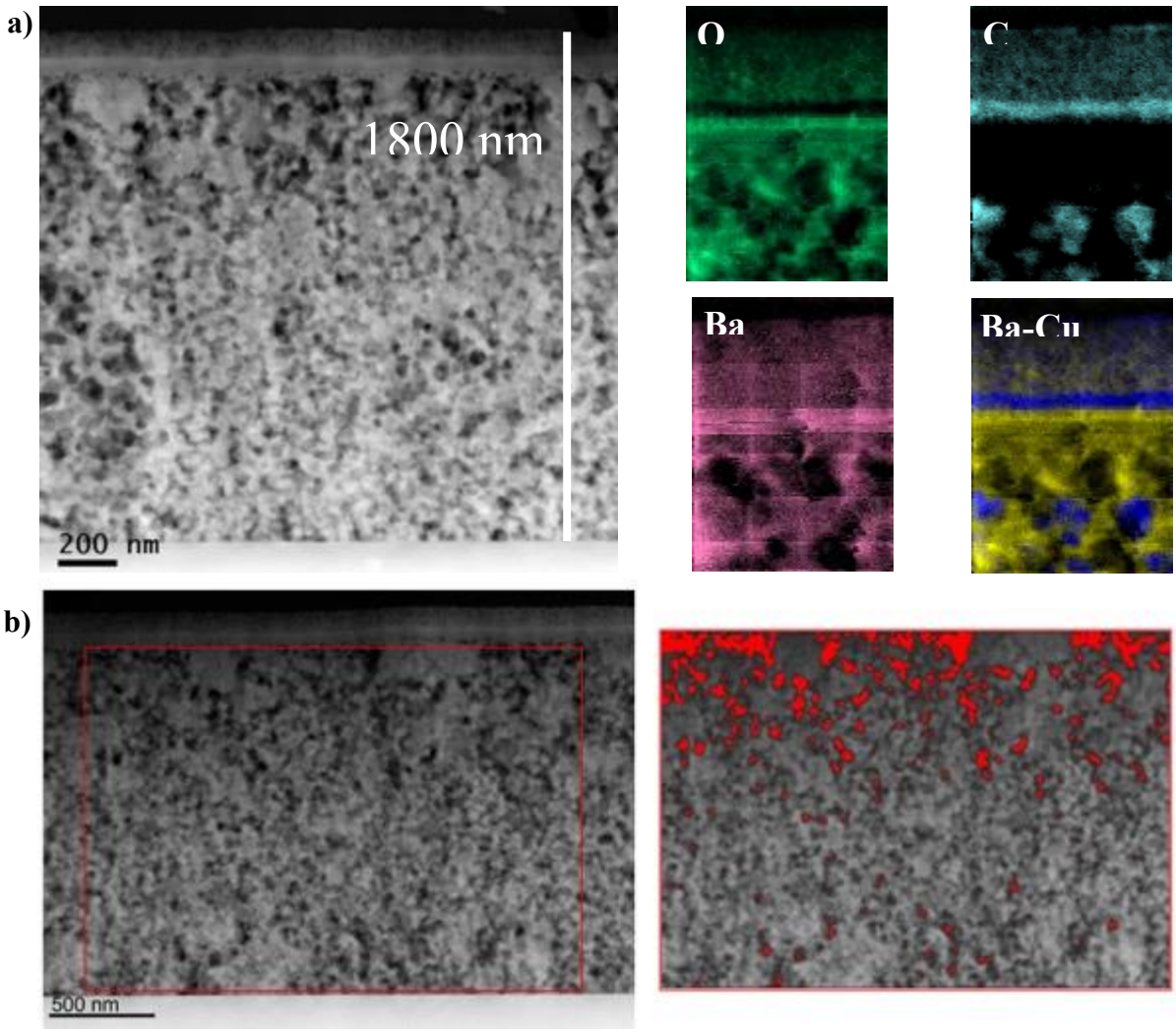

Figure 5.23. *(a) TEM image of an inkjet printed pyrolized layer using the Fast Mode together with EELS map for the several atoms forming the film: Oxygen, Copper, Barium and mixed Barium(yellow)-Copper(blue) maps. (b) Porosity analysis by ImageJ.*

TEM images revealed a very homogenously distributed microstructure, both in composition and grain size throughout the layer, being a full dense layer of nanocrystalline oxides and carbonates. A similar interlayer, rich in Copper, can be observed in the middle of the last 200nm, below surface, as in the previous pyrolized layer of section 5.3, while a thin layer (~50nm) just below it, rich in Barium. A low porosity 5.45±0.40% was calculated from the black holes inside the structure, which in this case the practical totality of the porosity appears towards the surface, and not so homogenous than in the previous case. Nevertheless, practically no thickness differences at the surface were observed and confirmed through TEM images, showing the good homogeneity of the sample (fig. 5.23).

In summary, we have obtained pyrolyzed films of in the range of 1800nm, dense and with a homogenous nano-microstructure and with low roughness, which indicates that the inkjet printing process with substrate heating was a complete success. We emphasize that these layers are very thick. We have been able to solve the problems related to crack formation thanks to the optimization of the solution, IJP process and pyrolysis. We expect that after the TLAG growth, these samples will have a thickness in the order of 1µm, which would confirm that one single deposition can reach this large thickness without cracking also with FF solutions, for the first time worldwide.

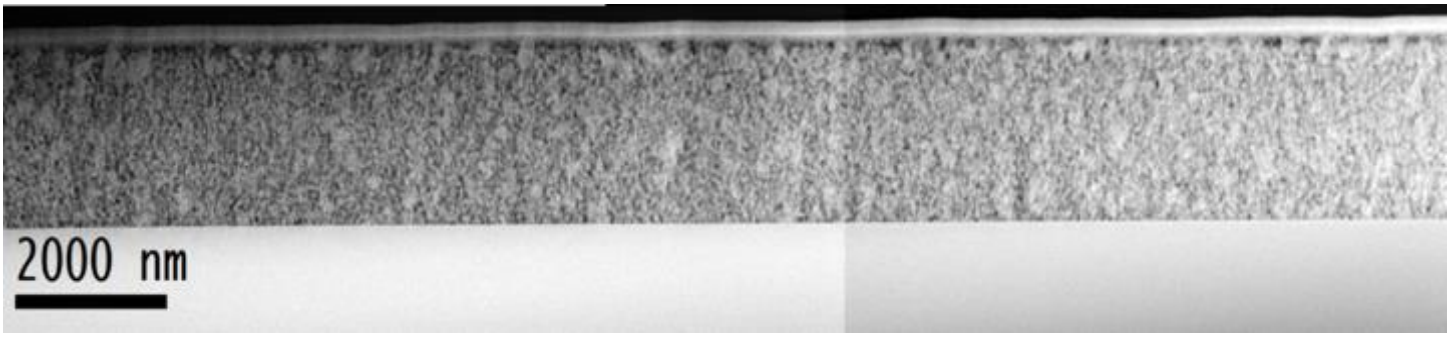

Figure 5.24. *TEM image showing a large dimension of the sample with a fine microstructure (18µm).*

5.5 Deposition on Coated Conductors

The unique properties of YBCO make this material suitable for high power generation, transmission and distribution applications. For these appealing applications YBCO coated conductors are the key materials. As such, the study of high throughput CSD methods like TLAG-CSD using inkjet printing technology to reach high thickness films with one single deposition was the purpose of this Thesis, as reported in literature [**191-196**].

YBCO is a ceramic oxide material which benefits from thin film multilayer deposition strategies onto flexible metallic substrates to reach long length Coated conductors (CCs). Nowadays, then superconducting CC's performances are similar to those achieved by superconducting films grown on single crystals. In contrast to the use of (00l)-oriented single-crystal substrates of SrTiO3(STO), the metallic substrate of the CC's has an inherent granularity (with in-plane and out-of-plane biaxial textures of just 2-3 degrees) and surface roughness in the range of 1-2 nanometres. These differences are translated into the surface of the buffered metallic substrate tape to be used to deposit our precursor solutions.

For the deposition of thick films on buffered metallic substrates from SuNAM were utilized. The precursor solution FF-E2 (see Table 4.1) was used, which consists of a 1M precursor solution using the 3:7 stoichiometry using a 1.8%vol. of ethanolamine as additive. Substrate heating at 50ºC was used during IJP deposition. We will analyse the effect of the substrate roughness and wettability of the buffered metallic substrates surface on the depositions matrices. Moreover, the tape architecture consisted of different buffer layers deposited on top of metallic substrates. Since the deposition is made now under substrate heating, and the heat capacity of single crystals is different from that of the buffered metallic materials, the deposited drops, and specially its drop impact diameter could be affected.

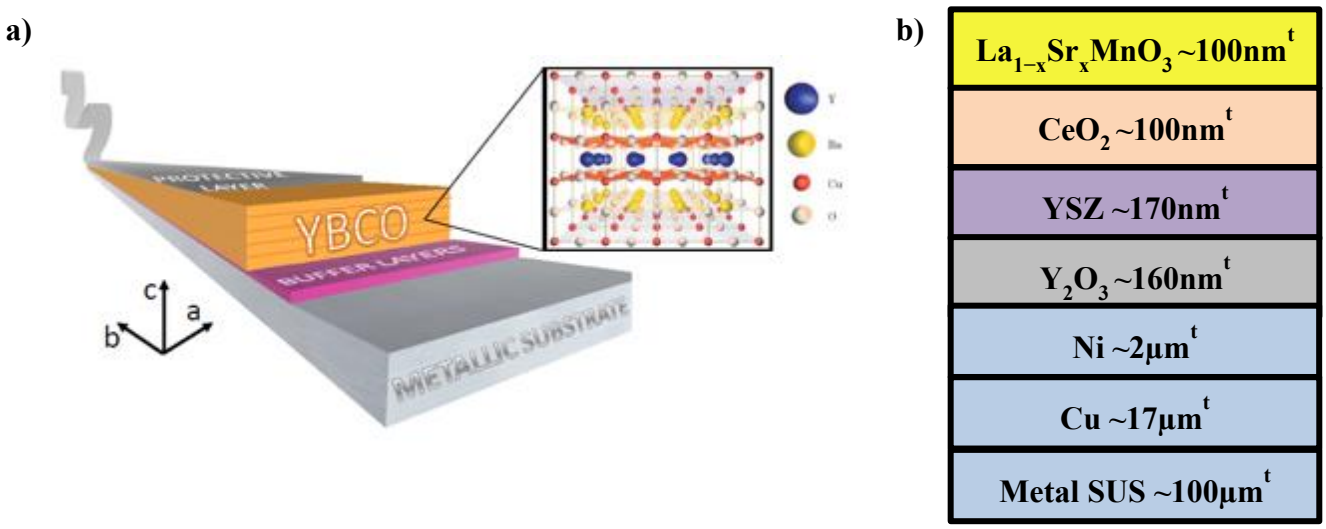

Figure 5.25. *a) Coated Conductor (CC) illustration, b) SUNAM LSMO-buffered architecture used.*

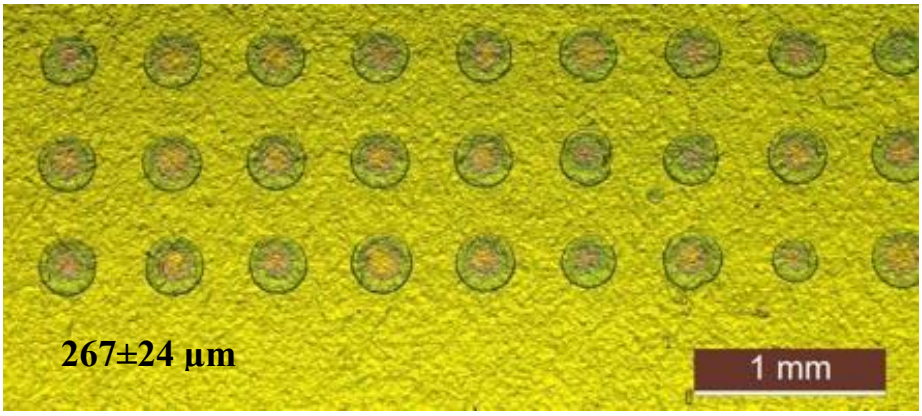

Figure 5.26. *OM image of the ejected drops at distances of 500 micrometres on SUNAM LSMO-buffered metallic tape, together with the average drop impact diameter measured (267±24 µm) at 50ºC.*

For this reason, again we first checked for the drop shapes and impact diameter by selecting a large drop pitch of 500 µm. As seen in Figure 5.26, the drop impact parameter and shapes do not differ much from those obtain on single crystals with substrate heating at 50ºC, and it is within the error bar (278±14µm vs 267±24µm). Yet, we screened for the best deposition matrix to ensure proper drop overlapping and liquid merging, without liquid accumulation. The tapes were also heated at 50ºC to ensure a better pinning of the liquid by enhancing solvents evaporation while deposition. The measured contact angle (10º) is the same as single-crystal STO substrates.

It is important to mention also that these tapes, due to its fabrication method and intrinsic flexibility (100µm in thickness), have some curvature along its length. Overall, made the deposition of inkjet printing samples more difficult than in single crystals. For that reason, most of the samples were deposited on tapes larger than the desired shape of the selected grid (usually 7x7 mm^2), but it could even be bigger.

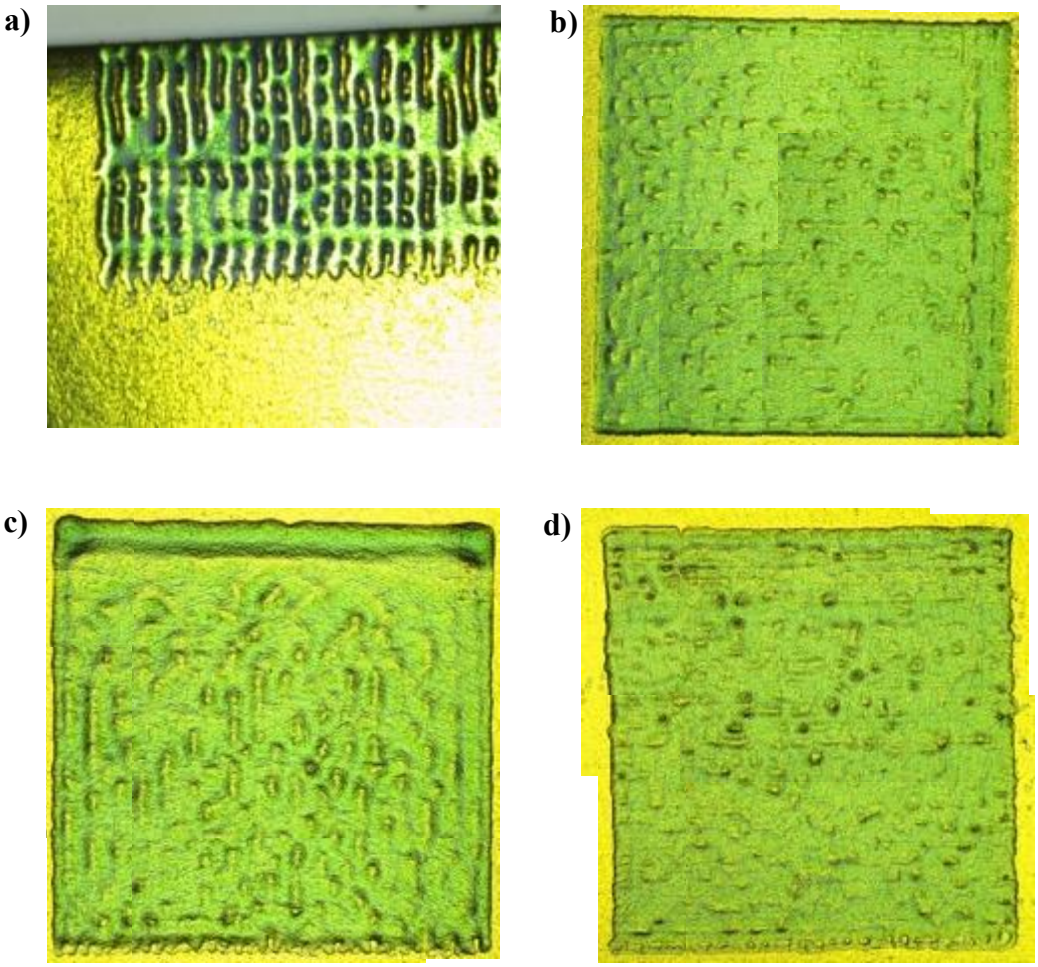

Figure 5.27. *Optical microscope images of the several deposited patterns on SUNAM LSMO tapes, with different drop and line pitches as indicated (XxY): (a) 200×22µm, (b) 175×25µm, (c) 150x30µm, (d) 100x50µm.*

We started the screening of the best deposition matrix on buffered metallic substrates by using the optimized grid used for single-crystal substrates with substrate heating. However, the deposition matrix did not ensure proper drop overlapping, generating unconnected patterns along the substrate (see Figure 5.27). For this reason, we decreased the drop distances, since the problem was identified to be the drop pitch, as the drops fall in the subsequent next position too far away to be properly fully connected.

A priori, some deposition matrices made, such as 150x30µm, lead to liquid dragging to the very first printed lines, generating thickness inhomogenities along the sample, while others like both 175x25µm and 100x50µm seemed suitable situations to obtain homogenous layers. However, after pyrolysis, the only defect-free layers obtained were the ones using the grid of 100x50µm. Our assumption is that the principal cause of the crack formation were the edges of the sample due to the liquid accumulation occurred during deposition. For this reason, we found out that the optimized grid for the deposition on CCs was of 100x50µm.

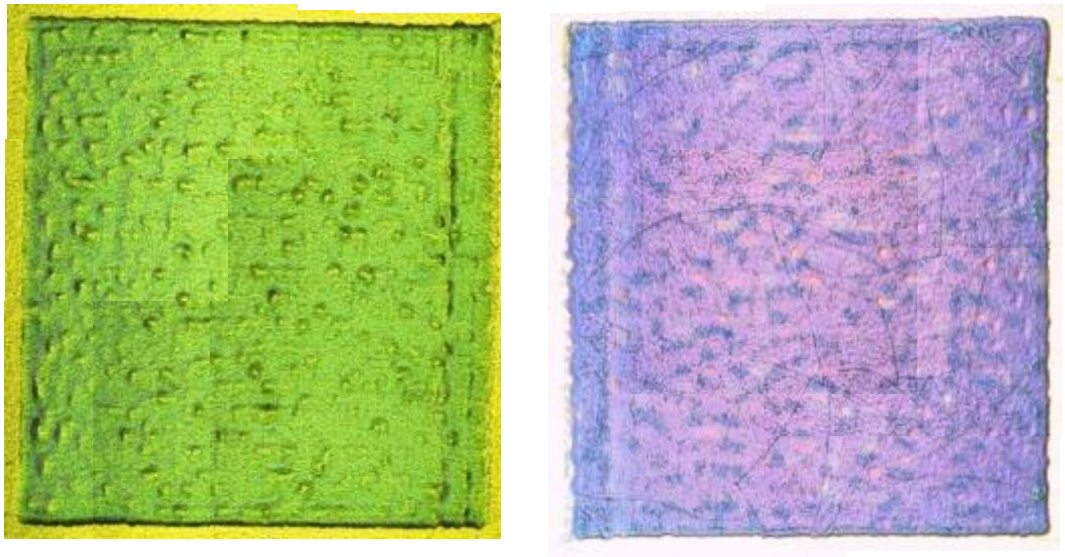

Figure 5.28. *Optical microscope images of crack-free SUNAM LSMO-buffered tapes. Deposited and cracked pyrolized film using the 175x25µm deposition matrix.*

The resulting pyrolized samples using a 100x50µm matrix were crack-free layers (see Figure 5.28). Provided that the optimized solution used was the FF+1,8% EA (FF-E2) and the deposition was made using substrate heating, the resulting samples were defect-free thick films in one single deposition. Here we can demonstrate the good performance of the technique, which can be introduced on buffered metallic substrates with good reproducibility and homogeneity. Having long buffered metallic substrate we were able to extend the deposition to 20x10mm^2 to confirm the reproducibility of the results, as shown in Figure 5.29:

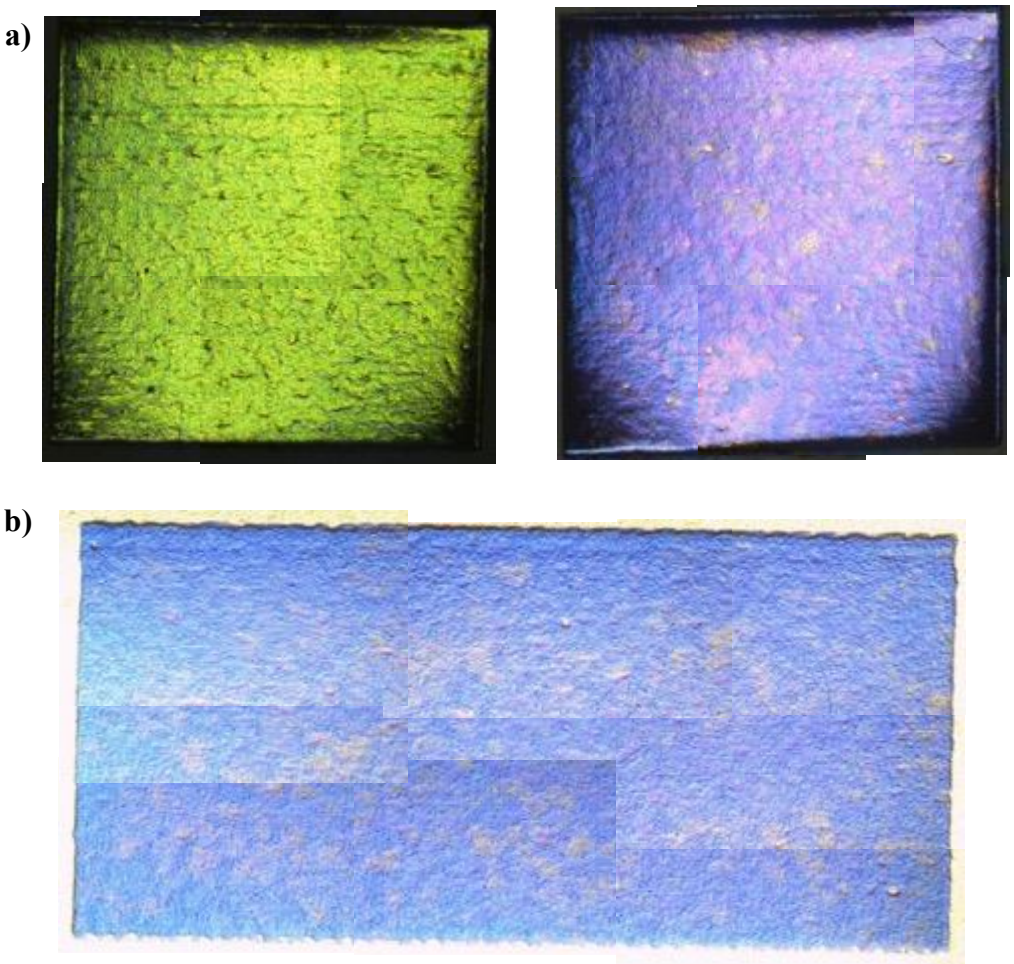

Figure 5.29. *Optical microscope images of crack-free SUNAM LSMO-buffered tapes. (a) Deposited and Crack-free pyrolized film using the 100x50µm deposition matrix. (b) Pyrolized film over a 20x10 mm^2.*

Profilometry analysis of these pyrolyzed sample confirm that similar results to those obtained in single crystals with substrate heating were reached. For example, in the analysed sample of Figure 5.27, the resultant RMS of the sample was 100nm in an analysed surface of 1x1 mm^2, being the largest difference in thickness of 160nm. In addition, the resultant thickness of the sample was on the same order of magnitude as the samples deposited in single crystals, in the range of 1700nm. As shown in Figure 5.30:

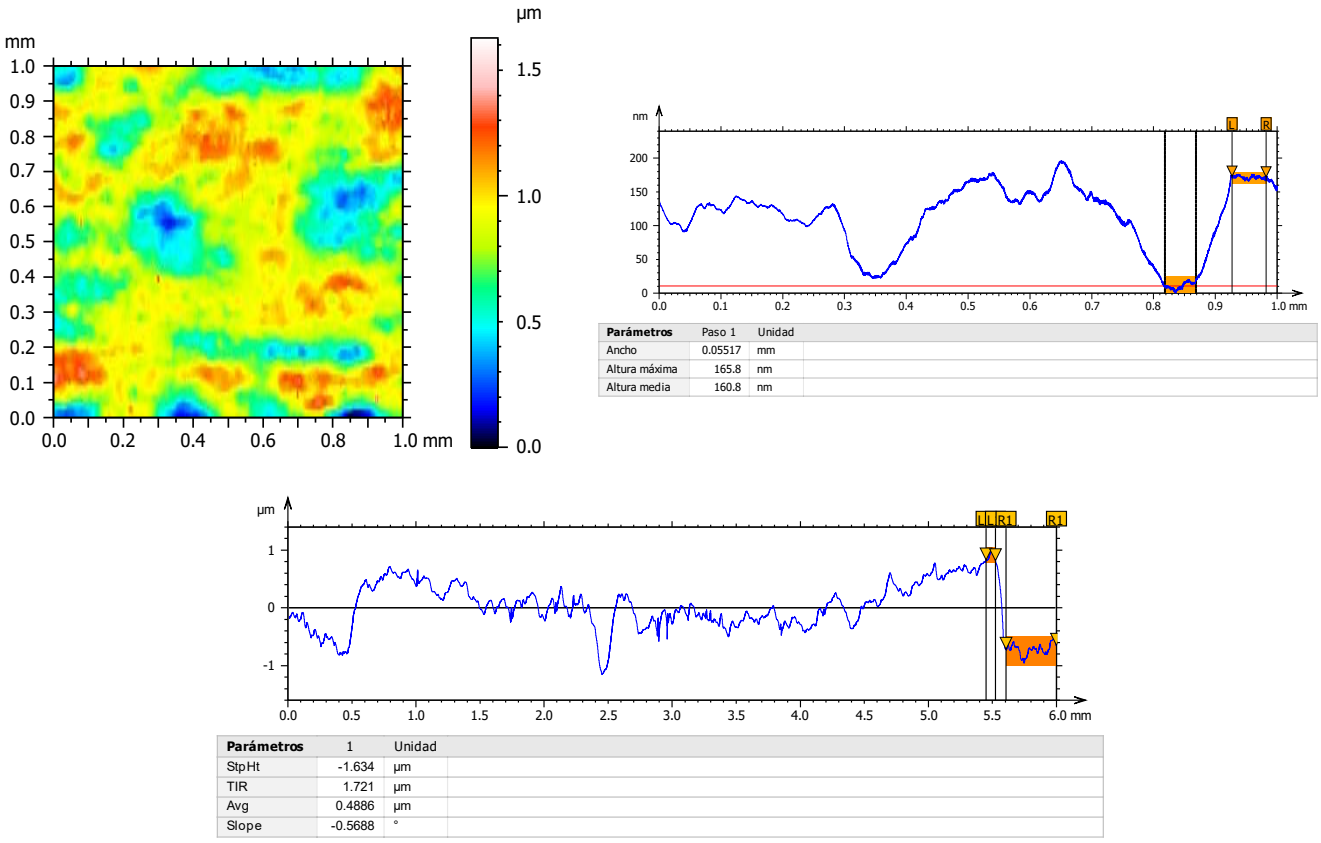

Figure 5.30. *Profilometer measurements of a crack-free pyrolized film over a 20x10 mm^2 SUNAM LSMO buffered tape, with an average thickness of 1700nm and maximum surface roughness of 160nm.*

Summarizing, we have found that the roughness on the surface is pretty similar to the ones obtained using the inkjet printing technique using the Fast Mode and substrate heating. With such results we can offer the possibility to print very high thick films in one single deposition over coated conductors.

5.5.1 Multifilamentary patterned depositions on Coated Conductors

Inkjet Printing is a deposition technique that offers the possibility to do patterned samples. One example was the one presented in chapter 3 with the combinatorial studies. With such advantage, we explored the deposition of multifilamentary patterned samples. It is known that single superconducting coatings on wide metallic tapes proved to have very high AC losses in self and external fields [197]. It has been demonstrated that dividing the full coating into multifilamentary stripes substantially reduce AC losses, as the creation of large current loops area is impeded by track separation [198]. For this reason, patterning of straight lines for the development of superconducting tapes with low AC losses could have special interest in many applications [**199**].

The printed lines require to be homogeneous, with a narrow width (≈100-150 nm) and with as close as possible to square profile to be used as proper applicable conductors. To obtain tracks it is necessary an ink with a strong pinning behaviour to the substrate. In this sense, a precise control of the deposition process is required; to avoid the merging of the printed lines and avoid liquid accumulation to reach the desired pattern.

We have been mentioning the importance of the ink physicochemical properties, such as viscosity and contact angle to control the morphology of the deposition. In addition, we have revealed the importance of enhancing solvent evaporation to increase the pinning of the solution to the substrate. Considering that our propionate-based solution has been optimized to reach these conditions while using inkjet printing technology, our proposal here is to test the 1M+1.8% EA (FF-E2) solution for patterning purposes. In this way and to advance in the field of AC losses reduction, this section seeks to advance in the formation and control of uniform and continuous YBCO tracks.

In this particular case, we had two options: Either using our discrete Slow Mode, to configure our desired patterning through our Python interface while using two nozzles, or to use our continuous Fast Mode to avoid possible nozzle clogging, which in turn increases the rate of deposition.

Fast Mode was preferred in the sense that the process can be more attractive for research and industrial groups. However, we finally decided that a combination of both processes could also be possible. The discrete mode has a very low deposition rate due to the specific movement of the nozzles at each specified x,y-coordinate of the deposition matrix, because it need to use more than one nozzle to be effective. However, we found that we can make continuous depositions if only one single nozzle is used in our Slow Mode deposition technique.

In this case, since only one nozzle is required for the deposition of samples, the specific movement of the second or other nozzles to print on top of the substrate are not involved in the process, thus the deposition end up being practically the same as in the Fast Mode, since it is only one nozzle that is jetting the solution for each specific coordinate point, and the deposition rate end up being the same, which is 0.5 mm/s.

In this way, we can make the desired deposition matrix by inputting the desired points where the drops will be deposited through our Python interface, while still depositing in continuous mode, so we are able to specify the length and width of the printed lines, together with its separation for each stripe, without having very slow depositions, regarding the time that would take to print samples if more than one nozzle would be used. We selected the deposition matrix used for full films in coated conductors, that is 100x50µm.

In our first attempt, we selected that for each stripe, 3 deposited lines would combine to form the desired straight track, using a deposition matrix of 100x50µm, with a separation for each track of 500µm. That would imply that for each track, the drops would be jetted continuously with a separation of 100 microns, forming 3 lines that will be separated by 50 microns each, in order to obtain a good overlapping. However, the width of the lines at the first attempts were not as much as straight as one would expect.

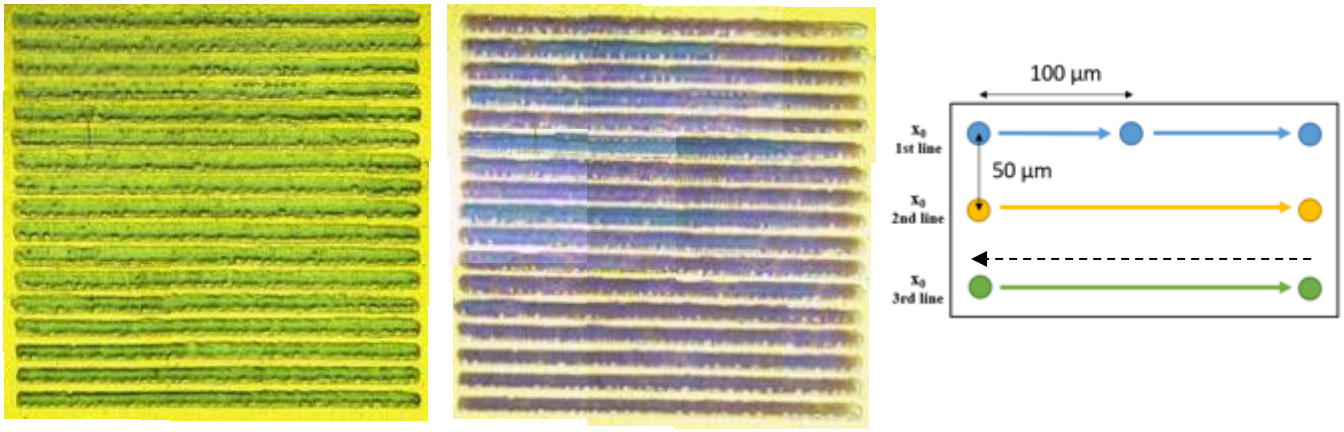

Figure 5.31. *Optical microscope images of a crack-free pyrolized multifilamentary film over a SUNAM LSMO buffered tape. Each stripe equals to 3 deposited lines of a deposition matrix of 100x50µm deposition matrix.*

Since the separation of each track was of 500µm from the first printed line, around 250±25µm are left between the tracks. As observed in the Figure 5.31 though, especially the last printed line did not completely merge, leaving some morphology resembling "indentations". In addition, there was some liquid accumulated on the very edges of each stripe, which lead to inhomogenities due to changes on the thickness at different zones of the stripes, with lengths around 450±50µm for each stripe. In theory, the stripes should be located narrower to obtain proper current percolation, with much less bulging and liquid recoil, creating indentations.

For these reasons, it was decided that the next sample would have only two deposited lines per track, and that the separation of each stripe would have the same size as the tracks, that is 200 microns. In this case, the deposition matrix proposed was using “steps”, as in the usual deposition procedure used in both inkjet printing systems, which was not considered at the first attempt to print samples. Such stepped deposition, used in the previous samples with substrate heating it has to be properly specified in the Python coordination map. That is printing one deposited line at a given initial point, while the second line will be printed at the very end of the recently printed line, in contrast to start printing again at the same initial point of the latter (Fig. 5.31 vs 5.32). With this deposition matrix, the resultant sample was much more smooth and straighter, and the separation of each track was much narrower.

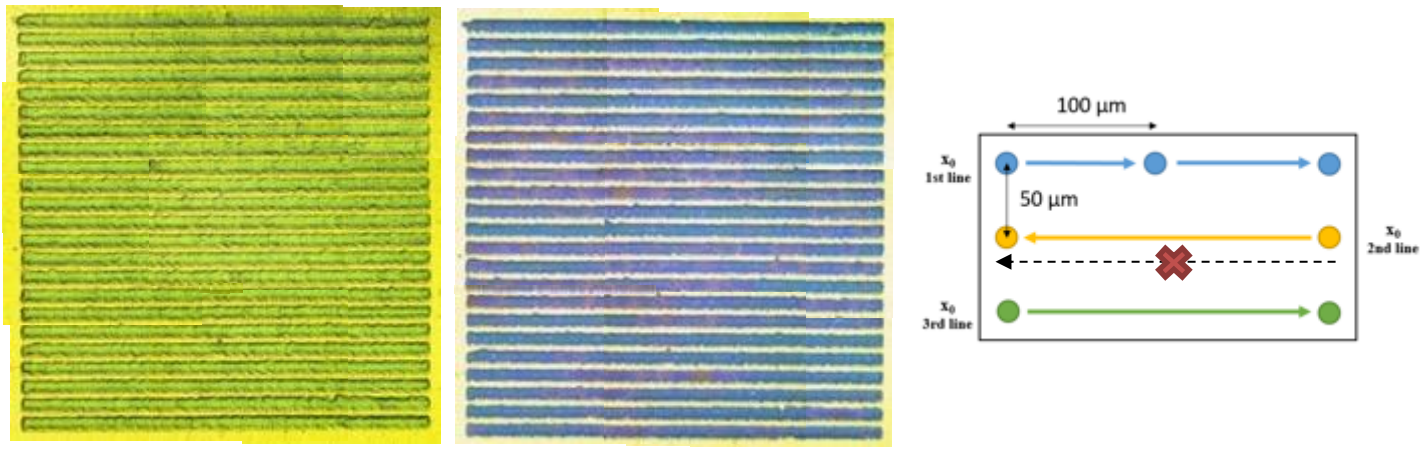

Figure 5.32. *Optical microscope images of a crack-free pyrolized multifilamentary film over a SUNAM-LSMO buffered tape. Each stripe equals to 2 deposited lines of a deposition matrix of 100x50µm deposition matrix.*

As observed (Fig. 5.32), the sample resulted on a very interesting pattern of crack-free stripes. Thanks to the optimization of the solution, and the use of substrate heating, the sample was much better in terms of morphology (comparison with Fig. 5.31). The lines were more well defined, straighter and more homogeneous, although with a semi-rounded shape (shown by perfilometry in Figure 5.33).

Calculations from these perfilometry profiles give that stripes had a FWHM width of 215±10µm with a FWHM distance between stripes of 196±9µm. The average thickness of the stripes of that sample after pyrolysis were 1.1±0.04µm. However, we identified some thickness variations within each stripe of 1±0.23µm. This thickness variations are expected to be translated to ≈500±0.1nm thick YBCO stripes after the TLAG growth. As future work, investigations in the direction to minimize the thickness inhomogeneity within each stripe could be envisaged by further tuning the drop overlapping specially by using nozzles with a narrower orifice diameter. This should generate smaller drops with less drop impact diameter, enhancing the capacity to tune the drop distribution.

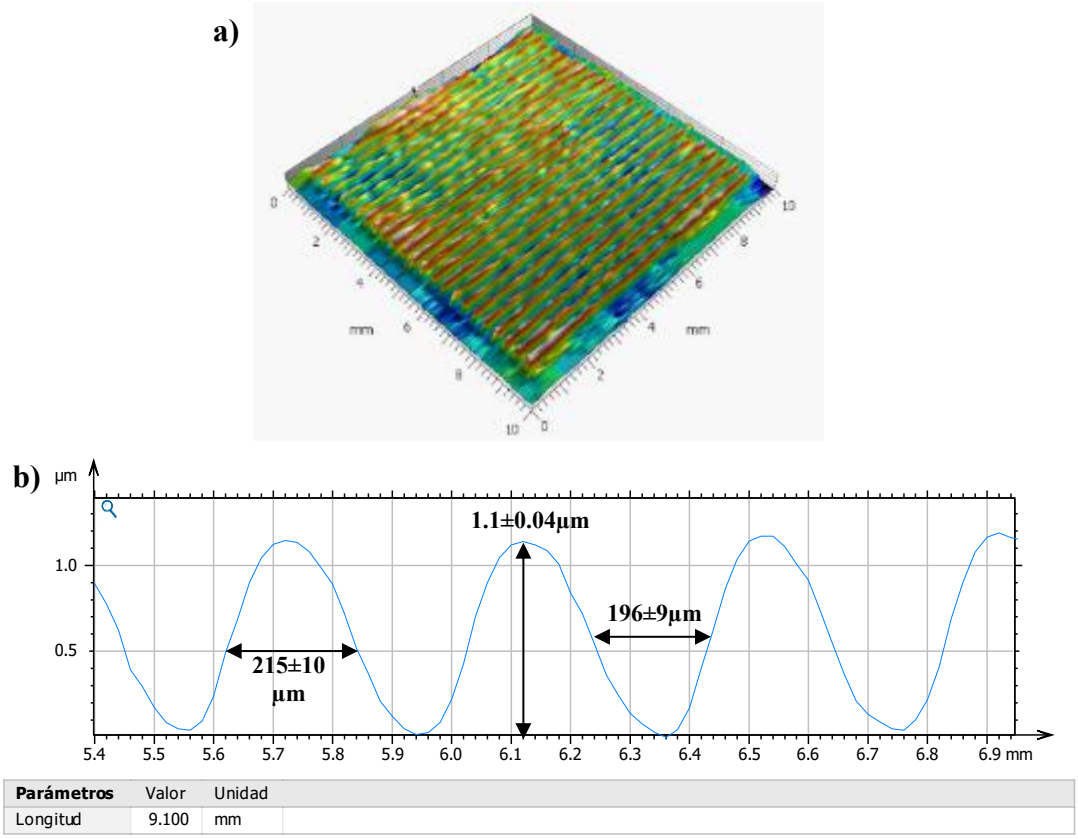

Figure 5.33. *Profilometer measurements of a multifilamentry sample. (a) 3D representation of two stripes. (b) Thickness measurement of the stripes and OM measurements of the distances.*

The developments carried out confirm the feasibility to generate crack-free layers using our optimized deposition procedure through inkjet printing technology. We are able to directly print YBCO precursor tracks without the need to use pre-patterning procedures, such as in the case lithographic techniques [**78**], avoiding time-consuming procedures and making the process attractive to some applications. Nonetheless, further improvements should be done if we want to use these multi-lane deposition as multifilament samples for low ac-losses devices like ac-cables, transformers or generators. For that purpose, a thorough study of the YBCO growth of the multifilament pyrolyzed samples should be attained, and the multifilament profiles should be evaluated after growth. However, these studies were beyond this Thesis work. Additionally, a proper comparison with the possible applicability of the device specifications is required, which has not been done in this thesis, although promising results could be expected.

5.6 TLAG Growth of YBCO thick films made by inkjet printing with substrate heating

Regarding the origin of the pyrolized samples previous to TLAG growth, several parameters can also affect the performance of the process and the growth rate, being especially important the film composition, homogeneity, porosity and thickness [**200-202**]. Since the deposited films by inkjet printing are usually very thick, if compared to other CSD deposition methods, we wanted to obtain information regarding its compatibility with the TLAG crystallization method.

To do so, we printed several samples with fast mode and substrate heating at 50ºC, using our optimized grid of 200x22µm and our optimized solution of 1M+1.8%$_{v/v}$ EA (FF-E2) over 5x5 mm^2 STO substrates. Usually, since we wanted to optimize the deposition and pyrolysis conditions of our inkjet printed samples, either (001)-oriented STO or LAO were suitable substrates to perform the study, because in terms of chemical compatibility and lattice mismatch were similar.

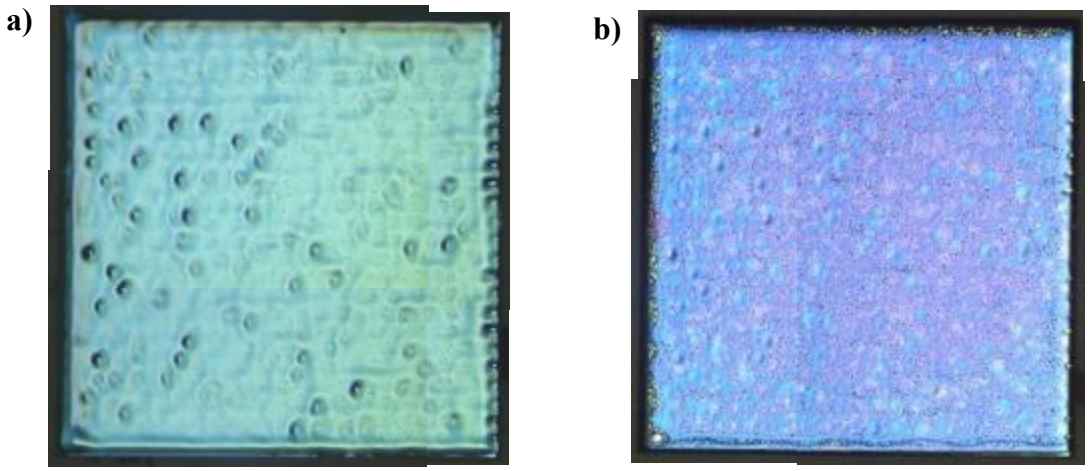

Figure 5.34. *(a) and (b) Optical microscope images of a deposited and crack-free pyrolized film over a 5x5mm^2 STO substrate.*

Most of the samples made present smooth surfaces and defect-free layers. It is important to mention however that we found more reliable to print on larger substrates (10x10 or 10x5 mm^2) than smaller ones (5x5 mm^2) mostly because the liquid could spread better thought the substrate allowing for less liquid dragging towards the edges of the substrates. In the specific case example shown in Fig. 5.34, a crack from a thicker part of the deposition is observed due to the mentioned issue of liquid dragging, however, to study the compatibility of the TLAG growth on thick films, such defect does not affect at all the microstructure (Figure 5.35).

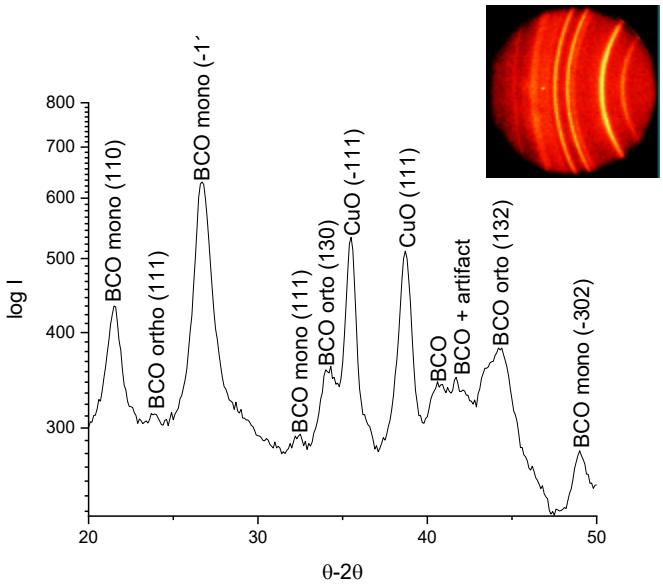

Figure 5.35. *XRD diffraction pattern of the sample from Figure 5.29.*

Since our samples have usually a very high thickness, around 1700-1800 nm after pyrolysis in this particular case, we wanted to make sure that we could eliminate the $BaCO_3$. This analysis was done using the P-route as it was easier to disentangle the $BaCO_3$ elimination reaction from the proper crystallization of YBCO, although $BaCO_3$ is more complicated to eliminate. Profilometry measurements on the sample revealed very low surface roughness with thickness beyond 1700nm after pyrolysis, as revealed in the next Fig. 5.36.

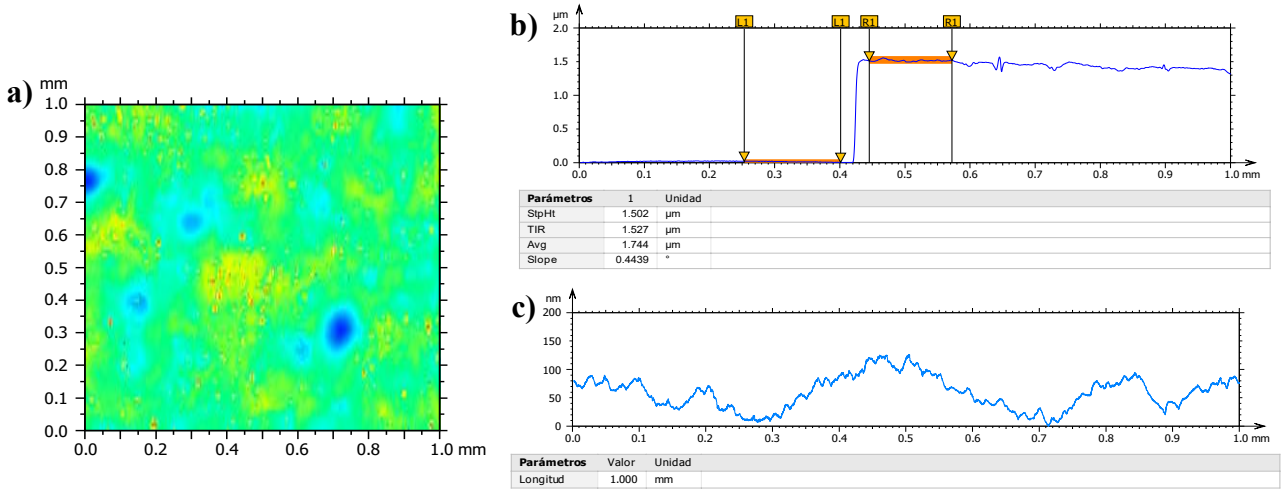

Figure 5.36. a*) 2D profilometer map of the previous sample. b) 2D profilometer measurement of the thickness (Average = 1744 nm). c) Surface roughness measurement, with less than 100nm inhomogenities.*

We performed a quench on one of the deposited samples after heating at low PO2 and before performing the high PO_2 jump where the transient liquid is formed. This should enable us to confirm the viability and compatibility of thick IJP printed layers in terms of $BaCO_3$ elimination. The sample was heated at 14ºC/min up to 835ºC, at $PO_2 = 10^{-5}$ bar, with a 2 minutes' dwell and 1.5ºC/min of cooling ramp. Afterwards, it is sealed on a vacuum container to be immediately measured using X-ray diffraction, avoiding ambient contamination and the regression of the reaction.

It is worth to mention that monoclinic barium carbonate has to transform first to its orthorhombic phase in order to react with copper oxide to form BaCuO compounds. Thus, it is preferred that there is little to none of monoclinic $BaCO_3$ presence in the pyrolized films because it might slow down the YBCO growth process [Silvia]. However, in the inkjet printed samples, the thickness of the samples makes it the preferred crystal structure. Nonetheless, we were able to almost eliminate the correspondent $BaCO_3$ completely to form the Ba-Cu-O in solid phase at the low stage of the P-route approach.

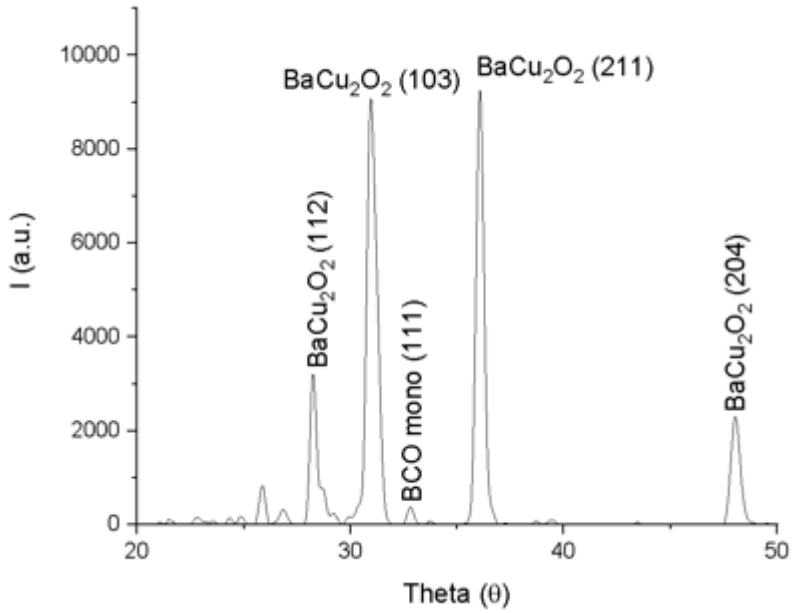

Figure 5.37. *XRD-GADDS diffraction pattern, normalized and base-substracted, of the TLAG quenched sample using the P-route approach at 10^{-5} bar and 835ºC under a heating ramp of 14ºC/min.*

The XRD measurement have shown that almost all the BCO was decomposed at such kinetic conditions. Since the $BaCO_3$ elimination reaction is detrimental for the correct development of the TLAG process, and it is in fact the limiting step of the reaction, we can claim that the inkjet printed films up to 1.8 micron in thickness after pyrolysis are fully compatible with the TLAG methodology. These results allowed us to perform a full growth process of printed samples to study the superconducting performance of the thick films. In this case, we followed a PO_2-route method by using the following conditions: A heating ramp of 14ºC/min up to 835ºC, a pressure jump from 10^{-5} bar to 1 mbar at this temperature followed by a 2 minutes' dwell. The cooling ramp was of 1.5ºC/min.

The resultant microstructure composition of the sample can be observed in the following figure:

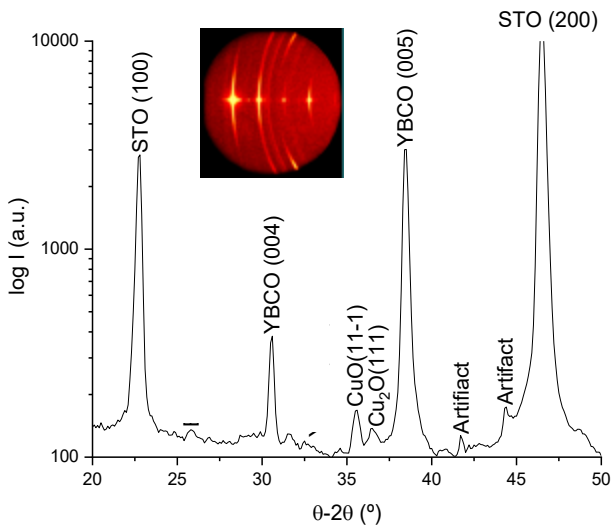

Figure 5.38. *XRD diffraction pattern of the TLAG grown sample using the P-route approach from 10^{-5} bar to 1 mbar at 835ºC, with a 2 minutes' dwell under a heating ramp of 14ºC/min.*

Almost no secondary phases could be seen in the diffraction pattern: the presence of CuO is expected and predominant, due to the addition of excess copper present on the stoichiometry of the precursor solution (3:7), while all $BaCO_3$ have finally disappeared after the pressure jump. The peaks corresponding to the YBCO phase are the most intense, corresponding to the epitaxial [00L] peaks. From these experiments, we could conclude that TLAG is compatible with the inkjet printing samples prepared. Both the decomposition reaction of $BaCO_3$ at the low-pressure stage of P-route, together with the successful synthesis of almost fully c-axis epitaxial YBCO layers through the TLAG methodology allow us to obtain thick films prepared with inkjet printing techniques.

The combination of both techniques (TLAG and IJP), together with the usage of Fluorine-Free precursor solutions, make another step towards implementing superconducting materials at a reduced cost and in environmentally friendly manner. In this case, inkjet printing technology allows for depositing thick samples in the range of 1800nm after pyrolysis in one single deposition, which per se it is a technology that allow to reduce time-consuming processes and reduce the production cost.

Once the X-ray diffraction patterns detected the formation of epitaxial YBCO synthesis with successful results, the samples were characterized by means of TEM and SEM techniques, while the superconducting measurements were carried out at a SQUID magnetometer.

SEM images of the sample grown via P-route (Figure 5.39) revealed that YBCO grains were homogenously distributed through the whole film and with great epitaxy along the c-axis, with some secondary phases aggregated on top of the surface. The crystalline growth was far more oriented and homogenous, with no dewetting on the samples. Dewetting is the result of the formed eutectic liquid to not fully disperse across the film. This phenomenon leads to visible holes in the film.

These holes are detrimental to the critical current density of the superconducting film inhibiting the electrical current percolation across the film, which is not observed in this case. Particles precipitates at the surface correspond to the CuO originating from the excess copper needed for the TLAG method. Overall, it can be concluded that the sample grown through P-route is homogenous and shows epitaxial YBCO formation, so it is expected that these samples will present competitive Jc values.

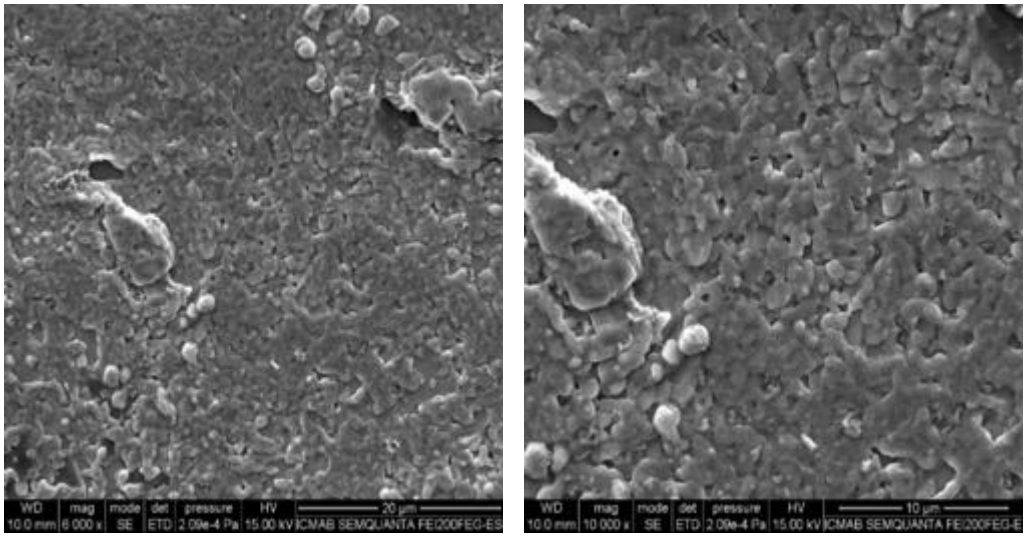

Figure 5.39. *SEM images of inkjet printing samples using Fast Mode and substrate heating with an average thickness of 800nm after growth, showing good YBCO epitaxy.*

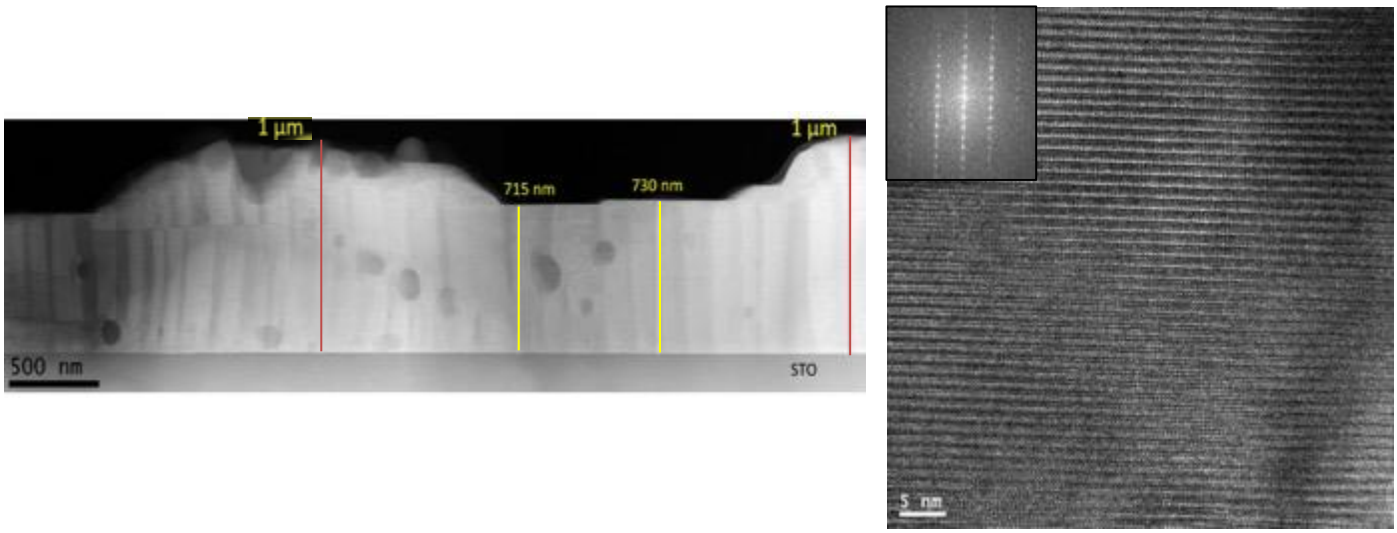

Figure 5.40. *TEM and HRTEM images of inkjet printing samples grown using the P-route of TLAG.*

In agreement with XRD diffraction and SEM imaginary, TEM images (Fig. 5.40) revealed a compact dense YBCO structure, with very low porosity and good microstructure homogeneity throughout the layer. In addition, TEM images revealed thicknesses arising from 700nm up to 1 micron thick layers, distributed along the sample, which confirm the availability of the inkjet printing technology to grow YBCO thick layers in the range of 1 micron in one single deposition.

We have found several regions of misoriented grains on top of epitaxial layers, for example as in Figure 5.40, where half of the layer is c-YBCO and other half is misoriented, with a misalignment of 5º or even higher values. In this region however, it can be proved that the growth performed offers new possibilities to optimize and grow samples in the range of 700nm to 1µm epitaxial c-oriented YBCO layers. TEM images had also revealed the appearance of secondary phases. Either as an inclusion or on top of the epitaxial YBCO layers. While mostly of the secondary phases belong to CuO aggregates, expected due to the excess of Cu on the precursor solution stoichiometry, also misoriented or random oriented YBCO layers, together with unreacted Ba-Cu-O, and undesired secondary phase resulted unreacted liquid. All those phases could severely affect current percolation, thus diminishing the superconducting values of the material.

Several samples grown through both growth routes were submitted to resistance and magnetization measurements. The critical temperature values are not significantly very different between these samples, becoming superconductor at near 90K values, with a very sharp transition, indicating a proper superconducting transition. From the promising XRD patterns and SEM images, we have shown that the samples grown through P-route presented high YBCO epitaxy and homogenous grain distribution. Assuming that the film thickness was around 800nm as average thickness, the superconducting critical current density was calculated in the temperature range from 5 to 100K.

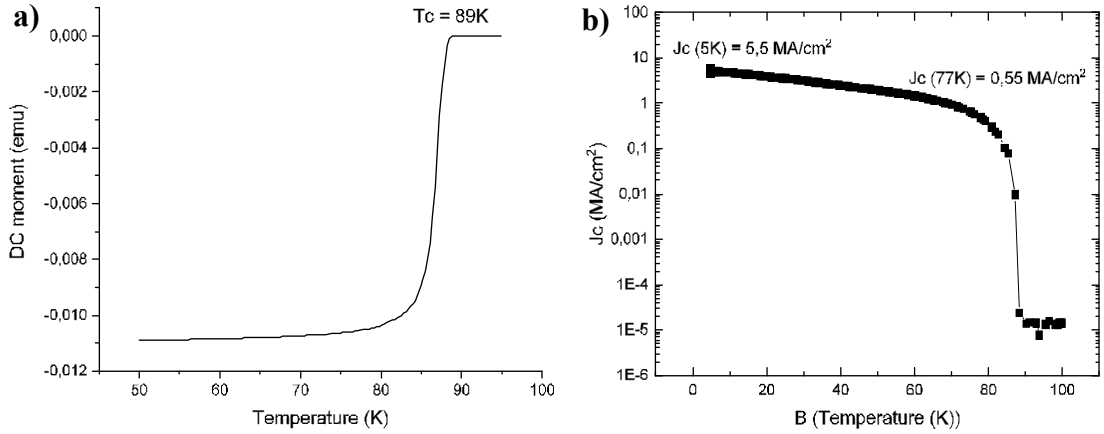

Figure 5.41. *a) Critical temperature measurement by SQUID magnetometry. b) Temperature dependence of the critical current density of inkjet printing samples using Fast Mode and substrate heating with an average thickness of 800nm after growth, measured by SQUID magnetometry.*

The Jc values obtained are already in the range where further tuning is expected to give competitive values. We should bear in mind that the processing conditions were not varied. Our assumption is that such high thick layers require further optimization regarding the growth process, in order to reduce the amount of undesired secondary phases that affect the percolation of current. The Jc value obtained, 0.55 MA/cm2 at 77K and self-field, giving an I_C = 42 MA/cm, and can be further improved in the close future.

We must mention that the study on TLAG growth was not the objective on this thesis, but with the results obtained we can confirm its good compatibility with this process. Regarding the superconducting properties, we still need a fine-tuning of the parameters to achieve a higher performance. Nonetheless, the samples shown an abrupt Tc and some degree of Jc values considering that are the first attempt to use the TLAG growth method for samples in this thickness range while utilizing the IJP methodology.

We can confirm that IJP in combination with the fast growth rates achieved to the Transient Liquid Assisted Growth (TLAG), with growth rates in the range of 100-1000 nm/s, results in a very appropriate combination of techniques that could allow to produce high-throughput and cost-effective functional superconducting CCs materials to be used in many applications once properly optimized.

5.7 Summary

While using the discrete Slow Mode for the deposition of samples using inkjet printing technology, we saw that homogenous crack-free layers could be obtained. Nonetheless, the printing method was very time-consuming due to the usage of multiple nozzles and its specific direction specified in our developed Python coordination maps, by which 5x5 mm^2 deposition over single crystals could last up to 2 hours. For that reason, the methodology was discarded as a suitable process to be scaled-up at industrial levels.

On the other hand, in order to increase the deposition rate of the samples, another modality can be used. That is the Fast Mode, where the solution is deposited using one single nozzle, in which the plate velocity increased severely. We had to find the proper deposition matrix for this particular deposition technique since the increase of the rate of deposition also lead to a different liquid behaviour, as seen also in Chapter 3, in terms of drop and line overlapping. We found that by increasing the drop pitches of the deposition matrix led to more homogenous layers, and that by using lab-made propionate salts together with ethanolamine as additive could lead to the development of crack-free layers.

Another aspect that we found detrimental to achieve crack-free thick layers was the enhancing of solvent evaporation present on the solution. Our solution, composed of high-boiling point solvents, help to redistribute the solution over the substrate thanks to the rheological properties and low contact angle achieved. However, as the rate of deposition increases, and subsequently the plate velocity does too, such as in the case of the Fast Mode at room temperature or the deposition of samples using Varnish additive in the homemade inkjet printer, there has to be an equilibrium between what is well performed in terms of liquid merging to avoid liquid dragging or the formation of defects on the sample.

In this regard, inkjet printing depositions over substrate heating seemed the most suitable arrangement to avoid such related issues, and to enhance the solvent removal to pin the liquid better into the substrate. We found the optimal deposition matrix to obtain homogenous samples, by proper drop overlapping, and also crack-free layers with very high thicknesses in one single depositions, which are translated to up to 1 micron thick YBCO layers after the TLAG growth methodology. TEM images of both pyrolized and grown YBCO films revealed very high thicknesses and homogenous microstructures.

We had to optimize the percentage in volume of ethanolamine. Ethanolamine can act as a reducing agent during pyrolysis, to form undesired and aggregated secondary phases such as Cu (I) oxides and metallic Cu species that could diminish the performance of the TLAG growth process. For that matter, we change the content of ethanolamine from 2%, which was used as a proper EA content for the Slow Mode, to 1.8% to avoid secondary phases to appear. Moreover, the use of substrate heating together with the deposition of the optimized precursor solution led to the achievement of well deposited and pyrolyzed layers also on coated conductor substrate. Defect-free multifilamentary samples were also demonstrated, although further studies are required to minimize the inhomoegenities and evaluate the potentiality for their use in devices.

Summarizing, the substrate heating together with the Fast Mode Inkjet Printing methodology is a good alternative to obtain competitive superconducting layers, with high throughput and reduced cost in combination with the TLAG-CSD method. A reproducible methodology to achieve thicker films, if compared to other CSD techniques, in one single deposition has been achieved by using a Fluorine-Free solution together with ethanolamine as additive, which in turn is more environmentally friendly if compared to the state of the art of other CSD solutions used worldwide.

6.

Conclusions

Inkjet Printing can be used as a combination of Chemical Solution Deposition (CSD) methods together with printed electronics to reach high prospection into the synthesis of functional materials. Being compatible with reel-to-reel manufacture processes, it makes it attractive at industrial scale. Inkjet printing methodologies are able to achieve high thicknesses in one single deposition, which reduces time-consuming processes and costs of production for materials, making it a useful tool for the functionalization of ceramic oxides at both lab and industrial levels.

Throughout this thesis, we have evaluated the potential of using this deposition method to obtain thick $YBa_2Cu_3O_{7-x}$ (YBCO) superconducting layers based on the use of Fluorine-Free (FF) propionate-based precursors solutions, with more environment friendly metal salts, to explore the synthesis of 1000nm thick range YBCO layers using our ICMAB TLAG-CSD growth method.

The rheology of solutions with different solvents and concentrations was thoroughly studied in order to obtain the most homogenous films as possible. We concluded that a mixture of high boiling point solvents (>100°C) was required to reach optimal homogenous depositions. Otherwise, nozzle clogging occurs. The driving waveform of the inkjet piezoelectric actuator was adapted to the solution parameters, achieving stable and reproducible drops. We optimized the drop pitch and line pitch in order to avoid liquid accumulation on the substrates, based on each inkjet deposition mode, and more specifically we studied the effect of the solution deposition rate.

In this work, two different modalities of inkjet printing depositions were presented, based on the rate of deposition and its associated moving plate velocity. We saw that there is not a single answer to solve the associated issues regarding liquid movement and defect formation that occur while using inkjet printing systems, but are closely related to control the solvent evaporation during pinning of the solution precursors onto substrate and to the mechanical strengths of the oxy-carbonates formed during the decomposition of the metalorganic salts.

In this work, we demonstrate that the substitution of trifluoroacetates precursors to fully Fluorine-Free precursors implied the apparition of a lot of defects during the deposition and the pyrolysis that needed to be studied and avoided. For high thicknesses cases, the film encounters difficulties to sustain itself during the strong densification of the pyrolysis, leading to the formation of cracks, specially once the critical thickness (t_c) is surpassed. We studied the associated decomposition reactions of the organic precursors, demonstrating that a lot of stresses are being generated in the film, and we specially identified correlation between the formation of defects and the decomposition of carboxylate compounds around 240ºC. For that reason, we proposed and studied three different approaches to solve the formation of cracks:

- Fast mode deposition and use of UV-varnish additive. We used an UV-curing polymeric additive compound in our homemade inkjet printing system, with a very fast plate movement speed (1 cm/s). In this case, the polymerization of the varnish allowed for the creation of a film that retains in place the precursor solution to avoid liquid dragging.

- Discrete deposition with ethanolamine as additive. The slow rate of deposition for this discrete deposition mode (0.017 mm/s), allowed for the fast evaporation of solvents to better pin the liquid on the substrate, which in combination with an amine additive, resulted in crack-free pyrolized layers of very good homogeneity and low porosity.

This strategy allowed us to perform high-throughput experimentation studies using a combinatorial chemistry approach to prepare compositional gradient and analyse the crystallization process.

- Fast mode deposition with substrate heating using ethanolamine as additive. This mode enabled us to increase the deposition rate up to 0.5 mm/s. However, the increase of the moving plate velocity led to liquid dragging to the very first printed lines of our samples, which resulted in huge inhomogeneities at the surface of our printed samples. For this reason, the heating of the substrates was explored to enhance the solvent evaporation. With an appropriate tuning of conditions and amount of additive, crack free layers with low porosity and homogenous microstructure, reaching up to 1800nm in thickness after pyrolysis in one single deposition, were obtained.

While the use of an UV-curing varnish allowed us to obtain homogenous deposited samples, its role during pyrolysis was not enough to suppress the tension forces that are being generated during the densification, so the generation of cracks and other defects could not be avoided. Even though several changes in the heating ramps were made, and the pyrolysis stress relief mechanisms were identified by means of in-situ imaging during the heat treatment, we could not overcome the problems that occur during the pyrolysis. This suggested us to explore and re-formulate the precursor solution with the aim to modify the intrinsic stress behaviour of the film during its densification.

Through these studies, Fluorine-Free propionate-based precursor solutions, using ethanolamine as additive, were investigated to produce superconducting YBCO films by inkjet deposition. The rheology of the solutions with different %vol. of ethanolamine was thoroughly studied in order to obtain the most stable composition for inkjet printing, to achieve the most homogenous films as possible and to avoid nozzle clogging or drop formation inhibition based on Z numbers.

However, we encountered that the preparation of thick layers could negatively influence the gas transport during pyrolysis (such as CO) which acted as a reducing agent. Such effect reduced copper species during pyrolysis, to form undesired and aggregated secondary phases such as Cu (I) oxides and metallic Cu species, which could have a deleterious effect on the ultrafast growth of the superconducting layers by the TLAG process. For that matter, we had to properly optimize the content of ethanolamine to avoid secondary phases to appear, which we successfully achieved.

By in-situ characterization tools we analyse the pyrolysis process of our inkjet printed deposited layers and identified the main role of ethanolamine during the decomposition of carboxylate precursors. We concluded that during the decomposition of the metal precursors, ethanolamine helps to strongly densify and keep the oxy-carbonate phases homogeneously distributed and in nanometric size. By proper tuning of the conditions, crack-free layers were obtained after the pyrolysis thermal treatment. Pyrolized layers up to 1700-1800nm were obtained in a reproducibly manner.

In fact, the Slow Mode available at the MicroDrop Inkjet Printer system allowed for the solution to pin better onto the substrate thanks to the enhancement of solvent evaporation. Our observations concluded that the evaporation rate is critical for the homogeneous dispersion of the liquid, avoid liquid dragging and obtain crack free layers. With all these optimizations, we could confirm the competitiveness of IJP as a Chemical Solution Deposition method for the preparation of YBCO thick films.

These conditions were used to demonstrated the powerfulness of ink-jet printing to generate compositional gradients where two different solutions could be selectively used. We verified the interest on high-throughput experimentation with combinatorial chemistry approaches and initial machine learning studies to enable fast identification of experimental growth conditions.

In particular, Drop-on-demand inkjet printing was successfully used to deposit combinatorial samples in the form of stripes of different composition, obtaining a homogeneous surface distribution during the pyrolysis step. Moreover, the methodology developed here is of general use for many different functional materials with different needs of fast screening and optimization.

On the other hand, in order to demonstrate the practical use of ink jet printing in the fabrication of TLAG superconducting films, we studied the way to obtain homogeneous pyrolyzed layers at higher deposition rates. A Fast Mode where the solution is deposited using one single nozzle, in which the plate velocity can be increased severely (from 0.5mm/s to 1cm/s) was studied. We had to find again the proper conditions, since the increase of the deposition rate lead to a different liquid behaviour.

At room temperature, we found that a modification of the deposition matrix was rather effective. While short drop pitch values lead to liquid accumulation at the edges, large drop pitch values gave unconnected patterns. In particular, the best combination resulted was a deposition matrix of 250x19μm at plate velocity of 0.5mm/s. This matrix enabled us to reach defect-free layers however large surface roughness giving rise to strong bugling was perceived.

Subsequently, a substrate heating approach was used to study the reduction of the surface roughness obtained using the optimized Fast Mode. Our assumption was that substrate heating would help to the critical steps of high boiling point solvent evaporation, by better pinning the liquid and generating homogenous patterns. Successfully, an optimal deposition matrix was found which enabled to reach low roughness and crack-free thick layers (of 1800 nm) in one single depositions. TEM images of both pyrolized and grown YBCO films revealed the very high thicknesses and homogenous microstructures. Overall, we demonstrated that the Fast Mode Inkjet Printing with substrate heating was a successful methodology to obtain thick superconducting layers, which gave rise to 1μm thick YBCO grown films with the TLAG growth methodology.

Next, we expanded these findings to explore IJP depositions on coated conductors' substrates, using the architecture of SuNAM metallic tape with an LSMO buffer layer. We re-tuned the deposition matrix and achieved high thickness homogeneous and crack-free pyrolyzed layers similarly as with single crystals substrates. In addition, we used this same methodology to draw multifilamentary patterns with the IJP system on coated conductors' substrates, achieving narrow straight lines in the range of 215±10μm with a separation of 196±9μm. Such depositions confirm the potentiality of the metalorganic precursor solution developed and the IJP mode investigated in realization of low ac-losses superconducting coated conductors.

We finally verified that these ink jet printed deposited layers satisfied the requirements for TLAG growth, although further optimization is required for the optimization of their superconducting properties.

As final outlook, we want to state the relevant role of the evaporation of the solvent and the need to tune the different IJP parameters to obtain high quality layers. We found that in order to achieve crack-free thick layers, a compromise between solvent evaporation and liquid deposition speed was needed. We want to emphasize the relevance of properly formulating the precursor solution to be employed. Our solution was composed of high-boiling point solvents and contained the precise amount of specific amine, which also ensured the rheological properties to properly distribute the solution over the substrate.

However, as the rate of deposition was increased, a re-optimization of the ink jet printing parameters was needed to ensure proper liquid merging and at the same time avoid liquid dragging to avoid the formation of defects. In this case, a key parameter was the substrate heating to enhance the solvent evaporation at the high deposition rates.

Finally, we want to remark that only by the complementarity of the characterization techniques employed we could understand the deposition, evaporation and pyrolysis processes to identify the relevant mechanisms and optimize the multiple parameters. Especially important were the in-situ technique (thermal analysis and in-situ visualization), the rheological characterization and the transmission electron microscopy.

This thesis demonstrated the feasibility of using DoD inkjet printing technologies for solution deposition of coated conductors at high throughput and reduced cost. Additionally, it opened the path towards the fabrication of patterned tapes for reduced ac-losses and the fabrication of compositional gradients, both things only possible by this deposition technique, by which we expect further development and progress in the state-of-the art.

7.
Appendix

7.1 Appendix A

Here, we submit the in-situ imaging of the pyrolysis of the several samples made through the pyrolyzer system (chapter 3 & 5). Also we include some of the videos related to the intrinsic movement of the moving plate of our inkjet printing systems and/or its different deposition modes (chapter 4 & 5). Youtube web-links:

Video 1 – In-situ Imaging of the pyrolysis using a UV-Curable Varnish:

https://youtu.be/OH1n8HkA98I

Video 2 - Discrete Deposition Mode - MicroDrop IJP System:

https://youtu.be/eXHG1hhHuHg

Video 3 - Fast Mode deposition - MicroDrop IJP System:

https://youtu.be/y_zIRGnSTuk

Video 4 - In-situ Imaging of the Pyrolysis of an IJP films using substrate heating and Fast Mode:

https://youtu.be/E0GVW6HYRHs

7.2 Appendix B

To obtain information regarding the decomposition of barium carbonate, the formation of Ba-Cu-O liquids and the formation of epitaxial YBCO, ultra-fast acquisition of in-situ XRD synchrotron system were made. With the aim of defining the intermediates and secondary phases during in the interesting growth regions using the P_{O2}-route for thick films made by inkjet printing, and check for the compatibility of the TLAG process for thick inkjet printed samples.

The in-situ XRD experiments were performed on ternary $BaCO_3$-Y_2O_3-CuO pyrolized inkjet printed films using the Fast Mode and substrate heating, with the precursor solution of 1M+1.8%EA in 1-butanol and propionic acid as solvents. In-situ XRD synchrotron analysis were carried out at DiffAbs beamline at SOLEIL synchrotron with a beam energy of 18 keV. An area detector (X-ray hybrid pixel area detector, XPAD) was used with acquisition times per data point of 100 ms [**203**]. To follow random phases, grazing XRD scans were recorded, whereas to follow YBCO growth the Bragg conditions with the (005) peak were met (θ–2θ geometry).

The experiments were run in a DHS 1100 Anton Paar heater covered with a graphite dome, equipped with a double connection to the vacuum pumps and to the gas inlet system. Electrovalves were used to modulate the total pressure, while an oxygen sensor was used to pre-set the PO2. For the PO2-route used, a combination of N2 and Air gases were mixed with a mass flow controller to meet the required conditions PO2 conditions.

We analyzed the resulting diffraction patterns among time, resulting in the total decomposition of Barium carbonate species of the sample, the formation of Ba-Cu-O species, liquid formation, but also the formation of secondary phases such as metallic Cu. All of the secondary species though, disappear once epitaxial YBCO begins to nucleate and grow.

The resulting growth rate of the sample was of 30 nm/s, much less than the obtained on samples made with other CSD methodologies, implying that the TLAG growth of thick samples made with inkjet printing require further optimization. Nevertheless, in-situ XRD measurements confirm the compatibility of TLAG for inkjet printing samples.

7.3 Appendix C

Thermo-Mechanical Analysis is a novel in-situ characterization technique that aims for the identification of the mechanical properties of the films at different stages of the pyrolysis process, such as the viscous deformation behaviour of the films, especially at the first stages of the thermal process.

Regarding our situation, we wanted to use in-situ technique to identify different behaviours on the films regarding the mode of deposition used, that is the discrete Slow Mode or the Fast Mode to compare the film behaviour under temperature for both of them. TMA consist on the application of a given force value (N) with the use of a glass probe to measure film viscosity.

To do so, the film viscosity was calculated by the following expression, based on the Stoke's equation, with some simplifications, relating the velocity of the probe to the experimental conditions and the viscosity of the film by the following expression:

$$v = \frac{F}{6\pi\eta R^2}\frac{(2H - h_0)^2 h_0}{4(H - h_0)^2}$$

where F is the applied load; η, viscosity; H, the film thickness; h0, the probe-substrate distance and R the radius of the hemispherical probe end.

Being as it is, an equation of velocity based on a given displacement over time, to obtain the viscosity values (η), an integration of the equation must be done by (v = -dh0/dt), which gives:

$$t = \alpha\left\{\frac{2}{2 - \frac{h_0}{H} - 2 + ln\left[\left(2 - \frac{h_0}{H}\right)^3 \frac{h_0}{H}\right]}\right\}$$

Where:

$$\alpha = \left(\frac{6\pi R^2}{F}\right)$$

When time is normalized to α and h_0 in front of the film thickness H, we have:

$$\tau = -\left\{\frac{2}{2-\delta} - 2 + ln[(2-\delta)^3\delta]\right\}$$

Where:

$$\tau = \frac{t}{\alpha}; \quad \delta = \frac{h_0}{H}$$

Changing the time and displacement scales until the theoretical and experimental curves overlap result on the proper fitting of the TMA curves. As an example, as α is the ratio between Δt and Δτ, when δ=1 implies that the probe enters in contact with the film upper surface, and δ=0 results on the asymptotic value of the displacement.

From the value of α the viscosity can be obtain as:

$$\eta = \frac{F}{6\pi R^2 \alpha}$$

In this sense, the viscosity values obtained are related to several aspects and characteristics of the film, such as porosity, thickness and homogenous microstructure.

Our assumption was that films deposited under the substrate heating regime had higher viscosity values, and present higher mechanical resistance to defect formation, such as cracks. With this hypothesis in mind, an increase in viscosity would imply a decrease on film deformation due to stress, minimizing defect formation.

We analysed several samples from different inkjet printing types of deposition, especially those coming from the different performed Modes of deposition to check for the similarities and differences in terms of mechanical resistance and viscosity. We wanted to make sure the reliability of the measurements to prove that the glass probe was correctly set and that displaces to touch the substrates of the sample by optical microscope and profilometer measurements.

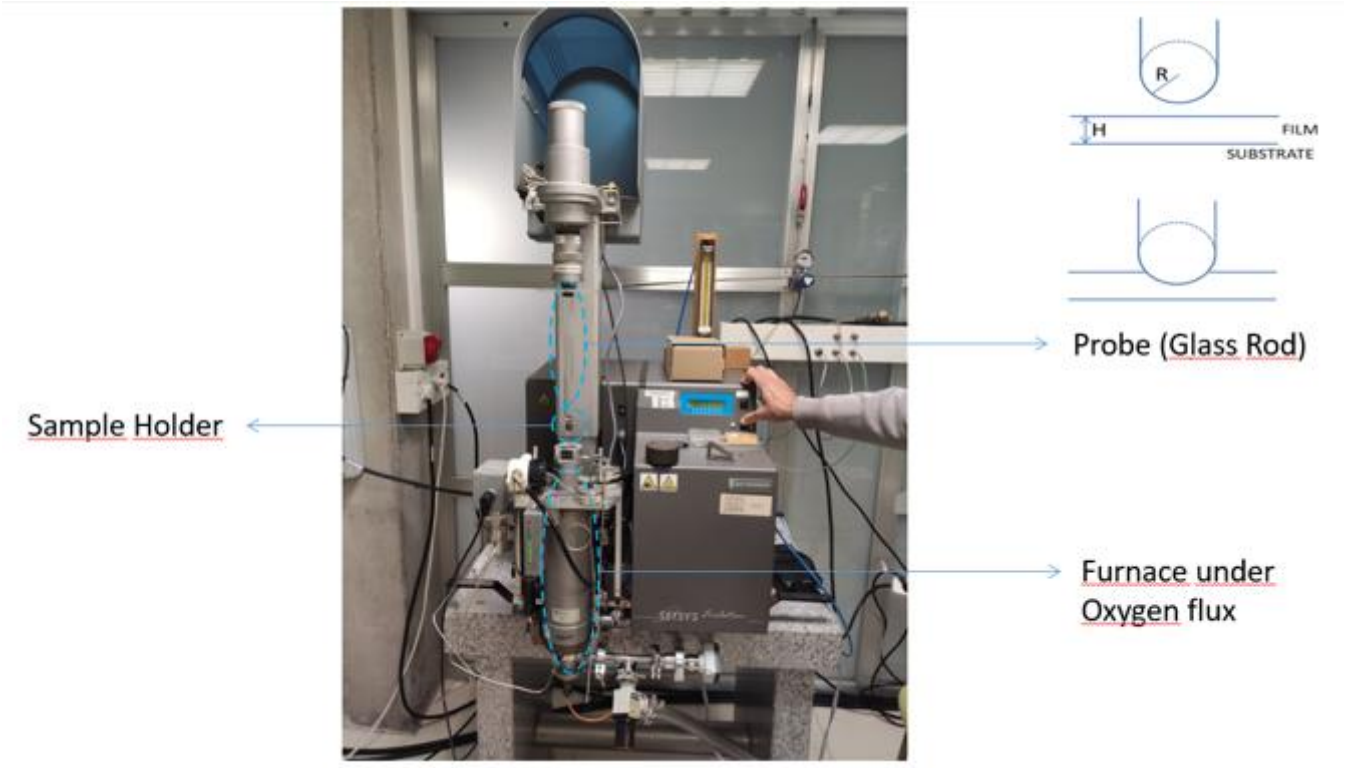

Figure 7.1. *Image of the TMA system.*

As seen, profilometer results show that the TMA measurements were correct, both in terms of probe displacement and applied force, to reach the desired experimental set to compare the results on both samples. In Fig. 7.2, two measurements made on films dried at 100ºC after deposition were transferred to the TMA system the next day that they were deposited:

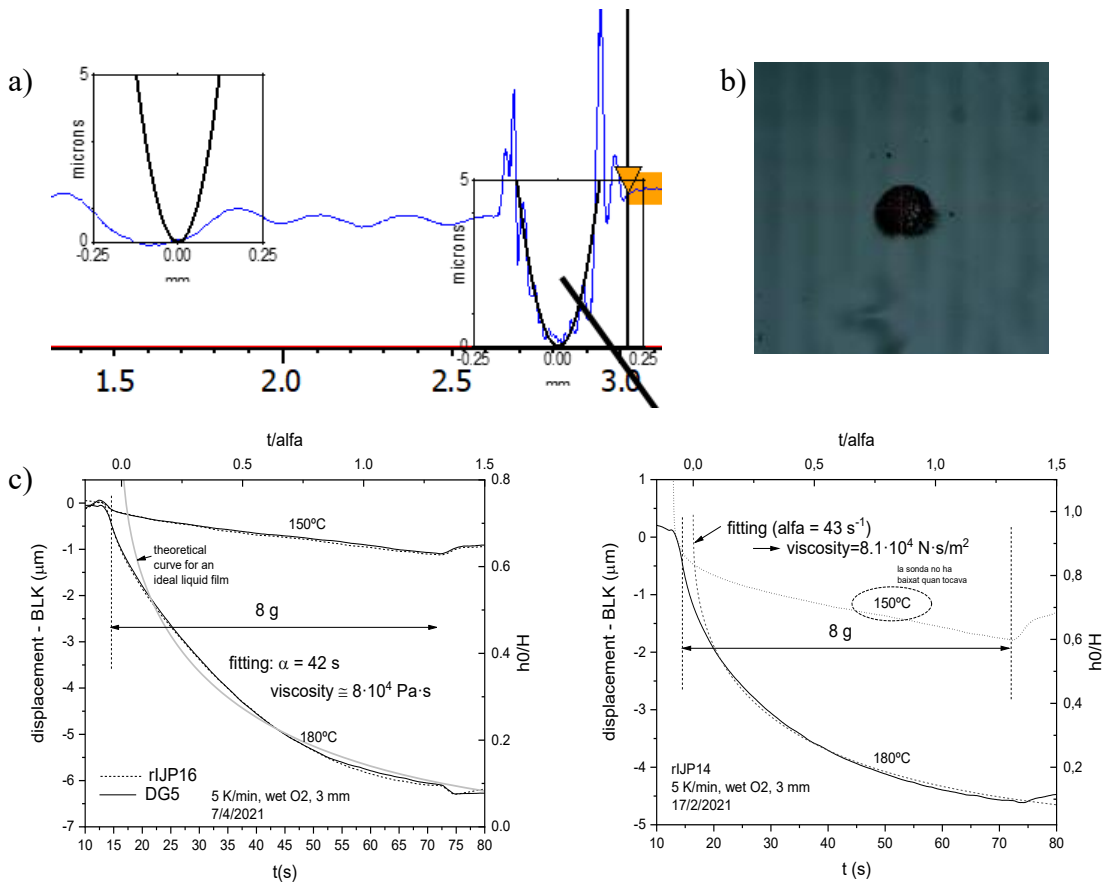

Figure 7.2. *a) Profilometer measurement of the applied glass probe to the film. b) Optical microscope image of the probe footprint. c) TMA fitting curves for Discrete Mode and Continuous Mode with substrate heating.*

Unexpectedly, as we made sure that analysis was properly set, both viscosity measurements on the discrete slow mode and the fast mode with substrate heating gave the same viscosity results. This implies that the film microstructure, thickness and pyrolysis did not come from the mechanical resistance parameters of the films, but rather on the intrinsic chemical properties of the precursor solution and more importantly, the type of deposition by which the samples were prepared rather than other factors.

8.
References

1. Larbalestier D., Gurevich A., Feldmann D. M. and Polyanskii A. High-Tc superconducting materials for electric power applications. Nature, 414: 368–77, (2001).
2. Hahn S., Kim K., Hu X., Painter T., Dixon I., Kim S., Bhattarai K. R., Noguchi S., Jaroszynski J. and Larbalestier D. C. 45.5-Tesla Direct-Current Magnetic Field Generated with a High-Temperature Superconducting Magnet. Nature, 570: 496–9, (2019).
3. Haran K. S., Kalsi S., Arndt T., Karmaker H., Badcock R., Buckley B., Haugan T., Izumi M., Loder D., Bray J. W., Masson P. and Stautner E. W. High power density superconducting rotating machines - Development status and technology roadmap. Supercond. Sci. Technol., 30, (2017).
4. Chow C. T., Ainslie M. D. and Chau K. T. High temperature superconducting rotating electrical machines: An overview. Energy Reports, 9: 1124–5, (2023).
5. MacManus-Driscoll J. L. and Wimbush S. C. Processing and application of high-temperature superconducting coated conductors. Nat. Rev. Mater., 6: 587–604, (2021).
6. D. Larbalestier, A. Gurevich, D.M. Feldmann, and A. Polyanskii. High Tc superconducting materials for electric power applications. Nature, 414: 368, (2001).
7. M. Tinkham. Introduction to Superconductivity. McGraw-Hill, Singapore, (1996).
8. Orenstein, J. Advances in the Physics of High-Temperature Superconductivity. 288(April), 468–475, (2000).
9. MacManus-Driscoll J. Materials Chemistry and Thermodynamics of ReBa2Cu3O7-x. Adv. Mater. 9 457–73, (1997).
10. Maggio-Aprile, I., Renner, C., Erb, A., Walker, E., & Fischer. Direct vortex lattice imaging and tunnelling spectroscopy of flux lines on YBa2Cu3O7-δ. Physical Review Letters, 75(14): 2754–2757, (1995).

11. Llordés, A.; Palau, A.; Gázquez, J.; Coll, M.; Vlad, R.; Pomar, A.; Arbiol, J.; Guzmán, R.; Ye, S.; Rouco, V.; Sandiumenge, F.; Ricart, S.; Puig, T.; Varela, M.; Chateigner, D.; Vanacken, J.; Gutiérrez, J.; Moshchalkov, V.; Deutscher, G.; Magen, C.; Obradors, X., Nanoscale strain-induced pair suppression as a vortex-pinning mechanism in high-temperature superconductors. Nat. Mat., 11: 329-336, (2012).
12. MacManus-Driscoll J. L., Foltyn S. R., Jia Q. X., Wang H., Serquis A., Civale L., Maiorov B., Hawley M. E., Maley M. P. and Peterson D. E. Strongly enhanced current densities in superconducting coated conductors of YBa2Cu3O7-x + BaZrO3. Nat. Mater., 3: 439, (2004).
13. Engel S., Thersleff T., Hühne R., Schultz L. and Holzapfel B. Enhanced flux pinning in YBa2Cu3O7 layers by the formation of nanosized BaHfO3 precipitates using the chemical deposition method. Appl. Phys. Lett., 90: 7–9, (2007).
14. Figueras J., Puig T., Obradors X., Kwok W. K., Paulius L., Crabtree G. W. and Deutscher G. The loss of vortex line tension sets an upper limit to the irreversibility line in YBa2Cu3O7. Nat. Phys. 2 402–7, (2006).
15. Coll M., Ye S., Rouco V., Palau A., Guzman R., Gazquez J., Arbiol J., Suo H., Puig T. and Obradors X. Solution-derived YBa2Cu3O7 nanocomposite films with a Ba2YTaO6 secondary phase for improved superconducting properties. Supercond. Sci. Technol., 26: 015001, (2013).
16. Palau A., Bartolomé E., Llordés A., Puig T. and Obradors X. Isotropic and anisotropic pinning in TFA-grown YBa2Cu3O7-x films with BaZrO3 nanoparticles. Supercond. Sci. Technol. 24: 125010, (2011).
17. Miura M., Maiorov B., Baily S. A., Haberkorn N., Willis J. O., Marken K., Izumi T., Shiohara Y. and Civale L. Mixed pinning landscape in nanoparticle-introduced YGdBa2Cu3Oy films grown by metal organic deposition Phys. Rev. B., 83: 184519, (2011).
18. Gutiérrez J., Puig T. and Obradors X. Anisotropy and strength of vortex pinning centers in YBa2Cu3O7−x coated. Appl. Phys. Lett., 90: 162514, (2007).
19. Plain J., Puig T., Sandiumenge F., Obradors X. and Rabier J. Microstructural influence on critical currents and irreversibility line in melt-textured YBa2Cu3O7-x reannealed at high oxygen pressure. Phys. Rev. B - Condens. Matter Mater. Phys. 65 1–10, (2002).
20. Izumi T. and Nakaoka K. Control of artificial pinning centers in REBCO coated conductors derived from the trifluoroacetate metal-organic deposition process. Supercond. Sci. Technol., 31: 034008, (2018).

21. X. Obradors, T. Puig, A. Pomar, F. Sandiumenge, N. Mestres, M. Coll, A. Cavallaro, N. Roma, J. Gazquez, J.C. Gonzalez, O. Castano, J. Gutierrez, A. Palau, K. Zalamova, S. Morlens, A. Hassini, M. Gibert, S. Ricart, J.M. Moreto, S. Pinol, D. Isfort, and J. Bock. Progress towards all-chemical superconducting YBa2Cu3O7-coated conductors. Superconductor Science and Technology, 19: S13, (2006).
22. D.P Norton. Synthesis and properties of epitaxial electronic oxide thin-film materials. Materials Science and Engineering, R43: 139, (2004).
23. J.R. Waldram. Superconductivity of Metals and Cuprates. Institute of Physics Publishing, London, (1996).
24. F. Beech, S. Miraglia, A. Santoro, and R.S. Roth. Neutron study of the crystal structure and vacancy distribution in the superconductor Ba2YCu3O7. Physical Review B, 35: 8778, (1987).
25. Jareño Cerulla, J. Transient Liquid Assisted Growth of Superconducting Nanocomposite Films. PhD Thesis, Universitat Autonoma de Barcelona, (2020).
26. M.K. Wu, J.R. Ashburn, C.J. Torng, P.H. Hor, R.L. Meng, L. Gao, Y.Q. Huang, Z.J.and Wang and C.W. Chu. Superconductivity at 93K in a new mixed-phase YBa-Cu-O compound system at ambient pressure. Physical Review Letters, 58: 908, (1987).
27. Raffy H., Li Z. and Auban-Senzier P. Transport properties of very overdoped nonsuperconducting Bi2Sr2CuO6+δ thin films Phys. Rev. B 106 1–9, (2022).
28. Vignolle B., Carrington A., Cooper R. A., French M. M. J., Mackenzie A. P., Jaudet C., Vignolles D., Proust C. and Hussey N. E. Quantum oscillations in an overdoped high-Tc superconductor. Nature 455 952–5, (2008).
29. Durrell J. H. and Rutter N. A. Importance of low-angle grain boundaries in YBa2Cu3O7-δ coated conductors. Supercond. Sci. Technol. 22 013001, (2009).
30. X. Obradors and T. Puig. Coated conductors for power applications: materials challenges. Superconductor Science and Technology, 27: 044003, (2014).
31. Foltyn S. R., Civale L., Macmanus-Driscoll J. L., Jia Q. X., Maiorov B., Wang H. and Maley M. Materials science challenges for high-temperature superconducting wire. Nat. Mater. 6 631–42, (2007).
32. Kang S., Goyal A., Li J., Gapud A. A., Heatherly L., Thompson J. R., Christen D. K., List F. A., Paranthaman M. and Lee D. F. High-Performance High-Tc superconducting wires Science. (80-311): 1911–5, (2006).

33. M. Paranthaman and T. Izumi. High-performance YBCO-coated superconductor wires. Materials Research Bulletin, 8: 533, (2004).
34. Iijima Y., Tanabe N., Kohno O. and Ikeno Y. In-plane aligned YBa2Cu3O7−x thin films deposited on polycrystalline metallic substrates Appl. Phys. Lett., 60: 769, (1999).
35. Shiohara Y., Yoshizumi M., Takagi Y. and Izumi T. Future prospects of high Tc superconductors-coated conductors and their applications. Phys. C Supercond. its Appl., 484: 1–5, (2013).
36. Y. Iijima and K. Matsumoto. High-temperature-superconductor coated conductors: technical progress in Japan. Superconductor Science and Technology, 13: 68, (2000).
37. Malozemoff A. P. Second-Generation High-Temperature Superconductor Wires for the Electric Power Grid. Annu. Rev. Mater. Res., 42: 373–97, (2012).
38. Goyal, M. Paranthaman, and U. Schoop. The RABITS approach: using rolling assisted biaxially textured substrates for high-performance YBCO superconductors. Materials Research Bulletin, 8: 552, (2004).
39. Y. Iijima, K. Kakimoto, Y. Yamada, T Izumi, T. Saitoh, and Y. Shiohara. Research and development of biaxially textured IBAD-GZO templates for coated conductors. Materials Research Bulletin, 8: 564, (2004).
40. Matias V. and Hammond R. H. YBCO superconductor wire based on IBAD-textured templates and RCE of YBCO: Process economics. Phys. Procedia, 36: 1440–4, (2012).
41. Braccini V., Xu A., Jaroszynski J., Xin Y., Larbalestier D. C., Chen Y., Carota G., Dackow J., Kesgin I., Yao Y., Guevara A., Shi T. and Selvamanickam V. Properties of recent IBAD-MOCVD coated conductors relevant to their high field, low temperature magnet use. Supercond. Sci. Technol. 24 035001, (2011).
42. Jha, A. K.; Matsumoto, K., Superconductive REBCO Thin Films and Their Nanocomposites: The Role of Rare-Earth Oxides in Promoting Sustainable Energy. Front. Phys., 7, 82. (2019).
43. Miura M., Ichikawa H., Sutoh Y., Nakaoka K., Yoshizumi M., Yamada Y., Izumi T. and Shiohara Y. Development of multi-turn reel-to-reel crystallization large furnace for high production rate of YBa2Cu3Oy coated conductors derived from TFA-MOD process. Phys. C Supercond. its Appl. 469 1336–40, (2009).
44. R.W. Schwartz, T. Schneller, and R. Waser. Chemical solution deposition of electronic oxide films. Comptes Rendus Chimie, 7: 433, (2004).
45. T. Schneller, R. Waser, M. Kosec, and D. Payne. Chemical solution deposition of functional oxide thin films. Springer, (2013).

46. Albiss, B. A., & Obaidat, I. M. Applications of YBCO-coated conductors: a focus on the chemical solution deposition method. J. Mater. Chem.,20, 1836-1845 (2010).
47. M. S. Bhuiyan et al. Solution-derived textured oxide thin films - a review. Supercond. Sci. Technol. 19 R1, (2006).
48. Gokhale P, Mitra D, Sowade E, Mitra KY, Gomes HL, Ramon E, Al-Hamry A, Kanoun O, Baumann RR. Controlling the crack formation in inkjet-printed silver nanoparticle thin-films for high resolution patterning using intense pulsed light treatment. Nanotechnology. Dec 8;28(49):495301, (2017).
49. T. Honjo, Y. Nakamura, Y. Shiohara, Y. Iijima, and others. Fabrication and growth mechanism of YBCO coated conductors by TFA-MOD process. Physica C: Superconductivity, 392:873881, (2003).
50. Haertling G. H. Ferroelectrics 116: 51, (1991).
51. D. E. Wesolowski, M. Yoshizumi, and M. J. Cima. Trajectory-property relationships in MOD derived YBCO films. Physica C: Superconductivity and its applications, 450(1-2):7682, 2006.
52. L. Ciontea. Metal propionate synthesis of epitaxial. J. Phys.: Conf. Ser. 97: 012302, 2–8. (2008).
53. Rasi, S. Advanced Thermal Analysis of REBCO Superconductor Precursor Films and Functional Oxides. PhD Thesis, Universitat de Girona, (2019).
54. X. Obradors, T. Puig, S. Ricart, M. Coll, J. Gazquez, A. Palau, and X. Granados. Growth, nanostructure and vortex pinning in superconducting YBa2Cu3O7 thin films based on trifluoroacetate solutions. Superconductor Science and Technology, 25: 123001, (2012).
55. Pop, C.; Villarejo, B.; Pino, F.; Mundet, B.; Ricart, S.; de Palau, M.; Puig, T.; Obradors, X., Growth of All-Chemical High Critical Current $YBa_2Cu_3O_{7-\square}$ Thick Films and Coated Conductors. Supercond. Sci. Technol. 2019, 32, 015004.
56. Palmer X., Pop C., Eloussifi H., Villarejo B., Roura P., Farjas J., Calleja A., Palau A., Obradors X., Puig T. and Ricart S. Solution design for low-fluorine trifluoroacetate route to YBa2Cu3O7 films. Supercond. Sci. Technol. 29 024002, (2016).
57. Llordés, K. Zalamova, S. Ricart, A. Palau, A. Pomar, T. Puig, A. Hardy, M. K. Van Bael, and X. Obradors. Evolution of Metal Trifluoroacetate Precursors in the Thermal Decomposition towards High Performance YBa2Cu3O7 Superconducting Films. Chemistry of Materials, 22(5):16861694, 2010.

58. Gupta A., Jagannathan R., Cooper E. I., Giess E. A., Landman J. I. and Hussey B. W. Superconducting oxide films with high transition temperature prepared from metal trifluoroacetate precursors. Appl. Phys. Lett. 52 2077–9, (1988).
59. Solovyov, V.; Dimitrov, I. K.; Li, Q., Growth of Thick $YBa_2Cu_3O_7$ Layers Via a Barium Fluoride Process. Supercond. Sci. Technol., 26, 013001, (2013).
60. McIntyre P. C., Cima M. J. and Ng M. F. Metalorganic deposition of high-Jc Ba2YCu3O7−x thin films from trifluoroacetate precursors onto (100) SrTiO3. J. Appl. Phys. 68 4183–7, (1990).
61. Izumi T., Yoshizumi M., Matsuda J., Nakaoka K., Kitoh Y., Sutoh Y., Nakanishi T., Nakai A., Suzuki K., Yamada Y., Yajima A., Saitoh T. and Shiohara Y. Progress in development of advanced TFA-MOD process for coated conductors Phys. C Supercond. its Appl. 463–465 510–4, (2007).
62. Dong, Z.; Ding, F.; Zhang, H.; Shang, H.; Huang, D.; Xu, W.; Li, T.; Zou, Q.; Gu, H., Preparation of High Performance YGdBCO Films by Low Fluorine TFA-MOD Process. J. Rare Earths 2020, 38, 755-762.
63. Wu W., Feng F., Zhao Y., Tang X., Xue Y., Shi K., Huang R., Qu T., Wang X., Han Z. and Grivel J. C. A low-fluorine solution with a 2:1 F/Ba mole ratio for the fabrication of YBCO films. Supercond. Sci. Technol. 27 055006, (2014).
64. Nasui, M., Petrisor., T., Mos, R. B., Gabor, M. S., Mesaros, A., Goga, F., Ciontea, L., & Petrisor, T. (2015). Fluorine-free propionate route for the chemical solution deposition of YBa2Cu3O7-x superconducting films. Ceramics International, 41(3), 4416–4421.
65. Yang, X., Wang, W. T., Liu, L., Huo, B. L., Wang, M. J., Yang, G. S., Tian, Z. J., Xia, Y. D., & Zhao, Y. Rapid Pyrolysis of $YBa_2Cu_3O_{7-\delta}$ Films by Fluorine-Free Polymer-Assisted Chemical Solution Deposition Approach. Journal of Superconductivity and Novel Magnetism 32(12), (2019).
66. Chu J., Zhao Y., Khan M. Z., Tang X., Wu W., Shi J., Wu Y., Huhtinen H., Suo H. and Jin Z. Insight into the Interfacial Nucleation and Competitive Growth of YBa2Cu3O7-δ Films as High-Performance Coated Conductors by a Fluorine-Free Metal-Organic Decomposition Route. Cryst. Growth Des. 19 6752–62, (2019).
67. Wesolowski D. E., Patta Y. R. and Cima M. J. Conversion behavior comparison of TFA-MOD and non-fluorine solution-deposited YBCO films. Phys. C Supercond. its Appl. 469 766–73, (2009).
68. Milonopoulou, V., Forster, K. M., Formica, J. P., Kulik, J., Richardson, J. T., & Luss, D. (1994). Influence of oxygen partial pressure on the kinetics of $YBa_2Cu_3O > 7- x$ formation. 9(2), 275–285.

69. Kursumovic, A.; Tomov, R. I.; Hühne, R.; MacManus-Driscoll, J. L.; Glowacki, B. A.; Evetts, J. E., Hybrid Liquid Phase Epitaxy Processes for $YBa_2Cu_3O_7$ Film Growth. Supercond. Sci. Technol. 2004, 17, 1215-1223.
70. Soler, L.; Jareño, J.; Banchewski, J.; Rasi, S.; Chamorro, N.; Guzman, R.; Yáñez, R.; Mocuta, C.; Ricart, S.; Farjas, J.; Roura-Grabulosa, P.; Obradors, X.; Puig, T., Ultrafast Transient Liquid Assisted Growth of High Current Density Superconducting Films. Nat. Comm. 2020, 11, 344.
71. Rasi, S., Queraltó, A., Banchewski, J., Saltarelli, L., Garcia, D., Pacheco, A., Gupta, K., Kethamkuzhi, A., Soler, L., Jareño, J., Ricart, S., Farjas, J., Roura-Grabulosa, P., Mocuta, C., Obradors, X., & Puig, T. Kinetic Control of Ultrafast Transient Liquid Assisted Growth of Solution-Derived YBa2Cu3O7-x Superconducting Films. Advanced Science, 2203834, 1–12, (2022).
72. Y. Yamada, Supercond. Sci. Technol. 13, 82, (2000).
73. P. Vermeir, J. Feys, J. Schaubroeck, K. Verbeken, P. Lommens, I. Van Driessche. Influence of sintering conditions in the preparation of acetate-based fluorine-free CSD YBCO films using a direct sintering method. Mater. Res. Bull., 47, 4376. (2012).
74. Y. Wu, G. Jiang, J. Zhu, D. Wu, X. Quan, J. Shi, H. Suo, Y. Zhao, Su- percond. Sci. Technol. 34, 05LT01. (2021).
75. Saltarelli, L., Gupta, K., Rasi, S., Kethamkuzhi, A., Queraltó, A., Garcia, D., Gutierrez, J., Farjas, J., Roura-Grabulosa, P., Ricart, S., Obradors, X., & Puig, T. Chemical and Microstructural Nanoscale Homogeneity in Superconducting YBa2Cu3O7-x Films Derived from Metal-Propionate Fluorine-free Solutions. ACS Applied Materials and Interfaces. (2022).
76. de Gans, B.-J., Duineveld, P. C. P. C., Schubert, U. S. U. S., Gans, B. B. De, Duineveld, P. C. P. C., & Schubert, U. S. U. S. (2004). Inkjet Printing of Polymers: State of the Art and Future Developments. Advanced Materials, 16(3), 203–213.
77. B. Derby. Inkjet printing of functional and structural materials: fluid property requirements, feature stability and resolution. Annual Review of Materials Research, 40: 395, (2010).
78. M. Vilardell. Inkjet printing: a flexible manufacturing of functional ceramic coatings by Chemical Solution Deposition. Universitat Autònoma de Barcelona, Bellaterra, (2014).
79. G.D. Martin, S.D. Hoath, and I.M. Hutchings. Inkjet printing - the physics of manipulating liquid jets and drops. Engineering and Physics, 105: 012001, (2008).
80. O. Basaran, H. Gao, and P. Bhat. Nonstandard inkjets. Annual Review of Fluid Mechanics, 45: 85, (2013).

81. W.G. Hawkins and I. Rezanka. Thermal ink jet printing. Imaging Science and Technology Report, 7: 1, (1992).
82. A.S. Yang, C.H. Cheng, and F.S. Hsu. PZT actuator applied to a femto-liter droplet ejector. Journal of Mechanical Science and Technology, 21: 1732, (2007).
83. T. Takahashi. Adaptability of piezoelectric inkjet head. International Conference on Digital Printing Technologies 17, 17: 323, (2001).
84. C. Bardeau, D. Fressard, P. Atten, and B. Barbet. Formation of isolated drops in a continuous jet. 10th International Congress on Advances in Non-Impact Printing Technologies, (1994).
85. A. Atkinson, J. Doorbar, A. Hudd, D.L. Segal, and P.J White. Continuous ink-jet printing using sol-gel "ceramic" inks. Journal of Sol-Gel Science and Technology, 8: 1093, (1997).
86. J.M. Schneider, N.R. Lindblad, C.D. Hendricks, and J.M. Crowley. Stability of an electrified liquid jet. Journal of Applied Physics, 38: 2599, (1967).
87. H. Dong, W.W. Carr, and J.F. Morris. An experimental study of drop-on-demand drop formation. Physics of Fluids, 18: 072102, (2006).
88. D.B. Bogy and F.E. Talke. Experimental and theoretical study of wave propagation phenomena in drop-on-demand ink jet devices. IBM Journal of Research and Development, 28: 3, (1984). Science and Technology, 19: S13, (2006).
89. P.H. Chen, W.C. Chen, and S.H. Chang. Bubble growth and ink ejection process of a thermal ink jet printhead. International Journal of Mechanical Sciences, 39: 683, (1997).
90. H. Wijshoff. The dynamics of the piezo inkjet printhead operation. Physics Reports, 491: 77, (2010).
91. N. Reis, C. Ainsley, and B. Derby. Ink-jet delivery of particle suspensions by piezoelectric droplet ejectors. Journal of Applied Physics, 97: 094903, (2005).
92. Villarejo, B. PhD dissertation. Synthesis of Defect Free $YBa_2Cu_3O_{7-x}$ Films over 1 μm by CSD Using Inkjet Printing. Universitat Autònoma de Barcelona, Bellaterra, (2018).
93. M. Vilardell, X. Granados, S. Ricart, I. Van Driessche, A. Palau, T. Puig, and X. Obradors. Flexible manufacturing of functional ceramic coatings by inkjet printing. Thin Solid Films, 548: 489, (2013)
94. Villarejo, B., Pop, C., Ricart, S., Mundet, B., Palau, A., Roura-Grabulosa, P., Farjas, J., Puig, T., & Obradors, X. Pyrolysis study of solution-derived superconducting YBa2Cu3O7films: Disentangling the physico-chemical transformations. Journal of Materials Chemistry C, 8(30), 10266–10282. (2020).

95. S.D. Hoath, I.M. Hutchings, G.D. Martin, T.R. Tuladhar, M.R. Mackley, and D. Vadillo. Links between ink rheology, drop-on-demand jet formation, and printability. Journal of Imaging Science and Technology, 53: 041208, (2009).

96. D. Jang, D. Kim, and J. Moon. Influence of fluid physical properties on ink-jet printability. Langmuir, 25: 2629, (2009).

97. J. Heinzl and C. Hertz. Ink-jet printing. Advances in Electronics and Electron Physics, 65: 91, (1985).

98. J.K. Spelt and A.W. Neumann. Solid surface tension: the equation of state approach and the theory of surface tension components. Theoretical and conceptual considerations. Langmuir, 3: 588, (1987).

99. J.F. Padday. Wetting, spreading and adhesion. Academic Press, London, (1978).

100. J. Eggers and E. Villermaux. Physics of liquid jets. Reports on Progress in Physics, 71: 036601, (2008).

101. J.E. Fromm. Numerical calculation of the fluid dynamics of drop-on-demand jets. IBM Journal of Research and Development, 28: 322, (1984).

102. Smith, P. J., Shin, D. Y., Stringer, J. E., Derby, B., & Reis, N. Direct ink-jet printing and low temperature conversion of conductive silver patterns. Journal of Materials Science, 41(13), 4153–4158. (2006).

103. J. Lyklema. Fundamentals of Interface and Colloid Science: Liquid Fluid Interfaces. Academic Press, (2005).

104. Uhlmann D. R. and Chalmers B. Interaction Between Particles and a Solid-Liquid Interface J. Appl. Phys. 35 2986, (1964).

105. A. Marmur. Solid-surface characterization by wetting. Annual Review of Materials Research, 39: 473, (2009).

106. T. Stoebe, Z. Lin, R.M. Hill, M.D. Ward, and H.T. Davis. Surfactant-enhanced spreading. Langmuir, 12: 337, (1996).

107. R.G. Good and L.A. Girifalco. A theory for estimation of surface and interfacial energies, III. Estimation of surface energies of solids from contact angle data. The Journal of Physical Chemistry, 64: 561, (1960).

108. D. B. van Dam and C. Le Clerc. Experimental study of the impact of an ink-jet printed droplet on a solid substrate. Physics of Fluids, 16(9):3403-3414, 2004.

109. Brian Derby. Inkjet Printing of Functional and Structural Materials: Fluid Property Requirements, Feature Stability, and Resolution. Annual Review of Materials Research, 40(1):395-414, (2010).

110. R.J. Hunter. Foundations of Colloid Science. Oxford University Press, (2001).

111. S. Stolen and T. Grande. Chemical Thermodynamics of Materials: Macroscopic and microscopic aspects. Wiley, (2004).

112. D. Myers. Surfaces, interfaces and colloids: Principles and applications. Wiley, (1999).

113. D. Bonn, J. Eggers, J. Indekeu, J. Meunier, and E. Rolley. Wetting and spreading. Review of Modern Physics, 81: 739, (2009).

114. M. Mulqueen and P.D.T. Huibers. Handbook of Applied Surface and Colloid Chemistry: Measuring equilibrium surface tensions. Wiley, (2002).

115. X.D. Wang, X.F. Peng, J.F. Lu, T. Liu, and B.X. Wang. Contact angle hysteresis on rough solid surfaces. Wiley Periodicals, (2004).

116. C.W. Extrand. An experimental study of contact angle hysteresis. Journal of Colloid and Interface Science, 191: 378, (1999).

117. E. Chibowski. On some relations between advancing, receding and Young contact angles. Advances in Colloid and Interface Science, 133: 51, (2007).

118. G.D. Nadkarni and S. Garoff. An investigation of microscopic aspects of contact angle hysteresis: pinning of the contact line on a single defect. Europhysics Letters, 20: 523, (1992).

119. W.A. Zisman. Relation of the equilibrium contact angle to liquid and solid constitution. Advances in Chemistry, 43: 1, (1964).

120. Yunker, P. J.; Still, T.; Lohr, M. A.; Yodh, A. G., Suppression of the Coffee-Ring Effect by Shape-Dependent Capillary Interactions. Nature, 476, 308-311, (2011).

121. Y. Rotenberg, L. Boruvka, and A. W. Neumann. Determination of surface tension and contact angle from the shapes of axisymmetric fluid interfaces. Journal of colloid and interface science, 93(1):169183, (1983).

122. S. H. Anastasiadis, J. K. Chen, J. T. Koberstein, A. F. Siegel, J. E. Sohn, and J. A. Emerson. The determination of interfacial tension by video image processing of pendant fluid drops. Journal of colloid and interface science, 119(1):5566, (1987).

123. Calleja, A.; Ricart, S.; Palmer, X.; Luccas, R. F.; Puig, T.; Obradors, X., Water Determination of Precursor Solutions with Oxidant Cations by the Karl Fischer Method: The YBCO-TFA Case. J. Sol-Gel Sci. Techn., 53, 347-352, (2010).

124. Tsai, M.-H., & Hwang, W.-S. Effects of Pulse Voltage on the Droplet Formation of Alcohol and Ethylene Glycol in a Piezoelectric Inkjet Printing Process with Bipolar Pulse. Materials Transactions, 49(2), 331–338. (2008).

125. H. Y. Gan, X. Shan, T. Eriksson, B. K. Lok, and Y. C. Lam. Reduction of droplet volume by controlling actuating waveforms in inkjet printing for micro-pattern formation. Journal of micromechanics and microengineering, 19(5):055010, 2009.

126. Meulen, M. Van Der. (2014). Meniscus Motion and Drop Formation.

127. Ruffieux, S., Kalaboukhov, A., Xie, M., Chukharkin, M., Pfeiffer, C., Sepehri, S., Schneiderman, J. F., & Winkler, D. The role of kinetic inductance on the performance of YBCO SQUID magnetometers. (2020).

128. Soler, L. PhD dissertation. Liquid-assisted ultrafast growth of superconducting films derived from chemical solutions. Universitat Autònoma de Barcelona, Bellaterra, (2019).

129. Zeleňák, V., Vargová, Z., & Györyová, K. Correlation of infrared spectra of zinc(II) carboxylates with their structures. Spectrochimica Acta – Part A: Molecular and Biomolecular Spectroscopy, 66(2), 262–272. (2007).

130. Deacon, G. B., & Phillips, R. J. Deacon G Phillips R. Coord. Chem. Rev., 33, 227–250. (1980).

131. Kakihana, M., & Nagumo, T. Assignment for the Infrared Spectrum of Solid Sodium Propionate from Low-Temperature Measurements in Combination with 13C Isotopic Shifts. Zeitschrift Fur Naturforschung - Section A Journal of Physical Sciences, 42(5), 477–484. (1987).

132. Rasi, S., Ricart, S., Obradors, X., Puig, T., Roura-Grabulosa, P., & Farjas, J. Radical and oxidative pathways in the pyrolysis of a barium propionate-acetate salt. Journal of Analytical and Applied Pyrolysis, 141(May), 104640. (2019).

133. Rasi, S., Silveri, F., Ricart, S., Obradors, X., Puig, T., Roura-Grabulosa, P., & Farjas, J. Thermal decomposition of CuProp2: In-situ analysis of film and powder pyrolysis. Journal of Analytical and Applied Pyrolysis, 140(April), 312–320. (2019).

134. Rasi, S., Ricart, S., Obradors, X., Puig, T., Roura, P., & Farjas, J. Thermal decomposition of yttrium propionate: film and powder. Journal of Analytical and Applied Pyrolysis, 133(March), 225–233. (2018).

135. Mos, R. B., Nasui, M., Gabor, M. S., Varga, R., Ciontea, L., Petrisor, T., & Petrisor, T. Synthesis, crystal structure and thermal decomposition study of a new barium acetato-propionate complex. Journal of Analytical and Applied Pyrolysis, 92(2), 445–449. (2011).

136. Nasui, M., Petrisor, T., Mos, R. B., Mesaros, A., Varga, R. A., Vasile, B. S., Ristoiu, T., Ciontea, L., & Petrisor, T. Synthesis, crystal structure and thermal decomposition kinetics of yttrium propionate. Journal of Analytical and Applied Pyrolysis, 106, 92–98. (2014).

137. Nasui, M., Mos, R. B., Gabor, M. S., Varga, R. A., Ciontea, L., Petrisor, T., & Petrisor, T. Synthesis, crystal structure and thermal decomposition of a new copper propionate [Cu(CH3CH2COO)2]·2H 2O. Journal of Analytical and Applied Pyrolysis, 92(2), 439–444. (2011).

138. R Urlaub, U Posset, and R Thull. Ft-ir spectroscopic investigations on sol-gel-derived coatings from acid-modified titanium alkoxides. Journal of Non-Crystalline Solids, 265(3):276284, (2000).

139. Rasi, S., Roura-Grabulosa, P., & Farjas, J. Application of thermal analysis and kinetic predictions to YBCO films prepared by chemical solution deposition methods. Journal of Thermal Analysis and Calorimetry, 142(5), 2077–2086. (2020).

140. https://www.microfab.com/dispensing-devices/low-temp-devices

141. https://services.icmab.es/nanoquim/

142. Stringer, J., & Derby, B. Formation and stability of lines produced by inkjet printing. Langmuir, 26(12), 10365–10372. (2010).

143. J. B. Szczech, C. M. Megaridis, D. R. Gamota, and J. Zhang. Fine-line conductor manufacturing using drop-on demand PZT printing technology. IEEE transactions on electronics packaging manufacturing, 25(1):26-33, 2002.

144. Amruth, C., Szymański, M. Z., Łuszczyńska, B., & Ulański, J. Inkjet Printing of Super Yellow: Ink Formulation, Film Optimization, OLEDs Fabrication, and Transient Electroluminescence. March, 1–10. (2019).

145. Liu, X., Tarn, T. J., Huang, F., & Fan, J. (2015). Recent advances in inkjet printing synthesis of functional metal oxides. Particuology, 19, 1–13.

146. S. Morlens, N. Roma, S. Ricart, A. Pomar, T. Puig, and X. Obradors. Thickness control of solution deposited YBCO superconducting films by use of organic polymeric additives. Journal of materials research, 22(8):23302338, (2007).

147. B.J. De Gans and U.S. Schubert. Inkjet printing of well-defined polymer dots and arrays. Langmuir, 20: 7789, (2004).

148. Allen, N. S. Photoinitiators for UV and visible curing of coatings: Mechanisms and properties. Journal of Photochemistry and Photobiology A: Chemistry, 100(1–3), 101–107. (1996).

149. Lee, D. J., Oh, J. H., & Bae, H. S. Crack formation and substrate effects on electrical resistivity of inkjet-printed. Materials Letters, 64(9), 1069–1072. (2010).

150. Park, S., Jang, S., Lee, D., Oh, J., & Kim, H. Two-step flash light sintering process for crack-free inkjet-printed Ag films. 015013.

151. L. A. Chow, B. Dunn, K. N. Tu, and C. Chiang. Mechanical properties of xerogel silica films derived from stress versus temperature and cracking experiments. Journal of Applied Physics, 87(11):77887792, (2000).

152. Godard, N., Mahjoub, M. A., & Schenk, T. On the importance of pyrolysis for inkjet-printed oxide piezoelectric thin films †. 3740–3747. (2020).

153. Dawley, J. T., Clem, P. G., Boyle, T. J., Ottley, L. M., Overmyer, D. L., & Siegal, M. P. Rapid processing method for solution deposited YBa2Cu3O7-d thin films. 402, 143–151. (2004).

154. Gómez-Núñez, A.; Alonso-Gil, S.; López, C.; Roura, P.; Vilà, A., Role of Ethanolamine on the Stability of a Sol–Gel ZNO Ink. J.Phys. Chem. C 2017, 121, 23839-23846.

155. Rasi, S., Ricart, S., Obradors, X., Puig, T., Roura-Grabulosa, P., & Farjas, J. Effect of triethanolamine on the pyrolysis of metal-propionate-based solutions. Journal of Analytical and Applied Pyrolysis, 143(July), 104685. (2019).

156. https://www.microdrop.de/positioning-system.html

157. https://www.microdrop.de/autodrop-pipettes.html

158. Van Driessche, I., Feys, J., Hopkins, S. C., Lommens, P., Granados, X., Glowacki, B. A., Ricart, S., Holzapfel, B., Vilardell, M., Kirchner, A., & Bäcker, M. Chemical solution deposition using ink-jet printing for YBCO coated conductors. Superconductor Science and Technology, 25(6), (2012).

159. Kordás, K., Mustonen, T., Tóth, G., Jantunen, H., Lajunen, M., Soldano, C., Talapatra, S., Kar, S., Vajtai, R., & Ajayan, P. M. Inkjet printing of electrically conductive patterns of carbon nanotubes. Small, 2, 1021–1025. (2006).

160. Park, E. E. S. Application of Inkjet-Printing Technology to Micro-Electro Mechanical Systems. 102. (2013).

161. Mattana, G.; Loi, A.; Woytasik, M.; Barbaro, M.; Noël, V.; Piro, B. Inkjet-Printing: A New Fabrication Technology for Organic Transistors. Adv. Mater. Technol. 2017, 2, No. 1700063.

162. Feys, J., Vermeir, P., Lommens, P., Hopkins, S. C., Granados, X., Glowacki, B. A., Baecker, M., Reich, E., Ricard, S., Holzapfel, B., Van Der Voort, P., & Van Driessche, I. Ink-jet printing of $YBa_2Cu_3O_7$ superconducting coatings and patterns from aqueous solutions. J. Mater. Chem., 22(9), 3717–3726. (2012).

163. Lau, G. K., & Shrestha, M. Ink-jet printing of micro-elelectro-mechanical systems (MEMS). Micromachines, 8(6), 1–19. (2017).

164. Liu, Y.; Derby, B., Experimental Study of the Parameters for Stable Drop-on-Demand Inkjet Performance. Phys. Fluids, 31, 032004. (2019).

165. Loi, A. PhD Dissertation, Inkjet printing: technique and applications for organic electronic devices. (2013).

166. Queraltó, A., Banchewski, J., Pacheco, A., Gupta, K., Saltarelli, L., Garcia, D., Alcalde, N., Mocuta, C., Ricart, S., Pino, F., Obradors, X., & Puig, T. Combinatorial screening of cuprate superconductors by drop-on-demand inkjet printing. ACS Applied Materials and Interfaces, 13(7), 9101–9112. (2021).

167. Queraltó, A., Pacheco, A., Jiménez, N., Ricart, S., Obradors, X., & Puig, T. (2022). Defining inkjet printing conditions of superconducting cuprate films through machine learning. Journal of Materials Chemistry C, 6885–6895.

168. N. Imanaka, T. Masui, Y. Mayama, K. Koyabu, Synthesis of crystalline yttrium oxycarbonate in a single phase, J. Solid State Chem. 178, 3601–3603. (2005).

169. Kato, M.; Jonassen, H. B.; Fanning, J. C. Copper(II) Complexes with Subnormal Magnetic Moments. Chem. Rev., 64, 99−128. (1964)

170. U. Hwang, H. Park, K. Koo, Behaviour of barium acetate and titanium isopropoxide during the formation of crystalline barium titanate, Ind. Eng. Chem. Res. 43, 728–734. (2004).

171. Wang, X., Hanson, J. C., Frenkel, A. I., Kim, J. Y., & Rodriguez, J. A. Time-resolved studies for the mechanism of reduction of copper oxides with carbon monoxide: Complex behaviour of lattice oxygen and the formation of suboxides. Journal of Physical Chemistry B, 108(36), 13667–13673. (2004).

172. Goldstein, E. A., & Mitchell, R. E. Chemical kinetics of copper oxide reduction with carbon monoxide. Proceedings of the Combustion Institute, 33(2), 2803–2810. (2011).

173. Rasi, S.; Soler, L.; Jareño, J.; Banchewski, J.; Guzmán, R.; Mocuta, C.; Kreuzer, M.; Ricart, S.; Roura, P.; Farjas, J.; Obradors, X.; Puig, T., Relevance of the Formation of Intermediate Non-Equilibrium Phases in YBCO Film Growth by Transient Liquid Assisted Growth. J.Phys. Chem. C 2020, 124, 15574-15584.

174. Evans, J. R. G.; Edirisinghe, M. J.; Coveney, P. V.; Eames, J., Combinatorial Searches of Inorganic Materials Using the Ink-Jet Printer: Science, Philosophy and Technology. J. Eur. Ceram. Soc. 2001, 21, 2291-2299.

175. Bag, M.; Jiang, Z.; Renna, L. A.; Jeong, S. P.; Rotello, V. M.; Venkataraman, D., Rapid Combinatorial Screening of Inkjet-Printed Alkyl-Ammonium Cations in Perovskite Solar Cells. Mater. Lett. 2016, 164, 472-475.

176. Zhigadlo, N. D.; Iranmanesh, M.; Assenmacher, W.; Mader, W.; Hulliger, J., Exploring Multi-Component Superconducting Compounds by a High-Pressure Method and Ceramic Combinatorial Chemistry. J. Supercond. Nov. Magn. 2016, 30, 79-84.

177. Cayado, P.; Erbe, M.; Kauffmann-Weiss, S.; Jung, A.; Hänisch, J.; Holzapfel, B., Chemical Solution Deposition of $Y_{1-x}Gd_xBa_2Cu_3O_{7-\square}$-$BaHfO_3$ Nanocomposite Films: Combined Influence of Nanoparticles and Rare-Earth Mixing on Growth Conditions and Transport Properties. RSC Adv., 2018, 8, 42398.

178. Cayado, P.; Erbe, M.; Kauffmann-Weiss, S.; Bühler, C.; Jung, A.; Hänisch, J.; Holzapfel, B., Large Critical Current Densities and Pinning Forces in CSD-Grown $GdBa_2Cu_3O_{7-x}$-$BaHfO_3$ Nanocomposite Films. Supercond. Sci. Technol. 2017, 30, 094007.

179. Matsushima, K.; Taka, C.; Nishida, A., Variations of Superconducting Transition Temperature in $YbBa_2Cu_3O_{7-\square}$ Ceramics by Gd substitution. J. Phys.: Conf. Ser. 2018, 969, 012059.

180. Zhang, S.; Xu, S.; Fan, Z.; Jiang, P.; Han, Z.; Yang, G.; Chen, Y., Broad Temperature Study of RE-Substitution Effects on the In-Field Critical Current Behavior of REBCO Superconducting Tapes. Supercond. Sci. Technol. 2018, 31, 125006.

181. Miura, S.; Yoshida, Y.; Ichino, Y.; Tsuruta, A.; Matsumoto, K.; Ichinose, A.; Awaji, S. Vortex Pinning at Low Temperature under High Magnetic Field in SmBa2Cu3Oy Superconducting Films with High Number Density and Small Size of BaHfO3 Nano-Rods. Supercond. Sci. Technol. 2015, 28, No. 114006. (9)

182. Rijckaert H., Cayado P., Nast R., Sierra J. D., Erbe M., Dominguez P. L., Hänisch J., de Buysser K., Holzapfel B. and van Driessche I. Superconducting HfO2-YBa2Cu3O7-δ nanocomposite films deposited using ink-jet printing of colloidal solutions. Coatings 10 1–15, (2020).

183. Ohno K, Uchiyama H and Kozuka H. Understanding of the development of in-plane residual stress in sol-gel-derived metal oxide thin films J. Appl. Phys. 111 014901, (2012).

184. Cop P., Kitano S., Niinuma K., Smarsly B. M. and Kozuka H. In-plane stress development in mesoporous thin films. Nanoscale 10 7002–15, (2018).

185. Zalamova K., Romà N., Pomar A., Morlens S., Puig T., Gázquez J., Carrillo A. E., Sandiumenge F., Ricart S., Mestres N. and Obradors X. Smooth stress relief of trifluoroacetate metal-organic solutions for YBa2Cu3O7 film growth. Chem. Mater. 18 5897–906, (2006).

186. L. Volynskii, S. Bazhenov, O. V. Lebedeva, and N. F. Bakeev. Mechanical buckling instability of thin coatings deposited on soft polymer substrates. Journal of Materials Science, 35(3):547554, (2000).

187. H. Jiang, D. Y. Khang, J. Song, Y. Sun, Y. Huang, and J. A. Rogers. Finite deformation mechanics in buckled thin films on compliant supports. Proceedings of the National Academy of Sciences, 104(40):1560715612, (2007).

188. Lee, S. H., Shin, K. Y., Hwang, J. Y., Kang, K. T., & Kang, H. S. Silver inkjet printing with control of surface energy and substrate temperature. Journal of Micromechanics and Microengineering, 18(7). (2008).

189. Song, J. W., Kim, J., Yoon, Y. H., Choi, B. S., Kim, J. H., & Han, C. S. Inkjet printing of single-walled carbon nanotubes and electrical characterization of the line pattern. Nanotechnology, 19(9). (2008).

190. Lim, T., Han, S., Chung, J., Chung, J. T., Ko, S., & Grigoropoulos, C. P. Experimental study on spreading and evaporation of inkjet printed pico-liter droplet on a heated substrate. International Journal of Heat and Mass Transfer, 52(1–2), 431–441. (2009).

191. Bartolomé, E., Vlad, V. R., Calleja, A., Aklalouch, M., Guzmán, R., Arbiol, J., Granados, X., Palau, A., Obradors, X., Puig, T., & Usoskin, A. Magnetic and structural characterization of inkjet-printed TFA YBa2Cu3O7-x/MODCZO/ ABADYSZ/SS coated conductors. Superconductor Science and Technology, 26(12). (2013).

192. Nakaoka, K., Yoshizumi, M., Usui, Y., Izumi, T., & Shiohara, Y. High-rate fabrication of {YBCO} coated conductors using TFA-MOD method. Physics Procedia, 27(0), 196–199. (2012).

193. Shiohara, Y.; Taneda, T.; Yoshizumi, M., Overview of Materials and Power Applications of Coated Conductors Project. Jap. J. Appl. Phys. 2012, 51, 010007.

194. Calvert, P., Inkjet Printing for Materials and Devices. Chem. Mater. 2001, 13, 3299-3305.

195. Van Driessche et al. Supercond. Sci. Technol. 25 065017, (2012).

196. M. Vilardell, X. Granados, S. Ricart, I. Van Driessche, A. Palau, T. Puig, X. Obradors, Flexible manufacturing of functional ceramic coatings by inkjet printing, Thin Solid Films, Volume 548, Pages 489-497, 2013.

197. Hopkins, S. C., Joseph, D., Mitchell-Williams, T. B., Calleja, A., Vlad, V. R., Vilardell, M., Ricart, S., Granados, X., Puig, T., Obradors, X., Usoskin, A., Falter, M., Bäcker, M., & Glowacki, B. A. Inkjet printing of multifilamentary YBCO for low AC loss coated conductors. Journal of Physics: Conference Series, 507(PART 2). (2014).

198. B.A. Glowacki and M. Makoros. Superconducting-magnetic heterostructures: a method of decreasing AC losses and improving critical current density in multifilamentary conductors. Journal of Physics: Condensed Matter, 21: 254206, 223. (2009).

199. N. Amemiya, S. Kasai, K. Yoda, Z. Jiang, G.A. Levin, P.N. Barnes, and C.E. Oberly. AC loss reduction of YBCO coated conductors by multifilamentary structure. Superconductor Science and Technology, 17: 1464, (2004).

200. Shiohara, Y.; Endo, A., Crystal Growth of Bulk High-Tc Superconducting Oxide Materials. Mat. Sci. Eng. R 1997, 19, 1-86.

201. Brandon, D., & Kaplan, W. D. Microstructural Characterization of Materials. John Wiley & Sons, Ltd. (2008).

202. Majkic, G.; Pratap, R.; Xu, A.; Galstyan, E.; Higley, H. C.; Prestemon, S. O.; Wang, X.; Abraimov, D.; Jaroszynski, J.; Selvamanickam, V., Engineering Current Density over 5 kA mm^{-2} at 4.2K, 14T in thick film REBCO tapes. Supercond. Sci. Technol. 31, 10LT01. (2018).

203. Gueriau, P.; Réguer, S.; Leclercq, N.; Cupello, C.; Brito, P. M.; Jauvion, C.; Morel, S.; Charbonnier, S.; Thiaudière, D.; Mocuta, C., Visualizing mineralization processes and fossil anatomy using synchronous synchrotron X-ray Fluorescence and X-ray diffraction mapping. J. R. Soc. Interface 2020, 17, 20200216.